

**A UNIFYING CONCEPTUAL MODEL TO DESCRIBE
WATER, VAPOR, AND SOLUTE TRANSPORT
IN DEEP ARID VADOSE ZONES**

By

Michelle A. Walvoord

Submitted in Partial Fulfillment of the Requirements for the Degree of
Doctor of Philosophy in Hydrology

New Mexico Institute of Mining and Technology

Socorro, New Mexico

May, 2002

ABSTRACT

Current understanding of the movement of water and solutes in deep desert vadose zones represents a major knowledge gap among the hydrologic science community. A particularly critical aspect in closing this gap is supplying a hydrologic framework that explains both matric potential and chloride vadose zone profiles typically observed beneath interdrainage regions of desert floors. This research seeks to close that gap. The conceptual model of deep arid system hydrodynamics (DASH) formulated as part of this study relies on vapor transport and the hydrologic role of desert plants that have become established during the past 10 to 15 thousand years in the southwestern U. S. as critical elements in explaining the observations. According to the DASH model and supported by field observations, desert vegetation sustains very negative matric potentials at the base of the root zone and effectively buffers the deep vadose zone over very long time scales from most hydrologic near-surface transients, such as episodic precipitation events. A nonisothermal, multiphase flow and transport code, FEHM, is used to numerically simulate the DASH conceptual model and other conceptual flow models previously proposed. Model results generated using the DASH paradigm match both characteristic matric potential profiles and chloride profiles, whereas model results generated using the other conceptual models that were tested deviate dramatically from observed matric potential data. A unifying theory for the hydrology of desert

vadose zones is particularly timely considering current water stresses and contaminant issues associated with desert regions.

A sensitivity analysis tests the applicability of the DASH model to a wide range of desert vadose zone parameters and conditions. The sensitivity analysis also enables assessment of the factors that control moisture movement in deep vadose zones. The results indicate that most thick desert vadose zones have been locked in slow drying transients for many thousands of years, since the desert vegetation became established. A hydrodynamic condition, as opposed to a hydrostatic condition, characterizes deep vadose zones in equilibrium with the dry hydraulic conditions imposed by desert vegetation. Long response times, on the order of 10^4 - 10^6 years, are required to reach this hydrodynamic equilibrium, which exceeds the typical time scale of major climate shifts.

Two case studies demonstrate the application of the DASH model to interpretation of measured hydraulic and solute profiles from deep arid vadose zones. The DASH model approach enables paleohydrologic reconstruction and yields information about current vapor and liquid fluxes between the base of the root zone and the water table. Both case studies emphasize the influence of desert vegetation on deep vadose zone hydrodynamics. Desert vadose zone hydraulic profiles cannot be resolved apart from their climate and vegetation histories.

ACKNOWLEDGMENTS

First and foremost, I am indebted to my advisor and mentor Dr. Fred Phillips for providing invaluable guidance throughout my graduate career. He continually challenged me to think broadly while narrowing the focus of my research to address specific questions and attending to details. I have come to appreciate that this type of balance in scientific research is truly an art. I am extremely grateful to the members of my Ph.D. committee and of the diversity they collectively brought to the table. Dr. Jan Hendrickx and Dr. Robert Bowman offered thoughtful comments based on their expertise in semiarid vadose zone hydrology and geochemistry. Dr. William Pockman brought in the perspective of a plant biologist, a well-needed addition to my research. Dr. Andrew Wolfsberg provided extremely helpful assistance from both technical and conceptual aspects to ensure that I “kept it real”. Also, lively discussions with Mitchell Plummer, Dr. Scott Tyler, and Dr. Phillip Stauffer helped shape the direction of my work. Thanks to Peter Hartsough, I look back at our long days in the field at the NTS with a grin. A unique cast of characters have added the spice to my experience both within and outside of the academic domain – you know who you are – and for that I thank you a million times over! I am especially grateful to Tristan Wellman for his enthusiasm and support that helped push me along and kept me smiling. Finally, I am truly appreciative of my parents whose unflagging love and support I felt every step of the way even thousands of miles away.

TABLE OF CONTENTS

	Page
ABSTRACT	
ACKNOWLEDGMENTS.....	ii
TABLE OF CONTENTS.....	iii
LIST OF TABLES.....	x
LIST OF FIGURES.....	xii
Chapter 1. INTRODUCTION.....	1
1.1. Motivation for Study.....	1
1.2. Questions.....	2
1.2.1. Controls on Moisture Movement in Thick Vadose Zones.....	2
1.2.2. Deep Vadose-Zone Hydraulic Response.....	3
1.2.3. Holocene-Pleistocene Xeric Transition	4
1.2.4. Paleohydrologic Archive Potential.....	5
1.2.5. Vegetation Type Proxy for Desert-Floor Recharge.....	5
1.3. Research Approach.....	6
Chapter 2. BACKGROUND AND PREVIOUS STUDIES.....	8
2.1. Introduction.....	8

2.2. Matric Potential as a Hydrologic Indicator	9
2.2.1. Hydraulic Potentials in the Vadose Zone.....	9
2.2.2. Conventional Hydrostatic Equilibrium Model.....	11
2.2.3. Unit Gradient Model.....	12
2.2.4. Hydrologic Interpretations of Observed Matric Potential Profiles.....	13
2.3. Chloride as a Hydrologic Tracer.....	17
2.3.1. Chloride Deposition.....	17
2.3.2. Chloride Transport Behavior.....	18
2.3.3. Chloride Mass Balance Method.....	19
2.3.4. Hydrologic Interpretations of Observed Chloride Profiles.....	21
2.4. Implications of the Downward-Only Flux Assumption.....	24
2.5. Implications of the Zero Flux Assumption.....	24
2.6. Deuterium and Oxygen-18 as Hydrologic Tracers	25
2.6.1. δD and $\delta^{18}O$ Fractionation.....	26
2.6.2. Hydrologic Interpretations of Observed δD and $\delta^{18}O$ Profiles.....	26
2.7. Chlorine-37 as a Hydrologic Indicator.....	29
2.7.1. $\delta^{37}Cl$ Fractionation.....	29
2.7.2. Hydrologic Interpretations of Observed $\delta^{37}Cl$ Profiles.....	30

Chapter 3. DEEP ARID SYSTEM HYDRODYNAMIC MODEL

DEVELOPMENT.....	31
3.1. Introduction.....	31
3.2. Conceptual Model.....	31

3.3.	Mathematical and Numerical Models.....	35
3.4.	Boundary Conditions, Initial Conditions and Input Parameters.....	38
3.5.	Testing the DASH Conceptual Model.....	41
3.6.	Development of the Current Moisture Flux Regime.....	45
3.7.	Chloride Transport.....	47
3.8.	Stable Chlorine Isotope Transport.....	49
3.9.	Hydrodynamic Equilibrium State.....	51
3.10.	Summary.....	54

Chapter 4. CONTROLS ON DESERT VADOSE ZONE MOISTURE

	FLUXES AND HYDROLOGIC RESPONSE TIMES.....	58
4.1.	Introduction.....	58
4.2.	Geothermal Gradient.....	59
4.3.	Soil Type and Saturated Permeability.....	62
4.4.	Water Table Depth.....	64
4.5.	Fixed Root-Zone Potential Condition.....	67
4.6.	Enhanced Vapor Diffusion.....	69
4.7.	Transition Reversal.....	71
4.8.	Conceptual Limitations.....	75
	4.8.1. Lateral Flow.....	77
	4.8.2. Preferential Flow.....	79
	4.8.3. Hydraulic Functions.....	80
4.9.	Summary.....	81

Chapter 5. SITE-SPECIFIC CASE STUDY 1: Nevada Test Site.....	84
5.1. Introduction.....	84
5.2. Description of Study Location.....	85
5.2.1. Regional Geology.....	87
5.2.2. Local Geology.....	88
5.2.3. Local Hydrology.....	91
5.2.4. Current Climate and Vegetation.....	91
5.2.5. Regional Paleoclimate.....	92
5.2.6. Regional Paleoecology.....	93
5.3. Field and Laboratory Methods.....	95
5.3.1. Sample Collection.....	95
5.3.2. Laboratory Methods.....	98
5.4. Results From Deep Vadose-Zone Cores.....	100
5.4.1. Frenchman Flat.....	100
5.4.2. Yucca Flat.....	103
5.4.2.1. Soil Characteristics.....	103
5.4.2.2. Water Content.....	107
5.4.2.3. Water Potential Profiles.....	110
5.4.2.4. Chloride Profiles.....	112
5.4.2.5. Nitrate Profiles.....	115
5.4.2.6. Stable Isotope Profiles.....	118
5.4.2.7. Estimation of Geothermal Gradient.....	120
5.5. Chloride Mass Balance Approach for Paleohydrologic Reconstruction.....	120

5.5.1.	Deep Cores from Frenchman Flat and Yucca Flat.....	120
5.5.2.	Yucca Flat Shallow Series Cores.....	123
5.6.	Nitrogen Fluxes.....	124
5.7.	Discussion of Spatial Variability at Yucca Flat.....	128
5.8.	DASH Model Method.....	130
5.9.	DASH Model Results.....	133
5.9.1.	Matric Potentials.....	133
5.9.2.	Chloride.....	135
5.9.3.	Paleoflux Histories.....	137
5.9.4.	Current Moisture Flux Regime.....	139
5.9.5.	Discussion of DASH Model Application.....	141
5.10.	Implications for CMB Application to Desert Vadose-Zone Profiles.....	143
5.11.	Summary.....	145
 Chapter 6. CASE STUDY 2: TRANS-PECOS REGION.....		147
6.1.	Introduction.....	147
6.2.	Description of Study Location.....	151
6.2.1.	Regional Geology.....	153
6.2.2.	Local Geology.....	155
6.2.3.	Local Hydrology.....	157
6.2.4.	Current Climate.....	158
6.2.5.	Current Regional Vegetation.....	159
6.2.6.	Site Vegetation.....	161

6.2.7.	Paleoclimate.....	167
6.2.8.	Regional Paleoecology.....	168
6.2.9.	Regional Historic Vegetation Changes.....	170
6.3.	Field and Laboratory Methods.....	172
6.3.1.	Sample Collection.....	172
6.3.2.	Laboratory Methods.....	174
6.4.	Results from the Trans-Pecos Cores.....	175
6.4.1.	Soil Characteristics.....	175
6.4.2.	Water Content.....	177
6.4.3.	Water Potential.....	178
6.4.4.	Chloride, Bromide and Fluoride.....	180
6.4.5.	Nitrate.....	186
6.4.6.	Chlorine-37.....	188
6.5.	Chloride Mass Balance Application.....	190
6.6.	Nitrogen Fluxes.....	193
6.7.	Comparison of Nitrogen Fluxes at Case Study Sites 1 and 2.....	195
6.8.	DASH Model Application.....	197
6.9.	Interpretation of Trans-Pecos Vadose Zone Profiles.....	202
6.9.1.	McKeel Desertscrub Site.....	202
6.9.1.1.	Matric Potential.....	202
6.9.1.2.	Chloride.....	203
6.9.1.3.	Current Moisture Fluxes.....	205
6.9.1.4.	Chlorine-37.....	206

6.9.1.5. Evidence of Isolated Flushing.....	207
6.9.2. Miller Ranch Creosote – Grassland Ecotone Sites.....	208
6.9.2.1. Matric Potential.....	208
6.9.2.2. Chloride.....	211
6.9.3. Juniper Stand Site.....	217
6.9.4. Discussion of Profile Interpretations.....	221
6.10. Summary.....	224
Chapter 7. CONCLUSIONS.....	226
7.1. Influence of Climate and Vegetation Transitions on Vadose Zone Moisture Flux Regimes.....	227
7.2. Deep Vadose Zone Hydraulic Response.....	229
7.3. Subsurface Controls on Moisture Fluxes in Deep Vadose Zones.....	229
7.4. Paleohydrologic Records in Deep Vadose Zones.....	231
7.5. Vegetation Type and Moisture Flux Relationships.....	232
REFERENCES.....	233
APPENDIX A – FEHM Model Description.....	245
APPENDIX B – Data from Nevada Test Site Unsaturated Zone Cores.....	266
APPENDIX C – Data from Trans-Pecos Unsaturated Zone Cores.....	287

LIST OF TABLES

	Page
Table 3-1. Stable chlorine isotope transport parameters and values at 20 °C.....	38
Table 3-2. Base case input parameters.....	40
Table 3-3. Initial and boundary conditions for testing the three conceptual models.....	42
Table 3-4. Comparison of “current” moisture fluxes for the base case estimated using a CMB approach to the DASH model results.....	47
Table 4-1. Summary of equilibrium response times calculated from the DASH model sensitivity analysis.....	61
Table 4-2. Parameters used in sensitivity analysis for three soil types.....	62
Table 4-3. Summary of equilibrium response times calculated from the DASH model transition reversal simulations.....	73
Table 5-1. Soil texture data from the Yucca Flat cores.....	106
Table 5-2. Calculated chloride mass balance ages and nitrogen fluxes for the Yucca Flat Shallow Series cores.....	126
Table 5-3. Input parameters for Frenchman Flat (PW-series cores) and Yucca Flat (UE6s/UE6e) site-specific simulations.....	132

Table 5-4. Simulation histories and associated surface boundary conditions from the Frenchman Flat and Yucca Flat cores.....	133
Table 5-5. Comparison of current net moisture fluxes estimated using a CMB approach and the modeling approach taken in this study.....	144
Table 6-1. Summary of site location and coring information.....	173
Table 6-2. Summary table for hydraulic, physical, and geochemical measurements completed on Trans-Pecos core samples.....	185
Table 6-3. Calculated chloride mass balance ages, measured accumulated nitrogen and calculated nitrogen fluxes for the Trans-Pecos cores.....	194
Table 6-4. Input parameters for Trans-Pecos site-specific simulations.....	200
Table 6-5. Simulation histories and associated surface boundary conditions that best match profile data from the Trans-Pecos cores.....	201

LIST OF FIGURES

	Page
Figure 2-1. Conventional hydrostatic equilibrium model.....	12
Figure 2-2. Unit gradient model.....	13
Figure 2-3. Vadose-zone potential profiles under desert floor environments in Nevada and West Texas.....	14
Figure 2-4. Idealized chloride concentration vadose-zone profile.....	20
Figure 2-5. Vadose-zone chloride profiles under desert floor environments in Nevada, West Texas, New Mexico and Southeastern Washington...	22
Figure 2-6. Theoretically predicted deuterium profiles for quasi-steady-state evaporation under isothermal and non-isothermal conditions.....	27
Figure 3-1. Seasonal variation of water potentials at various depths from sites in the Mojave Desert, NV and in the Chihuahuan Desert, TX.....	34
Figure 3-2. Schematic depiction of the base case vadose zone prototype.....	39
Figure 3-3. Plot of diffusion coefficient as a function of volumetric water content as defined by the <i>Conca</i> and <i>Wright</i> [1992] function.....	41
Figure 3-4. Simulated matric potential profiles for the reduced recharge model, zero recharge model , DASH model, and observed profiles	43
Figure 3-5. Simulated chloride profiles for the reduced recharge model, zero-recharge model , DASH model, and observed profiles.....	44

Figure 3-6.	Simulated net moisture flux profiles for times after the xeric boundary condition transition using the DASH model.	45
Figure 3-7.	Simulated moisture flux profile for present conditions using the DASH model.....	47
Figure 3-8.	Simulated chloride profile at t = 15 kyr using the DASH model compared with the analytic diffusion solution at t = 15 kyr.....	49
Figure 3-9.	Simulated $\delta^{37}\text{Cl}$ profiles using the DASH model at several snapshots in time.....	50
Figure 3-10.	Simulated steady-state matric potential profile for the base case using the DASH model.....	52
Figure 3-11.	Simulated steady-state moisture flux profiles for the base case using the DASH model.....	53
Figure 4-1.	Simulated steady-state matric potential profiles for variable geothermal gradient using the DASH model.....	60
Figure 4-2.	Simulated steady-state matric potential profiles for variable soil types using the DASH model.....	63
Figure 4-3.	Response time as a function of saturated permeability.....	63
Figure 4-4.	Simulated steady-state matric potential profiles with the Base Case properties for variable water table depths using the DASH model.....	65
Figure 4-5.	Compiled steady-state matric potential profiles for variable water table depths and response time graph.....	65
Figure 4-6.	Simulated steady-state moisture flux profiles for variable water table depths using the DASH model.....	66

Figure 4-7. Simulated steady-state matric potential profiles for variable fixed root-zone matric potential values using the DASH model.....	69
Figure 4-8. Calculated response time as a function of the vapor enhancement factor.....	71
Figure 4-9. Transient matric potential profiles using the DASH model and recording the switch from dry conditions to downward fluxes	74
Figure 4-10. Vadose zone profile response to a 10 year, 5 mm yr ⁻¹ infiltration event.....	75
Figure 5-1. Location of Case 1 study site.....	86
Figure 5-2. Cross-section through Yucca Flat and Frenchman Flat depicting local subsurface geology.....	89
Figure 5-3. Map view of Nevada Test Site.....	90
Figure 5-4. Paleolake level reconstruction of Lake Lahonton located in the Great Basin.....	93
Figure 5-5. Vegetation plotted as a function of time and elevation for the northern Mojave Desert using packrat middens.....	94
Figure 5-6. Hollow-stem auger drilling and sample collection of vadose zone core, UE6s, at Yucca Flat, Nevada Test Site.....	96
Figure 5-7. Split-spoon sampler lined with brass sleeves for core collection.....	96
Figure 5-8. Map of Yucca Flat Shallow Series core locations.....	97
Figure 5-9. Measured water potential profiles from the Frenchman Flat cores.....	101
Figure 5-10. Measured chloride profiles from the Frenchman Flat cores.....	102
Figure 5-11. Measured stable isotope profiles from the Frenchman Flat cores.....	102

Figure 5-12.	Stable isotope relationships from Frenchman Flat cores.....	103
Figure 5-13.	Soil texture trilinear diagram from Yucca Flat cores.....	104
Figure 5-14.	Grain-size distribution profiles from the UE6s, A1 and A3 cores....	105
Figure 5-15.	Grain-size distribution profiles from the UE6e core.....	106
Figure 5-16.	Dry bulk density measurements from the UE6s core.....	107
Figure 5-17.	Measured gravimetric water content from the UE6s core.....	108
Figure 5-18.	Measured gravimetric water content from the UE6e core.....	109
Figure 5-19.	Measured gravimetric water content from the shallow series cores..	109
Figure 5-20.	Measured water potential profile from the UE6s core.....	110
Figure 5-21.	Measured water potential profiles from the Yucca Flat Shallow cores.....	111
Figure 5-22.	Measured chloride concentration profiles from UE6s and UE6e cores.....	113
Figure 5-23.	Measured chloride concentration profiles from the Yucca Flat Shallow Series cores.....	115
Figure 5-24.	Nitrate concentration profile from the UE6s core.....	116
Figure 5-25.	Nitrate profiles from the Yucca Flat Shallow Series cores.....	117
Figure 5-26.	Measured stable isotope profiles from the UE6s core.....	119
Figure 5-27.	Stable isotope relationships from the UE6s core.....	120
Figure 5-28.	Graph of chloride mass balance age with profile depth from the NTS cores and paleoflux reconstruction	122
Figure 5-29.	Graph of chloride mass balance age with depth from the Yucca Flat Shallow Series cores.....	124

Figure 5-30.	Nitrate profile from the buried clean sand column, NTS8.....	128
Figure 5-31.	Model-simulated matric potential profiles developed over time in response to climate/vegetation transitions at the NTS.....	134
Figure 5-32.	Model-simulated chloride profiles developed over time in response to climate/vegetation transitions at the NTS.....	136
Figure 5-33.	Surface boundary condition sequences used in model simulations to best match observed vadose-zone profile data from the NTS.....	138
Figure 5-34.	Model-predicted liquid flux profiles at several snapshots in time.....	138
Figure 5-35.	Model-predicted moisture flux profiles at t = 0 (the present).....	140
Figure 6-1.	Location of Case 2 study sites in the Trans-Pecos region, West Texas.....	152
Figure 6-2.	Areal extent of the Chihuahuan Desert.....	154
Figure 6-3.	Physiographic features of the western Trans-Pecos region.....	156
Figure 6-4.	Photos of the Mc Keel desert scrub site, near the SA and SB core locations.....	163
Figure 6-5.	Photos of the Miller Ranch recently-encroached desert scrub site, near the DA core location.....	164
Figure 6-6.	Photos of the Miller Ranch grassland site, near the GD and GS core locations.....	165
Figure 6-7.	Photos of the Miller Ranch juniper site, near the JA and JB core locations.....	166
Figure 6-8.	Drilling using the hollow-stem augering method.....	173
Figure 6-9.	Core sample collection in brass-sleeves lining the split spoon.....	174

Figure 6-10.	Stratigraphic columns for the Trans-Pecos cores.....	175
Figure 6-11.	Gravimetric water content measurements from the Trans-Pecos cores.....	177
Figure 6-12.	Graph of gravimetric water content means and standard deviations for the Trans-Pecos cores.....	178
Figure 6-13.	Water potential measurements from the Trans-Pecos cores.....	179
Figure 6-14.	Measured chloride concentration profiles from the Trans-Pecos cores.....	181
Figure 6-15.	Measured bromide concentration profiles and Cl:Br ratios from the Trans-Pecos cores.....	182
Figure 6-16.	Measured fluoride concentration profiles from the Trans-Pecos cores.....	184
Figure 6-17.	Measured nitrate profiles, with chloride profiles for comparison, from the Trans-Pecos cores.....	187
Figure 6-18.	Measured nitrate concentration profiles from the Trans-Pecos cores.....	188
Figure 6-19.	Measured $\delta^{37}\text{Cl}$ profile, with the chloride porewater concentration profile for comparison, from the SA Trans-Pecos core.....	190
Figure 6-20.	Graph of chloride mass balance age with profile depth from the Trans-Pecos cores.....	192
Figure 6-21.	Graph of annual inorganic N deposition based on 20 years of data from Panther Junction, Big Bend National Park, Texas.....	195

Figure 6-22.	Soil moisture characteristic curves developed from field condition measurements in the SA, SB, JA and JB cores.....	199
Figure 6-23.	Soil moisture characteristic curves developed from field condition measurements in the layered DA, GS and GD cores.....	199
Figure 6-24.	Model-simulated matric potential profiles developed over time in response to climate/vegetation transitions at McKeel site.....	202
Figure 6-25.	Model-simulated chloride profiles developed over time in response to climate/vegetation transitions at the McKeel site.....	204
Figure 6-26.	Apparent chloride mass balance (CMB) age distribution for the SA measured profile compared with the model-simulated profile.....	204
Figure 6-27.	Model-predicted moisture flux profiles at t = 0 (the present) at the McKeel desert scrub site.....	205
Figure 6-28.	Model-simulated $\delta^{37}\text{Cl}$ profiles developed over time in response to climate/vegetation transitions at the McKeel site.....	207
Figure 6-29.	Model-simulated matric potential profiles developed over time in response to climate/vegetation transitions at GD Miller Ranch site..	209
Figure 6-30.	Measured matric potential profiles at the Miller Ranch grassland – creosote ecotone site.....	211
Figure 6-31.	Model-simulated chloride profiles developed over time in response to climate/vegetation transitions at the GD Miller Ranch site.....	212
Figure 6-32.	Apparent chloride mass balance age distribution for the GD measured profile compared with the model-simulated profile.....	213

Figure 6-33.	Model-simulated chloride profiles developed over time in response to climate/vegetation transitions at the GS Miller Ranch site.....	214
Figure 6-34.	Apparent chloride mass balance age distribution for the GS measured profile compared with the model-simulated profile.....	215
Figure 6-35.	Model-simulated chloride profiles developed over time in response to climate/vegetation transitions at the DA Miller Ranch site.....	216
Figure 6-36.	Apparent chloride mass balance age distribution for the DA Measured profile compared with the model-simulated profile.....	217
Figure 6-37.	Model-simulated steady-state matric potential profiles compared to measured data from JA and JB.....	218
Figure 6-38.	Model-predicted moisture flux profiles at steady state at the Juniper Miller Ranch site.....	218
Figure 6-39.	Model-simulated matric potential profiles for a specified root-zone matric potential condition of -500 m.....	219

This dissertation is accepted on behalf of the
Faculty of the Institute by the following committee:

Fred M Phillips

Advisor

Walter T Pugh

Arthur Wapner *Andrew Wolfberg*

Robert Bowman

Hendricks

Date

I release this document to the New Mexico Institute of Mining and Technology.

Mitchell A. Walwood

Student's Signature

April 15, 2002

Date

CHAPTER 1.

INTRODUCTION

1.1. Motivation for Study

Rising pressure of population in arid and semiarid regions increases the need for reliable water resources and necessitates assurances of safe waste disposal. Is there significant downward moisture movement through interdrainage desert-floor environments that will recharge the aquifers below [*Gee and Kirkham*, 1984; *Stone*, 1984; *Stone and McGurk*, 1985; *Stephens and Knowlton*, 1986; *Stephens*, 1994]? Or, do thick vadose zones serve as effective barriers to moisture flow and contaminant migration from the surface or from a repository to the water table [*Winograd*, 1981; *Reith and Thompson*, 1992]? The initial step in addressing these questions involves understanding the processes that control moisture-flux regimes in desert vadose zones and the timescales on which these processes operate. Are thick desert vadose zones in equilibrium with surface climatic conditions or are the hydraulic measurements obtained from deep profiles a response to paleoclimatic conditions? Do the same concepts and controlling factors for unsaturated flow and transport in humid-regions apply to arid-region vadose zones? In this study, I examine the existing conceptual models applied to arid-region flow and transport in thick vadose zones and assess

their merit based on their ability to explain measured matric potential and chloride profiles.

Moisture fluxes through desert vadose zones comprised of unconsolidated material are typically very small and difficult to quantify. Despite many advances in soil physics in the past half-century, certain shortcomings of the commonly-employed equations and assumptions persist when they are applied in desert environments. Measured profiles of environmental tracer solutes, especially chloride, are commonly used in vadose zone hydrology to quantify groundwater recharge from the vadose zone. The conventional chloride mass balance (CMB) approach relies on the assumption of 1-D downward water movement. Yet matric potential profiles taken from the same sites as chloride profiles used to estimate recharge indicate upward water movement, at least in the top 20-40 meters [Scanlon *et al.*, 1997a]. How can this paradox be reconciled? In attempts to resolve this apparent discrepancy and better understand the hydrological role of vadose zones in arid regions, this study employs an integrated field and modeling based approach.

1.2. Questions

1.2.1. Controls on Moisture Movement in Thick Vadose Zones

A fundamental understanding of the important controls on flow and transport in most hydrologic environments was arrived at several decades ago. This is not the case for arid vadose zones. Conventional theory and conceptual models of unsaturated flow and transport developed for humid and irrigated soils identifies factors such as the amount of precipitation, soil hydraulic properties (particularly

unsaturated permeability, porosity and water content) and soil heterogeneity as largely controlling humid-region unsaturated flow and transport. Do these same factors dictate the hydraulic regime in deep desert soils or do other factors exert greater influence?

Question 1: What physical properties or environmental conditions exert predominant control on the direction and rate of water movement in very dry and thick desert vadose zones under interdrainage regions?

1.2.2. Deep Vadose Zone Hydraulic Response

Interpretation of vadose-zone matric potential profiles depends on the presumption of the system state as steady or transient. For example, a measured matric potential profile displaying an upward flow gradient indicates the persistence of upward fluxes over what length of time: a day, a season, a decade, or much longer? Such inquiry begs the question: how quickly do deep vadose zones equilibrate to drying and wetting surface conditions? Are diurnal and/or seasonal changes preserved in the subsurface? If so, to what depths do transients typically propagate? If deep vadose zones require extremely long times for drying, measured profiles that exhibit very negative matric potential values at significant depths may constitute reliable evidence that drying trends have persisted for thousands of years.

Question 2: What are the timescales for response of thick desert vadose zones to rapid changes in surface boundary conditions?

1.2.3. Holocene-Pleistocene Xeric Transition

Arid vadose zones in the southwestern U. S. typically exhibit characteristic chloride “bulges” with high concentrations in the upper 10-20 meters and more dilute concentrations at greater depths. Typical profiles contain chloride bulge inventories equivalent to 10-15 kyr of atmospheric deposition (more detail provided in the following chapter). Although several explanations have been offered to explain these profiles, the most plausible and generally accepted for the Southwest is that a climatically-controlled change in the regional water balance prior to the Holocene resulted in a dramatic reduction in recharge through these thick vadose zones [Phillips, 1994]. A critical assumption for the reduced recharge hypothesis is that one-dimensional downward flow below the root zone characterizes the flow regime. Accordingly, the residual soil-water flux below the root zone equals the flux across the water table interface as groundwater recharge. For the most extreme reduced recharge case, the zero recharge model, the residual soil-water flux below the root zone ceased coincident with the onset of the Holocene. Assuming that the profile has had sufficient time to drain, no-flow conditions describe the flow regime below the root zone. The reduced recharge and zero recharge models suffer from a fundamental weakness: total hydraulic potential profiles, corresponding to the typical chloride bulge profiles, display *upward flow* gradients in the upper 20-40 meters [Scanlon *et al.*, 1997a]. A conceptual model to interpret vadose-zone profile data should be internally consistent. Can an alternative consequence of the Holocene-Pleistocene climate shift as expressed in thick vadose zones (as opposed to a reduction or cessation in infiltration) offer reconciliation?

Question 3: What aspects of the processes within desert vadose zones, and their histories, can explain both the observed solute profiles and the matric potential profiles?

1.2.4. Paleohydrologic Archive Potential

Recent studies have recognized the potential of thick desert vadose zones as archives of paleohydrologic information due to their very small soil-water fluxes. However, the standard chloride mass balance (CMB) approach assumes downward-only advection, which may not accurately describe the flow regime in deep vadose zones. Improved profile data interpretation, particularly paleohydrologic reconstruction, should ensue from implementing a correct conceptual model of the system hydrodynamics. What are the implications of interpreting observed desert vadose zone profiles by applying humid-region vadose zone concepts?

Question 4: How do the unusual hydrodynamics of arid vadose zones affect their potential use as archives of paleohydrology?

1.2.5. Vegetation Type Proxy for Desert-Floor Recharge

Estimating recharge using deep vadose zone profiles requires considerable time and effort and provides only point measurements. From a water resource management and sustainability perspective, point recharge estimates are useful only to the degree to which they can be spatially extrapolated. Basin-scale water balances require quantification of all recharge components, including the contribution of

desert-floor recharge. A desirable upscaling approach from point measurements to the basin scale would avoid massive efforts to drill and analyze hundreds to thousands of vadose zone cores spatially distributed regularly throughout the basin. Accordingly, we would like to find a suitable *proxy* for interdrainage region desert-floor recharge to minimize drilling efforts. Necessary attributes for an appropriate proxy include a strong linkage with deep vadose zone moisture fluxes and a readily observable quality. Vegetation type may best satisfy these requirements: desert vegetation appears to exert a major control on moisture fluxes in water-limited environments [Gee *et al.*, 1994]. In the final stage of this study, I explore the utility of using vegetation type, an easily observed surface property, as a proxy for recharge. The project is designed to provide a basis for innovative desert-floor recharge upscaling methods that maximize efficient field efforts.

Question 5: How does the interaction of different types of desert plants and the hydraulic state of the root zone ultimately affect groundwater recharge?

1.3. Research Approach

This study seeks to examine processes and factors influencing flow and transport over long timescales in deep desert vadose zones through integrative numerical modeling and field investigations. Results from numerical simulations of multiphase flow under non-isothermal conditions coupled with transport of solute tracers are compared with observed data from deep arid vadose zones in the southwestern US. First, flow and transport simulations using a generic thick vadose

zone prototype allow multiple conceptual models regarding long-term moisture and solute movement in desert vadose zones to be tested. Based on these results and field observations, an alternative conceptual model is developed to best match the characteristic shapes and magnitudes of hydraulic and environmental tracer data from deep vadose zone profiles. Simulations that incorporate the improved conceptual model provide the means to investigate the flow regimes of vadose zones in equilibrium with current xeric surface conditions and determine response times to approach equilibrium. Next, a detailed sensitivity analysis enables identification of the major controls on current desert vadose zone moisture fluxes and the parameters that regulate system response times. The final two research initiatives involve application of the knowledge gained in the early work by addressing specific sites in the northern Mojave Desert in Nevada and the Chihuahuan Desert in West Texas. Site-specific modeling applied to matric potential and chloride data from deep alluvial vadose zones at the Nevada Test Site incorporates the improved conceptual model. An iterative, inverse-type modeling approach enables paleoflux retrodiction and yields estimates of current fluxes through the deep vadose zone at each site. Paleoflux reconstructions and current recharge assessments using the technique developed in the study are compared to interpretations obtained from conventional methods. And finally, a vadose-zone core sampling campaign across ecotones in the Trans-Pecos region of West Texas enables investigation of the linkages between vegetation, the hydraulic state of the root zone, and recharge. Site-specific modeling applied to the Trans-Pecos vadose-zone profiles provides additional quantification of these relationships.

CHAPTER 2.

BACKGROUND AND PREVIOUS STUDIES

2.1. Introduction

Current soil-water fluxes within arid unconsolidated vadose zones in interdrainage areas (regions away from channels and arroyos) are generally thought to be very low [Scanlon *et al.*, 1999], perhaps negligible below the soil root zone, and therefore difficult to quantify. This chapter describes some common methods to estimate fluxes through unsaturated, unconsolidated alluvium in desert interdrainage regions and the assumptions employed for each technique. Commonly applied methods include a soil-physics based approach and environmental tracers. The soil-physics approach incorporates measured hydraulic data (from below the root zone) and hydraulic characteristic data into the unsaturated flow equation [Stephens and Knowlton, 1986]. The highly non-linear relationships between moisture content, matric potential, and hydraulic conductivity may result in large uncertainties in the flux calculations [Scanlon, 1991]. Environmental tracer methods have gained popularity over physical methods for estimating soil-moisture fluxes in vadose zones [Allison, 1988; Allison *et al.*, 1994; Phillips, 1994]. Environmental tracer approaches avoid the problematic issues mentioned above by allowing for the direct measurement of chemical or isotopic constituents, without requiring estimation of variably

saturated soil properties. And, unlike physical methods, the accuracy of common environmental tracer methods does not decrease with decreasing soil moisture content/ soil moisture flux, but rather generally increases [Scanlon, 1991].

Vadose zone hydraulic and environmental tracer data have also been used to estimate paleofluxes. Studies in vadose zone hydrology over the past two decades have recognized the potential of deep desert vadose zones as records of past groundwater recharge and paleoclimate due to their very slow water fluxes [Edmunds and Walton, 1980; Scanlon, 1991; Cook *et al.*, 1992; Stone, 1992; Phillips, 1994; Murphy *et al.*, 1996]. Some desert vadose zones apparently contain archives of very old infiltration (up to 120,000 yrs) [e.g. Tyler *et al.*, 1996]. Despite the identification of thick vadose zones as valuable hydrologic archives, uncertainty regarding the vadose-zone hydrodynamics clouds the utility of chloride and matric potential profiles from desert vadose zones as paleohydrologic tools. To correctly ascertain paleohydrologic information from archived vadose-zone porewater, we must first understand the effect and persisting signature of paleoclimatic and paleovegetation changes on solute and moisture profiles. An adequate conceptual model of the current and past hydrologic conditions should be able to explain both physical hydrologic and solute concentration profiles.

2.2. Matric Potential as a Hydrologic Indicator

2.2.1. Hydraulic Potentials in the Vadose Zone

Soil-water moves in response to a hydraulic potential gradient comprised predominantly of the following components: the gravitational potential (z), the matric

(or pressure) potential (ψ), and the osmotic potential (π) [Hillel, 1980]. The elevation above a reference level, generally designated as the water table, defines the gravitational potential. The matric potential describes the interaction between the liquid and the solid matrix. Capillary and adsorptive forces attract and bind water to the matrix, thereby reducing the potential energy below that of bulk water [Hillel, 1980]. By convention, matric potentials in unsaturated soil (i.e. below the reference atmospheric pressure) are negative and become increasingly negative as the soil dries [Stephens, 1996]. The osmotic potential describes the reduction of soil-water potential energy due to the presence of solutes. Osmotic potentials are calculated based on the van't Hoff equation:

$$\pi = -(nC\chi RT)/g \quad (1)$$

where π = osmotic potential (in m), n = number of osmotically active particles; C = solute concentration (in mol kg⁻¹); χ = osmotic coefficient; R = gas constant, 8.3142 J mol⁻¹ K⁻¹, T = temperature (in degrees Kelvin), and g = acceleration due to gravity (m s⁻²). Osmotic potentials are *generally* much smaller (< 10 %) than matric potentials in arid vadose zones (as supported by data collected during this study), and therefore osmotic effects contribute little to water potentials which is the sum of matric and osmotic potentials. Water potential is related to the relative humidity in the soil by the Kelvin equation:

$$h = \pi + \Psi = RT/M_w g \ln(p/p_0) \quad (2)$$

where: h = water potential (in m), π = osmotic potential (in m), Ψ = matric potential (in m), R = gas constant, 8.3142 J mol⁻¹ K⁻¹, T = temperature (in degrees Kelvin), M_w

= molecular mass of water (in kg mol⁻¹), g = acceleration due to gravity (m s⁻²) and p/p₀ = relative humidity of the soil atmosphere.

Approaches that use hydraulic potential data employ Darcy's law for unsaturated flow: $q = -K(\mathbf{q}, h) \frac{d(h+z)}{dz}$ (3)

where :q = darcy flux [L T⁻¹], K(θ,h) = unsaturated hydraulic conductivity [L T⁻¹], h = water potential [L], and z = height above the water table [L].

Two common conceptual models that address vadose zone potentials include the conventional hydrostatic equilibrium model and the unit gradient model.

2.2.2. Conventional Hydrostatic Equilibrium Model

According to the conventional hydrostatic equilibrium model, also termed static fluid distribution and gravity capillarity equilibrium, presented in soil physics text books [i.e. Koorevaar *et al.*, 1983; Jury *et al.*, 1991; Looney and Falta, 2000a,b] and papers on desert vadose zone hydrology [i.e. NRC, 1995; Scanlon *et al.*, 1997a; Scanlon *et al.*, 1999], a no-flow condition results when the matric potential (ψ) equally balances the gravitational potential (z) (Figure 2-1). This analysis assumes that solutes have a negligible effect on flow, i.e. π = 0. So, if h = ψ = -z, then Equation (3), reduces to $q = -K(\mathbf{q}, h) \frac{d(-z+z)}{dz} = -K(\mathbf{q}, h) \times 0 = 0$. At steady state, matric potentials plotting below the hydrostatic equilibrium line in Figure 2-1 indicate upward flow, and matric potentials plotting above indicate downward flow. Presuming that water fluxes through desert soils in interdrainage regions are either

very small or zero, we would expect observed profiles to plot close to the hydrostatic equilibrium line if this theory is adequate.

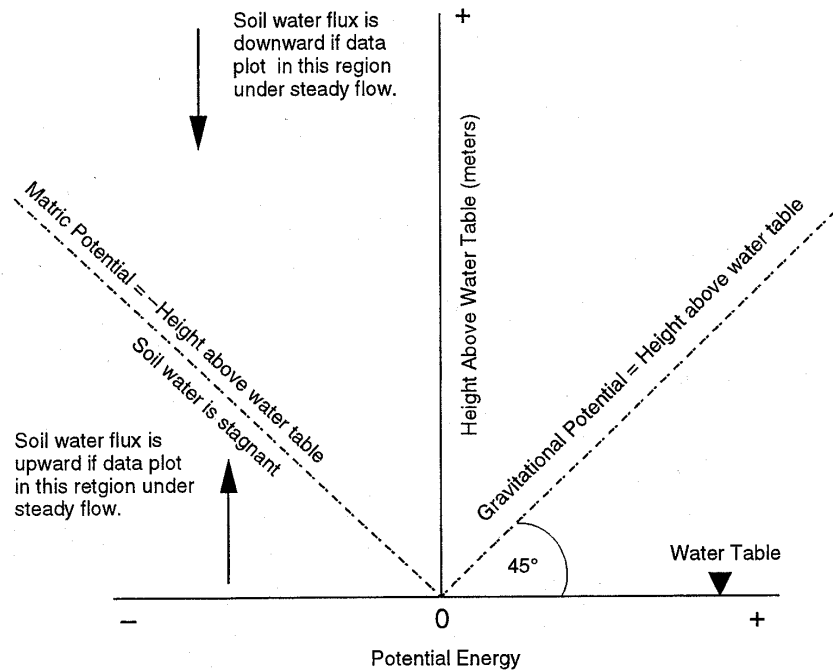


Figure 3.2 The relationship of the equilibrium matric potential to height above the water table. If the soil water is stagnant, the matric potential is exactly balanced by the gravitational potential represented by the height above the water table. A simple measure of the direction of flow can be made by plotting matric potential head (calculated from field measured water potentials by subtracting the osmotic potential) versus the height above the water table.

Figure 2-1. Conventional hydrostatic equilibrium model (from Figure 3.2 from the *National Research Council* [1995] Ward Valley report).

2.2.3. Unit Gradient Model

An alternative to the conventional hydrostatic equilibrium model, the unit gradient model postulates that matric potentials below the active root zone contribute little to the total hydraulic gradient, exhibiting a uniform matric potential profile as illustrated on the hypothetical profile in Figure 2-2. In this case, $d\psi/dz = 0$. And, if

$$h = \psi \text{ (i.e. } \pi = 0), \text{ Equation (3) becomes: } q = -K(q, h) \left(\frac{dh}{dz} + \frac{dz}{dz} \right) = -K(q, h)(0+1) = -K(q, h).$$

In words, the hydraulic gradient below the root zone, or shallow ψ fluctuation zone,

equals unity in the vertical downward direction and the downward soil-water flux equals the unsaturated hydraulic conductivity [Gardner, 1964; Nimmo *et al*, 1994]. According to the steady-state unit gradient model, the downward flux below the root zone equals the flux across the water table interface, or recharge rate, [Stephens, 1996].

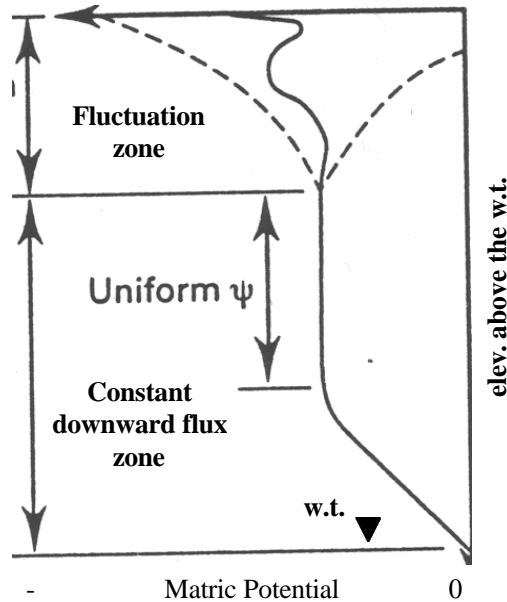


Figure 2-2. Unit gradient model (modified slightly from Figure 1 in Nimmo *et al*. [1994]).

2.2.4. Hydrologic Interpretations of Observed Matric Potential Profiles

Contrary to both conceptual models mentioned above, measured matric potentials from thick vadose zones in the arid southwestern U.S. deviate markedly from the conventional hydrostatic equilibrium line and from a uniform profile required for the unit gradient model. Observed desert vadose-zone matric potential profiles from interdrainage areas are typically curved, with extremely negative matric potentials near the surface and an exponential increase with depth (Figure 2-3).

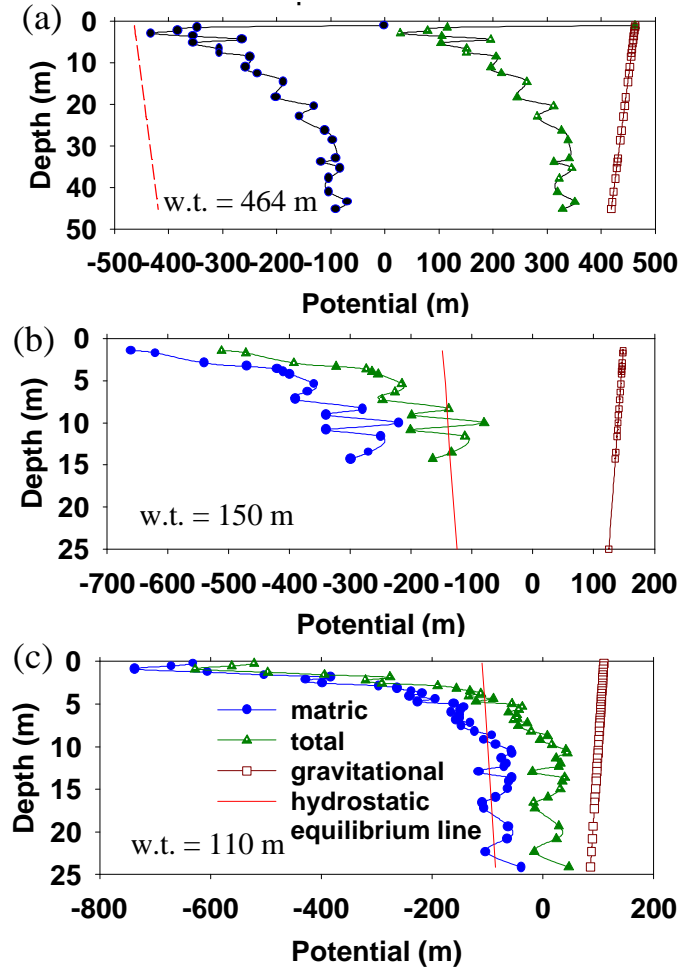


Figure 2-3. Vadose-zone potential profiles under desert floor environments in: (a) Yucca Flat, Nevada Test Site, NV, (b) the Chihuahuan Desert in West Texas [Scanlon *et al.*, 1990]; and (c) the High Plains in Texas [Scanlon *et al.*, 1999]. The legend in (c) applies to all graphs in this figure.

Comparison of observed matric potential profiles to their corresponding hydrostatic equilibrium line in Figure 2-3 yields a divergent flux interpretation. The slope of the total potential $[d(\psi+z)/dz]$ at hydrostatic equilibrium in Figure 2-1 equals zero and indicates no-flow. In contrast, the slopes of the total potentials corresponding to the observed profiles in Figure 2-3 are negative (for z defined at height above the water table) in the shallow part of the profile indicating an upward hydraulic gradient and positive in the deeper profile indicating a downward hydraulic

gradient. Capillary forces draw soil water upward and dominate flow processes to depths of about 10-30 meters in the profiles depicted in Figure 2-3. Similarly, *Scanlon et al.* [1997a] report that water potential measurements in interdrainage areas of many basins in the southwest generally indicate an upward driving force for water movement in the top 20 to 40 m. Below, the hydraulic gradient reverses, and soil water drains by gravity. This divergent flux pattern raises several concerns, the most obvious regarding the equilibrium state of the profile. The lack of a moisture source to supply fluxes at the plane of divergence located deep in the profile raises questions regarding the merit of a steady-state assumption. An alternative assumption is that the divergent moisture flux pattern reflects a temporary phenomenon resulting from transient flow processes [*Scanlon*, 2000]. A transient interpretation evokes several questions. What are typical response times associated with thick desert vadose zones? And to what depths do diurnal and seasonal surface transients actually propagate? The study presented here explicitly addresses the former question. Long-term monitoring studies address the latter question and report minimal temporal variability in matric potential measurements below depths of ~ 3-5 m under desert vegetation [e.g. *Enfield et al.*, 1973; *Scanlon et al.*, 1999; *Fischer*, 1992; *Gee et al.*, 1994; *Andraski*, 1997]. During a five-year monitoring period, *Andraski* [1997] observed that matric potentials under vegetated sites in the Mojave Desert remained between -600 m to -400 m at 1.55 to 4.5 m depth. Vegetated desert vadose zones below a few meters appear to be buffered from diurnal and seasonal surface transients at least on the decadal timescale.

Application of the unit gradient conceptual model to the observed matrix potential profiles in Figure 2-3 also yields a divergent flux interpretation. A unit gradient model interpretation would imply that the “fluctuation zone” (depicted in Figure 2.2) extends to depths of 10 - 30 m (site-specific depth that ψ profiles become essentially uniform), below which the downward soil-water flux equals the unsaturated hydraulic conductivity. Although some desert vegetation species have been documented to extend their roots to depths of 10 to 25 m [Canadell *et al.*, 1996], it is unlikely that an active rooting zone depth of this magnitude is ubiquitous over the biogeographical range of sites that these types of ψ profiles are measured. Canadell *et al.* [1996] reports an average *maximum* rooting depth in deserts of 5.2 ± 0.8 m. The unit gradient conceptual model also suffers from the lack of a moisture source to supply the downward flux unless transients propagate to depths of 10 – 30 m, a supposition contrary to observations [e.g. Enfield *et al.*, 1973; Fischer, 1992; Andraski, 1997].

Despite the noted concerns regarding application of the conventional hydrostatic equilibrium and unit gradient models as applied to deep desert vadose zone ψ profiles from interdrainage areas, the interpretations agree that moisture fluxes are upwards from the depth interval of ~ 3 to $\sim 20 \pm 10$ m at the time of observation. Yet, traditional environmental tracer approaches, including the simple chloride mass balance set of equations, typically assume downward flow below the root zone. This assumption necessarily produces positive (downward) residual soil-water fluxes and recharge estimates.

2.3. Chloride as a Hydrologic Tracer

The chloride mass balance (CMB) approach is one the least expensive environmental tracer methods and possesses several advantages over physical methods, including increased accuracy of small fluxes through dry soils and its utility for paleohydrologic reconstruction [Allison, 1988; Allison *et al.*, 1994; Phillips, 1994]. A set of simplifying assumptions reduces the standard CMB analysis to a few back-of-the-envelope calculations. Despite the many advantages of the CMB method, the assumptions required to use the CMB may render it inaccurate. Sound interpretation of chloride profiles relies on the validity of CMB assumptions applied to specific hydrologic regimes.

2.3.1. Chloride Deposition

Stable chloride is continually deposited on the ground surface both in precipitation and as dry fallout [Allison, 1988; Phillips, 1994]. Oceanic salts are a major source of chloride, and therefore chloride concentration in precipitation is strongly controlled by distance from the coast [Junge and Werby, 1957]. In arid climates, dry deposition and dust make significant contributions (up to 33%) to the total chloride deposition flux [Dettinger, 1989]. For simplification, chloride deposition is generally considered to be constant at a given geographic location. The assumption of constant chloride input equivalent to the present-day value may be valid for analyzing relatively young (or shallow) soil chloride profiles [Liu *et al.*, 1995]. However, the assumption of constant chloride deposition over the period recorded in arid vadose zone profiles has generated concern regarding uncertainties in

CMB age and flux estimates [Murphy *et al.*, 1996; Ginn and Murphy, 1997; Scanlon *et al.*, 1997a; Scanlon, 2000]. Although the chloride concentration in precipitation may not vary significantly over the timescales of most hydrologic interests (the distance to the coast is constant), the precipitation rate may vary greatly. Murphy *et al.* [1996] acknowledged that using current precipitation rates for CMB calculations when analyzing deep chloride profiles in the Pasco Basin of southeastern Washington may yield poor results considering the large fluctuations in paleoprecipitation discerned from pollen records. Tyler *et al.* [1996] expressed similar recognition concerning chloride profiles in deep (230-270 m) vadose zone cores in the arid southern Great Basin. However, Tyler *et al.* suggested that the total chloride flux is more uniform over time than may be expected considering paleoprecipitation fluctuations alone; an increase in the dry chloride input from dust accumulation during dry climatic periods may counterbalance the decrease in wet chloride input. Still, it is important to bear in mind that the accuracy of the information obtained from chloride profiles in thick vadose zones strongly depends on the validity of the chloride source input function used in calculations [Scanlon, 2000].

2.3.2. Chloride Transport Behavior

The nonvolatile chloride ion generally exhibits chemically conservative (non-sorbing) transport behavior making it an ideal tracer, assuming the source function is understood [Allison, 1988]. In some cases, particularly in highly basic soils, the chloride anion may be repelled from the negatively charged mineral surfaces of the porous medium through which it passes, resulting in a faster transport relative to the

neutral H₂O molecule [Gvirtzman and Gorelick, 1991]. Although typically not considered in most models, this effect of anion exclusion may be significant over long timescales [Hendrickx and Walker, 1997].

As water exits the soil via evapotranspiration, chloride is left behind, thereby increasing the salt concentration of the remaining porewater. Soil-water chloride may be transported through advection, dispersion and diffusion. In situations in which soil-water fluxes are extremely low, solute diffusion may be the main mechanism of chloride transport.

2.3.3. Chloride Mass Balance Method

The fundamental assumptions intrinsic to chloride mass balance theory include that all chloride is atmospherically derived (i.e. has no sources or sinks in the vadose zone) and that chloride deposition continues over time [Allison, 1988]. In addition to these assumptions, several others are often applied to significantly simplify calculations. These include: (1) one-dimensional vertically downward, piston-type flow describes the flow regime; (2) chloride deposition rate is constant with time or can be averaged over the relevant time period; (3) steady-state flow conditions prevail; and (4) chloride behaves conservatively. In theory, chloride concentration should increase with depth throughout the evapotranspiration zone and approach a constant value below the root zone under steady-state flow conditions (Figure 2-4). A mass balance argument can then be applied to the chloride ion to calculate the residual flux (net downward soil-water flux) [Phillips, 1994]. Higher chloride values correspond to lower soil-water fluxes.

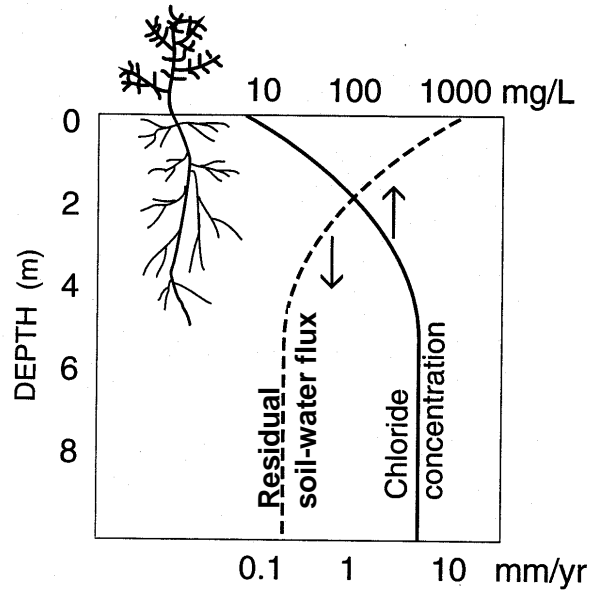


Figure 2-4. Idealized chloride concentration vadose-zone profile (from *Fabryka-Martin et al.* [1997]).

A simple mass balance equation can be written for chloride as follows:

$$C_p q_p + J_d = C_{sw} q_{sw} + C_{ET} q_{ET} \quad (4)$$

where: C_p = chloride concentration in precipitation [$M L^{-3}$], q_p = precipitation rate [$L T^{-1}$], J_d = chloride dry deposition [$M L^{-2} T^{-1}$], C_{sw} = chloride concentration in soil water [$M L^{-3}$], q_{sw} = residual soil-water flux [$L T^{-1}$], C_{ET} = chloride concentration in evaporated/transpired water [$M L^{-3}$], and q_{ET} = evapotranspiration rate [$L T^{-1}$]. For purposes of calculations, the wet (precipitation) and dry chloride mass fluxes are often combined into one chloride mass flux term, J_{Cl} [$M L^{-2} T^{-1}$]. Chloride concentration in evapotranspired water is considered negligible, since chloride is non-volatile. The conventional CMB equation simplifies to:

$$J_{Cl} = C_{sw} q_{sw} \quad \text{or} \quad q_{sw} = J_{Cl} / C_{sw}. \quad (5)$$

If steady-state flow conditions are not assumed, the equation becomes:

$$q_{sw}(z, t) = \mathbf{q}(z) \frac{\partial z}{\partial t} = \frac{J_{Cl}}{C_{sw}(z)} \quad (6)$$

Separation of variables and integration yields:

$$t = \frac{\int_0^z (\mathbf{q} \times C_{sw}) dz}{J_{Cl}}, \quad (7)$$

where: t = time [T], or apparanet chloride mass balance “age”, z = depth [L], and θ = moisture content [$L^3 L^{-3}$]. If dispersion is not assumed to be negligible, the 1-D solute flux equation written in terms consistent with the equations above is:

$$J_{Cl} = -D_h(\mathbf{q}, \mathbf{u}) \frac{\partial C_{sw}}{\partial z} + C_{sw} q_{sw}, \quad (8)$$

where: J_{Cl} = solute flux [$M L^{-2} T^{-1}$], D_h = the hydrodynamic dispersion coefficient [$L^2 T^{-1}$], which is a function of θ (moisture content) and v (average soil moisture velocity [$L T^{-1}$]). Rearranging to solve for residual soil-moisture flux, q_{sw} , yields:

$$q_w = \frac{1}{C_{sw}} \left[J_{Cl} + D_h(\mathbf{q}, \mathbf{n}) \frac{\partial C_{sw}}{\partial z} \right] \quad (9)$$

2.3.4. Hydrologic Interpretations of Observed Chloride Profiles

In practice, chloride profiles exhibit much more complexity than the idealized profile depicted in Figure 2-4, and require detailed interpretation. Measured chloride concentration profiles from arid vadose zones in the southwestern U. S. typically display a shallow bulge containing very high concentrations and much lower, relatively uniform concentrations at depth (Figure 2-5) [Phillips, 1994]. Departure

from the idealized profile records a violation in the steady flow assumption [Wood, 1999].

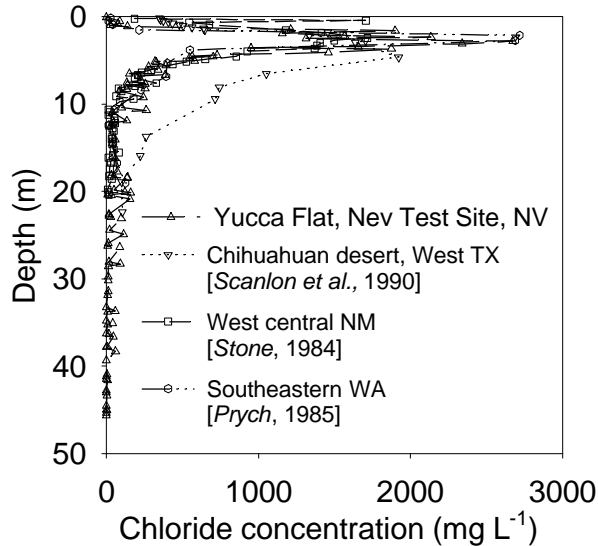


Figure 2-5. Vadose-zone chloride profiles under desert floor environments in Nevada, West Texas, New Mexico and Southeastern Washington. Chloride values are reported as porewater concentrations.

Observed chloride inventories contained within the shallow bulge often correspond to ~15 kyr of atmospheric deposition and accumulation based on long-term average estimates of chloride deposition [Phillips, 1994]. Substantial evidence supports the occurrence of a climate shift from cool, wet conditions to warmer, drier conditions at 12-15 ka in southwestern U. S. [Benson *et al.*, 1990; Morrison, 1991; Phillips *et al.*, 1992; Allen and Anderson, 1993]. Accordingly, several studies attribute the character of the chloride bulge measured in southwestern U.S. vadose zones (Figure 2-5) to this well-documented paleoclimatic transition [Scanlon, 1991; Phillips, 1994]. Phillips [1994] provides a compelling argument for the widespread influence of the Pleistocene – Holocene climate shift and similar soil-moisture regime response by comparing chloride vadose zone profiles from many locations around the

western U. S. The comparison shows remarkably uniform chloride inventories (13-16 kyr). Also, the residual soil-water flux histories reconstructed using a chloride mass balance approach indicates a ubiquitous reduction in soil-water fluxes at about 15 ka by approximately 20 times [Phillips, 1994]. Presumably, the shift to lower precipitation rates and warmer temperatures brought upon a reduction in the amount of soil moisture in the root zone. The reduced recharge conceptual model posits that the climate shift translated to a lower downward soil-water surface flux resulting in higher chloride concentrations at the shallow depths than those measured deep in the profile. Along similar lines of reasoning but a more extreme interpretation, the zero recharge model proposes that soilwater has not infiltrated below the root zone since the arid climate shift at 12 – 15 ka, resulting in the accumulation of significant amounts of chloride within the root zone.

In addition to estimating soil-water ages, the CMB equations attempt to quantify current soil-water fluxes (restricted to depths below the region of chloride accumulation) [Phillips, 1994; Scanlon *et al.*, 1999; Scanlon, 2000; deVries *et al.*, 2000] and paleofluxes [Phillips, 1994; Tyler *et al.*, 1996]. CMB estimates of past and present fluxes pertain to the reduced recharge conceptual model. More dilute chloride concentrations deeper in the profile reflect higher soil water fluxes associated with a wetter past climate, whereas higher chloride concentrations within the bulge reflect much lower infiltration past the root zone associated with the current arid climate. Adoption of the zero flux assumption (zero recharge conceptual model) limits the CMB application to estimate paleofluxes and chloride ages calculated for depths below the base of the chloride bulge.

2.4. Implications of the Downward-Only Flux Assumption

Application of a downward-only flux assumption to vadose zone profiles influences soil-water flux estimations such that only positive values of recharge result. Violation of this ubiquitous assumption in vadose-zone profile analyses may have significant implications. For example, the CMB equations and the unit gradient model approach [Nimmo *et al.*, 1994] assume downward vertical flow in deep vadose zones and consequently produce positive estimates of recharge. Such estimates support the idea that diffuse recharge across extensive areas of arid and semiarid regions may significantly contribute to the overall basin-scale water balance. Stephens [1994] provides a summary table of diffuse recharge estimates from previous studies ranging from 0.01 to 100 mm yr⁻¹ from 17 semiarid and arid sites. Although the methods employed for quantifying the fluxes presented in the summary table varied from physical to chemical approaches, all analyses inherently included the assumption of downward flow in the deep profile. In the following chapter, I test the hypothesis that the downward flux assumption is not applicable to many interdrainage desert vadose zones, resulting in overestimates of recharge.

2.5. Implications of the Zero Flux Assumption

The assumption that no soil-water currently penetrates below the root zone in desert interdrainages regions limits the assessment of moisture movement in the *deep* vadose zone. On one hand, the zero flux assumption can be extended and applied to the entire vadose zone below the root zone. Alternatively, the zero flux assumption may be limited to the upper vadose zone below the root zone in recognition of the

possibility that the deeper vadose zone may be still in the process of draining Pleistocene age water. For the latter case, the zero recharge conceptual model provides no basis on which to quantify deep vadose zone drainage fluxes. In the following chapter, I test the hypothesis that the zero flux assumption associated with the zero recharge conceptual model is incomplete in explaining observed profiles from interdrainage desert vadose zones.

2.6. Deuterium and Oxygen-18 as Hydrologic Tracers

Advances in analytical isotope methods during the 1950s stimulated the development of isotope applications to hydrology. Among the most common isotopic tools applied to vadose zone profiles are the stable isotopes deuterium (^2H or D) and oxygen-18 (^{18}O) in the water molecule. The heavy water molecules are considerably less abundant in nature relative to the common light water molecule as reflected by the following isotopic proportions: $\text{H}_2^{16}\text{O} : \text{HDO} : \text{H}_2^{18}\text{O} = 1000 : 0.32 : 2$ [Merlivat and Coantic, 1975]. The stable isotopic signatures, generally reported as per mil deviation from Standard Mean Ocean Water (SMOW), or δ (‰), of sampled groundwater or soil water may enable derivation of one or more of the following pieces of information: precipitation source, temperature of precipitation or recharge, and soil-water transport behavior and processes. By convention:

$$\delta\text{D} = [(\text{R}_{\text{sample}} - \text{R}_{\text{SMOW}}) / \text{R}_{\text{SMOW}}] \times 1000 \quad (10\text{a})$$

$$\delta^{18}\text{O} = [(\text{R}_{\text{sample}} - \text{R}_{\text{SMOW}}) / \text{R}_{\text{SMOW}}] \times 1000 \quad (10\text{b})$$

where, R_{sample} = isotopic ratio between the heavy and light isotopes of the sample, and R_{SMOW} = isotopic ratio between the heavy and light isotopes of SMOW.

2.6.1. Deuterium and Oxygen-18 Fractionation

Within the hydrologic regime extending from the ground surface to water table, the stable isotopes of H₂O molecules fractionate when water changes physical state by evaporation, condensation, freezing and melting. The heavier isotopic molecules, HDO and H₂¹⁸O, preferentially concentrate (fractionate) in the less mobile phase relative to H₂¹⁶O molecules [Dinçer and Davis, 1984]. With regard to stable isotope behavior in desert vadose zones, evaporation and condensation comprise the main mechanisms of fractionation. Lighter isotopes preferentially fractionate into the vapor phase during evaporation due to their relatively higher vapor pressures, thereby isotopically enriching the remaining liquid. Differential diffusion rates of stable isotope water molecules also contribute to stable isotope fractionation in desert vadose zones, although presumably much less than by phase change (equilibrium) fractionation. Lighter isotopes, in both the vapor and liquid phases, diffuse at slightly higher rates compared to heavier isotopes inducing kinetic fractionation.

2.6.2. Hydrologic Interpretations of Observed δD and $\delta^{18}O$ Profiles

Most previous work regarding stable isotope vadose zone profiles in unsaturated systems has concentrated on quantifying evaporation and has focused on the upper few meters of soil. Theoretical work predicts the shape of δD and $\delta^{18}O$ profiles resulting from quasi-steady-state and transient evaporation under isothermal [Barnes and Allison, 1983] and non-isothermal conditions [Barnes and Allison, 1984; Barnes and Allison, 1988; Mathieu and Bariac, 1996; Shurbaji and Phillips, 1995] (Figure 2-6). Laboratory column experiments [Allison et al., 1983] and controlled

field experiments [Shurbaji *et al.*, 1995] conducted for soil-water profiles undergoing controlled evaporation support the theory. Evaporative profiles contain low values near the air-soil interface, a maximum isotopic value (enriched) at the depth of the evaporating front (using terminology of Barnes and Allison [1983, 1984]), and exponentially decreasing values with depth below the evaporation front. Low values at the surface, sometimes referred to as the “bone-dry” layer, result from the dominance of isotopically-fractionated light vapor. Fractionation resulting from evaporation in the bone-dry layer leaves an enriched source at the evaporation front. The enriched source diffuses downward counter to evaporative upward fluxes.

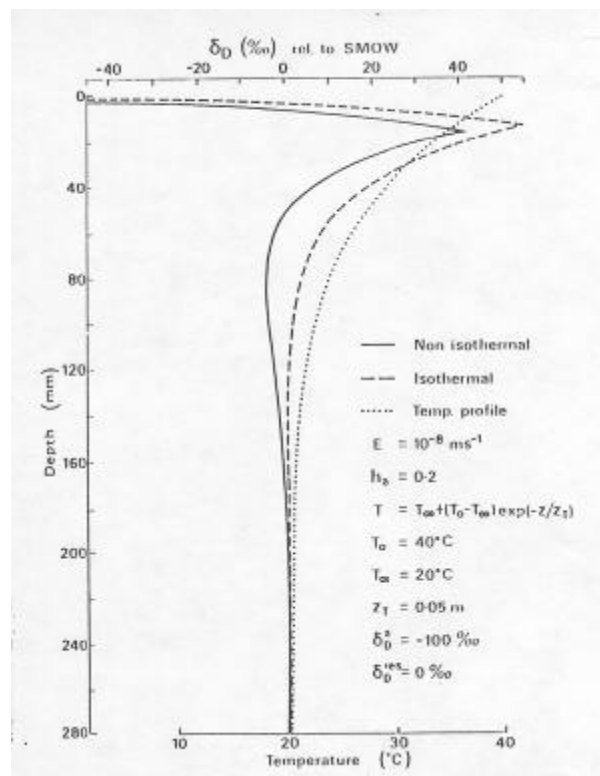


Figure 2-6. Theoretically predicted deuterium profiles for quasi-steady-state evaporation under isothermal and non-isothermal conditions [Barnes and Allison, 1988].

Numerous studies extend the stable isotope theoretical and experimental work to the field domain in the uppermost vadose zone in shallow arid and semiarid regions. *Barnes and Allison* [1988], report measured zones of isotopic enrichment extending to depths of 2-3 meters below the surface, below which values are essentially constant. A few studies attempt to interpret deeper stable isotope vadose zones profiles using a quantitative approach. *Fontes et al.* [1986] calculate evaporation rates from a 10 m deep water table in the Sahara based on measured stable isotope profiles and application of equations developed in *Barnes and Allison* [1983, 1984]. Analyses of deep stable isotope profiles of very thick vadose zones has generally been limited to qualitative interpretations since evaporation from the water tables > 20 m deep is thought to be unlikely [*deVries et al.*, 2000]. The stable isotope profiles from the Frenchman Flat cores (also used in the case study presented in Chapter 4) exhibit large amounts of fractionation and zones of enrichment extending to depths of 25-50 m. *Tyler et al.* [1996] attribute the existence of the depleted water below 25 –50 m to Pleistocene-age water infiltrated during a cooler, wetter climate. The relationship between δD and $\delta^{18}O$ values from samples in the shallow samples follow evaporative lines with slopes of three to four, suggesting that the soil water has undergone evaporation since precipitation. However, the timescales of differential evaporation reflected in stable isotope profiles remain uncertain. Do the isotopic profiles represent propagation of near-surface evaporation effects on the order of a season, decades, centuries, or much longer? Is the Pleistocene-age isotopic signature preserved in the soil water below 50 m [*Tyler et al.*, 1996]?

2.7. Chlorine-37 as a Hydrologic Indicator

Another stable isotope ratio used in hydrology, although much less commonly, is chlorine 37/35. Elemental chlorine consists of two stable isotopes, ^{37}Cl and ^{35}Cl , with natural abundances of 24.23 % and 75.77 %, respectively [Eggenkamp, 1997]. The chlorine stable isotopic signature is reported as per mil deviation from Standard Mean Ocean Chloride (SMOC), or δ (‰). Following this convention:

$$\delta^{37}\text{Cl} = [(R_{\text{sample}} - R_{\text{SMOC}}) / R_{\text{SMOC}}] \times 1000, \quad (10c)$$

where: R_{sample} = isotopic ratio between ^{37}Cl and ^{35}Cl of the sample, and R_{SMOC} = isotopic ratio between ^{37}Cl and ^{35}Cl in SMOC.

In nature, differences in the isotopic ratio of ^{37}Cl to ^{35}Cl do not vary significantly. Reported values generally deviate less than 1 ‰ from SMOC [Eggenkamp, 1997]. As such, the utility of $\delta^{37}\text{Cl}$ as a hydrologic indicator or tracer has been limited to diffusion-controlled hydrogeologic settings [Kaufman *et al.*, 1983; e.g. Desaulniers *et al.*, 1986].

2.7.1. $\delta^{37}\text{Cl}$ Fractionation

Fractionation of chlorine isotopes results during diffusion. The lighter ^{35}Cl isotope diffuses at a faster rate relative to the ^{37}Cl isotope. Experimentally determined diffusion coefficient ratios between ^{35}Cl and ^{37}Cl range from 1.0012 – 1.0023. Eggenkamp [1997] attributes this relatively large reported range to analyses performed in the 1950s and 1960s that were not as robust as the current analytical method and submits that the higher end of the range is probably more accurate. Eggenkamp [1997] uses an inverse modeling approach to calculate a diffusion

coefficient ratio ($D^{35\text{Cl}}/D^{37\text{Cl}}$) of 1.0023 based on profiles of $\delta^{37}\text{Cl}$ taken from sediment cores in Kay Bay, Indonesia and a well-known pore water history.

2.7.2. Hydrologic Interpretation of Observed $\delta^{37}\text{Cl}$ Profiles

Although not previously documented, it is anticipated that desert vadose zone profiles *may* exhibit measurable amounts of chlorine fractionation in the region of the chloride bulge, characterized by steep concentration gradients, *if* diffusion dominates chloride transport processes [Dr. C. Eastoe, personal communication, 2001]. Since no observable $\delta^{37}\text{Cl}$ fractionation is expected in hydraulic regimes dominated by advection, observation of chlorine isotopic fractionation in desert vadose zone profiles, would strongly imply a diffusion-dominated hydraulic regime.

CHAPTER 3.

DEEP ARID SYSTEM HYDRODYNAMIC MODEL DEVELOPMENT

3.1. Introduction

The reduced recharge and zero recharge conceptual models described in Chapter 2, invoked to explain vadose zone chloride profiles, do not adequately explain the corresponding matric potential profiles that indicate upward fluxes in the upper 20 ± 10 meters. A key assumption inherent in the reduced/zero recharge conceptual models and the corresponding chloride mass balance equations is downward-only/no flow. Resolution of the apparent discrepancy between chloride and matric potential profiles serves as the primary objective addressed in this chapter.

3.2. Conceptual Model

The coincidence in timing of the Holocene-Pleistocene climate shift at 12-15 ka and chloride bulge inventories in southwestern U.S. arid vadose zones strongly implies some linkage. However, the paleoclimate explanation alone fails to explain matric potential profiles measured in cores that contain characteristic chloride bulge profiles. Here, I propose that a more adequate and complete explanation requires a paleovegetation component to supplement the paleoclimate hypothesis. The

emphasis on vegetation primarily stems from two lines of reasoning. First, the general timeframe of the major floristic transitions documented in the (now) arid Southwest corresponds with the chloride inventories measured in southwestern arid vadose zone profiles. Paleobotanical assemblages preserved in fossilized packrat middens and stratigraphic palynological data reveal the retreat of a mixed-woodland assemblage of piñon (*Pinus*, spp.) or juniper (*Juniperus*, spp.) vegetation from the lower-lying regions in the Southwest following the late Pleistocene transition to a warmer, drier climate [Spaulding and Graumlich, 1986; Spaulding, 1990; Van Devender, 1986 and 1990]. A mosaic of grassland and desert shrubland has predominated since the woodland retreat. Similar trends documenting a Pleistocene-Holocene shift from mesic to xeric vegetation are observed in the Great Basin, the Mojave Desert, the Sonoran Desert and the Chihuahuan Desert, although particular plant species and transition timings may vary [Betancourt *et al.*, 1990]. The second reason for incorporating the role of vegetation in a conceptual model of arid vadose-zone hydrodynamics derives from modern multiyear monitoring studies, using lysimetry and in-situ soil psychrometry in deep desert soils. These monitoring studies provide evidence of the ability of desert vegetation to effectively capture all available soil moisture within the root zone and buffer the deep vadose zone from surface hydrologic transients. Multi-year lysimeter studies reported by Gee *et al.* [1994] suggest that vegetation is the primary factor controlling the water balance at three arid sites located near Las Cruces, New Mexico; Beatty, Nevada; and Richland, Washington. The investigators installed and monitored lysimeters at 4 to 18 meters deep under both non-vegetated and vegetated sites. The results showed that desert

vegetation eliminated deep infiltration at the Las Cruces and Beatty sites and significantly reduced infiltration at the Richland site [Gee *et al.*, 1994]. Multi-year lysimeter studies at Frenchman Flat, Nevada also demonstrated the large influence of plants on preventing net downward water movement below the upper few meters of the alluvium [Bechtel Nevada, 1998]. The lysimeter results from Gee *et al.* [1994] and Bechtel Nevada [1998] are consistent with the absence of seasonal matric potential transients propagating below depths of about 2-4 meters under desert vegetation, based on studies in which ψ was continuously measured by in-situ soil psychrometers, [e.g. Scanlon, 1991; Fischer, 1992; Andraski, 1997] (Figure 3-1). Andraski [1997] reported that moisture from precipitation that accumulates in the upper 75 cm is removed by evapotranspiration on a seasonal basis, and that seasonal matric potential variations remain confined to depths above 4 meters at the vegetated Beatty, Nevada site. Although these studies obviously do not show that sub-root-zone matric potentials have remained constant over the past 10-15 kyr, they do support a key assumption that matric potentials in deep desert root zones do not exhibit significant seasonal changes as might be expected based on precedents from studies in humid regions [i.e. Johnston, 1987]

The field observations described above and coincidence in timing of chloride inventories and paleovegetation transitions in the southwest provide the basis and justification for incorporating a fixed root-zone matric potential condition in a revised conceptual model of vadose zone hydrodynamics. The revised model assumes a constant very negative matric potential at 3-4 m depth following the establishment of desert vegetation. In addition to this fixed root-zone matric potential condition, the

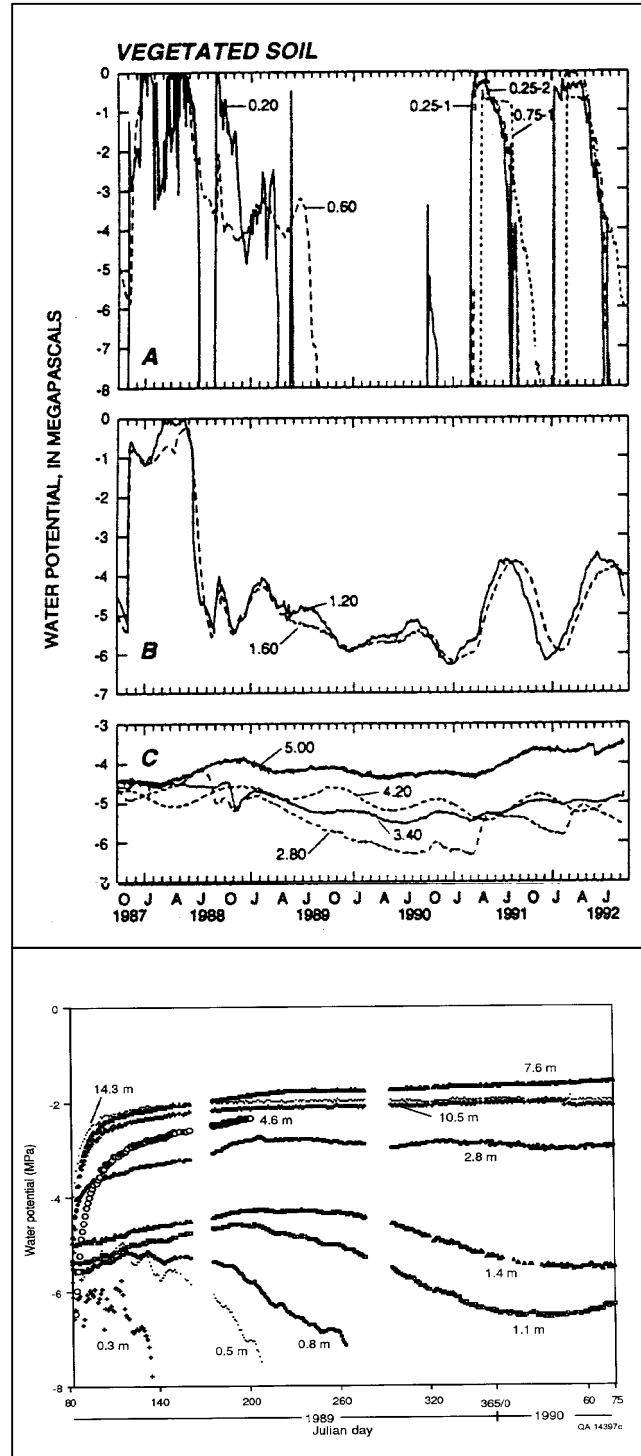


Figure 3-1. Seasonal variation of water potentials at various depths from sites in the Mojave Desert, Nevada (top) (taken from [Andraski, 1997]) and in the Chihuahuan Desert, Texas (bottom) (taken from [Scanlon, 1991]).

conceptual model, which I term the Deep Arid System Hydrodynamic (DASH) model, incorporates a temperature profile described by the mean annual geothermal gradient and includes the effect of both temperature and ψ on vapor density and vapor flux. Liquid and vapor can move both upward and downward, and at different rates and opposing directions from each other. In assuming a fixed root-zone ψ condition, the DASH conceptual model does not attempt to capture the seasonal moisture flux dynamics in the upper few meters such as the downward vapor flux in the upper ~1 meter of soil that should result from seasonal temperature variations [Milly, 1996].

3.3. Mathematical and Numerical Models

The FEHM (Finite Element Heat and Mass) computer code [Zyvoloski *et al.*, 1997a] developed at Los Alamos National Laboratory is used for simulating unsaturated flow and transport in accordance with the DASH conceptual model. FEHM simulates non-isothermal, multiphase, multi-component flow in porous media (detail provided in Appendix A). Governing equations for heat and mass transfer are solved using the finite-element method and a Newton-Raphson iterative procedure. Constitutive equations, represented as rational polynomials, describe the pressure- and temperature-dependent behavior of density, enthalpy and viscosity. FEHM incorporates vapor transport driven by changes in vapor density resulting from a temperature gradient (thermal vapor flux component) and from a matric potential gradient (isothermal vapor flux component). The van Genuchten capillary pressure functions [van Genuchten, 1980] describe the non-linear relationship between matric potential and saturation:

$$\mathbf{y} = \begin{cases} \mathbf{y}_{lr} & S_l \leq S_{lr} \\ \frac{1}{\mathbf{a}_G} \left[\hat{S}^{\frac{1}{I}} - 1.0 \right]^{1.0-I} & S_{lr} < S_l < S_{lmax} \\ 0 & S_l \geq S_{lmax} \end{cases} \quad (11)$$

where: \mathbf{y} = matric potential [L], \mathbf{y}_{lr} = matric potential at residual saturation [L], \mathbf{a}_G = a fitting parameter [L^{-1}], and $I = 1 - \frac{1}{n}$, another fitting parameter. The effective saturation S_l = measured saturation of liquid phase, S_{lr} = residual saturation of liquid phase, and S_{lmax} = maximum saturation of liquid phase. The van Genuchten-Mualem relative permeability function [van Genuchten, 1980; Mualem, 1976] describes the highly non-linear relationships between permeability and saturation:

$$R_l = \begin{cases} \frac{\left[1.0 - \left(\hat{S}^{\frac{1}{I}} \right)^I \right]^2 \sqrt{\hat{S}}}{1.0} & S_l < S_{lmax} \\ 1.0 & S_l \geq S_{lmax} \end{cases} \quad (12)$$

where: $R_v = 1.0 - R_l$, and R_l and R_v are values between 0 and 1. Here, R_l = relative permeability of liquid [L^2], and R_v = relative permeability of vapor [L^2].

The molecular water vapor diffusivity, D_{va} [$L^2 T^{-1}$], is represented in FEHM by the following equation from Pruess [1991] with slight modification:

$$D_{va} = t \beta f S_v D_{va}^0 r_v \frac{0.101325}{P} \left[\frac{T + 273.15}{273.15} \right]^q, \quad (13)$$

where: t = tortuosity factor, β = vapor enhancement factor, f = porosity, S_v = vapor saturation, r_v = vapor density [$M L^{-3}$] ($kg m^{-3}$), D_{va}^0 = the vapor diffusivity in free air at standard conditions [$L^2 T^{-1}$] ($2.4 \times 10^{-5} m^2 s^{-1}$), T = temperature [t]($^{\circ}C$), P = pressure

[$\text{M L}^{-1}\text{T}^{-2}$] (MPa), and \mathbf{q} = a unitless parameter set in FEHM at 2.334. The tortuosity factor, \mathbf{t} , is defined here as the ratio of the straight-line distance between two points to the distance between the same two points via the connected pores. In theory, \mathbf{tb} should not exceed a value of 1. The phenomenon of enhanced vapor diffusion [*Philip and de Vries, 1957*] can be mathematically represented, albeit crudely, by using $\beta > 1$.

Assumptions inherent in FEHM include: 1) Darcy's Law appropriately describes the movement of each phase 2) local thermal equilibrium between the fluid and the rock is maintained and 3) tracer solutions do not affect the heat and momentum transfer solution. Additional assumptions imposed in this study, but not inherent to FEHM, include: 1) one-dimensional vertical flow adequately represents the hydrodynamics, 2) air flow is negligible (see Appendix B in *Ross [1984]* for justification), 3) chloride is hydrologically conservative (non-sorbing and non-reactive) and non-volatile, 4) fractures, macropores, or other preferential flow paths do not exist and/or affect the system, and 5) the porous medium is incompressible.

Since stable chloride is non-volatile and non-sorbing, it is allowed to move only in the liquid phase and its transport is not retarded or enhanced with respect to fluid flow. Chloride does not exit through the root zone in the liquid phase, as does H_2O , since most plants preferentially exclude chloride when absorbing water through the roots [*Gardner, 1967*].

The stable chloride isotope signature, $\delta^{37}\text{Cl}$, is modeled by treating ^{37}Cl and ^{35}Cl as separate, nonvolatile solute species with different mass-based liquid diffusion coefficients. I employ the ratio of liquid diffusion coefficients determined by *Eggenkamp [1997]* (Table 3-1).

Parameter	Value
$D_1^{37\text{Cl}} / D_1^{35\text{Cl}}$	0.998 ^[1]
Chloride diffusion coefficient in pure water	$2.03 \times 10^{-9} \text{ m}^2\text{s}^{-1}$ ^[2]
Liquid diffusion coefficient at saturation (^{35}Cl)	$1.00 \times 10^{-9} \text{ m}^2\text{s}^{-1}$
Liquid diffusion coefficient at saturation (^{37}Cl)	$9.98 \times 10^{-10} \text{ m}^2\text{s}^{-1}$

Table 3-1. Stable chlorine isotope transport parameters and values at 20 °C. D_v = vapor diffusion coefficient D_l = liquid diffusion coefficient

References: ^[1] Eggenkamp [1997]; ^[2] Cussler [1984].

3.4. Boundary Conditions, Initial Conditions and Input Parameters

Figure 3-2 represents the physical system, a generic 200 m thick alluvium vadose zone, used for testing conceptual models of 1-D non-isothermal, multiphase flow and transport in arid regions. The top of the column represents the ground surface, and the bottom of the column represents the water table. Temperature gradients result from specifying temperatures at the top and bottom boundaries of 18°C and 25°C, based on a typical mean annual surface temperature in the desert southwest (top boundary) and average geothermal gradient of 35 °C km⁻¹ [Blankennagel and Weir, 1973; Ross, 1984], respectively.

Initially, the system is set at a uniform downward liquid flux of 10 mm yr⁻¹, representative of a relatively wet climate [Tyler *et al.*, 1996]. This flux represents the residual soil-water flux; i.e. the flux that penetrates below the root zone, through the vadose zone and across the water table. The initial solute profile consists of a uniform chloride porewater concentration of 10 mg L⁻¹. A prescribed chloride flux of 100 mg m⁻² yr⁻¹ at the surface boundary simulates continuous chloride deposition. This prescribed flux represents both dry and wet chloride deposition and is a typical

present-day value in the U.S. southwest [Dettinger, 1989]. The initial stable chlorine isotope profile consists of a uniform isotopic value of 0 ‰ $\delta^{37}\text{Cl}$.

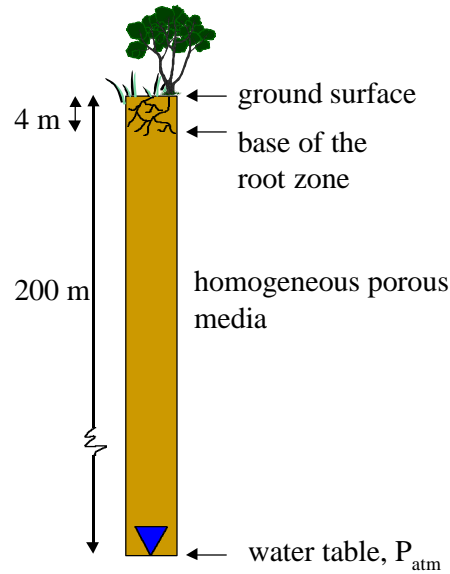


Figure 3-2. Schematic depiction of the base-case vadose zone prototype.

A switch to a drier climate is simulated by imposing a fixed negative matric potential (ψ) at 4 m depth, in accordance with observations from root zones underlying desert vegetation. The fixed root-zone condition of $\psi = -400$ m is within the -400 m to -1000 m range able to be sustained by desert vegetation [Pockman *et al.*, 1995; Pockman and Sperry, 2000]. An average precipitation rate of 200 mm yr^{-1} specified at the surface represents a typical value for the arid southwest. The imposed matric potential condition specified at the root zone node renders the model insensitive to the precipitation value. Transport results, however, *are* sensitive to the chloride deposition rate specified at the surface. The chloride deposition rate remains constant at $100 \text{ mg m}^{-2} \text{ yr}^{-1}$ by specifying an effective chloride concentration of 0.5

mg L⁻¹ in precipitation. The 0 ‰ $\delta^{37}\text{Cl}$ value of the incoming water remains unchanged.

The suite of input parameter values, designated as the “base case”, typifies average values measured in alluvial desert vadose zones (Table 3-2).

Parameter	Value
SOIL PROPERTIES	Type = Sand
Porosity	45 %
Rock thermal conductivity	2.5 W m ⁻¹ °C ⁻¹
Rock density	2500 kg m ⁻³
Rock specific heat	1000 J kg ⁻¹ °C ⁻¹
Saturated permeability	3 x 10 ⁻¹¹ m ²
Van Genuchten parameters α and n	4.5 m ⁻¹ , 1.9
Residual and maximum saturations	10 %, 96 %
Geothermal gradient	35 °C km ⁻¹
Water table depth	200 m
Base of the root zone depth	4 m
Effective chloride diffusion coefficient*	5 x 10 ⁻¹¹ m ² s ⁻¹
Chloride diffusion coefficient at saturation**	1 x 10 ⁻⁹ m ² s ⁻¹

* used for simulations in which solute diffusion coefficient is specified as a constant

**used for simulations in which chloride diffusion rate varies as a function of water content according to the *Conca and Wright* [1992] function (Figure 3-3).

Table 3-2. Base case input parameters.

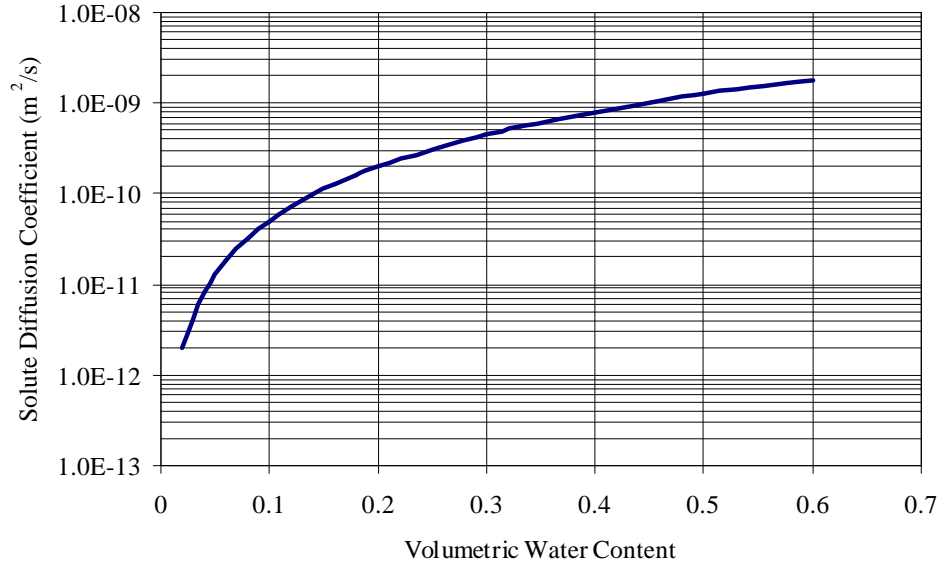


Figure 3-3. Plot of diffusion coefficient as a function of volumetric water content as defined by the *Conca and Wright* [1992] function.

3.5. Testing the DASH Conceptual Model

Comparison of results from the simulations described above run for the fixed root-zone potential condition to results produced for a reduced-flux boundary condition of 0.1 mm yr^{-1} and a zero-flux boundary condition enables the DASH model to be tested against the reduced recharge and zero recharge models (Table 3-3). The simulations proceed for 15 kyr subsequent to the transition from the initial steady-state downward flux to the imposed arid conditions identified with each conceptual model. The 15 kyr run-time criterion is based on typical measured chloride inventories in the southwestern U.S. [Phillips, 1994]. Model results, for the DASH and reduced recharge and zero recharge conceptual models, in the form of matric potential and chloride profiles are compared to typical observed profiles in Figures 3-4 and Figure 3-5. The reduced recharge model produces a much less negative matric potential profile and a broader chloride profile than observed profiles.

The zero recharge model produces peaked chloride profiles, strongly resembling observed profiles, but generates much less negative matric potentials than commonly observed. In contrast, both the matric potential and chloride profiles generated for the DASH model match observed profiles very well, thereby favoring the DASH conceptual model over the reduced recharge and zero recharge conceptual models.

Condition	Initial	Xeric Boundary	Xeric Boundary
Conceptual Model	All	DASH	Reduced Recharge/ [Zero Recharge]
Surface liquid flux*	10 mm yr ⁻¹	200 mm yr ⁻¹	0.1 mm yr ⁻¹ [1 x 10 ⁻³ mm yr ⁻¹]
Root zone ψ	N/A	- 400 m	N/A
Water table ψ	0 m	0 m	0 m
Surface temp.	18°C	18°C	18°C
Water table temp.	25°C	25°C	25°C
Chloride flux	100 mg m ⁻² yr ⁻¹	100 mg m ⁻² yr ⁻¹	100 mg m ⁻² yr ⁻¹
Source chloride conc.	10 mg L ⁻¹	0.5 mg L ⁻¹	1 g L ⁻¹ [100 g L ⁻¹]
Source $\delta^{37}\text{Cl}$ conc.	0 ‰	0 ‰	0 ‰

* represents *residual soil-water flux* (precipitation - evapotranspiration) for the initial condition, and the boundary conditions for the reduced recharge and zero recharge models; represents *precipitation* for the surface boundary condition in the DASH model.

N/A = not applied

Table 3-3. Initial and boundary conditions for testing the three conceptual models. Initial conditions are the same for all three test simulations. Bracketed and italicized values correspond specifically to the zero-recharge model.

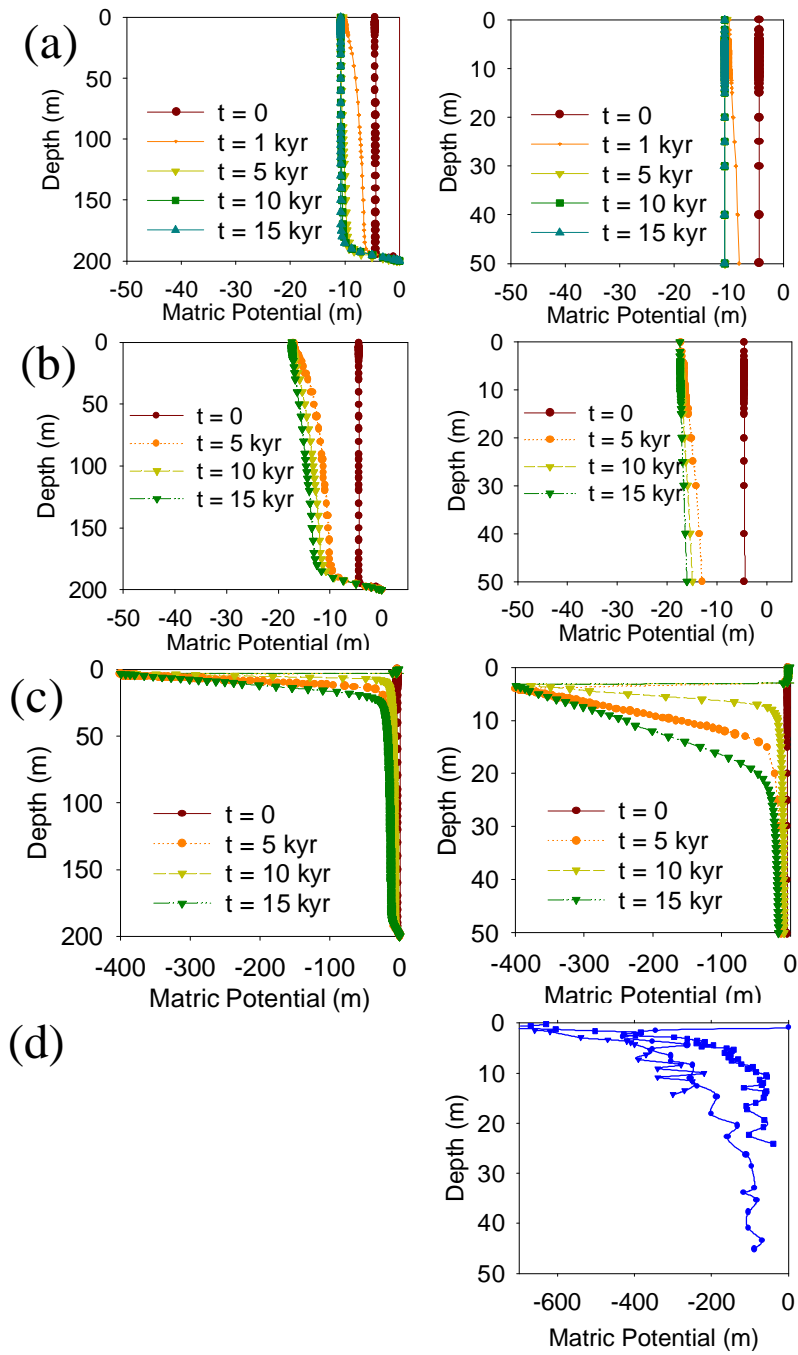


Figure 3-4. Simulated matric potential profiles for the (a) reduced recharge model, (b) zero recharge model, (c) DASH model and (d) observed profiles from Figure 2-3 for comparison. The left-hand side graphs display the entire 200 m thick vadose-zone profile and right-hand side graphs show only the upper 50 m.

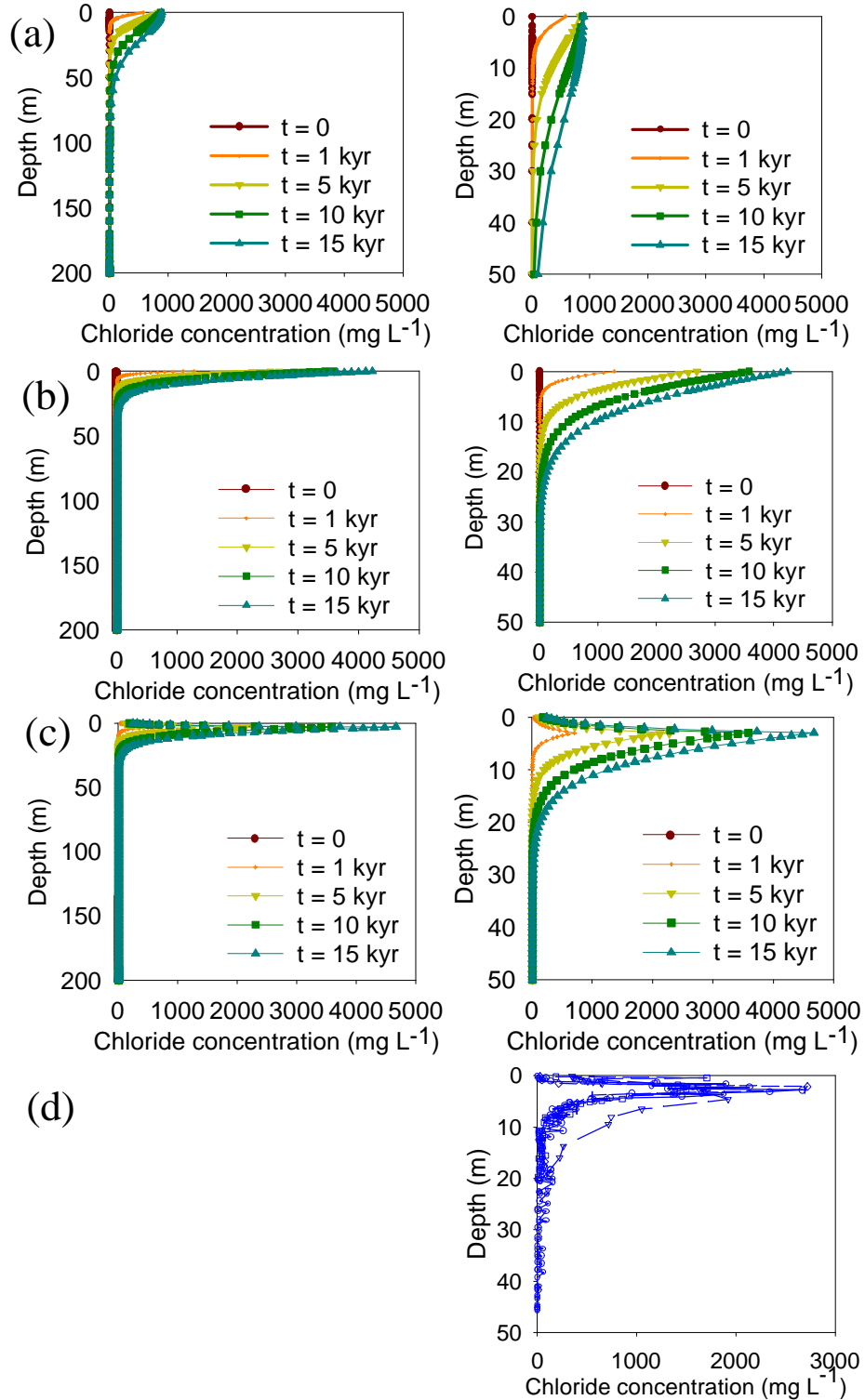


Figure 3-5. Simulated chloride profiles for the (a) reduced recharge model, (b) zero-recharge model, (c) DASH model, and (d) observed profiles from Figure 2-5 for comparison. Left graphs display entire the 200 m vadose zone thickness and right graphs display the upper 50 m. Chloride values are porewater concentrations.

3.6. Development of the Current Moisture Flux Regime

The DASH model moisture flux profiles spanning 15 kyr from the wet-to-dry transition show the development of a net moisture drying front that propagates downward through time (Figure 3-6). Above the drying front, moisture moves upwards towards the base of the root zone driven by capillary forces. Below the drying front, gravity-driven drainage accommodates drying as described by unit gradient flow. The deep downward flux is essentially proportional to the unsaturated permeability. The magnitude of the downward flux increases with depth from the drying front to the water table and decreases, in general, over time as the deep vadose zone dries. After 1 kyr (not shown on Figure 3-6), the drying front propagates to a depth of 15 m and the downward net moisture flux across the water table equals approximately 1 mm yr^{-1} . Through time, the rate of drying decreases exponentially. The drying front propagates to depths of 35 m, 54 m and 55 m after 5 kyr, 10 kyr, and 15 kyr, respectively. Likewise, the magnitudes of the deep vadose zone drainage fluxes decrease (Figure 3-6).

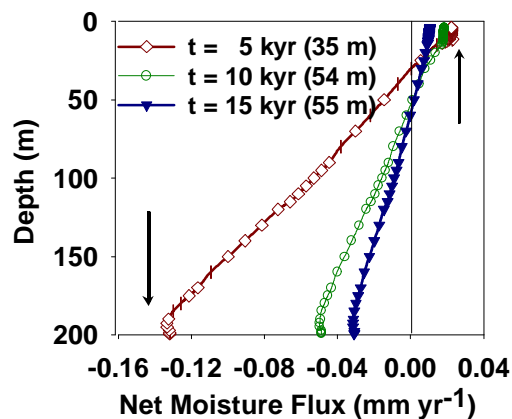


Figure 3-6. Simulated net moisture flux profiles for times after the xeric boundary condition transition using the DASH model. Negative values indicate downward fluxes, and positive values indicate upward fluxes. Values in parentheses indicate the depth of net flux divergence that corresponds to the designated simulation times.

The DASH model moisture flux profiles at 15 kyr from the switch to a drier climate represent the current conditions and indicate divergent liquid and net moisture fluxes and an upward total vapor flux (Figure 3-7). The upward vapor flux is sourced by evaporation from the water table and driven primarily by the geothermal gradient. The total vapor flux exceeds the liquid flux by at least an order of magnitude in the upper 25 m. Liquid flows upward in the upper 13 m and downward below. Downward liquid fluxes below 13 m increase with depth as a result of the divergent drying process. Calculated liquid and vapor fluxes in the region below the root zone and above the water table are extremely small, on the order of 10^{-2} mm yr⁻¹. In contrast to the very small fluxes predicted using the DASH model concept, the CMB approach based on the reduced recharge conceptual model, yields larger downward fluxes below the root zone and across the water table interface (Table 3-4). Furthermore, the DASH model flux distribution that reflects the current condition (Figure 3-7) illustrates that the net moisture flux below the root zone is not equivalent in magnitude *or direction* to the flux across the water table interface. The moisture flux distribution clearly violates the key steady-state assumption for the conventional hydrostatic equilibrium and the unit gradient models. The moisture flux distribution also contests the stagnant condition assumption for the zero recharge model. The transient state of vadose zone profiles given 15 kyr to approach equilibrium with the fixed root-zone ψ condition suggests an extremely slow response of the system.

	CMB-calculated flux (mm yr ⁻¹)	DASH model Liquid flux (mm yr ⁻¹)	DASH model vapor flux (mm yr ⁻¹)	DASH model Net moisture flux (mm yr ⁻¹)
Base of the root zone	-1.0	0.001	0.010	0.011
Water table interface	-10.0	-0.044	0.013	-0.032

Table 3-4. Comparison of “current” moisture fluxes for the base case estimated using a CMB approach to the DASH model results. Negative values indicate downward fluxes; positive values indicate upward fluxes.

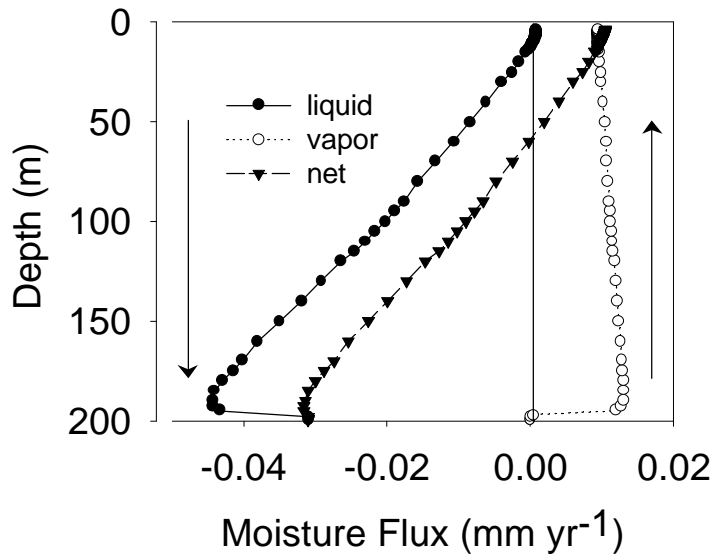


Figure 3-7. Simulated moisture flux profile for present conditions using the DASH model. Negative values indicate downward fluxes, and positive values indicate upward fluxes.

3.7. Chloride Transport

The simulated chloride bulge profiles using the DASH conceptual model result from a dramatic change in the moisture flux regime induced by the xeric transition. Initially, a downward advective chloride flux dominates chloride transport through the vadose zone producing a uniform concentration profile. Employing the DASH conceptual model, the imposed root-zone matric potential condition prevents the downward advective flux from the surface from penetrating below the root zone.

Consequently, chloride accumulates in the root zone. Concentration-driven diffusion counter to a small upward advective flux transports chloride below the root zone. Likewise, employing the zero recharge conceptual model requires that chloride accumulated near the surface can only be transported downward by diffusion. Recall, that the chloride results from simulating the zero recharge model and the DASH model both reproduced observed data. Also, the analytic solution for governing

$$\text{solute diffusion equation: } \frac{\partial C}{\partial t} = D_{\text{eff}} \frac{\partial^2 C}{dz^2}, \quad (14)$$

reproduces the characteristic shape of arid vadose zone chloride profiles for the following conditions:

$$C = 10 \text{ mg L}^{-1} \text{ at a } z > 3 \text{ m for } t = 0.$$

$$C = 4500 \text{ mg L}^{-1} \text{ } z = 3 \text{ m (root zone depth) for } t > 0.$$

$$C = 10 \text{ mg L}^{-1} \quad z \longrightarrow \quad \text{for } t > 0,$$

where: C = solute concentration (mg L^{-1}), t = time (s), z = depth (m), and D_{eff} = effective diffusion coefficient = $5 \times 10^{-11} \text{ m}^2 \text{ s}^{-1}$. The solution for 15 kyr of elapsed time is displayed graphically as a depth-concentration profile in Figure 3-8. The similarity between the simulated chloride profiles for the zero recharge and DASH models and the analytic diffusion solution confirms that diffusion is the main mechanism of chloride transport in these simulations and that the upward advective chloride flux contributes a negligible amount of chloride to the root-zone bulge (Figure 3-8).

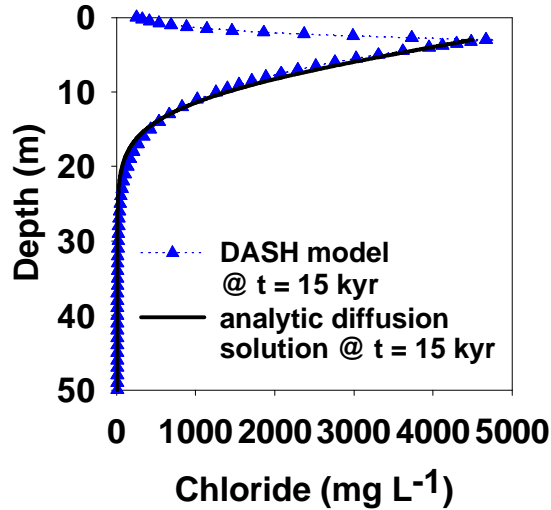


Figure 3-8. Simulated chloride profile at $t = 15$ kyr using the DASH model compared with the analytic diffusion solution at $t = 15$ kyr.

3.8. Stable Chlorine Isotope Transport

The effects of diffusion are clearly illustrated in the simulated $\delta^{37}\text{Cl}$ profiles (Figure 3-9). The profiles show a maximum in the root zone and a minimum below the root zone. Recall that the source $\delta^{37}\text{Cl}$ value, 0 ‰, remains constant throughout the simulation and is equivalent to the initial concentration. Therefore, the 5 ‰ range between minimum and maximum values in the simulated $\delta^{37}\text{Cl}$ profiles result purely from isotopic fractionation. Because of the slight differences in diffusion coefficients, ^{35}Cl migrates downward from the chloride peak at a faster rate relative to the ^{37}Cl molecules. This differentiation induces $\delta^{37}\text{Cl}$ depletion below the chloride bulge and leaves a zone of enriched solute close to the surface. Over a period of 15 kyr, the $\delta^{37}\text{Cl}$ maximum in the root zone reaches +1.3 ‰. Over the same period, the $\delta^{37}\text{Cl}$ minimum below the root zone reaches -3.7 ‰. The $\delta^{37}\text{Cl}$ minimum becomes more negative through time and progresses downward. The continuous depletion in

the $\delta^{37}\text{Cl}$ minimum results from increasing chloride concentration gradients near the chloride peak as chloride input from the surface continues to accumulate faster than it diffuses. Below ~ 50 m in the profile (for the 15 kyr period simulated), total chloride concentration gradients and concentration-driven diffusion rates are small. Therefore, isotopic fractionation is negligible and $\delta^{37}\text{Cl}$ values deviate imperceptibly from 0 ‰.

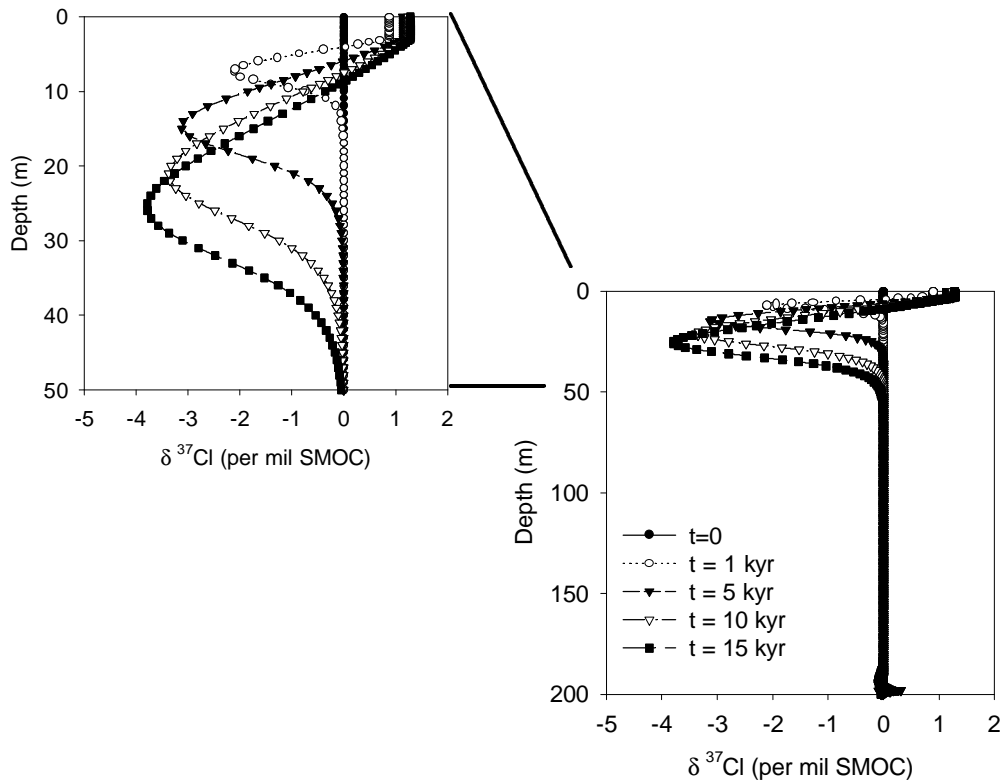


Figure 3-9. Simulated $\delta^{37}\text{Cl}$ profiles using the DASH model at several snapshots in time.

One important caveat to the $\delta^{37}\text{Cl}$ modeling results is that the assumption of a fixed root zone base location over thousands of years is highly idealized. A more realistic conceptualization is that the drying front depth fluctuates over many timescales and perhaps over several vertical meters during the last 15 kyr. The assumption of a fixed drying depth has little bearing on the majority of the DASH

model results, particularly because the DASH conceptual model applies to very deep vadose zones. However, this simplification has major implications for the comparison between model-predicted $\delta^{37}\text{Cl}$ profiles and observed profiles, the latter of which has likely experienced depth-fluctuating drying fronts. Therefore, measured $\delta^{37}\text{Cl}$ profiles may record much less fractionation than the 5 ‰ predicted under the idealized model conditions.

3.9. Hydrodynamic Equilibrium State

Simulations carried to steady state using the DASH model yield important insight into the equilibrium state of deep vadose zones and response to an arid climate shift. The lack of similitude between the DASH model-generated, steady-state matric potential profile and the profiles required for the steady-state conventional hydrostatic equilibrium and unit gradient models reveal a major misconception in conventional unsaturated flow theory as applied to desert vadose zones (Figure 3-10). The DASH model produces a curved matric potential profile at steady state (convex upward), similar to typical measured matric potential profiles in thick desert vadose zones (Figure 2-3). The curvature indicates a divergent liquid flow pattern in which liquid fluxes are upward in the upper vadose zone and downward below. The moisture flux profiles explain the apparent paradox regarding how a *divergent* liquid flow pattern can maintain a steady state and net-upward flux regime (Figure 3-11). Vapor transport controls the hydrodynamics at steady state. The upward thermal vapor flux, sourced by evaporation from the water table, decreases with height above the water table due to the decreasing temperature and vapor density gradients. To maintain

equilibrium, vapor condenses and supplies a downward liquid flux in the *deep* vadose zone. Above some depth (~ 90 m for the base case), capillary forces, imparted by the specified root-zone matric potential, exceed gravitational forces imparted to the liquid, and the liquid flux direction shifts to upward. This upward liquid flux is also supplied by vapor condensation. The upward liquid flux in the shallow vadose zone is extremely small due to the dry conditions and very low unsaturated permeability. In the shallow vadose zone, most of the flux is in the vapor phase driven upward by a large matric potential gradient. In the shallow vadose zone, the isothermal vapor phase flux accounts for most of the net flux, driven upward by a large matric potential gradient. The equilibrium state is characterized by dynamic interaction between vapor and liquid fluxes summing to a net-upward uniform moisture flux.

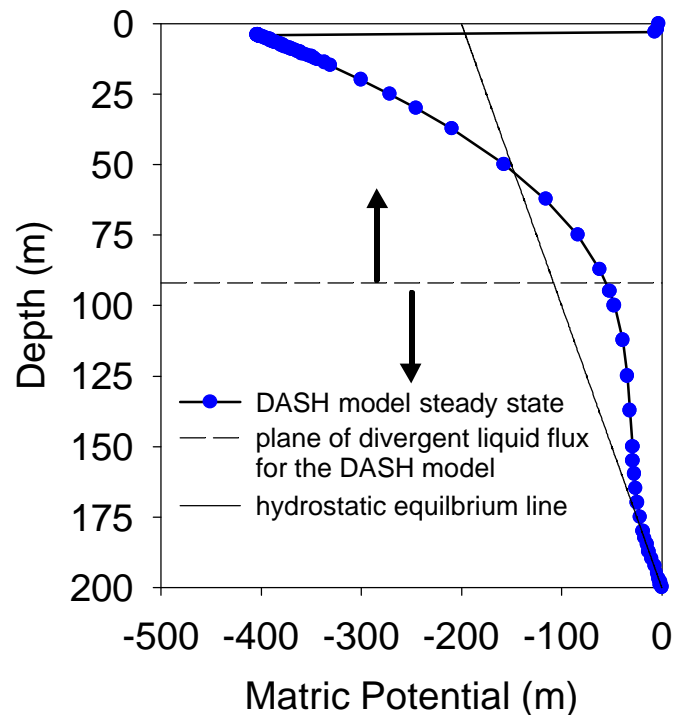


Figure 3-10. Simulated steady-state matric potential profile for the base case using the DASH model. The matric potential profile deviates markedly from the linear matric potential profile described by the conventional hydrostatic equilibrium model and from a uniform profile predicted by the unit gradient model (not shown here).

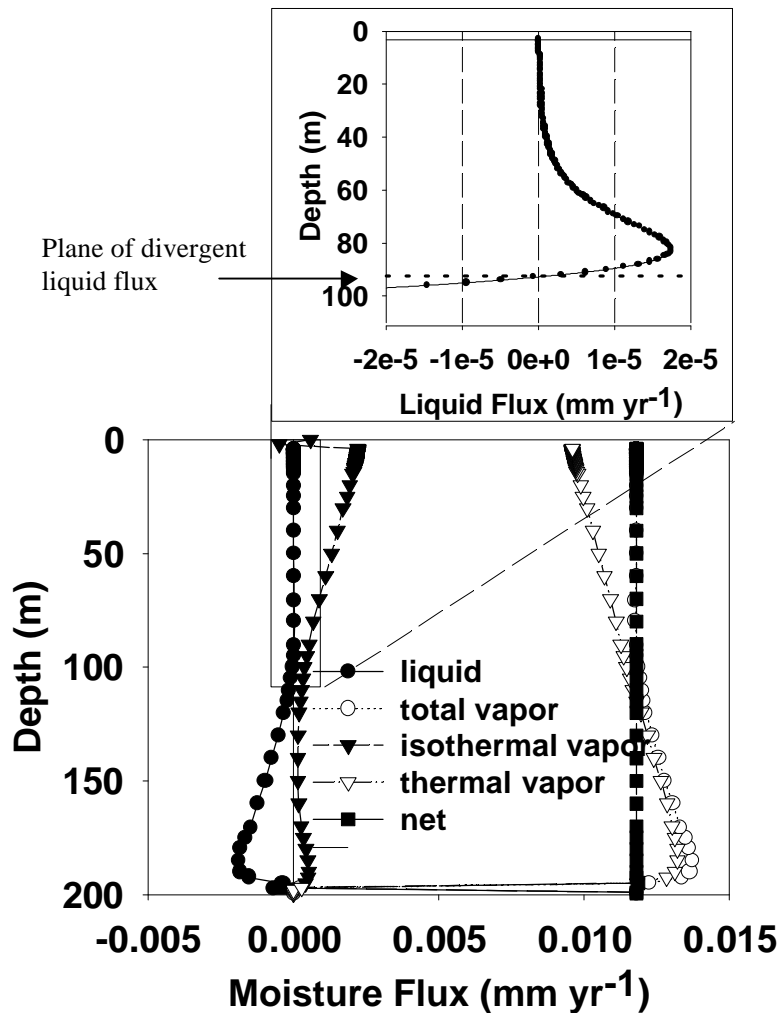


Figure 3-11. Simulated steady-state moisture flux profiles for the base case using the DASH model. The moisture flux profiles illustrate the dynamic interaction between liquid and vapor flux components to describe a net-upward flux steady state. Negative values indicate downward fluxes, and positive values indicate upward fluxes. The inset showing only the liquid flux component illustrates the plane of divergent liquid flux a depth of 92 m.

The transient history of the base-case simulation carried to steady state highlights the very slow response of deep vadose zones to an arid climate/ xeric vegetation shift. Modeled steady-state matric potential profiles that appear similar in character - both shape and magnitude - to measured profiles could suggest that

observed desert vadose zones are in equilibrium with current surface arid conditions. However, examination of the response times associated with the modeled steady-state profiles suggests the contrary. Here, the time required to complete an e-fold ($1-e^{-1}$ or 63% response from initial to final state) change in the matric potential profile defines the equilibrium response. This definition of the response time, or time constant, is frequently employed to characterize systems experiencing exponentially decreasing rates of change. In this case, the equilibrium response represents the propagation of drying conditions with depth below the root zone since the location of the fixed matric potential condition coincides with base of the root zone. The upper portion of the vadose zone profile equilibrates at a faster rate than the deeper portion of the profile due to the relatively higher hydraulic gradients near the base of the root zone. The calculated response time of 80 kyr exceeds typical timescales of long-term climate change, which are on the order of 10 to 15 kyr. Consequently, deep desert vadose zones with parameters similar to the base case may be characterized as maintaining a pseudo-steady state since response is so slow, but nevertheless remaining far from the "true" final steady state.

3.10. Summary

The DASH model challenges some of the conventional conceptual models of vadose-zone flow and transport as applied to arid to semiarid regions. The results bring into question the assumptions that recharge, although significantly reduced in magnitude, has continued through time, and that vapor fluxes are negligible compared to liquid fluxes in deep vadose zones. The DASH model results indicate that desert

vadose zones which exhibit matric potential and chloride profiles as shown here: 1) sustain upward moisture fluxes below the root zone and, 2) contribute a negligible amount to groundwater recharge. Furthermore, the net moisture flux below the root zone is not equivalent in magnitude *or direction* to the flux across the water table interface.

The Deep Arid System Hydrodynamic model reconciles the paradox between upward potential gradients measured in arid and semiarid vadose zones and the downward or no flow assumptions used to interpret corresponding chloride profiles. The DASH model prescribes a constant very negative matric potential at the base of the root zone, a boundary condition derived from field data and the characteristics of desert vegetation [e.g. *Fischer*, 1992; *Andraski*, 1997; *Scanlon*, 1991]. The fixed root-zone condition effectively intercepts all infiltration from precipitation and draws much of the pre-existing moisture from the upper vadose zone. The transition from a downward soilwater flux throughout the system to a very dry hydraulic state at the base of the root zone marks the major climate and vegetation shift at 10-15 ka to desert-like conditions in large areas of the southwestern US. The DASH model results indicate that the transition at 10-15 ka induced a reversal in moisture fluxes below the root zone in interdrainage desert soils from downward to upward. Planes of divergent liquid and net moisture fluxes have moved downward through time as the systems responds to drying conditions at the top and the deep porewater drains to the water table. Due to the slow response of the deep vadose zone to climate forcing, thick vadose zones are generally in a transient state. Consequently, downward liquid fluxes, although small in magnitude, continue to drain the deep vadose zone of much

of its pre-existing moisture. This has implications for contaminant migration in arid vadose zones. The direction of nonvolatile contaminant migration by advection depends on the location of the source with respect to the plane of the divergent liquid flux. Buried waste below the divergent plane would possess greater potential for solute species to reach the water table and contaminate groundwater. The continuous upward vapor flux through thick vadose zones serves as a mechanism for the upward migration of volatile species.

The DASH results also demonstrate the implications for recharge estimation and environmental tracer studies. Quantifying diffuse recharge by estimating soil water fluxes below the root zone and assuming that they are equivalent to groundwater recharge, i.e. fluxes across the water table interface, may not be appropriate in semiarid and arid regions. The work described in this chapter illustrates that not only are moisture fluxes just below the root zone unequal to recharge, they are opposing in direction. Furthermore, moisture fluxes through deep vadose zones estimated using the DASH model are at least an order of magnitude smaller than estimates obtained using a downward flux assumption, (i.e. the CMB equation). Results demonstrate that although the assumption that current soil-water does not penetrate below the root-zone may be valid in many cases, the zero recharge conceptual model does not capture the complexities of flow processes in deep vadose zones. Accordingly, the zero recharge model cannot explain observed matric potential profiles and does not predict the small, but potentially important, downward fluxes across the water table.

As thick desert vadose zones approach a steady state with the dry, hydraulic condition set in the root zone, the thermal vapor flux, driven by the geothermal gradient, dominates the hydrodynamics of the system. Vapor condenses as it moves upward through cooler regions of the vadose zone and returns a downward liquid flux. The gravitationally-driven liquid flux produces the characteristic nearly-uniform matric potentials of the deeper vadose zone. In actuality, this hydrodynamic equilibrium condition may be rarely achieved in deep vadose zone regimes since response times generally exceed the typical time scale of major climate change. More likely, desert vadose zones are locked in long-term drying transients that are so gradual that they appear to be at steady state.

CHAPTER 4.

CONTROLS ON DESERT VADOSE ZONE MOISTURE FLUXES AND HYDRAULIC RESPONSE TIMES

4.1. Introduction

In the previous chapter, I described simulations for a generic vadose zone prototype to explore the merit of the DASH conceptual model. Certainly, however, there is a high degree of variability in the properties of alluvial-fill vadose zones. In recognition of this fact, I perform a sensitivity analysis in which parameters are systematically varied from the Base Case set of input parameters (Table 3-2) and the resulting simulation solutions are compared to the base-case solution, described in Chapter 3. The sensitivity analysis serves two main purposes. First, varying parameters within a typical range of measured values helps evaluate whether the DASH model broadly applies to desert vadose zones or is limited to a narrow margin of special cases. Second, results from a sensitivity analysis indicate which parameters exert primary influence on flow and transport in deep desert vadose zones. Such an evaluation may channel future research efforts to focus on better characterizing the more sensitive parameters. Variables considered in the sensitivity analyses include geothermal gradient, soil type, saturated permeability, water table depth, specified root-zone matric potential, and vapor diffusion rate. Only one parameter is varied at a

time from the Base Case to simplify evaluation of parameter sensitivity. Simulations carried to steady state for the dry hydraulic condition fixed at the base of the root zone ($\psi_{rz} = -400$ m) from an initial uniform downward flux of 10 mm yr^{-1} (i.e. DASH model scenario given in Table 3-3) generate a range of response times associated with each variable. Measures of sensitivity include the equilibrium response time, defined as the time required to complete an e-fold (63% response from initial to final state) change in the matric potential profile the steady-state matric potential profile.

4.2. Geothermal Gradient

Since the base-case moisture-flux solution demonstrates the importance of thermal vapor transport at steady state, the magnitude of the geothermal gradient may be expected to exert a major control on the equilibrium state of deep desert vadose zones. Simulation results ranging from a low ($15 \text{ }^\circ\text{C km}^{-1}$) to a high ($65 \text{ }^\circ\text{C km}^{-1}$) [e.g. *Blankennagel and Weir, 1973*] geothermal gradient corroborate this expectation (Figure 4-1 a,b). Increasing geothermal gradients induce larger thermal vapor fluxes, thereby reducing the depth of liquid flux divergence and enhancing the curvature of the matric potential profile (Figure 4-1a). The larger net-upward moisture fluxes associated with higher geothermal gradients result in faster response times (Figure 4-1b, Table 4-1). A zero geothermal gradient case generates a longer response time by nearly an order of magnitude compared with the high ($65 \text{ }^\circ\text{C km}^{-1}$) geothermal gradient case (230 kyr vs. 30 kyr).

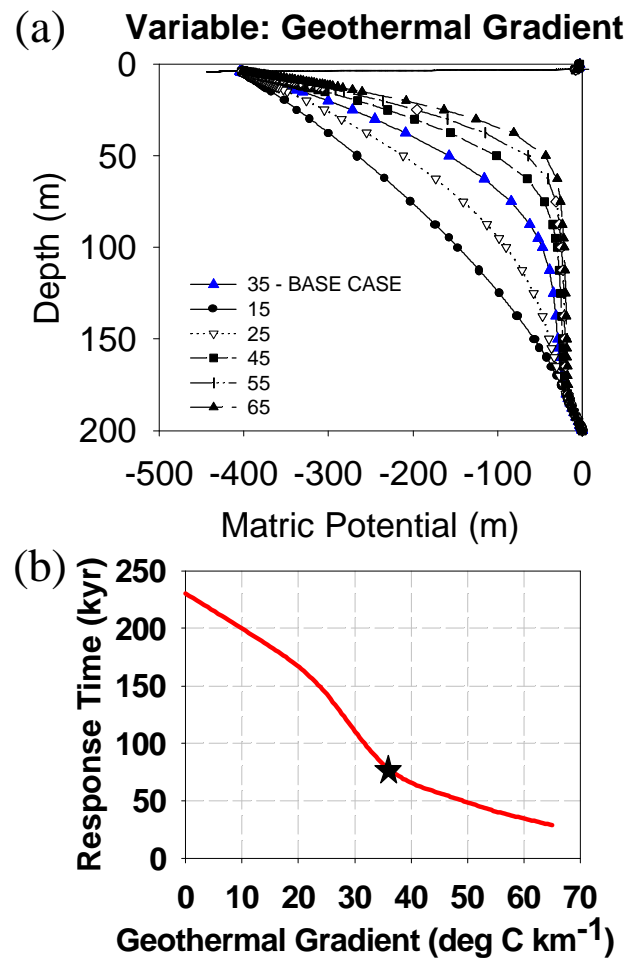


Figure 4-1. (a) Simulated steady-state matric potential profiles for variable geothermal gradient using the DASH model. (b) Response time as a function of geothermal gradient. The star represents results from the Base Case simulation.

Variable: soil type								
	sand*			silt	silty clay			
Response time (kyr)	80			400	250			
Variable: saturated permeability (k_{sat})								
k_{sat} (m^2)	1×10^{-9}	5×10^{-10}	1×10^{-10}	5×10^{-11}	3×10^{-11} *	1×10^{-11}	5×10^{-12}	
Response time (kyr)	32	34	59	72	80	104	119	

k_{sat} (m^2)	1×10^{-12}	5×10^{-13}	1×10^{-13}					
Response time (kyr)	175	197	275					
Variable: geothermal gradient (dT/dz)								
dT/dz (deg C km^{-1})	0	15	25	35	45	55	65	
Response time (kyr)	230	184	143	80	57	41	29	
Variable: water table depth (z_{wt})								
z_{wt} (m)	25	50	100	150	200*	400		
Response time (kyr)	0.24	11	47	80	80	80		
Variable: fixed root-zone matric potential (ψ_{rz})								
ψ_{rz} (m)	-50	-100	-200	-400*	-600	-800		
Response time (kyr)	31	45	66	80	87	88		
Variable: vapor diffusion enhancement factor (β)[§]								
β	0.5	0.75	1.0*	2.0	3.0	4.0	5.0	10.0
Response time (kyr)	122	97	80	55	44	37	32	16

Table 4-1. Summary of equilibrium response times calculated from the DASH model sensitivity analysis. * denotes value used in base case; [§] factor relative to vapor diffusion rate described by Fick's Law, assuming a tortuosity (τ) of 0.66; Values of $\beta > 1$ represent "enhanced" vapor diffusion.

4.3. Soil Type and Saturated Permeability

Simulations using the DASH conceptual model are run for various soil types, including a sand (Base Case), silt, and silty clay, with all other parameters being equal to the Base Case (Table 3-2). Saturated permeability and van Genuchten fitting parameters are varied (Table 4-2), whereas porosity, thermal conductivity, and rock specific heat remain constant for all simulations. The latter two parameters do not vary significantly over the range of values measured in typical alluvial sediments.

Soil type	Saturated permeability (k_{sat})	Van Genuchten soil parameters α and n (α , n)	Residual and maximum saturations (S_r , S_m)
Sand	$3 \times 10^{-11} \text{ m}^2$	4.5 m^{-1} , 1.9	10 %, 96 %
Silt	$8 \times 10^{-14} \text{ m}^2$	1.6 m^{-1} , 1.4	8 %, 96 %
Silty clay	$7 \times 10^{-15} \text{ m}^2$	0.5 m^{-1} , 1.1	16 %, 96 %

Table 4-2. Parameters used in sensitivity analysis for three soil types.

Simulation results in the form of steady-state matric potential profiles show little variation among the three soil types (Figure 4-2). However, the response times vary dramatically between each soil type considered (Table 4-1). The sand simulation produces a faster response than the silt and silty clay for a few reasons. Mainly, the higher saturated permeability of the sand, relative to the silt and silty clay, contributes to a shorter time required for the thick vadose zone to equilibrate to the dry hydraulic root zone condition. In the early to middle stages of drying, a downward liquid flux that is proportional to the unsaturated permeability accommodates drainage in the deep vadose zone. Simulation results generated by

varying the saturated permeability over several orders of magnitude for the sand confirm the importance of liquid permeability on deep vadose zone drying response times (Figure 4-3). The drier antecedent ($t \leq 0$) moisture conditions for the sand relative to the finer-grained soil types also favors a faster response in the sand, since the sand requires the smallest amount of moisture removal to equilibrate. However, this factor appears to be secondary to permeability in controlling the response time.

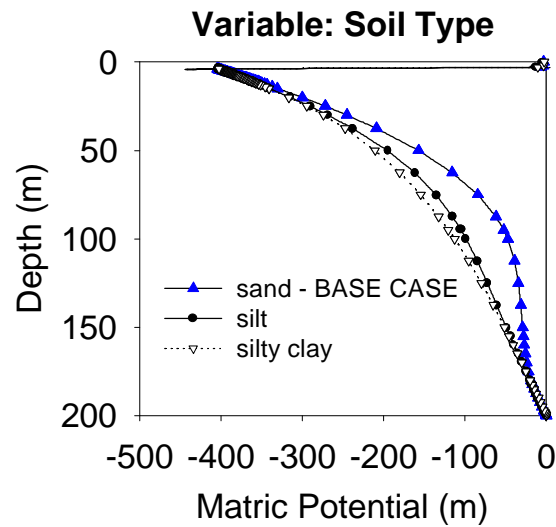


Figure 4-2. Simulated steady-state matric potential profiles for variable soil types using the DASH model. Soil texture properties are provided in Table 4-2.

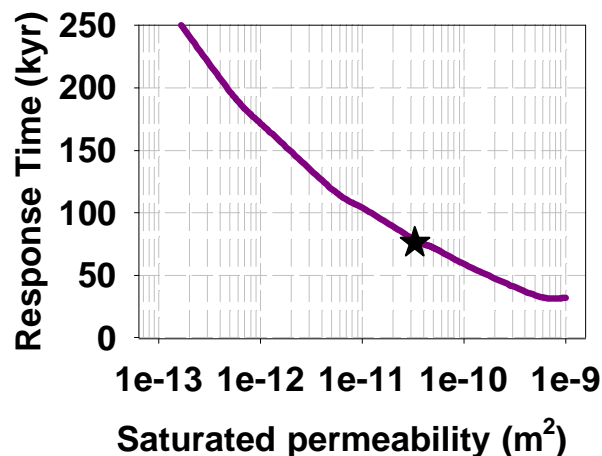


Figure 4-3. Response time as a function of saturated permeability. The star represents results from the Base Case simulation.

4.4. Water Table Depth

Since the water table serves as a boundary condition in the DASH model, the depth to water table factors strongly into the type of moisture flux regime that develops in desert vadose zones. A series of DASH model simulations for water table depths ranging from 25 m to 400 m using the Base Case (sand) soil type and a fixed root-zone matric potential of -400 m illustrates the flow regime's sensitivity to vadose zone thickness. The model-generated matric potential profiles at steady state for vadose zone thicknesses between 25 m and 100 m become increasingly more curved with decreasing vadose zone thickness to accommodate the increased overall steeper matric potential gradient (Figure 4-4 and Figure 4-5a). In contrast, steady-state matric potential profiles for vadose zone thicknesses greater than or equal to 150 m do not become less curved with increasing water table depth, but rather show relatively uniform values below depths of ~ 125 m (Figure 4-4 and Figure 4-5a). Model-calculated equilibrium response times reflect the influence of the water table depth on the flow regime for thinner vadose zones (< 150 m) (Table 4-1, Figure 4-5b). Calculated response times are as short as 240 years for the 25 meter thick vadose zone simulation. Response times increase rapidly with increasing vadose zone thickness and reach an asymptotic value of about ~ 80 kyr for water table depths ≥ 150 m due to the uniformity of the matric potential profiles below depths of ~ 125 m (Figure 4-5b). Vadose zones equal to or thicker than 150 m exhibit little sensitivity to the water table depth as shown by their overlapping matric potential profiles (Figure 4-5a), equivalent response times, (Figure 4-5b and Table 4-1) and similar net-upward steady-state fluxes (Figure 4-6).

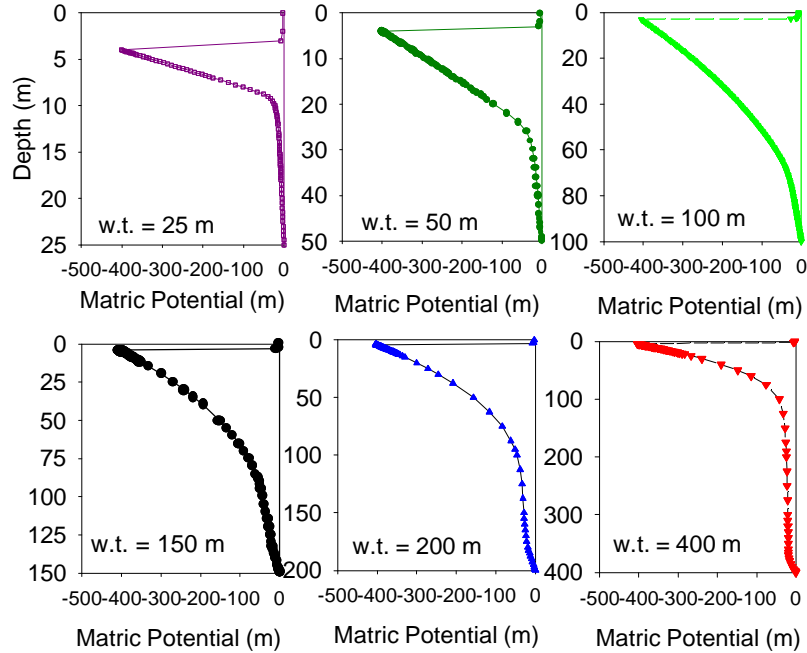


Figure 4-4. Simulated steady-state matric potential profiles with the Base Case properties for variable water table depths using the DASH model.

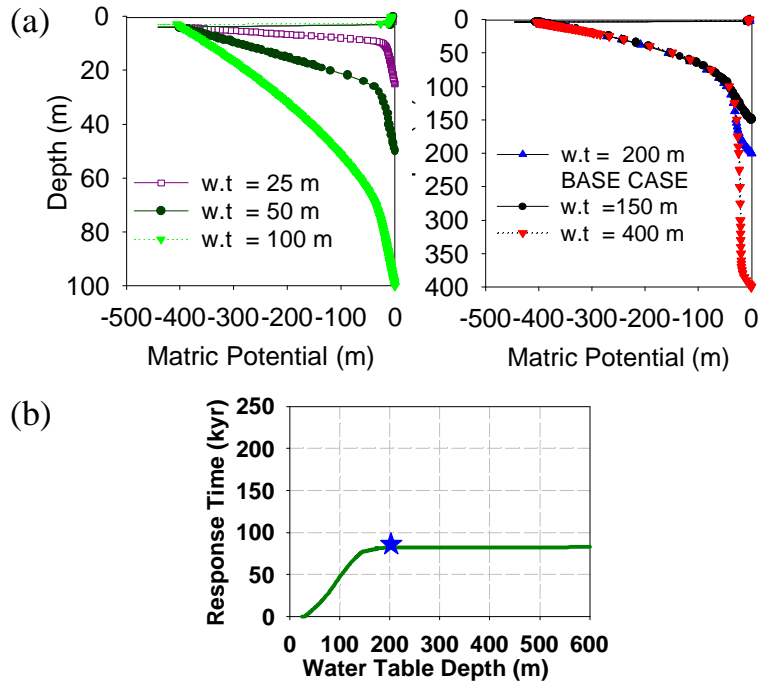


Figure 4-5. (a) Compiled steady-state matric potential profiles for water table depths of 25 to 100 m (left graph) and for water table depths of 150 to 400 m (right graph). The overlapping pattern in matric potential profiles in the lower graph suggests that a similar steady-state hydrodynamic regime develops for vadose zones exceeding 150 m in thickness (all other parameters being identical). (b) Response time as a function of water table depth. The star represents results from the Base Case simulation.

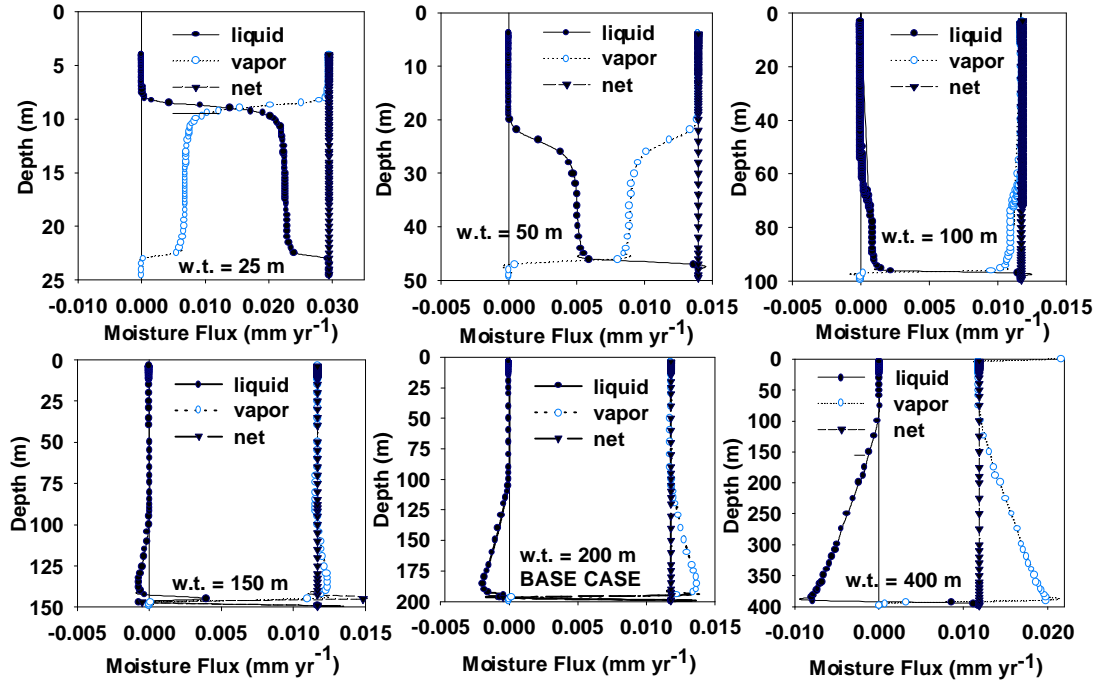


Figure 4-6. Simulated steady-state moisture flux profiles for variable water table depths using the DASH model. Negative values indicate downward fluxes, and positive values indicate upward fluxes. Note the change of scale on bottom axis for the upper left graph and the bottom right graph.

The steady-state divergent liquid flux pattern for the base case in Figure 3-11 does not develop in simulations in which the water table is < 100 m deep (Figure 4-6). This observation is consistent with the simulated plane of divergence located at a depth of 92 m for the 200-m thick base case vadose zone. Still, vapor transport dominates the steady-state moisture flux regime for water table depths exceeding 25 m. Generally, the upward vapor flux component exceeds the upward liquid flux component by at least an order of magnitude for thick (>25 m) desert vadose zones with these material parameters. In contrast, the upward liquid flux exceeds the upward vapor flux below 10 m for the simulation in which the water table is at a depth of 25 m (Figure 4-6). Capillarity draws enough water upward from the water

table in thinner vadose zones (< 25 m) to significantly increase the unsaturated permeability, and consequently increase the net upward moisture flux.

4.5. Fixed Root-Zone Potential Condition

Vegetation type and soil moisture availability strongly control the matric potential that fine plant roots must sustain within the root zone to survive. In order for the plant to take up water, there must be a driving force of water from the soil to the fine roots and to the larger roots that transport the water to the stem. A hydraulic potential gradient created by transpiration from the plant shoot and extending to the root xylem enables water uptake and transport [Steudle, 2000]. Water movement through the plant system is limited by xylem cavitation, the sudden change from liquid to vapor in normally water-filled xylem conduits [Pockman and Sperry, 2000]. Desert shrub species generally possess the ability to sustain more negative xylem matric potentials before experiencing cavitation than do more mesic species [Pockman and Sperry, 2000] rendering them comparatively more resistant to drought [Sperry *et al.*, 1998]. Desert species can maintain xylem matric potentials as low as -4 to -10 MPa [Pockman *et al.*, 1995; Pockman and Sperry, 2000]. Several causal factors including cavitation resistance, the ratio of root:leaf area and soil texture interact to set hydraulic limits and water uptake and transport through plant systems [Sperry *et al.*, 1998].

The complexity of these plant-soil water interactions exceeds the scope of this study. However, a sensitivity analysis addresses the variability of root-zone matric potentials within an observed range of water potentials sustained by desert plants

[Pockman *et al.*, 1995; Sperry *et al.*, 1998; Pockman and Sperry, 2000]. A series of simulations in which the specified matric potential at the base of the root zone (ψ_{rz}) was varied illustrates the sensitivity of the steady-state matric potential profiles and response times to the magnitude of the fixed ψ condition (Figure 4-7 a, b). Response times decrease with less negative ψ_{rz} values (Figure 4-7 b, Table 4-1). Although the driving force decreases with less negative ψ_{rz} values, the steady-state potential profiles for less negative ψ_{rz} values are closer than the steady-state profiles for highly negative ψ_{rz} values to the initial matric potential profiles (Figure 4-7a). Less moisture needs to be removed from the profiles maintained by less negative root-zone matric potentials to attain steady state, thereby requiring less time for equilibration. However, a point is reached (at about -500 m for this set of simulations) at which increasingly negative ψ_{rz} values have very little effect on the equilibrium response time (Figure 4-7b). At the dry end of the range, large changes in matric potentials correspond to very small differences in moisture content. Therefore, the amount of moisture required for removal for equilibration to a $\psi_{rz} = -500$ m upper boundary condition is very close the amount required for $\psi_{rz} < -500$ m.

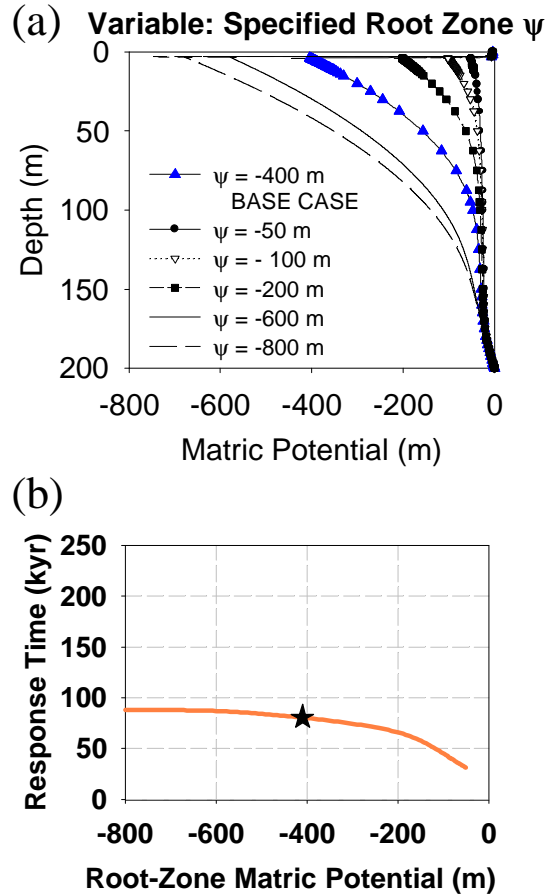


Figure 4-7. (a) Simulated steady-state matric potential profiles for variable fixed root-zone matric potential values using the DASH model. (b) Calculated response time as a function of fixed root-zone matric potential. The star represents results from the Base Case simulation.

4.6. Enhanced Vapor Diffusion

Water vapor fluxes result from spatial variations in vapor density, which is a function of both temperature and matric potential. Thermal vapor fluxes are driven by temperature gradients, whereas the isothermal vapor fluxes result from matric potential gradients. Vapor diffusion, described by Fick's Law, becomes increasingly more important to the overall transport of moisture as the porous medium dries. Laboratory experiments conducted on unsaturated material report vapor diffusion

enhancement, exceeding the rate predicted by Fick's Law by up to 18 times, at low liquid water saturations due primarily to the presence of "liquid islands" [*Philip and de Vries*, 1957]. According to the well-accepted hypothesis first proposed by *Philip and deVries* [1957], vapor is essentially transferred instantaneously from one side of the liquid island to the next, thereby enhancing vapor diffusion. *Silverman* [1999] measured vapor transport enhancement at the pore scale up to three times the vapor diffusion rate as described by Fick's Law. Laboratory experiments in the late 1960s – 1980s reported vapor diffusion rates deviating from that predicted by Fick's Law by factors of 0.42 to 4 (summarized in [*Silverman*, 1999]), which are considerably less than some of the large vapor enhancement values calculated by *Philip and deVries* [1957].

The set of simulations shown here explores the influence of enhanced vapor transport on drying response times by varying the vapor diffusivity from the Base Case value by factors of 0.5 to 10. This is accomplished by introducing a vapor enhancement factor (β) (Equation 13) that serves as a vapor diffusivity multiplier. For the Base Case, $\beta = 1$ and $\tau\beta = 0.66$. Values for β exceeding 3 to 4 (or perhaps less) are probably unlikely under field conditions (based on recent studies summarized in *Silverman*, 1999]), but are considered for comparison, nonetheless. The higher β values, and thus higher vapor diffusivities, result in significantly reduced response times (Figure 4-8, Table 4-1) emphasizing the strong control of vapor transport on the moisture redistribution in deep vadose zones undergoing drying, particular in the late stages of the drying process. The net moisture flux

values at steady state vary linearly with changes in the vapor diffusivity, thus confirming the control of vapor diffusion on the steady-state flow regime.

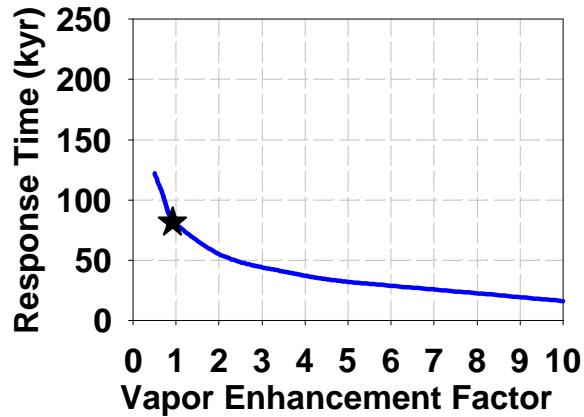


Figure 4-8. Calculated response time as a function of the vapor enhancement factor, β (defined in text). The star represents results from the Base Case simulation.

4.7. Transition Reversal

The sensitivity simulation results described above demonstrate that under a range of typical conditions and soil parameters, thick alluvial desert vadose zones respond extremely slowly to a change in surface boundary condition representative of a transition to an arid climate and establishment of xeric vegetation. The response in the reverse direction is expected to be considerably faster. In order to evaluate the response in desert vadose zones to a prolonged period of infiltration, transition reversals (dry-to-wet shifts) are simulated for different initial condition and infiltration rate combinations. Also, the response to a short-lived episodic infiltration event is also addressed by simulating a dry-to-wet-to-dry sequence. Specifically, the transition reversal simulations examine the behavior of the infiltrating water as it propagates with depth and the time required for matric potentials to equilibrate to the

change in the upper boundary condition. The infiltration event simulation addresses the wetting and drying behavior in the upper vadose zone and the time required to re-establish the matric potential profile expected for no episodic infiltration.

The initial condition for several of the dry-to-wet transitions consists of the dry steady-state solution for the Base Case. This somewhat unrealistic initial condition serves to bound the high end of calculated response times. A transient dry condition established upon 15 kyr of drying provides a more realistic initial condition and is used in the remainder of the transition reversal simulations. The “wet” boundary condition consists of a specified downward liquid flux ranging from 10 to 1 mm yr⁻¹. Table 4-3 records the initial and boundary condition combinations in addition to the corresponding simulation response time. As in the wet-to-dry simulations, the response time is characterized by an e-fold change in the matric potential profile from initial to final states. In all dry-to-wet simulations, the system responds rapidly (Table 4-3) compared to the wet-to-dry transitions for the Base Case (80 kyr). The shift to wetter conditions yields response times ranging from 50 years for the 15 kyr dry transient state initial condition and the highest infiltration rate to 375 years for the dry steady-state initial condition and lowest infiltration rate considered. The matric potential profiles shown for various “wetting” times suggest that even relatively short periods of wet conditions in which flow penetrates below the root zone induce a rapid and significant response in matric potential profiles (Figure 4-9). Infiltration could be hypothesized to result from rare, episodic, climate or weather events, but the very long timescales necessary to re-establish the highly negative matric potential profiles argues against such events during the Holocene in

places where these negative profiles are observed. This point is emphasized by a simulation in which water at rate of 5 mm yr^{-1} infiltrates past the root zone over a duration of 10 years using the Base Case set of parameters (Figure 4-10 a,b). The initial condition for the simulation consists of the 15 kyr dry transient state for the Base Case. The simulation proceeds for ten years with an infiltration specified at the surface at a constant rate of 5 mm yr^{-1} . After ten years, the wetting front has propagated to a depth of about 10 meters (Figure 4-10a). At this point, the dry hydraulic conditions are resumed at the based of the root zone (fixed matric potential = -400 m) and the profiles re-equilibrates (Figure 4-10b). Re-establishment of the pre-infiltration profile requires 5,000 years of persistent drying conditions.

Transition Reversal for the Base Case Set of Parameters

Initial condition	Upper Boundary Condition	Response Time (yr)	Simulation depicted in Figure 4-9
dry steady state	10 mm yr^{-1} downward flux	110	(a)
dry steady state	5 mm yr^{-1} downward flux	170	(b)
dry steady state	1 mm yr^{-1} downward flux	330	(c)
15 kyr dry transient state	10 mm yr^{-1} downward flux	50	(d)
15 kyr dry transient state	5 mm yr^{-1} downward flux	80	(e)
15 kyr dry transient state	1 mm yr^{-1} downward flux	175	(f)

Table 4-3. Summary of equilibrium response times calculated from the DASH model transition reversal simulations.

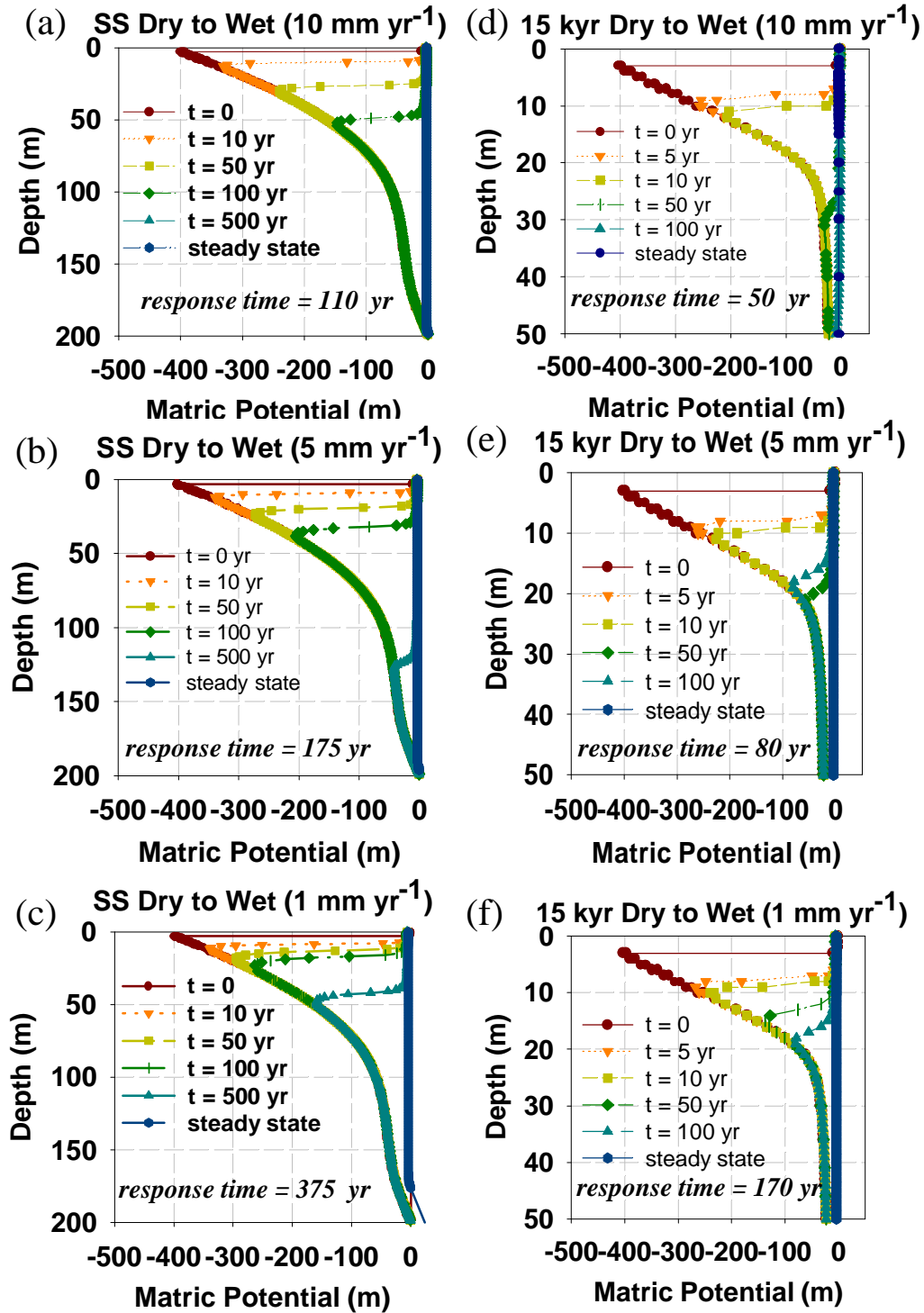


Figure 4-9. Transient matric potential profiles using the DASH model and recording the switch from the base case dry steady-state condition (a-c) or from the 15 kyr transient dry condition (d-f) to a specified downward flux of (a, d) 10 mm yr^{-1} and (b, e) 5 mm yr^{-1} and (c, f) 1 mm yr^{-1} .

The long duration required to restore the matric potential profile to its pre-infiltration condition provides additional support against episodic infiltration events during the Holocene where “pre-infiltration”-type profiles are observed. Also, the short-lived infiltration simulation results suggest that even if water that does episodically penetrate below the root zone of desert floors during wet periods, it is sucked back up when dry conditions resume rather than continuing to propagate downward in a slug-like fashion.

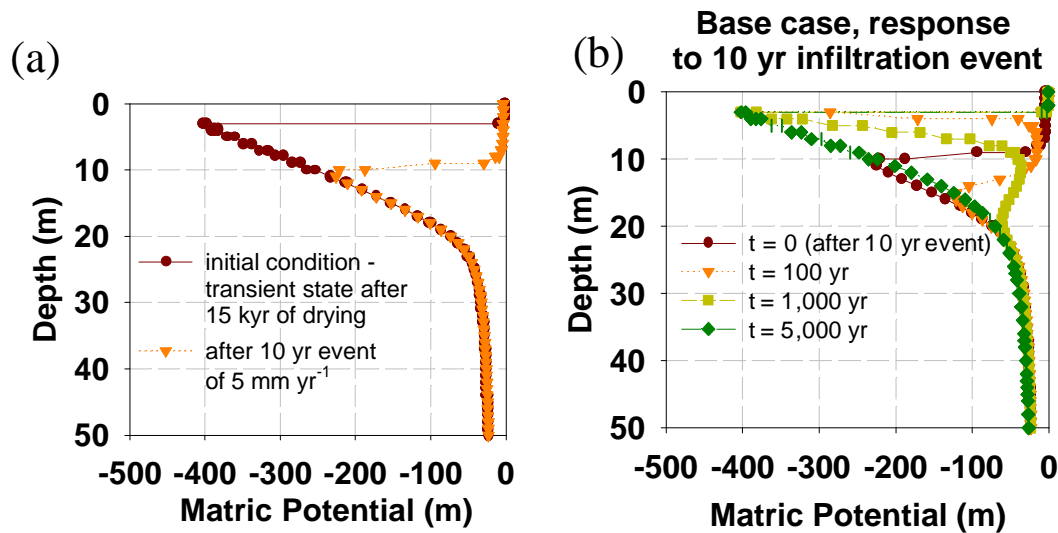


Figure 4-10. Vadose zone profile response to a 10 year, 5 mm yr⁻¹ infiltration event. The initial condition is the transient condition after 15 kyr years of drying for the Base Case. Matric potential profiles are shown for times (a) prior and subsequent to a 10 year, 5 mm yr⁻¹ infiltration event and (b) post-infiltration, re-equilibrating to the resumed dry hydraulic conditions in the root zone.

4.8. Conceptual Limitations

The fundamental assumptions intrinsic to the DASH conceptual model and related numerical simulations presented in this chapter include that: (1) flow is vertical and spatially uniform over the scale addressed for a given study, (2) efficient desert vegetation buffers the deep vadose zone from moisture transients, (3) chloride

deposition is constant through time or can be averaged over the relevant time period and, (4) chloride behaves conservatively. The conclusions obtained by applying the DASH model are limited to vadose-zone regimes in which these assumptions are valid. Violation of any of the assumptions at *isolated sites* would require a more complex conceptual model to describe the flow regime and environmental tracer distribution, but would not invalidate the broad conclusions drawn using the DASH conceptual model. Violations of any of the assumptions over large areal extents would necessitate careful reconsideration of some of the major conclusions of this study. The observed buffering capability of desert vegetation as monitored over multiple seasons by previous studies was discussed in both Chapter 2 and Chapter 3 (2.2.4. Hydrologic Interpretations of Observed Matric Potential Profiles and 3.2 Conceptual Model). The caveats regarding assumptions three and four were mentioned in Chapter 2 (2.3.1. Chloride Deposition and 2.3.2. Chloride Transport Behavior, respectively). The following discussion is intended to qualitatively evaluate the appropriateness and application extent of the DASH conceptual model to arid and semiarid vadose zones, with special consideration regarding the assumption of vertical, spatially-uniform flow. Lateral flow and preferential flow phenomena violate the assumption that flow is vertical and spatially (areally) uniform below the evapotranspiration zone. The following factors *may* contribute to deviation from vertical flow in unsaturated soil: geologic barriers or conduits (such as fractures, impervious layers, macropores, etc.), sloping surface topography, geologic heterogeneity, geologic anisotropy and multi-porosity media.

4.8.1. Lateral Flow

Numerous studies including field, laboratory and numerical modeling investigations cite the occurrence of multi-dimensional flow in unsaturated subsurface conditions. Horizontally-oriented geologic structures that act as conduits or barriers to flow in the unsaturated zone increase the likelihood of lateral flow by channeling horizontal flow and/or impeding vertical flow. But even more ubiquitous shallow subsurface features may encourage lateral flow. Spatially distributed vegetation, such as shrubs and trees, may induce lateral movement of moisture within the root zone. Geologic heterogeneity and unsaturated anisotropy enhances horizontal unsaturated flow. Layered geologic heterogeneity and hydraulic anisotropy are closely related under unsaturated conditions. A package of layered material, for example, in which the layers have different hydrologic properties may induce an unsaturated macroscopic anisotropy that is significantly greater than the saturated anisotropy. *McCord et al.* [1997] demonstrate that geologic heterogeneity imparts a strong control on flow through the unsaturated zone.

Geostatistics and stochastic modeling have been used to mathematically describe geologic media heterogeneity. Results from stochastic modeling of flow and transport in unsaturated heterogeneous media support the idea that the hydraulic conductivity anisotropy will vary as the hydraulic state of the media varies, i.e. state-dependent anisotropy [e.g., *Yeh et al.*, 1985; *Green and Freyberg*, 1995].

Even soils that are nearly isotropic at saturation may be highly anisotropic under unsaturated conditions when the moisture content is spatially variable [*Green and Freyberg*, 1995]. Following an episodic infiltration event, a moist, high-

conductivity layer parallel to the ground surface develops that may induce macroscopic anisotropy. *McCord et al.* [1991] provided compelling evidence, through field observations and numerical modeling, for a variable state-dependent anisotropy in the hydraulic conductivity of unsaturated texturally homogenous media resulting in lateral flow. Under saturated conditions, the soils in their study had an anisotropy ratio of about 1.5: 1, whereas the unsaturated anisotropy ratios ranged from 5.1 to 24.9.

Documented cases of significant lateral flow in dry soils, such as those described above, have been limited to the upper few meters where conditions are, at least temporarily, quite moist. In general, below a few meters, hydraulic gradients in the vertical direction greatly exceed those in the horizontal direction suggesting minimal lateral flow [i.e. *Hartsough*, 2000]. Therefore, the likelihood of deep vadose zone multi-dimensional flow is expected to be low and consequently bear slight limitation on the application of the DASH concepts to observed profiles. However, the development of lateral flow in the shallow soil zone may affect chloride profile analyses from a mass balance perspective. Lateral porewater movement and chloride transport in the upper few meters of the soil could result in a non-uniform effective chloride deposition. Apparent chloride mass balance ages may be biased either high or low depending on whether the soil column lies in a region of divergent or convergent lateral fluxes. However, below the root zone, redistribution by lateral solute diffusion may suppress that expression of lateral movement and chloride transport in the shallow vadose zone.

4.8.2. Preferential Flow

The occurrence of preferential flow, or bypass of the matrix, violates the common simplifying assumption of 1-D piston-type flow. On the basis of fundamental soil physics, preferential flow is more likely to occur under saturated or near-saturated conditions [e.g. *Johnston*, 1987] than under dry conditions typical of most desert vadose zones. The larger size of the macropores requires greater associated pressure potentials for fluid imbibition and transport according to the equation: $\Psi_c \geq -2\sigma/R$ (where Ψ_c = pressure potential required for pore imbibition, σ = surface tension, and R = pore radius) [*Jury et al.*, 1991]. Such large pressure potentials are representative of near-saturated conditions. Under low saturation (and associated low pressure potentials) the macropores should act as barriers and flow should occur only through the matrix.

Preferential flow will probably be most important near the soil surface following heavy precipitation events, where the combination of surface depressions, ephemeral channels, desiccation cracks, root tubules and high pressure potentials may result in non-piston flow. Many investigators conclude that preferential flow is not a significant component of flow in *deep* arid vadose zones based on the presence of distinct bomb-pulse tracer, tritium and chlorine 36, peaks, and low water potentials [e.g. *Scanlon*, 1991, 1992; *Phillips*, 1994]. Clearly, the validity of the piston-flow assumption depends on the temporal and spatial scales considered [*Scanlon*, 1991].

4.8.3. Hydraulic Functions

Another limitation of the modeling results presented in this chapter includes the shortcomings of using van Genuchten-Mualem hydraulic functions [*van Genuchten*, 1980; *Mualem*, 1976] to describe soils that are close to their residual water contents. Several authors express concern about applying common relationships of unsaturated hydraulic properties developed for moister conditions to very dry soils (< 10 %) [i.e. *Rossi and Nimmo*, 1994; *Khaleel et al.*, 1995; *Morel-Seytoux and Nimmo*, 1999]. *Morel-Seytoux and Nimmo* [1999] propose that different expressions are required to describe soil-water retention and unsaturated permeability for the very dry range (from oven dryness to field capacity), the middle range (field capacity to air entry pressure), and the wet range (from air entry pressure to saturated conditions). They suggest that an exponential form expression, modified from *Rossi-Nimmo* [1994], best applies to the very dry range. In addition, the traditional *Brooks-Corey* [1964] power law expression adequately satisfies the middle range, and a simple algebraic equation describes the relatively wet range [*Morel-Seytoux and Nimmo*, 1999].

The modeling study presented here does not incorporate different hydraulic functions for the dry, middle and wet ranges. The van Genuchten hydraulic functions (Equations 11 and 12) are applied across the entire range of wetness for a given soil type. Since the simulations described in this chapter focus on hypothetical vadose-zone prototypes to examine hydrodynamic processes, the issue of the van Genuchten hydraulic function applicability remains a very minor concern. However, there may be important implications for applying the DASH model to actual data sets and using

a relative permeability expression that is inaccurate or inapplicable in dry conditions, biased either high or low. Simulated response rates to boundary condition shifts will be affected. The sensitivity analysis for variable saturated permeability (k_{sat}) described in Section 4.3 (this chapter) provides a means of evaluating the importance of unsaturated permeability ($k(\psi)$) on response times, since k_{sat} serves as a match point for the $k(\psi) - \psi$ curve. Increasing k_{sat} shifts the relative permeability relationship towards higher $k(\psi)$ given the same ψ . Likewise, decreasing the k_{sat} shifts the relative permeability relationship towards lower $k(\psi)$ given the same ψ . The exponential relationship between drying response time and $\ln(k_{\text{sat}})$ (Figure 4-3) suggests the major control of (unsaturated) permeability on drying times. For studies aimed at determining matric potential profile development time, the unsaturated permeability must be accurately described by hydraulic functions appropriate for the water contents considered.

4.9. Summary

The DASH model applies to a broad range of deep alluvial-fill desert vadose zones as supported by the sensitivity analysis presented in this chapter. The base case moisture flux pattern generally describes the flux regimes simulated in all other cases, excepting scenarios in which the water table depth is less than 30 m and the geothermal gradient is zero. Excluding these cases, vapor transport dominates the hydrodynamic equilibrium state.

Under a range of typical conditions and soil parameters, thick alluvial desert vadose zones respond slowly to a change in surface boundary condition

representative of a transition to an arid climate and establishment of xeric vegetation. Equilibrium response times range from >1 kyr to 400 kyr, with most falling in the 20-100 kyr range. Response rates are particularly sensitive to soil texture, water table depth, and geothermal gradient. Coarse-textured soil with high permeability, shallow water tables, high geothermal gradients, and high vapor diffusion rates favor shorter response times. Soil texture strongly influences response times but imparts little control on the equilibrium state as depicted by matric potential profiles. For the base case, a water table depth of 150 m constitutes the threshold value. Water table depths exceeding 150 m produce identical equilibrium states and response times. Geothermal gradient strongly affects both equilibrium response times and equilibrium states, but probably plays a minor role in the current hydraulics of deep vadose zones that are far from the hydrodynamic equilibrium state. The response time dependence on the geothermal gradient and the vapor diffusivity would not be as strong as shown in this sensitivity analysis if only the early to mid-drying stages were evaluated rather than the complete drying process. And since the results of this study suggest that thick desert vadose zones are generally in mid-drying phases, the calculated equilibrium response times are more useful from a heuristic perspective than from an applied perspective.

Simulations conducted in the “reverse” direction (dry to wet) emphasize the relatively quick response of desert vadose zones subjected to prolonged periods of infiltration. Soil water penetrating below the root zone induces a significant response in the magnitude of matric potentials and profile shape. The long time scales necessary to re-establish the highly negative matric potential profiles argue against

episodic infiltration over extensive areas, in places where these negative profiles are observed. However, the analysis does not rule out the possibility of isolated flushing over small areas, which leads to an important caveat in applying the DASH model to vadose zone data. The assumption of spatially uniform, one-dimensional vertical flow limits the DASH conceptual model to cases in which lateral flow and/or preferential flow is absent or minimal. It seems likely that low moisture contents in the deep vadose zone greatly reduce the likelihood of lateral and preferential flow phenomena. A potential concern for violating the DASH set of assumptions resides in the possibility of spatial redistribution of chloride at the surface and/or within the upper few meters where conditions are sometimes wet.

CHAPTER 5.

CASE STUDY 1: NEVADA TEST SITE

5.1. Introduction

The Deep Arid System Hydrodynamics (DASH) conceptual model presented in Chapters 3 and 4 explains matric potential and chloride profiles typically observed in deep desert vadose zones. Results from numerical implementation of the DASH model suggest that vapor transport, both thermal and isothermal, and xeric vegetation are major controlling factors in deep desert vadose zone hydrology. Desert plants can prevent moisture from infiltrating below the root zone, impart very low matric potentials to the soil, and induce upward moisture fluxes below the root zone. This type of moisture flux regime is not consistent with a main assumption of the conventional chloride mass balance (CMB) method: downward advective transport [Allison *et al.*, 1994]. In light of this reinterpretation, how valid are calculations using the CMB approach to desert vadose zones? In order to investigate this question and improve the use of deep vadose zone porewater archives as paleohydrologic indicators, I employ an integrated field and modeling based approach. Site-specific modeling, using measured matric potential and chloride profiles from the Nevada Test Site, allows reconstruction of the vadose-zone moisture-flux history and recharge estimation associated with each location. Comparison of the DASH

modeling results to a conventional CMB paleorecharge reconstruction enables assessment of the CMB application to deep vadose-zone profiles.

A portion of this chapter addresses the spatial variability and shallow (< 5 m) distribution of porewater solutes including chloride and nitrate at Yucca Flat, one of the study sites within the Nevada Test Site. The main purpose of the shallow chloride distribution sub-study is to assess the applicability of extrapolating one-dimensional results inferred from vertical profiles to the surrounding area. Another focus of the shallow spatial distribution sub-study is on patterns of elevated levels of nitrate found beneath the modern rooting depth at Yucca Flat. The data challenges the theory the nitrogen fluxes and nutrient availability are major limiting factors in desert biological processes at the Yucca Flat study site.

5.2. Description of Study Location

This site-specific study focuses on two arid alluvial basins within the geographic borders of the Nevada Test Site (NTS) in southern Nevada: Frenchman Flat and Yucca Flat (Figure 5-1). The NTS served as a location for a series of underground nuclear explosions directed by the U.S. Atomic Energy Commission beginning in 1957 [Winograd and Thordarson, 1975]. The potential threat of groundwater contamination from subsurface nuclear bomb detonations motivated an extensive campaign to study the hydrogeology of the NTS and the surrounding region. This research takes advantage of the wealth of local hydrogeologic data and interpretations gathered as part of the initiative to characterize the NTS hydrogeology. This study uses data from the three deep cores at Frenchman Flat collected as part of

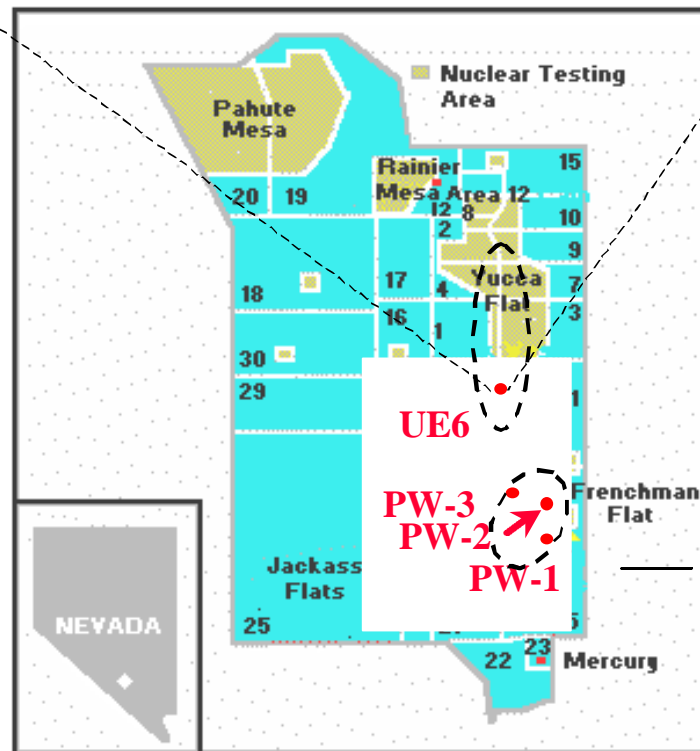


Figure 5-1. Location of Case 1 study site.

a research endeavor conducted in the 1990s to better understand the local hydrogeology surrounding the Radioactive Waste Management Site [Tyler *et al.*,1996]. This study also benefits from a tangible remnant of the NTS

characterization initiative from the 1970s: a previously unanalyzed core that sampled a 464 m thick vadose zone in Yucca Flat (Figure 5-1) through mostly alluvial material. The UE6e core was stored at the USGS Core Library in Mercury, NV, from 1974, when it was drilled, until sampled by this research project. Completion of a modern-day drilling project to recover unsaturated core, using air as the drilling fluid, to a comparable depth would be extremely costly (~\$750,000) and time-intensive (months of continuous work). Additional vadose zone cores considered in this present study include UE6s and the Yucca Flat Shallow Series cores, all located near the original UE6e borehole.

5.2.1. Regional Geology

The Nevada Test Site is located in the south-central part of the Great Basin section and exhibits typical Basin and Range topography. The NTS lies within the miogeosynclinal belt of the Cordilleran geosyncline, in which 11,000 m of marine sediments accumulated during the Precambrian and the Paleozoic Eras. The region is also within a Tertiary volcanic province in which extrusive rocks, locally more than 4,000 m thick, were erupted. Quaternary detrital sequences, mainly alluvium, fill most of the low-lying regions [Winograd *et al.*, 1975].

Two major periods of deformation affected the region. Orogenic activity in the late Mesozoic and perhaps early Tertiary resulted in uplift, folding and thrust faulting of the Precambrian and Paleozoic rocks. During the middle to late Cenozoic, the region underwent normal block faulting, which produced the Basin and Range

topography. Major displacements (on the order of kilometers) along strike slip faults resulted during both periods of deformation [Winograd *et al.*, 1975].

The most common Tertiary volcanic rock types, in order of decreasing abundance, are ash-flow tuff, ash-fall tuff, rhyolite lavas, rhyodacite lavas, and basalt. The tuffs are predominantly rhyolitic and quartz-latic in composition [Winograd *et al.*, 1975]. Most tuffs were deposited in the Miocene and Pliocene, a few are of Oligocene age. The two most prominent mountain ranges are the Spring Mountains to the south and the Sheep Range to the east. Ridges and valleys in the area generally trend north to northwest.

5.2.2. Local Geology

The PW-series wells, PW-1, PW-2, and PW-3, are located on an alluvial fan within the Frenchman Flat drainage basin. The wells are positioned on the apexes of an equilateral triangle, separated from each other by approximately 1.6 km (1 mile). PW-1 and PW-2 are positioned on relatively old pediment surfaces in contrast to PW-3, which was drilled on a much younger alluvial fan [Estrella *et al.*, 1993]. Surface elevations at the Frenchman Flat site range from 970 - 1000 m.

The UE6e, UE6s and Yucca Flat Shallow Series wells are located in Yucca Flat at a surface elevation of approximately 1200 m. Yucca Flat is an elliptical alluvial north-trending plain separated from Frenchman Flat to the south by the C P Hills, French Peak and Massachusetts Mountain (Figure 5-2). The valley is bounded to the north by Quartzite Mountain, part of the Belted Range. Half-pint Range bounds Yucca Flat to the east, and Shoshone Mountain and the Elena Range provides

the western boundary (Figure 5-3). The bounding hills and mountain ranges consist of Proterozoic to Permian sedimentary rocks, Cretaceous intrusive rocks and Tertiary volcanic deposits [Swadley and Hoover, 1990]. A desiccated lake, Yucca Lake, is located at the southern end of Yucca Flat. The closed structural basin underlying Yucca Flat receives basin-fill sediments from the uplands transported by intermittent streams. The UE6e, UE6s, and Yucca Flat Shallow Series boreholes are located on the bajada region, close the intersection of the alluvial fans and the valley wall. Surface elevations at the Frenchman Flat site range from 970 - 1000 m. The surface elevation at the Yucca Flat site is approximately 1200 m

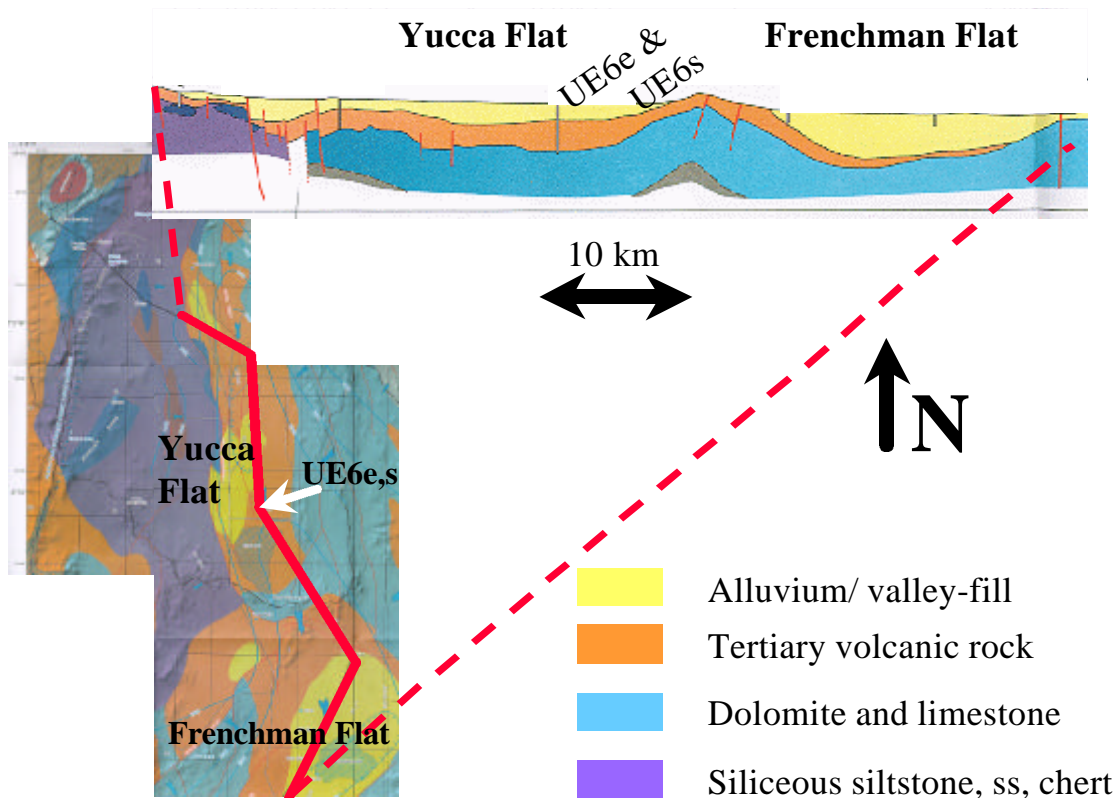
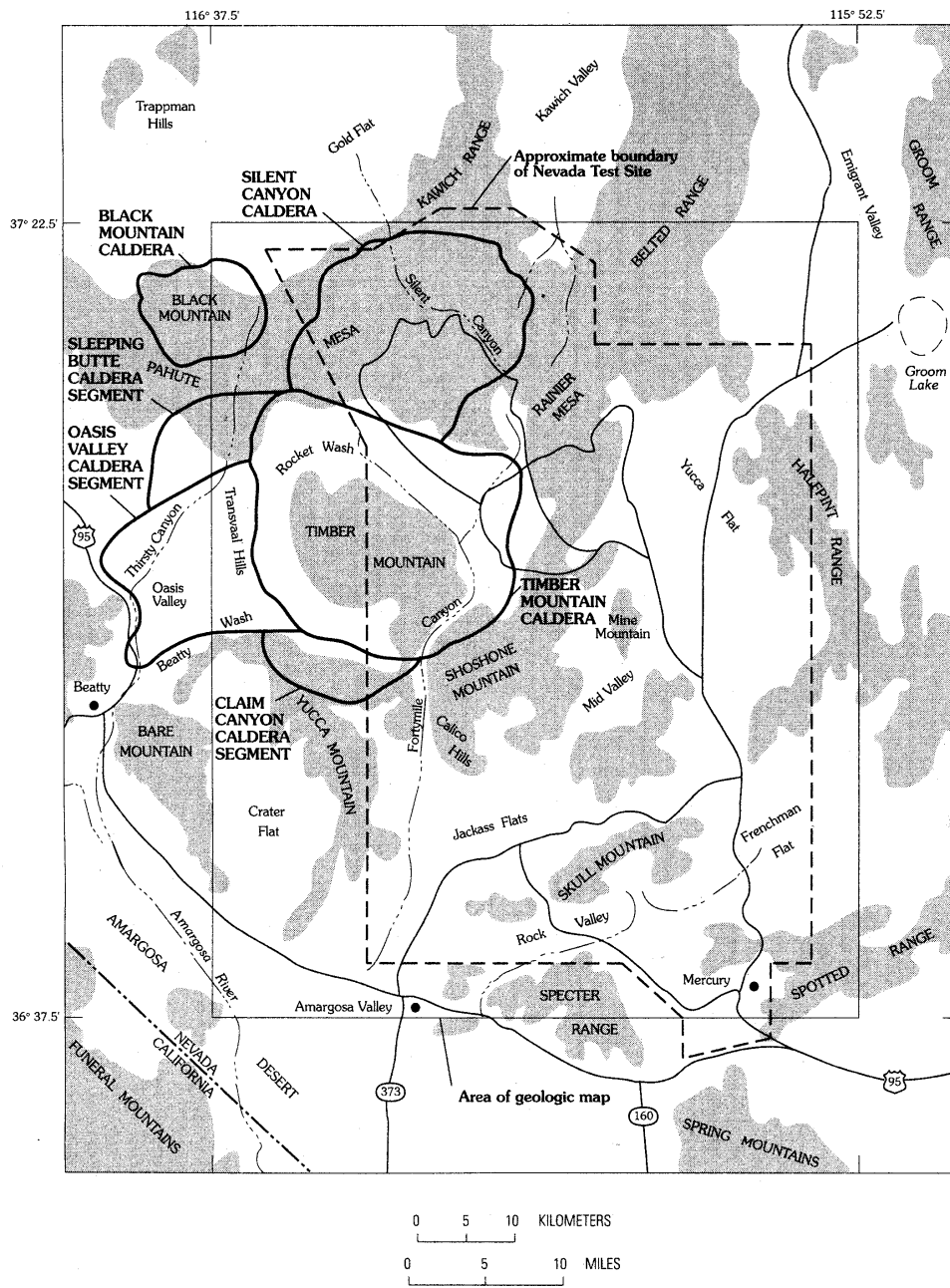


Figure 5-2. Cross-section through Yucca Flat and Frenchman Flat depicting local subsurface geology (modified from [Laczniak *et al.*, 1996]).



INDEX MAP SHOWING LOCATION OF GEOLOGIC MAP, NEVADA TEST SITE, SELECTED GEOGRAPHIC FEATURES, AND UPLAND AREAS (SHADED)

Figure 5-3. Map view of Nevada Test Site (from Frizzell and Shulters, 1990]. Shading represents topographically high areas.

5.2.3. Local Hydrology

Water table depth ranges from 230 m to 280 m in the Frenchman Flat wells and is approximately 460 m at the Yucca Flat wells, making the latter one of the deepest unconsolidated vadose zones in the continental United States. Hydrologic patterns in the Yucca Flat and Frenchman Flat structurally and topographically closed basin are typical of alluvial valleys found within the Great Basin. Groundwater recharge occurs predominantly in the flanking mountains and moves laterally towards the valley [*Laczniak et al.*, 1996]. Since the playas within the Yucca Flat and Frenchman Flat basins are dry except after precipitation events, *Winograd and Thordarson* [1975] infer that intrabasin groundwater movement is downward into the progressively older aquifers, rather than upward towards the playa surface. Groundwater flow through a deep Paleozoic carbonate aquifer accommodates interbasin east-southeast groundwater movement in the local study region [*Winograd and Thordarson*, 1975].

5.2.4. Current Climate and Vegetation

The NTS lies within the most arid part of the United States. The mean annual precipitation in the alluvial valleys ranges from 75 mm yr⁻¹ to 150 mm yr⁻¹ and generally does not exceed 250 mm yr⁻¹ on the ridges and mesa tops [*Winograd and Thordarson*, 1975]. Estimates of potential evapotranspiration range from 5-25 times that of the annual precipitation [*Meyers*, 1962]. Precipitation trends exhibit strong seasonal variability with highs in the months of February and August. Average

monthly temperatures range from a minimum of 17 °C in January to 22 °C in July [<http://nadp.sws.uiuc.edu>].

Local vegetation varies as a function of elevation, to a first order approximation, owing to the differences in precipitation and temperature within the Nevada Test Site. Below about 1200 m, vegetation consists of typical Mojave Desert species: burrow bush (*Ambrosia dumosa*), creosote bush (*Larrea tridentata*), and a variety of yuccas (*Yucca* sp.). At slightly higher elevations, blackbrush (*Coleogyne ramosissima*) and joshua trees (*Yucca beviifolia*) dominate and give way to sagebrush (*Artemisia tridentata*), juniper (*Juniperus* sp.), and piñon pine (*Pinus monophylla*) above elevations of ~1800 m.

5.2.5. Regional Paleoclimate

Major climatic changes profoundly affect the water balance and ecosystem of a region. Closed-basin lakes are thought to respond synchronously to changes in climate [*Benson et al.*, 1990]. Accordingly, ancient lake deposits in the Great Basin contain a useful record of paleoclimate. Paleohydrologic reconstructions based on lacustrine deposits in the Owens River system in southeastern California indicate a major wet period between 150 ka and ~120 ka followed by a climate trending towards increasing aridity with several fluctuations [*Smith et al.*, 1997]. Subsequent to 120 ka, only one significantly wetter period has been positively identified, between 24 ka and 10 ka, that induced Searles Lake, one of the major lakes in the Owens River system, to overflow [*Jannik et al.*, 1991]. *Morrison* [1991] and *Benson* [1991] report a dramatic increase in the level of Lake Lahonton from 14.5 to 13 ka (radiocarbon),

followed by a dramatic drop in lake level (Figure 5-4). Similar trends in lake levels are documented by evidence in closed-basin lakes in western Nevada [Benson *et al.*, 1990]. For example, Lake Bonneville reached its highest level around 14.5 ka and subsequently dropped sharply due in part to catastrophic downcutting and later by climate forcing [Benson *et al.*, 1990; Oviatt, 1997]. Based on climate model simulations, Hostetler and Benson [1990] suggest that a northward shift in the polar jet stream at 13.5 ka in the Great Basin resulted in a shift to arid conditions similar to today and coincident desiccation of many of the Pleistocene era closed-basin lakes.

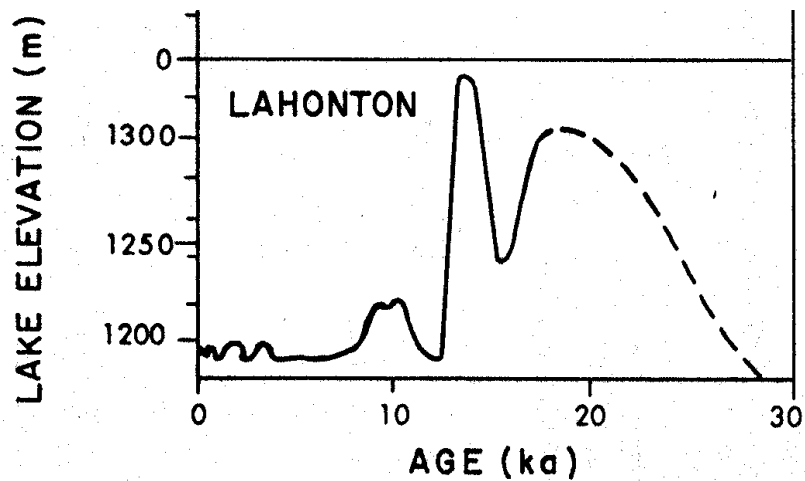


Figure 5-4. Paleolake level reconstruction of Lake Lahonton located in the Great Basin (after [Morrison, 1991]). Timescale in radiocarbon ka.

5.2.6. Regional Paleoecology

Paleoecological reconstructions from the northern Mojave Desert supply another means of evaluating paleoclimate. Some of the pioneering work using packrat middens as paleoecological archives was performed in the southern Great Basin [i.e. Wells and Jorgensen, 1964; Wells and Berger, 1967]. Both this early work and more recent studies indicate changes in the Mojavean ecosystem during the

late Quaternary. Between 1,000 m and 1,800 m in elevation, juniper and piñon-juniper woodlands persisted until replaced by desert scrub in the early Holocene. Full-glacial Mojave Desert supported xerophytic juniper woodlands below elevations of 1,000 m [Spaulding and Graumlich, 1986]. Spaulding [1990] approximates the ecotone between pygmy conifer woodland and desert scrub as a function of time and elevation based on compiled packrat midden and paleovegetation data from central-southern Nevada (Figure 5-5). At an elevation of 970 m (equivalent to the general elevation at Frenchman Flat), desert scrub replaced woodland between 14 and 11 radiocarbon ka (depending on classification of the site as mesic or xeric). Likewise, desert scrub replaced woodland at a xeric site elevation of 1200 m (equivalent to the general elevation at Yucca Flat) between 12 and 9 radiocarbon ka.

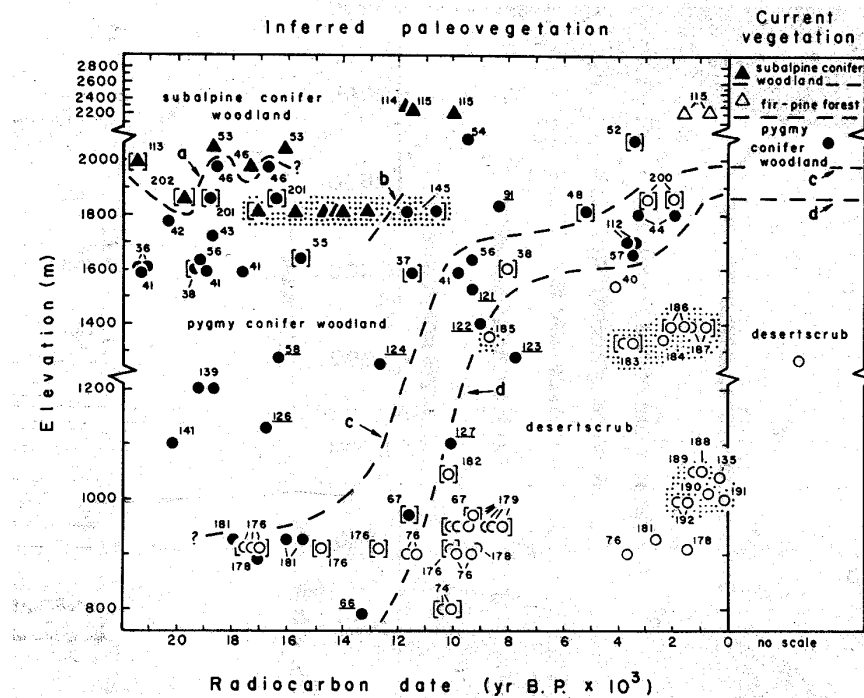


Figure 5-5. Vegetation plotted as a function of time (in radiocarbon ka) and elevation for the northern Mojave Desert using packrat middens [from Spaulding, 1990].

5.3. Field and Laboratory Methods

5.3.1. Sample Collection

Desiccated sediment samples from an archived core, UE6e, which was drilled as an exploratory hole at Yucca Flat in 1974, were acquired in June 1997 from the USGS core library in Mercury, NV. The total depth of the UE6e borehole (N 248,107 m, E 209,763 m; surface elevation = 1,1955.5 m) is 1200 m, including a 464 m thick vadose zone. Core material consists of alluvial material down to the bedrock contact at 409 m. Bedrock consists of Tertiary volcanic tuffs and Paleozoic carbonates [Winograd and Thordarson, 1975]. The top 40 meters were not cored in 1974. In order to obtain data in this interval, a new borehole was drilled during a two week period extending from February 25– March 5, 1998 (Figure 5-6). The location of UE6s (N 248,047 m, E 209,763 m), 60 m south of UE6e, was intended to be close enough to the original borehole to possess the same flux history, yet far enough away from the UE6e drilling pad (40 m radius) to reduce the possibility of anthropogenic disturbance on the hydraulic and environmental tracer profiles. The drilling method for UE6s consisted of hollow stem augering, without drilling fluids, to reach a completion depth of 45 m. A 61 cm split-spoon sampler, lined with four 15.25 cm brass sleeves and driven ahead of the augers by hammer percussion, was used to collect soil samples (details provided in [Hartsough, 2000]). Samples in the brass sleeves were immediately capped with tight-fitting plastic caps, and sealed with electrical tape and parafilm to prevent moisture loss (Figure 5-7). The sealed, sleeved samples were then individually placed into Mason jars that were then sealed with electrical tape and parafilm. Samples were transported to New Mexico Institute of

Mining and Technology and the Desert Research Institute (both Reno, NV and Las Vegas, NV locations) for analyses.



Figure 5-6. Hollow-stem auger drilling and sample collection of vadose zone core, UE6s, at Yucca Flat, Nevada Test Site.



Figure 5-7. Split-spoon sampler lined with brass sleeves for core collection.

Additional sample collection at the Yucca Flat site entailed hand augering. Seven shallow (~5 m) boreholes were hand-augered during October, 1998 within a 50 meter radius of the UE6s site (Figure 5-8) with the intent of examining the degree of spatial variability in terms of soil texture, water potential, and chloride profiles. Limited spatial variability would support using data from the UE6s core to supplement the missing shallow data from the deep UE6e core. The shallow cores follow two transects, A and B, perpendicular to one another. Spacing between each core ranges from 6 m to 10 m in order to deliberately sample within and far from observed microdrainages (Figure 5-8).

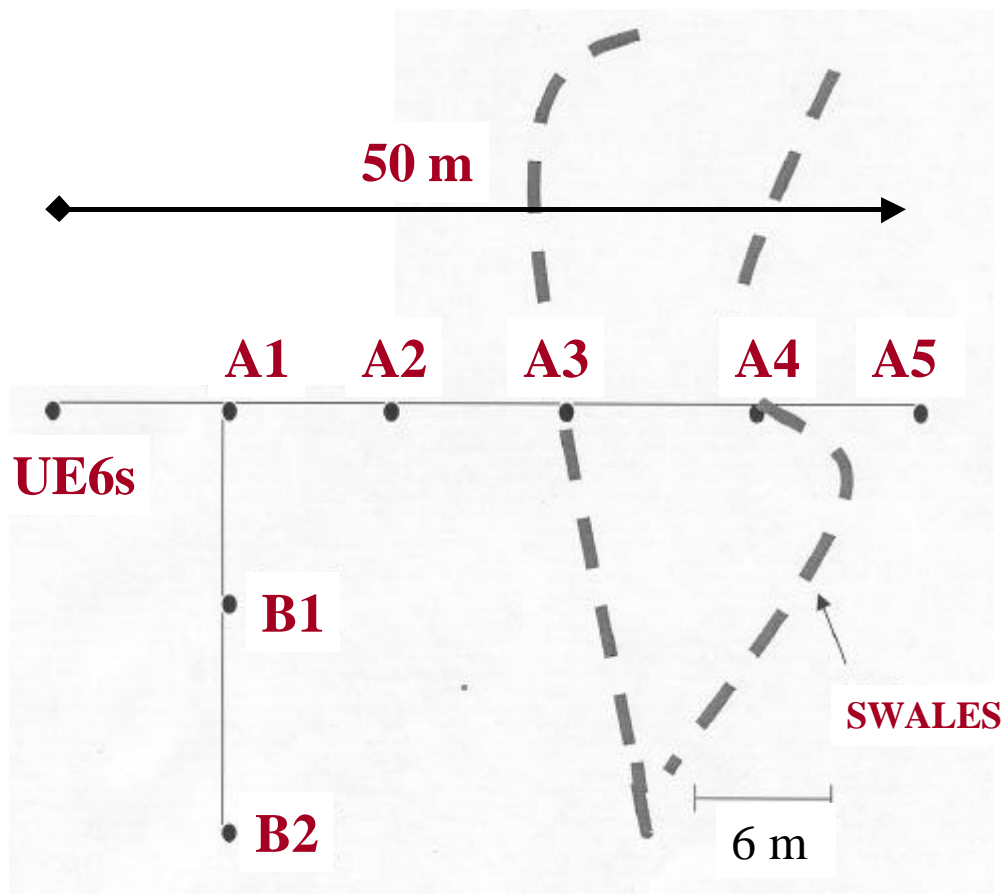


Figure 5-8. Map of Yucca Flat Shallow Series core locations (from [Hartsough, 2000]).

Samples brought to the surface using the hand-auger tool were immediately double-bagged in heavy zip-loc bags and stored in a cooler on-site. A concerted effort was made to expel most air from each sample bag, particularly for the samples to be analyzed for water potential. Samples were transported to New Mexico Institute of Mining and Technology and the Desert Research Institute, in Reno, NV for sample analyses.

5.3.2. Laboratory Methods

Leachate aliquots from the UE6e archived sediment samples, ranging from 41 m - 409 m in depth, were analyzed for chloride concentrations using both high performance liquid chromatography (HPLC) and ion chromatography (IC) methods.

Soil sample analyses for all other Yucca Flat cores included gravimetric water content, water potential, bulk density, and porewater concentrations of selected anions. Gravimetric water content was measured by weighing the “wet” samples soon and then again after oven drying at 105°C. The dry samples were weighed every 24 hours until the weight change was less than 5 % [ASTM, 1992]. Water potential measurements were obtained using a Decagon CX-2 water potential meter soon after sample collection to minimize post-collection moisture loss following the procedure in [Gee *et al.*, 1992]. The water potential meter operates using a chilled mirror hygrometer to determine the relative humidity of the soil sample. Relative humidity is converted to water potential using the Kelvin equation. The CX-2 water potential meter measures soil samples in the range of 0 to –10 MPa with an accuracy

of ± 0.1 MPa and in the range of -10 MPa to -40 MPa with an accuracy of ± 1 % [<http://www.decagon.com>].

Bulk density measurements of coarse peds were obtained using the clod method [Black, 1965]. The clod method required coherent samples. Oven-dried coherent samples tied with thin pieces of thread were individually weighed using a triple-beam balance. The samples were then dipped into melted paraffin at 60 °C (a few degrees above the melting temperature) and allowed to drain. After the paraffin solidified, the waxed samples were reweighed and then suspended in water and weighed again. The bulk density for each sample was calculated as follows:

$$\rho_b = \frac{\rho_w W_{sa}}{W_{sa} - W_{spw} + W_{pa} - W_{pa} \left(\frac{\rho_w}{\rho_p} \right)}, \quad (15)$$

where: ρ_b = dry bulk density [$M L^{-3}$], ρ_w = water density [$M L^{-3}$], W_{sa} = weight of dry sample in air [M], W_{spw} = weight of sample with paraffin in water [M], W_{pa} = weight of paraffin coating in air [M], and ρ_w = paraffin density [$M L^{-3}$] (0.9 g cm^{-3}). The paraffin was kept at a temperature just above its melting point to promote rapid solidification of the paraffin upon removal of the dipped sample and prevent paraffin imbibition into the pores of the sample.

Soil-water extracts for anion analysis were prepared by adding $18 \text{ } \Omega$ de-ionized H_2O to soil samples in 1:1 mass proportions. The mixtures were then placed in a shaker device and rotated for 24 hours and centrifuged for 30-60 minutes. The supernatant was then analyzed for chloride, bromide and nitrate concentrations using ion chromatography (IC) and high pressure liquid chromatography (HPLC) (details in [Hartsough, 2000]).

Grain size analyses were performed on selected samples following ASTM Method D 422-63 [ASTM, 1992] at the Desert Research Institute in Reno, NV. Gravel and sand fractions were estimated by sieving analysis, and the silt and clay fractions were calculated via the hydrometer method [Hartsough, 2000].

Deuterium and oxygen-18 soil-water analyses for samples from the UE6s core were completed at the Desert Research Institute in Las Vegas, NV using the toluene distillation method described in *Ingraham and Shadel* [1992].

5.4. Results from Deep Vadose-Zone Cores

5.4.1. Frenchman Flat

Data from the PW-series wells drilled at Frenchman Flat have been previously published, and descriptions of sample collection and analyses are detailed in *Estrella et al.* [1993], *REECo* [1994] and *Tyler et al.* [1996]. Temperature profiles measured in the PW-series wells indicate a local geothermal gradient of 11 -14 °C km⁻¹, which falls on the low end of the range of measured geothermal gradients in the Great Basin [Davisson et al., 1994; Blankennagel and Weir, 1973]. Hydraulic and soil analyses completed on samples from the 3 boreholes (PW-1, PW-2, and PW-3) that penetrated the entire vadose zone include gravimetric water content, water potential, bulk density, saturated hydraulic conductivity, water retention, porosity and grain size distribution [Estrella et al., 1993; REECo, 1994]. Measured tracer concentrations include Cl⁻, Br⁻, δD and δ¹⁸O [Estrella et al., 1993]. Only data from core samples, as opposed to cuttings, are presented here. Data from a shallow nearby borehole, ST-1,

is used to supplement the PW-1 data set due to limited recovery in upper portion of PW-1 [Tyler *et al.*, 1996].

Water potential profiles for the PW-series wells exhibit a curved exponential character [Estrella *et al.*, 1993] (Figure 5-9). The most negative measured water potentials below 2-m depth (above which may be seasonally variable) are -850 m at 8.3 m for PW-1, -225 m at 9.0 m for PW-2 and -770 m at 15.2 m for PW-3.

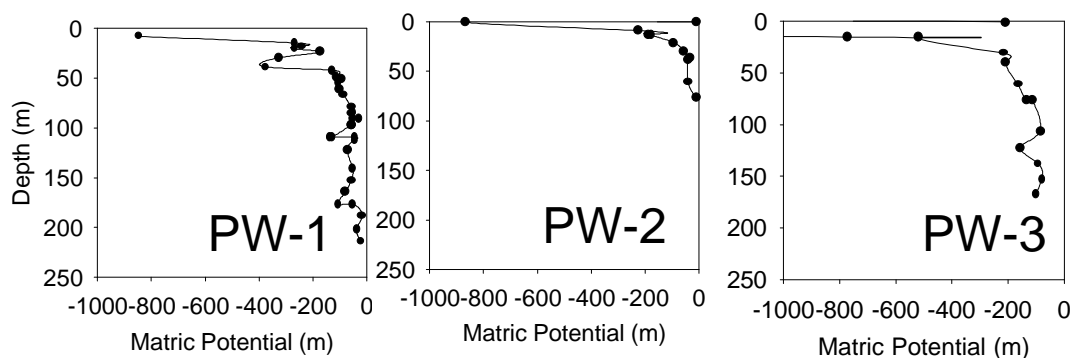


Figure 5-9. Measured water potential profiles from the Frenchman Flat cores (data from Estrella *et al.* [1993]).

Two of the three chloride profiles in Frenchman Flat, PW-1 and PW-3, display double bulges, a primary (shallow) and a secondary (deeper) bulge (Figure 5-10). Tyler *et al.* [1996] attribute the secondary bulges to chloride accumulation during an earlier arid period that was advected downward during an intermediate pluvial period. The absence of a secondary bulge in PW-2 is attributed to complete flushing of chloride during the pluvial period. Tyler *et al.* [1996] cite geomorphic control as the main cause of disparity in the PW-series chloride data. Unlike the other wells, PW-2 is located within a channelized zone associated with alluvial fan morphology. A surface lineament, representing the intersection of two alluvial fans, crosses PW-2 from NE to SW. This intersection may have focused overland flow and increased the likelihood of infiltration past the root zone [Tyler *et al.*, 1996].

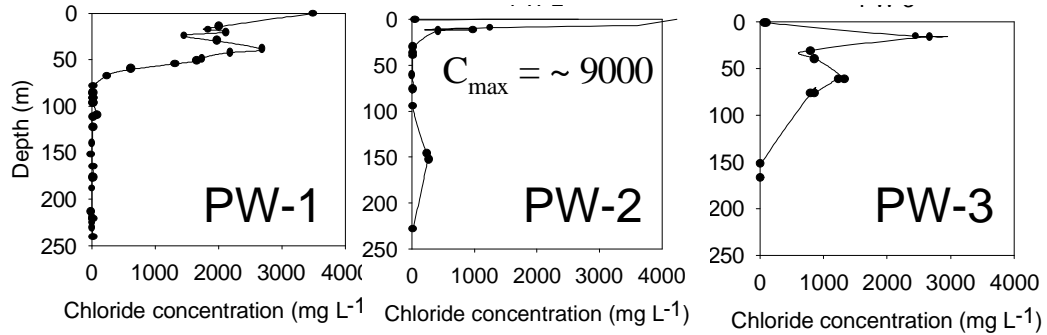


Figure 5-10. Measured chloride concentration (in porewater) profiles from the Frenchman Flat cores (data from *Estrella et al.* [1993]).

Results from stable isotope analyses show δD and $\delta^{18}O$ enrichment in the upper 40-50 m for all three profiles (Figure 5-11). Plots of the relationship between δD and $\delta^{18}O$ values show deviation from the composition of local precipitation (shown as the local meteoric water line (MWL) from *Tyler et al.* [1996]) (Figure 5-12). Linear regressions of the measured values exhibit slopes of 3-4 from the local MWL, indicative of evaporation, in shallow PW-2 and PW-3 samples and all PW-1 samples. Deep samples (below 40 m) show little evidence of evaporation in PW-2 and PW-3.

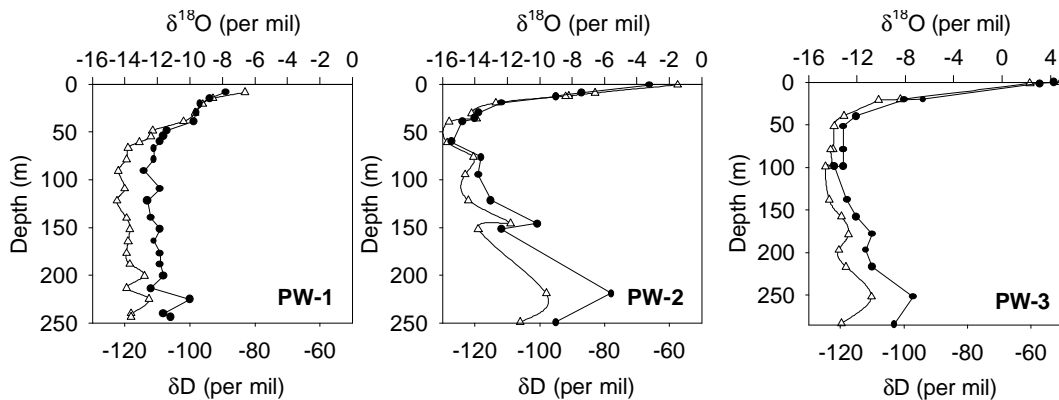


Figure 5-11. Measured stable isotope profiles from the Frenchman Flat cores (data from *Estrella et al.* [1993]). Black circles represent δD values (bottom axis). Open triangles represent $\delta^{18}O$ values (top axis).

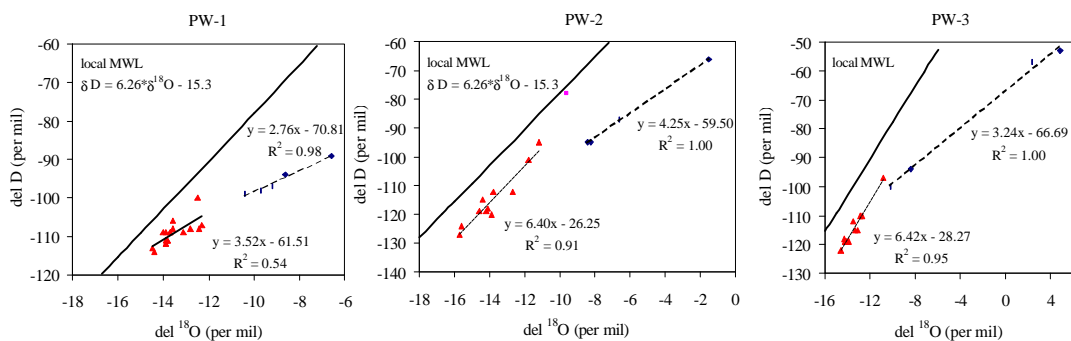


Figure 5-12. Stable isotope relationships from Frenchman Flat cores. (Data from *Estrella et al.* [1993]). Shallow samples (< 20 m depth) = diamond symbol; deep samples (> 20 m depth) = triangle symbol.

5.4.2. Yucca Flat

Results from Yucca Flat include data from the archived UE6e borehole, the 45 m borehole designated as UE6s, drilled as part of this study, and the Yucca Flat Shallow Series cores, designated as A1, A2, A3, A4, A5, B-1, and B-2 (Figure 5-8). The A series shallow cores run along the west-east transect with A1 located closest to UE6s and getting progressively further away with higher number designation. The B series shallow cores run north-south, perpendicular to the A transect and heading south from the A1 core.

5.4.2.1. Soil Characteristics

Most alluvial material from the Yucca Flat vadose zone cores fall under the classification of sandy loams (Figure 5-13, data in Appendix B) with little soil development, limited aggregation, very low organic carbon content and low water contents. Calcic horizons or other impeding layers were not observed in any of the borings. Many of the large grains do show significant carbonate coatings. Grain-size distribution profiles show the textural variations with depth (Figure 5-14) and (Figure

5-15). Maximum, minimum and average weight percentages of gravel, sand, silt and clay range are provided in Table 5-1 for the UE6e, UE6s, A1 and A3 Yucca Flat cores (raw data in Appendix B). The considerably larger range between minimum and maximum values for the UE6e core relative to the other 3 cores results from the greater sampling vertical distribution of UE6e which spans 400 m in contrast to 5 to 45 m in the other cores.

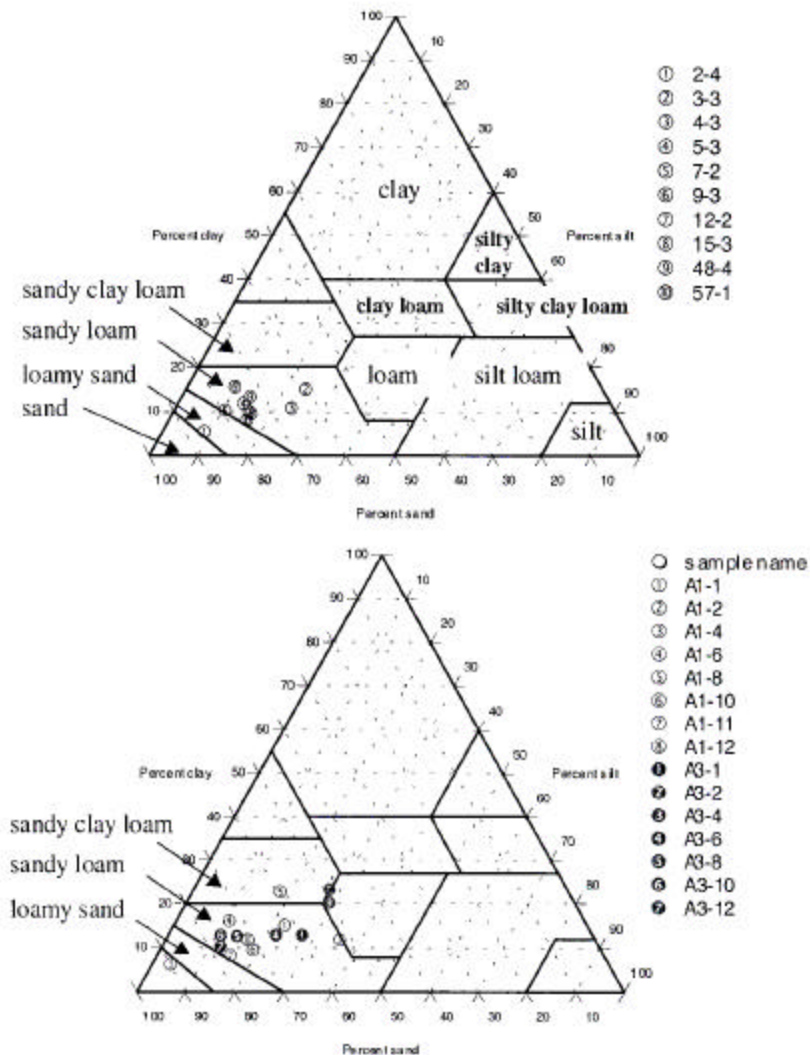


Figure 5-13. Soil texture trilinear diagram from Yucca Flat cores based on weight percentages of sand (50 - 2000 μm dia.), silt (2-50 μm dia.) and clay (< 2 μm dia.). The top trilinear diagram plots samples from the UE6s core. The bottom trilinear diagram plots samples from A1 and A3, two of the Yucca Flat shallow series cores.

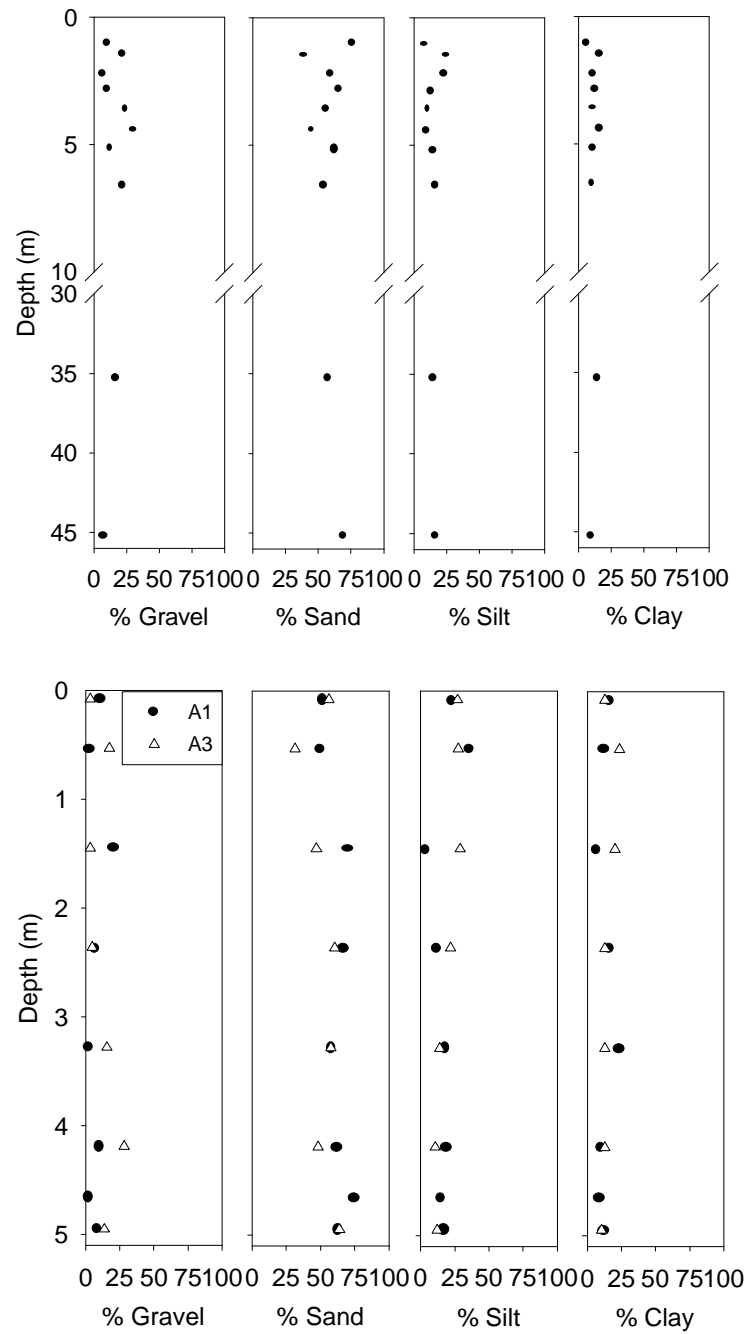


Figure 5-14. Grain-size distribution profiles from the UE6s core (top) and two of the shallow series cores (A1 and A3). Values are reported as weight percentages. Data in Appendix B.

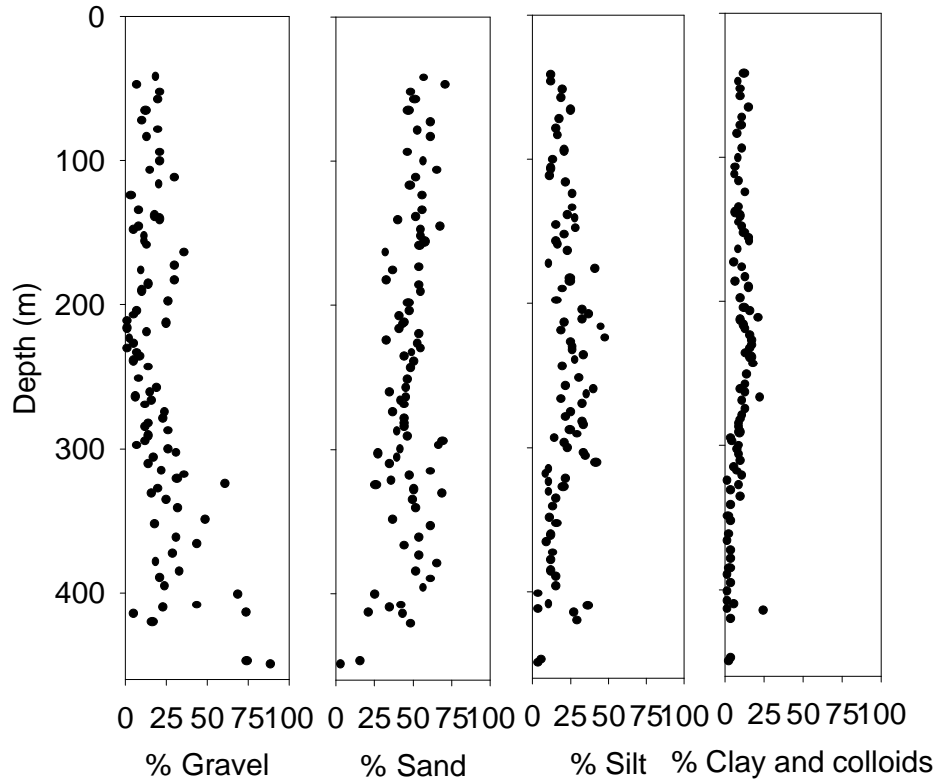


Figure 5-15. Grain-size distribution profiles from the UE6e core. Values are reported as weight percentages. Data in Appendix B.

	UE6e	UE6s	A1	A3
Maximum % gravel	89.5	30.5	20.1	28.1
Minimum % gravel	1.2	6.7	1.9	3.3
Maximum % sand	71.6	75.7	74.7	63.9
Minimum % sand	3.4	38.6	49.7	31.4
Maximum % silt	48.1	24.0	35.3	29.1
Minimum % silt	3.5	8.2	3.4	10.7
Maximum % clay	64.4	15.8	23.1	23.5
Minimum % clay	4.7	5.7	6.5	10.6
Average % gravel	21.1	15.9	7.8	12.3
Average % sand	47.6	57.9	61.8	52.1
Average % silt	21.7	14.8	17.5	20.3
Average % clay	9.6	11.3	13.0	15.2

Table 5-1. Soil texture data from the Yucca Flat cores. Values are reported as weight percentages. Compiled from data given in Appendix B.

The mean bulk density for 130 semi-consolidated UE6s samples is 1.52 g cm^{-3} , with a standard deviation of 0.15 g cm^{-3} (Figure 5-16, data in Appendix B). Lack of sample consolidation precluded bulk density measurements using the clod method [Black, 1965] for the UE6e archived core and the Yucca Flat Shallow Series cores. The mean bulk density value from UE6s is used in converting gravimetric water contents to volumetric water contents for UE6e and the Yucca Flat Shallow Series samples.

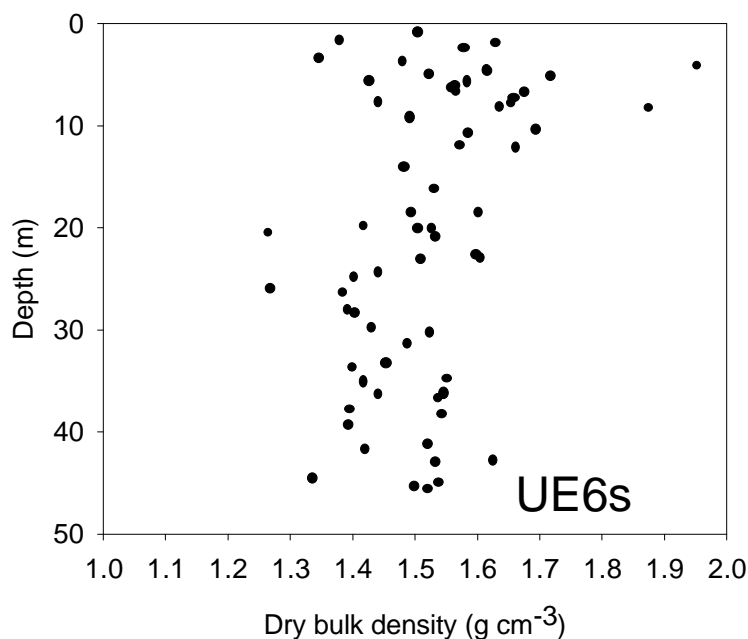


Figure 5-16. Dry bulk density measurements from the UE6s core. Data in Appendix B.

5.4.2.2. Water Content

The mean gravimetric water content of 109 UE6s samples is 0.11 with a standard deviation of 0.03 (Figure 5-17, data in Appendix B). Gravimetric water content measurements reported from 88 UE6e samples, measured after collection in

1974, average slightly higher with a mean of 0.14 and a standard deviation of 0.04 (Figure 5-18, data in Appendix B). The average gravimetric water content for the Yucca Flat Shallow Series samples is 0.08 with a standard deviation of 0.03 (Figure 5-19). The mean gravimetric water content for individual cores ranges from 0.07 to 0.09. The relatively lower water contents measured in the shallow cores are reasonable considering their shallow collection depths and the late summer collection time. The gravimetric water contents measured in the Yucca Flat Shallow Series cores are comparable to values from the UE6s core in the 1-5 m depth interval. The elevated water contents measured within the top 1 m of UE6s presumably are the result of a major precipitation event just prior to drilling the UE6s borehole.

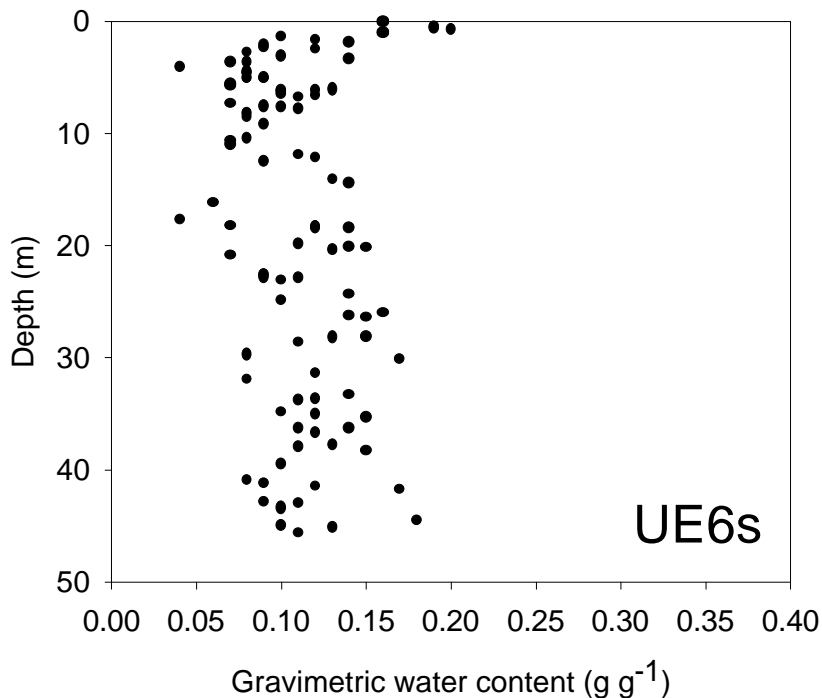


Figure 5-17. Measured gravimetric water content from the UE6s core. Data in Appendix B.

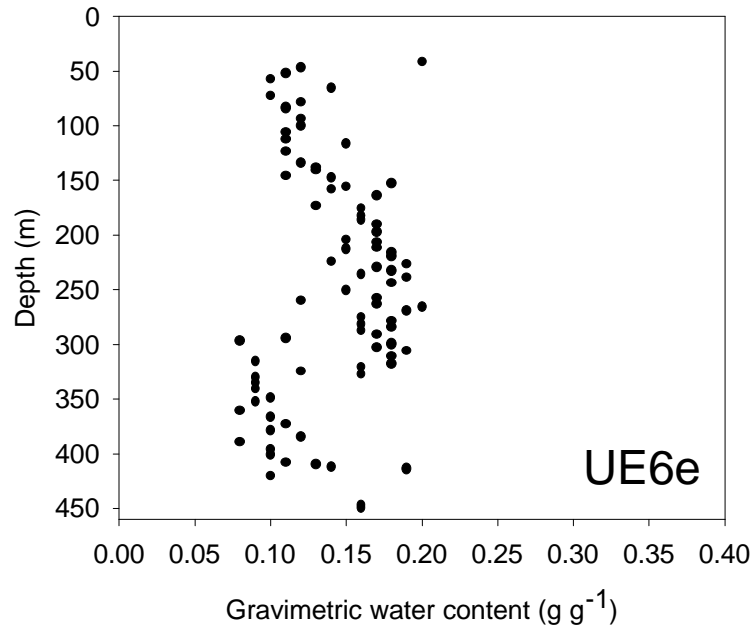


Figure 5-18. Measured gravimetric water content from the UE6e core. Data in Appendix B.

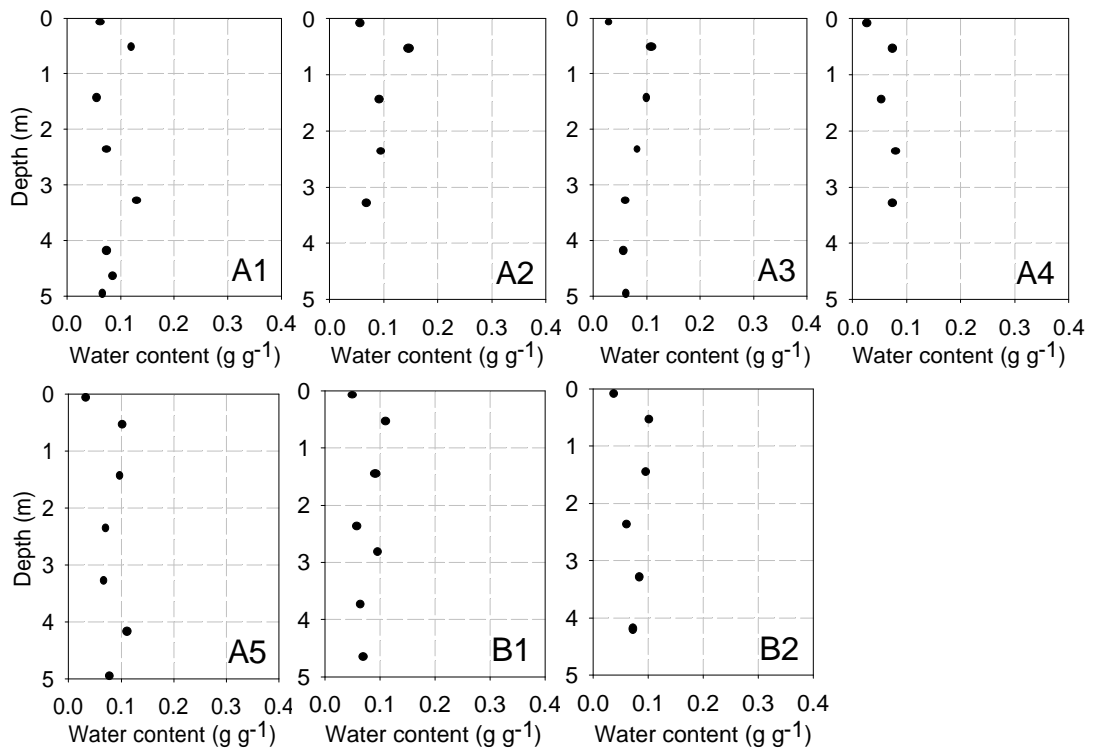


Figure 5-19. Measured gravimetric water content from the shallow series cores. Data in Appendix B.

5.4.2.3. Water Potential Profiles

The measured water potential profile from UE6s displays the characteristic curvature of desert vadose zones suggestive of upward liquid and isothermal vapor flow in the upper 25 meters of the profile (Figure 5-20). The most negative water potential measurement in the UE6s core is -456 m at a depth of 2.2m (data in Appendix B).

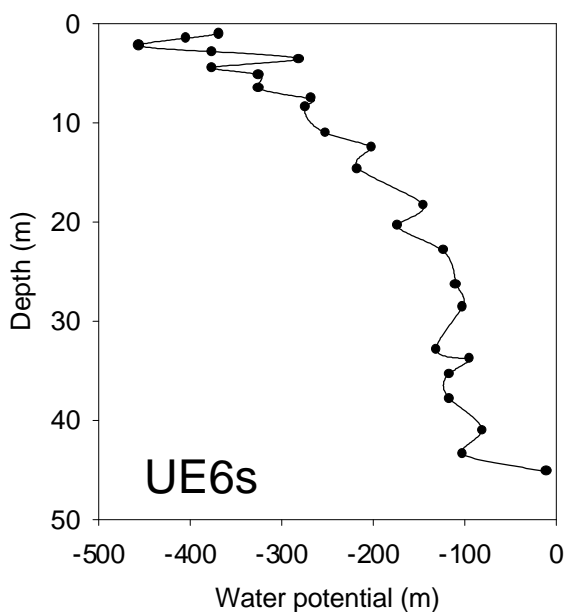


Figure 5-20. Measured water potential profile from the UE6s core. Data in Appendix B.

The measured water potential profiles from the Yucca Flat Shallow Series cores also display very negative water potentials (Figure 5-21). Although there is some degree of variability in water potential profiles measured between the shallow cores, the profiles are relatively consistent. Measurements in the depth interval from 1.5- 5 m range between -600 and -300 m, which correspond well with UE6s water potentials at the same depth interval. Extremely negative water potentials at the

surface in all of the Yucca Flat Shallow Series cores reflect nearly complete evaporation from the surface to produce a “bone-dry” layer. In contrast, near-surface water potential measurements from the nearby UE6s core are very high, just barely negative. Such dramatic differences in near-surface water potentials are not surprising considering the mid-winter, post-precipitation timing of UE6s collection in contrast to the late-summer timing of collection of the Shallow Series cores. The near-surface water potentials exhibit extreme seasonal fluctuations. From this limited view into the seasonal variation of water potentials at the Yucca Flat site, it appears that transient effects propagate to a depth of 1.5 to 2 m. Continuous long-term monitoring of water potentials at various depths would be required to estimate the dampening depth of seasonal fluctuations in a robust fashion.

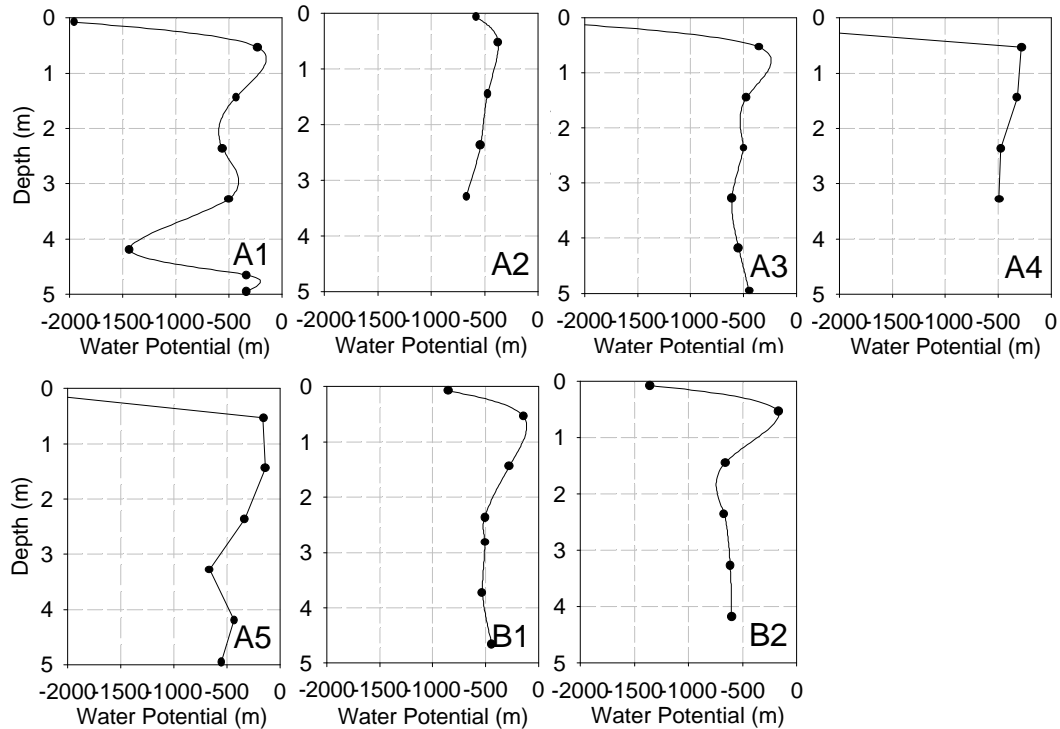


Figure 5-21. Measured water potential profiles from the Yucca Flat Shallow Series cores. Data in Appendix B.

5.4.2.4. Chloride Profiles

The measured chloride profile for UE6s displays a characteristic chloride bulge (Figure 5-22). Chloride concentrations just below the surface are low, reflecting active leaching. Maximum porewater chloride concentrations of 2200 - 2500 mg L⁻¹ are located about 3 m below the surface in the UE6s core (data in Appendix B). Below the shallow bulge, concentrations are relatively low in UE6s and also throughout the deeper UE6e profile (Figure 5-22). However, the average porewater concentration in UE6e is 82 mg L⁻¹, which is 36 mg L⁻¹ higher than the average below-the-bulge concentration in UE6s of 46 mg L⁻¹. This discrepancy may reflect one or more of the following: 1) systematic contamination in the archived UE6e core during drilling or storage, 2) chloride leaching from the alluvial material in the deeper strata but not in the shallow strata 3) considerable spatial variation in pre-Holocene infiltration between the two sites located 60 m apart, 4) a transition from an earlier lower soil-water flux period to a higher soil-water flux period coincident with the end of the UE6s record and beginning of the UE6e record around 12 ka (41 m depth) or 5) a systematic laboratory analysis error on samples from either of the cores. Although none of these possibilities can be absolutely ruled out, the first reason seems most plausible [Hartsough, 2000]. Explanations 2 and 4 are conceivable, but localization of the transitions at the break between UE6s and UE6e supports a core-related cause. The variation associated with explanation 3 corresponds to CMB-calculated paleofluxes (discussed later) differing by almost 50 % across a distance of 61 m in a very flat region, which also seems unlikely. Considering that the samples for both cores were processed identically and in the

same laboratory less than one year apart, case 5 is equally doubtful. In summary, the most likely cause of slightly elevated chloride concentrations in UE6e over UE6s is that the archived samples were contaminated either during the drilling, collection or storing process. This is arguably the most unsatisfactory and least easily confirmed or disproved case. Regardless, chloride analysis indicates no secondary bulge contained within the vadose zone at the Yucca Flat site. The combined UE6s and UE6e profiles (vertical overlap between the 40 m – 45 m depth interval) contain a single chloride bulge in the upper 5-7 m (Figure 5-22).

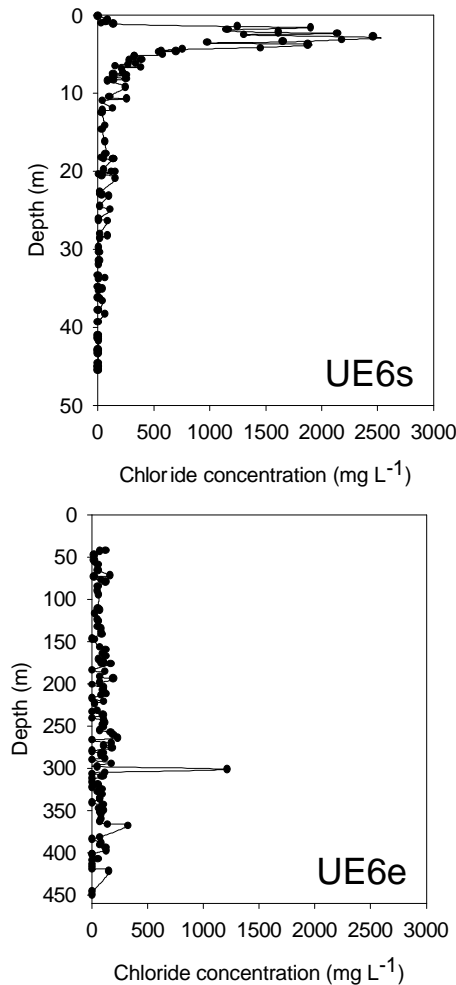


Figure 5-22. Measured chloride concentration profiles from the deep Yucca Flat cores. Values reported as porewater concentrations. Data in Appendix B.

The measured chloride profiles for the Yucca Flat Shallow Series cores illustrate similar character, but also display significant spatial variability within the upper 5 meters of the vadose zone (Figure 5-23). The chloride profiles exhibit the characteristic shape associated with desert vadose zones: low concentrations very near the surface, significant accumulation below with concentration peaks located at 2-4 m deep. This pattern corresponds well with the UE6s chloride profile. However, two anomalously low chloride profiles within the set of shallow cores are in striking contrast with all of the other profiles. Lower chloride peak concentrations and much less total chloride differentiates A3 and A4 from the rest of the profiles. The profiles from A4 also differs from all the rest in terms of its anomalously high chloride porewater concentration of about 1000 mg L^{-1} measured just below the surface. Near-surface concentrations for the UE6s core and all other Yucca Flat Shallow Series core do not exceed 100 mg L^{-1} . The locations of cores A3 and A4 coincide with small drainage channels observed in the field. The channels measure less than 50 cm in width and 10 cm of vertical relief.

The profiles at A5, B2 and to a lesser degree, A1, display what may be construed as double chloride bulges, centered at depths of about 2 and 3 meters. There are several possible explanations. First, the appearance of double chloride bulges may be simply an analytical artifact. Limited resolution of the measured profiles prevents definitive identification of a vertical separation between two chloride peaks. In each case (A1, A5, and B2), only one data point with a lower measured concentration defines the separation between the two peaks. Second, the vertical variation in the chloride profiles may reflect advection of the lower chloride

peak resulting from a major precipitation event, followed by subsequent chloride accumulation at the shallower depth. Considering the short distance between the two peaks, diffusion will effectively merge the two peaks in time. Third, water movement along a preferential horizontal flow pathway located at a depth of 2.5 may have contributed to some lateral flushing. This explanation seems the least plausible of the three mentioned. No horizontal hydrogeologic features, such as a caliche layer, were observed during collection of the Shallow Series cores. Also, the distribution of water potential measurements does not indicate significant horizontal flow gradients, at least at the time of collection.

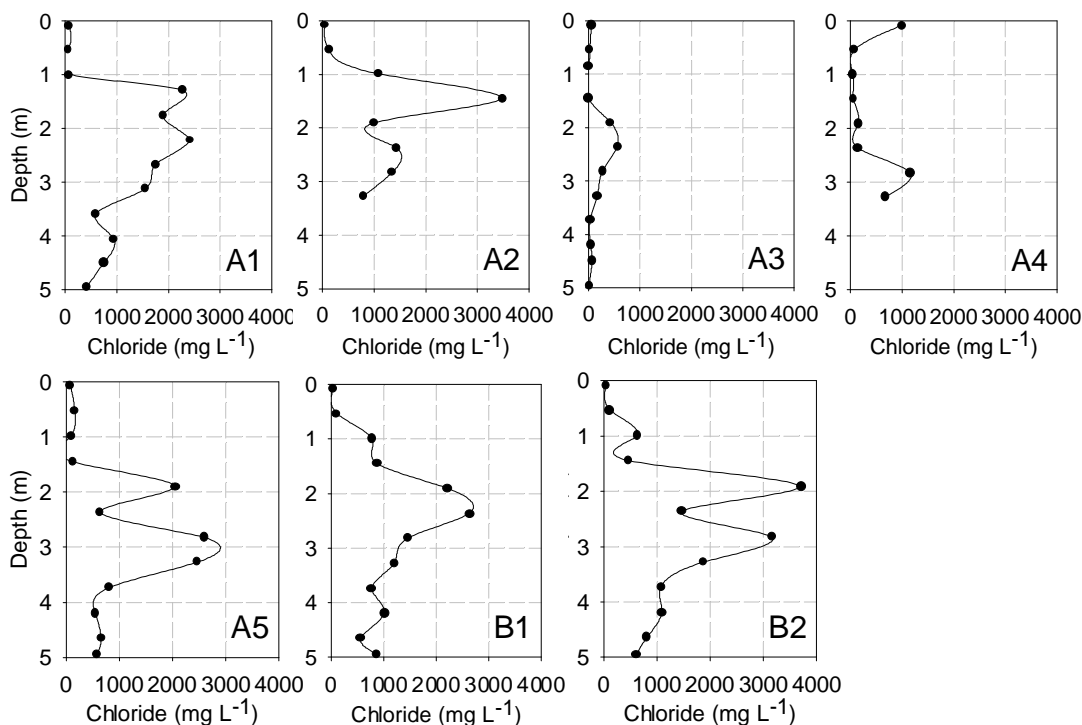


Figure 5-23. Measured chloride concentration profiles from the Yucca Flat Shallow Series cores. Values reported as porewater concentrations. Data in Appendix B.

5.4.2.5. Nitrate Profiles

The measured NO_3^- -N profile for UE6s parallels the chloride profile, displaying a solute bulge in the shallow vadose zone (Figure 5-24). The chloride and

nitrate profiles exhibit remarkably similar shape and concentration magnitudes. Just below the surface, nitrate concentrations are low, probably reflecting a combination of plant uptake and leaching. Maximum porewater NO_3^- -N concentrations of 2600 - 2800 mg L^{-1} are located about 3 m below the surface in the UE6s core (data in Appendix B). Below the shallow bulge, concentrations are relatively uniform.

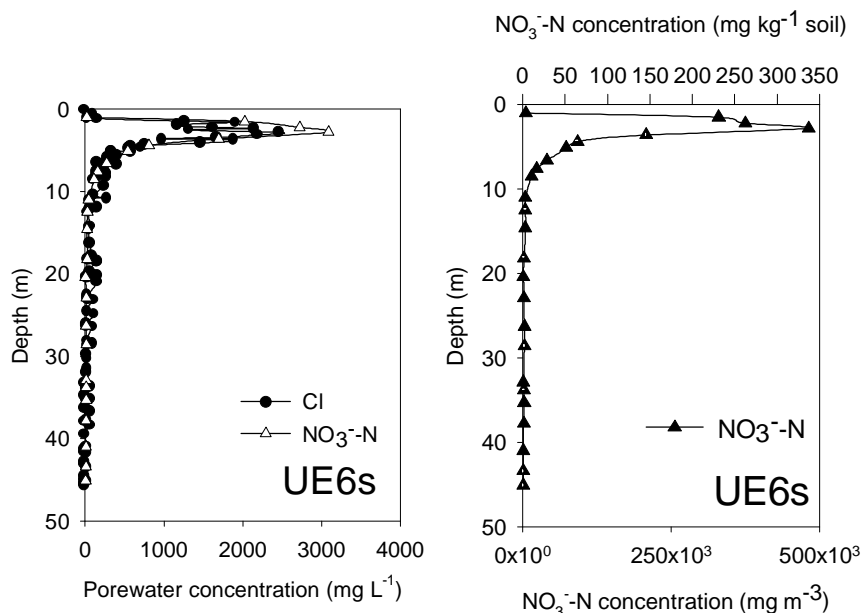


Figure 5-24. Nitrate concentration profile from the UE6s core with chloride profile (left) included for comparison. Values reported as NO_3^- -N and Cl porewater concentrations (left) and as NO_3^- -N soil mass (right, top axis) and NO_3^- -N soil volume (right, bottom axis) concentrations. Data in Appendix B.

The measured NO_3^- -N profiles for the Yucca Flat Shallow Series cores illustrate a pattern of spatial variability that closely resembles the pattern observed in the chloride profiles (Figure 5-25). Lower total amounts and peak concentrations of NO_3^- -N distinguish A3 and A4 profiles from the rest. Unlike the exceptionally high surface chloride value detected in A4, the surface NO_3^- -N value for A4 is low, which is consistent with other measured near-surface values.

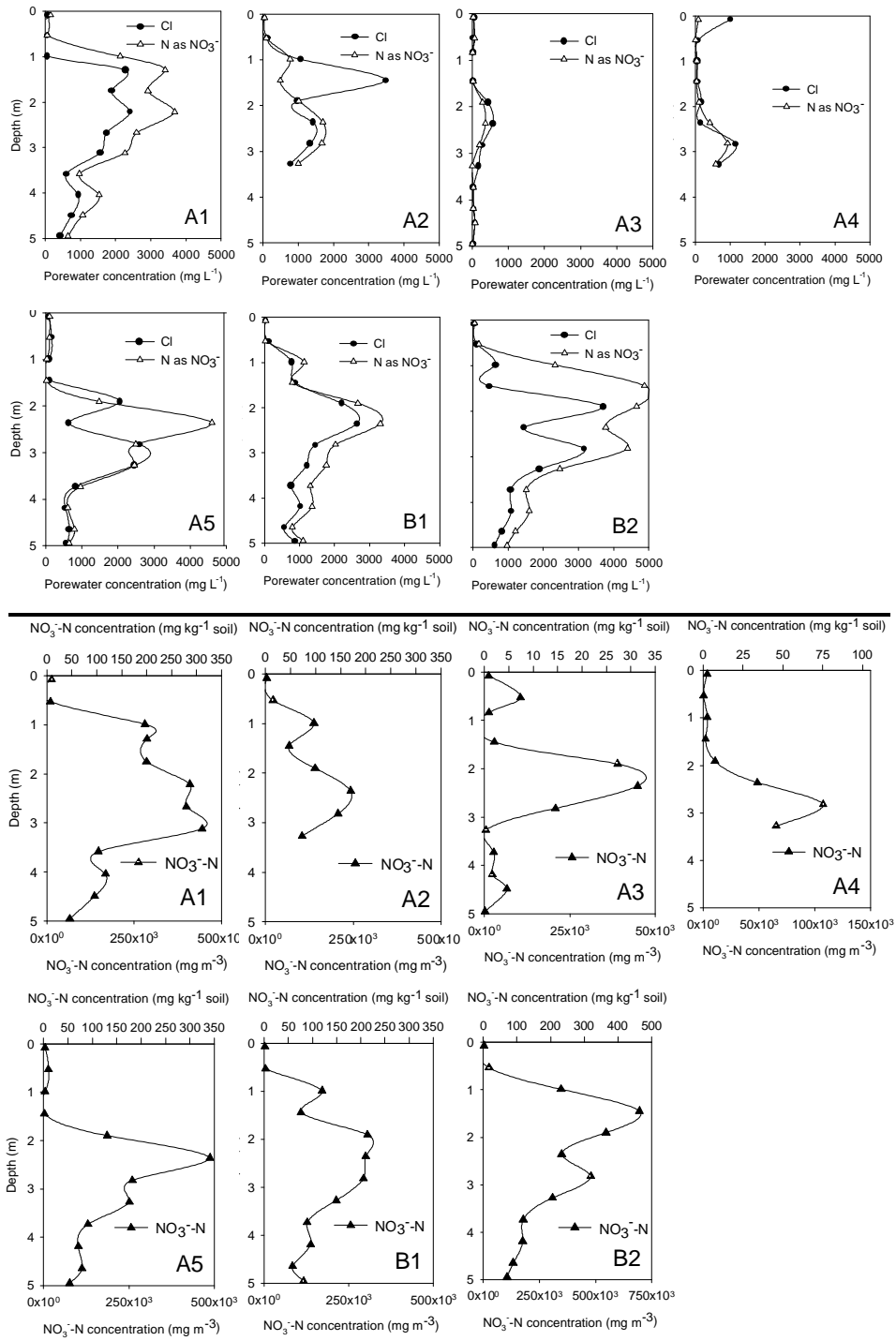


Figure 5-25. Nitrate profiles from the Yucca Flat Shallow Series cores with chloride profiles included for comparison (top graphs). Values reported as NO₃⁻-N and Cl porewater concentrations (top graphs) and as NO₃⁻-N soil mass (bottom graphs, top axis) and NO₃⁻-N soil volume (bottom graphs, top axis) concentrations. Data in Appendix B.

The nitrate profiles reveal two striking, and surprising, observations. First, the close correlation between the nitrate and chloride profiles suggests the dominant transport mechanisms for both solutes are similar. In other words, nitrate apparently behaves as a conservative tracer at this case study site. Since nitrogen is involved in many biological processes in the shallow subsurface, nitrate is generally not considered to behave conservatively. Second, the very large NO_3^- -N concentrations at several meters below the surface counter the commonly-held view that nitrogen losses from leaching past the rooting zone is minimal [West and Skujins, 1978; Schlesinger et al., 1990]. Nitrogen is often cited as a limiting factor in biological processes in desert environments [West and Skujins, 1978]. The observations of elevated nitrate and distribution patterns that follow chloride suggest that vegetation is not nitrogen-limited at the Yucca Flat site. Taken one step further, this inference may be expanded to submit that the vegetation is water-limited and not nutrient-limited. An alternative explanation is that nitrate in solution moves below the root zone when plants are not active. However, most of the plant species at this site continue to respire at least to some degree throughout the year [West and Skujins, 1978].

5.4.2.6. Stable Isotope Profiles

Results from stable isotope analyses show major δD and $\delta^{18}\text{O}$ enrichment in the upper 10 m of the UE6s core and some enrichment from 10-30 m (Figure 5-26). The relationship between δD and $\delta^{18}\text{O}$ values exhibits deviation from the composition of local precipitation (shown as the local meteoric water line) (Figure 5-27). A linear

regression of the measured values gives a slope of ~4 versus ~6 for the local meteoric water line (MWL), which is indicative of evaporation.

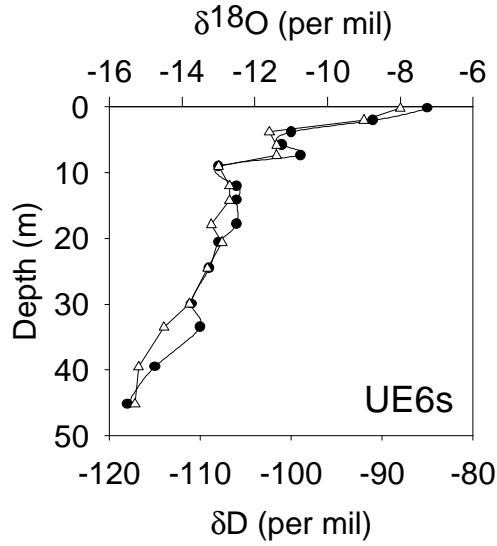


Figure 5-26. Measured stable isotope profiles from the UE6s core. Black circles represent δD values (bottom axis). Open triangles represent $\delta^{18}O$ values (top axis).

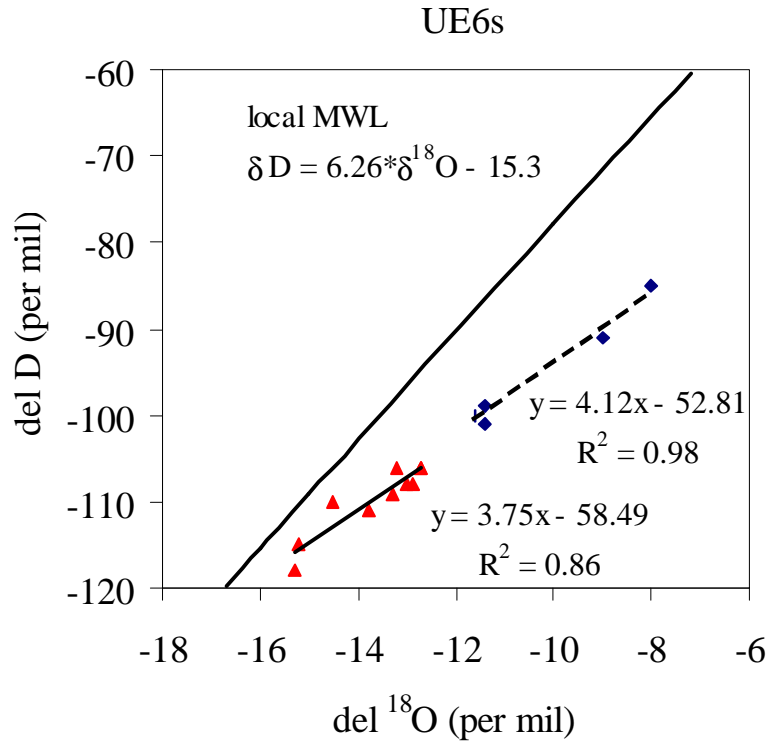


Figure 5-27. Stable isotope relationships from the UE6s core. The local meteoric water line (MWL) is plotted for reference. Shallow samples (< 20 m-depth) = diamond symbol; deep samples (> 20 m-depth) = triangle symbol.

5.4.2.7. Estimation of Geothermal Gradient

The lack of subsurface temperature data at the Yucca Flat UE6 site necessitated that I extrapolate a local geothermal gradient from a groundwater-temperature-contoured cross-section extending across Yucca Flat [Figure 7 in *Davisson et al.*, 1994]. The estimated geothermal gradient for the Yucca Flat site, $40\text{ }^{\circ}\text{C km}^{-1}$, exceeds the measured geothermal gradient at the Frenchman Flat wells by 3 to 4 times. The large difference is not unusual considering the relatively complex Basin-and-Range geology. Reported geothermal gradients within the Nevada Test Site range from 10 to $70\text{ }^{\circ}\text{C km}^{-1}$ [*Davisson et al.*, 1994; *Blankennagel and Weir*, 1973].

5.5. Chloride Mass Balance Approach for Paleohydrologic Reconstruction

5.5.1. Deep Cores from Frenchman Flat and Yucca Flat

Chloride mass balance calculations for the deep cores (PW-1, PW-2, PW-3, and UE6') assume a constant chloride flux at the surface of $105\text{ mg Cl m}^{-2}\text{ yr}^{-1}$, [following the analysis of *Tyler et al.*, 1996] which includes the contribution from both wet and dry deposition. This estimated long term average of $105\text{ mg Cl m}^{-2}\text{ yr}^{-1}$ is slightly higher than the current measured chloride deposition of $88\text{ mg m}^{-2}\text{ yr}^{-1}$ [*Hartsough et al.*, 2001] owing to the greater precipitation during the Pleistocene. The total amount of accumulated chloride varies widely among the four profiles considered. PW-1 and PW-3 yield total chloride ages of 95 – 110 kyr, whereas PW-2 yields a total age of 30 kyr (Figure 5-28). The combined cores from Yucca Flat, UE6s and UE6e, render a total chloride age of ~65 kyr. However, based on the

likelihood of contamination in the UE6e core mentioned previously, I opt to extrapolate the average deep core chloride concentration measured in UE6s (46 mg L^{-1}) to UE6e, thereby reducing the total profile chloride age to 33 kyr (shown in Figure 5-28 as the UE6' age-corrected vs. depth profile). The amounts of accumulated chloride contained above the bases of the single shallow bulges in the PW-2 and UE6s cores are 13 kyr and 9.5 kyr, respectively, and should reflect the timing of a significant reduction in infiltration rates brought on by climate change [Phillips, 1994]. The amounts of accumulated chloride contained above the bases of secondary bulges in the PW-1 and PW-3 cores are 82 kyr and 75 kyr, respectively, and should correspond to the timing of a pluvial condition related to the downward movement of the initial peak. In attempts to reconcile the PW-series paleohydrologic histories, Tyler *et al.* [1996] offer an advanced approach to chloride profile interpretation by accounting for solute dispersion in the Frenchman Flat cores. Consideration of solute dispersion reduces the CMB dates for the onset of pluvial conditions responsible for the secondary chloride bulges to 53 ka in PW-1 and 46 ka in PW-3. These modified CMB pluvial estimates may correspond to the earlier of two wet intervals reported by Quade [1986] who identifies marsh deposits forming between 60 and 40 ka and between 30 and 15 ka at locations 50-70 km south of Frenchman Flat. The modified CMB approach accounting for dispersion yields no quantification of the duration or average flux associated with the pluvial period. The paleohydrologic histories between the two cores in Frenchman Flat that contain secondary bulges and the core that records only a single peak (PW-2) remain incongruent despite the age reduction by accounting for dispersion.

The conventional CMB equation for estimating paleofluxes based on average chloride concentration in the deep portion of the profile [Phillips, 1994] yields apparent paleorecharge rates of 7.6 mm yr^{-1} , 4.4 mm yr^{-1} , 5.9 mm yr^{-1} and 2.3 mm yr^{-1} of PW-1, PW-2, PW-3, and UE6s, respectively [Tyler *et al.*, 1996]. For PW-1 and PW-3, these fluxes apparently reflect recharge dating back beyond the penultimate glaciation (prior to $\sim 110 - 120 \text{ ka}$), whereas for UE6e and PW-2, the estimated paleofluxes apparently reflect recharge prior to the onset of the Holocene at $10 - 15 \text{ ka}$ (Figure 5-28).

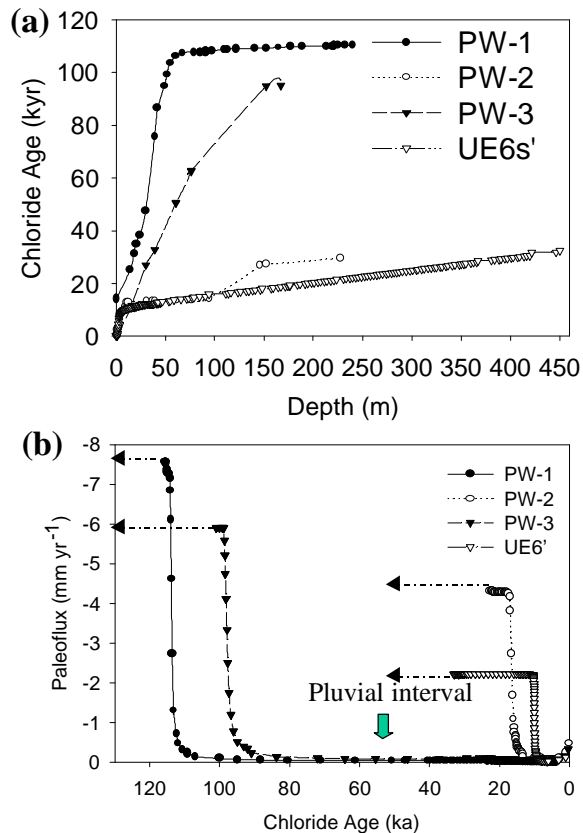


Figure 5-28. (a) Graph of chloride mass balance age with profile depth from the Frenchman Flat and Yucca Flat cores. UE6' refers to UE6s measured chloride data from 0 to 45 m and extrapolated from 45 to 464 m, based on an average below-bulge chloride value of 46 mg L^{-1} . (b) Paleoflux reconstruction using a conventional CMB approach. "Pluvial interval" was identified by Tyler *et al.* [1996] in cores PW-1 and PW-3 that display a secondary chloride bulge. Negative fluxes are downward.

5.5.2. Yucca Flat Shallow Series Cores

Chloride mass balance calculations for the Yucca Flat Shallow Series cores assume a constant chloride flux at the surface equal to the modern day estimate of $88 \text{ mg Cl m}^{-2} \text{ yr}^{-1}$ [Hartsough *et al.*, 2001]. The Shallow Series cores contain smaller inventories of chloride than the deep cores from Yucca Flat and Frenchman Flat considered in this study and thus represent shorter timeframes. Without high-resolution information on local temporal variations in chloride deposition, the best approach is to apply the modern day chloride deposition rate for Shallow Series CMB estimates, rather than a long-term average spanning the Pleistocene and Holocene. Chloride inventories stored within the upper Yucca Flat Shallow Series cores range from 1 kyr to 7.8 kyr of atmospheric deposition. The chloride age distributions calculated for Shallow Series cores correspond favorably with the UE6s chloride age distribution in the upper 5 meters, with the exception of the profiles from A3 and A4 (Figure 5-29). Cores A3 and A4 contain the lowest amount of accumulated chloride with inventories of 1.0 and 1.3 kyr, respectively. The Yucca Flat Shallow Series chloride bulges (Figure 5-23) are not fully captured in the vertical direction, which precludes estimating CMB paleofluxes.

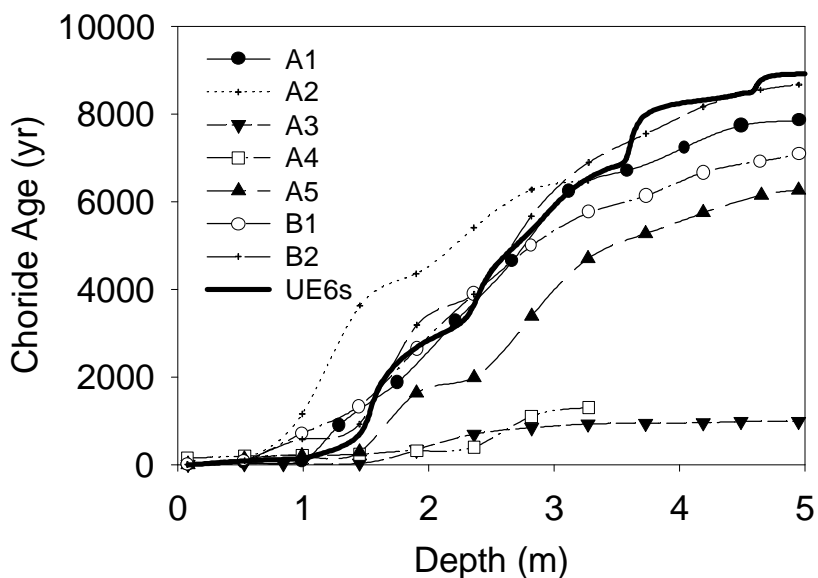


Figure 5-29. Graph of chloride mass balance age with depth from the Yucca Flat Shallow Series cores, with reference to results from the UE6s core CMB age profile.

5.6. Nitrogen Fluxes

Nitrogen fluxes for the UE6s core and the Yucca Flat Shallow Series cores are calculated based on the amount of NO_3^- -N amassed in the core within the sampled interval and the chloride mass balance age of the core at the total depth (Table 5-2). Vertical integration of the NO_3^- -N concentration profiles yields the accumulated nitrogen mass per area. Dividing the accumulated nitrogen mass per area by the calculated CMB age at the total depth (or depth considered) produces an estimate of the NO_3^- -N flux, averaged over the CMB accumulation age. Calculated NO_3^- -N fluxes range from 60 – 171 $\text{mg m}^{-2} \text{yr}^{-1}$. The average value of 105 $\text{mg m}^{-2} \text{yr}^{-1}$ determined for the Yucca Flat Shallow Series cores compares reasonably well to the NO_3^- -N flux determined for the UE6s core. A value of 95 mg NO_3^- -N $\text{m}^{-2} \text{yr}^{-1}$ calculated over the entire length of UE6s (45 m) reflects an average NO_3^- -N flux

spanning almost 13 kyr. The NO_3^- -N flux estimate for the UE6s core increases to 114 mg NO_3^- -N $\text{m}^{-2} \text{yr}^{-1}$ if just the upper 10 m and most recent 10 kyr are considered in the analysis. These results support the assumption that the solute signal in UE6s core below 10 m reflects an earlier period characterized by more mesic vegetation and climate, and thus lower losses of nitrogen past the root zone.

Hartsough et al. [2001] report an estimated modern NO_3^- -N deposition rate of 50-60 $\text{mg m}^{-2} \text{yr}^{-1}$ based on atmospheric NO_3^- -N data from the NADP, which is approximately half of the NO_3^- -N loss from the root zone calculated from the NO_3^- -N and chloride profiles (Table 5-2). This analysis implies that the desert plants at the Yucca Flat site do not use most of the NO_3^- -N in the root zone and consequently, NO_3^- -N periodically leaches through the root zone and accumulates in large quantities below. In other words, NO_3^- -N behaves as a conservative solute, such as chloride. The results actually indicate a net gain of nitrogen through the system. Obviously, an important source of nitrogen is being ignored in this assessment. Additional local sources of nitrogen may be related to the playa 1.8 km south of Yucca Flat and N-fixing cyanobacteria as suggested by *Hartsough et al.* [2001]. Playas provide a favorable environment for N-fixing bacteria and lichen. Eolian transport and deposition of added nitrogen from the playa may account for the apparent discrepancy in mass balance detected in the Yucca Flat Shallow Series cores. Probably though, a major factor not accounted for in the 50-60 $\text{mg m}^{-2} \text{yr}^{-1}$ N-atmospheric deposition estimate is the contribution of NH_4^+ -N. *Hartsough et al.* [2001] considered dry and wet deposition of NO_3^- -N only and assumed that very little NH_4^+ in soil water converts to NO_3^- -N since NH_4^+ is the form of nitrogen preferred for uptake by plants.

Although plants may indeed be using a significant portion of the atmospherically deposited $\text{NH}_4^+\text{-N}$, the contribution of $\text{NO}_3^-\text{-N}$ converted from NH_4^+ deserves consideration. NADP data from Red Rocks, NV, located about 100 km south of Yucca Flat, indicates that ammonium and nitrate each comprise about 50 % of the total inorganic nitrogen deposition. Annual total inorganic nitrogen wet deposition varies at the Red Rocks site from 40 to 160 $\text{mg m}^{-2} \text{yr}^{-1}$, with a mean of about 90 $\text{mg m}^{-2} \text{yr}^{-1}$ over the past 20 years on record [NADP/NTN, 2001; <http://nadp.sws.uiuc.edu/>]. These data indicate that the ammonium conversion to nitrate in shallow soils could account for the nitrogen mass balance discrepancy at the Yucca Flat site. However, the mass availability argument alone does not provide conclusive evidence of significant $\text{NH}_4^+\text{-N}$ to $\text{NO}_3^-\text{-N}$ conversion and the source of additional $\text{NO}_3^-\text{-N}$ remains speculative.

	UE6s	UE6s	A1	A2	A3	A4	A5	B1	B2
Total depth (m)	45.0	10.0	5.0	3.5	5.0	3.5	5.0	5.0	5.0
CMB age (yr)	12,800	10,600	7,900	6,500	1,000	1,300	6,300	7,100	8,700
Accumulated $\text{NO}_3^-\text{-N}$ (g m^{-2})	1,215	1,212	1,150	400	59	95	710	810	1,490
Calculated $\text{NO}_3^-\text{-N}$ flux ($\text{mg m}^{-2} \text{yr}^{-1}$)	95	114	146	62	60	73	114	114	171

Table 5-2. Calculated chloride mass balance ages and nitrogen fluxes for the Yucca Flat Shallow Series cores.

Limited data from a clean sand core used to monitor atmospheric deposition near the Yucca Flat cores suggests a relatively high local nitrate deposition rate. An array of 60 cm clean sand cores was installed in August, 1998; uncovered on September 25, 1998; and one column was extracted on August 18, 1999. Over the duration of 11 months, $230 \text{ mg m}^{-2} \text{ NO}_3^- \text{-N}$ accumulated in a 60 cm sand column (Figure 5-30). The data from the column indicates a nitrogen flux of $250 \text{ mg m}^{-2} \text{ yr}^{-1} \text{ NO}_3^- \text{-N}$, a value that is significantly higher than the previous estimate of $50\text{-}60 \text{ mg m}^{-2} \text{ yr}^{-1}$. A high nitrogen deposition value could help explain the high calculated $\text{NO}_3^- \text{-N}$ loss from the root zone. One caveat in relying on the measured deposition over the first year of monitoring involves the induced effects of vegetation disturbance during column installation. As such, the $250 \text{ mg m}^{-2} \text{ yr}^{-1} \text{ NO}_3^- \text{-N}$ may be biased toward the high end considering that the vegetation at the site was disturbed during column installation. If the actual nitrogen deposition is about $250 \text{ mg m}^{-2} \text{ yr}^{-1} \text{ NO}_3^- \text{-N}$, as suggested by the sand column data, then the $\text{NO}_3^- \text{-N}$ loss from the root zone is about 42 % of the total deposition, as opposed to 175 – 210 % as given in *Hartsough et al.* [2001].

Considering that nitrogen accumulation in desert soils and losses from the root zone are generally considered to be low [*Post et al.*, 1985; *Schlesinger et al.*, 1990], the tabulated results in Table 5-2 are quite significant and surprising. A large percentage of nitrogen appears to go unused by the desert plants, resulting in extremely high concentrations several meters below the surface and nitrogen behaving as a conservative solute below the root zone. These results may have important implications for regional or even global nitrogen balance and cycling

studies. Even ecological studies that do recognize that nitrogen leaching past the root zone may be significant in some regions [*Post et al.*, 1985], do not consider the relative immobility of continually accumulated nitrogen pools in desert vadose zones. *Post et al.* [1985] suggest a highly conservative turnover rate for the global nitrogen pool of 3,000 yr. If the vadose zone at the Yucca Flat site is representative of other desert vadose zones around the globe, a vast pool of nitrogen that is essentially locked up and has been for 10 – 15 kyr has gone unaccounted for (or at least considerably underestimated) in nitrogen balances.

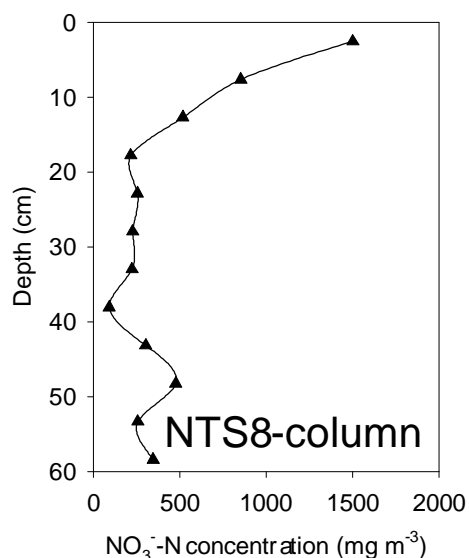


Figure 5-30. Nitrate profile from the buried clean sand column, NTS8, at Yucca Flat after 11 months of exposure to the atmosphere. Concentrations are given in mg NO₃⁻-N m⁻³ total soil volume.

5.7. Discussion of Spatial Variability at Yucca Flat

The spatial variability observed in the chloride and nitrate profiles taken from the Yucca Flat Shallow Series cores is quite high, particularly considering the absence of large-scale geomorphic features observed between core sites, similarity in soil texture, and relatively flat topography of the site. The vegetation pattern at

present displays uniformly distributed distinct shrub and grass clumps and contains about 70 ± 10 % bare ground. The vegetation and active root distribution at present and throughout the development of the chloride profiles may play a *minor* role in the variability observed in the solute profiles. However, the majority of the patch-scale variability in the Yucca Flat shallow series cores may be best attributed to fine-scale geomorphic processes since the two profiles (A3 and A4) with much lower amounts of accumulated chloride (integrated over a depth interval of 0-5 meters) than all the other profiles coincide with identified locations of small, shallow drainage channels (~5 cm vertical relief). Despite the major variation in solute profiles, shallow-series cores have very similar water contents and comparable water potential profiles. The Yucca Flat site resides at the distal end of a major basin, and overland flow occasionally must occupy these very small drainage channels. The low solute concentrations beneath the slight topographic depressions would at first imply increased deep infiltration beneath these features. However, the rather uniform distribution of vegetation and (presumably) roots as well as the similar hydraulic profiles beneath these sites would suggest that water infiltrates through the base of drainage channels from the occasional overland flow events and then moves laterally to be taken up by the adjacent vegetation. If such a phenomenon is the rule more than the exception, there are major implications for CMB applications and vadose zones chloride profile interpretation, in general. Not only would it be inappropriate to extrapolate or spatially upscale results from one vertical chloride profile, but even that point interpretation would be incorrect. Lateral movement of soil-water chloride would necessitate much more time-intensive field investigations that would involve

drilling a series of cores and averaging the amount of accumulated chloride retained in each core, rather than relying on one profile. Even then, the averaged CMB age estimate would not be very robust.

5.8. DASH Model Method

Site-specific modeling for each of the Nevada Test Site cores employs the Deep Arid System Hydrodynamic (DASH) conceptual model described in Chapter 3 as a basis for NTS vadose-zone profile reinterpretation. The complexities of the DASH model and the non-linearity associated with flow in unsaturated material, in general, require use of a numerical model to simulate non-isothermal multiphase flow and transport. The computer code I use for all numerical simulations is FEHM (Finite Element Heat and Mass) [Zyvoloski *et al.*, 1997]. I use average measured soil parameters and vary the surface boundary condition time sequence to best match the measured matric potential and chloride concentration profiles. Model input values associated with each core are listed in Table 5-3. The matric potential at the bottom boundary (water table) is fixed at 0 m for all simulations. Temperature gradients are established by specifying constant temperatures at the top and bottom boundaries. Table 5-4 lists the initial and time-varying boundary conditions for the PW-series and UE6 simulations, respectively. The initial solute profile consists of a uniform chloride porewater concentration unique to each core based on measured values. A prescribed solute flux of $105 \text{ mg m}^{-2} \text{ yr}^{-1}$ at the surface boundary simulates continuous atmospheric chloride deposition. Initially, the modeled systems are set to maintain a steady-state, uniform downward liquid flux (Table 5-4), representative of a

past wetter climate. Transitions to a drier climate and the establishment of xeric vegetation are simulated by specifying a negative matric potential (ψ) at the base of the root zone (3-4 m depth) to represent the effect of highly water-efficient desert vegetation. This observation-based xeric condition is an integral component of the DASH model. A specified downward flux at the surface for a given duration simulates a pluvial interval. In order to match the measured matric-potential and chloride profiles from Frenchman Flat and Yucca Flat, the timing and magnitude of pluvials and xeric transitions are varied within ranges considered reasonably consistent with independent paleoclimate records. For purposes of brevity, results from the numerous trial-and-error simulations are not shown here; only the best-fit simulation for each core is presented. The surface boundary conditions given in Table 5-4 and effective chloride diffusion coefficients provided in Table 5-3 produce solutions that best match the observed data. Effective chloride diffusion coefficients for the NTS cores range from 6×10^{-12} to $3 \times 10^{-10} \text{ m}^2 \text{ s}^{-1}$. These values fall within the distribution of experimentally determined chloride diffusion coefficients [*Conca and Wright, 1992; Schaefer et al., 1995*] for the range of moisture contents measured in the NTS cores.

	PW-1	PW-2	PW-3	UE6s'
Parameter				
Soil type: sandy loam to silt loam				
Porosity	0.38	0.39	0.37	0.45
[unitless]				
Saturated permeability	$2.2 - 5 \times 10^{-11}$	7.3×10^{-13}	$1.4 - 5 \times 10^{-13}$	1.6×10^{-12}
[m ²]				
van Genuchten alpha ¹	2.0-3.7	2.0	1.5 - 2.8	2.0
(α) [m ⁻¹]				
van Genuchten n ¹ (n)	1.49	1.39	1.38	1.40
[unitless]				
Residual, maximum	16 %, 88%	13%, 84%	12%, 82%	14 %, 82%
Saturations				
Geothermal gradient	13	12	14	40
[°C km ⁻¹]				
Water table depth	235	256	282	464
[m]				
Effective diffusion coefficient [m ² s ⁻¹]*	5×10^{-11}	1×10^{-10}	3×10^{-10}	6×10^{-12}

*determined through iterative solute transport modeling to match Cl profiles

¹ unsaturated soil fitting parameters described in *van Genuchten* [1980]

Table 5-3. Input parameters for Frenchman Flat (PW-series cores) and Yucca Flat (UE6s/UE6e) site-specific simulations. Values that show a range indicate incorporation of some heterogeneity. Average values for PW cores taken from *Estrella et al.* [1993].

	120 – ~100* ka	~100* - 14 ka	14 – 13 ka	13 – 0 ka	
Climate/	Mesic/	Arid/	Pluvial period	Arid/	
Vegetation	Woodland	Desert steppe		Desert scrub	
Surface Boundary Condition	PW-1	$Q = 7.6 \text{ mm yr}^{-1}$	$\psi_{tz} = -800 \text{ m}$	$q = 2 \text{ mm yr}^{-1}$	$\psi_{tz} = -800 \text{ m}$
	PW-2		$q = 4.4 \text{ mm yr}^{-1}$	$q = 4.4 \text{ mm yr}^{-1}$	$\psi_{tz} = -600 \text{ m}$
	PW-3	$Q = 5.9 \text{ mm yr}^{-1}$	$\psi_{tz} = -800 \text{ m}$	$q = 5 \text{ mm yr}^{-1}$	$\psi_{tz} = -900 \text{ m}$
			9.5+ ka		9.5 - 0 ka
			Mesic/		Arid/
		UE6	Woodland		Desert scrub
		$q = 2.3 \text{ mm yr}^{-1}$		$\psi_{tz} = -400 \text{ m}$	

ψ_{tz} – fixed matric potential at the base of the root zone (4 m depth for Frenchman Flat cores; 3 m depth for Yucca Flat core)

q – downward soil-water flux

* 110 ka for PW-1, 95 ka for PW-3

Table 5-4. Simulation histories and associated surface boundary conditions from the Frenchman Flat and Yucca Flat cores.

5.9. DASH Model Results

5.9.1. Matric Potentials

The model-generated matric potential profiles are shown for surface boundary transition times and the present day (Figure 5-31). Also shown in Figure 5-31 for comparison are measured data and the predicted profiles at steady state under the present surface boundary conditions for each location. Modeled present-day profiles compare well with observed data. In the case of PW-2 and UE6, only the profiles at

13 ka/ 9.5 ka, at present and the projected steady state are shown. The time required for an e-fold matric potential change (63 % change from the initial profile to the steady-state profile) from the onset of xeric conditions in the Frenchman Flat cores is calculated to be ~ 300 kyr (± 50 kyr) in contrast to ~ 100 kyr for the Yucca Flat core.

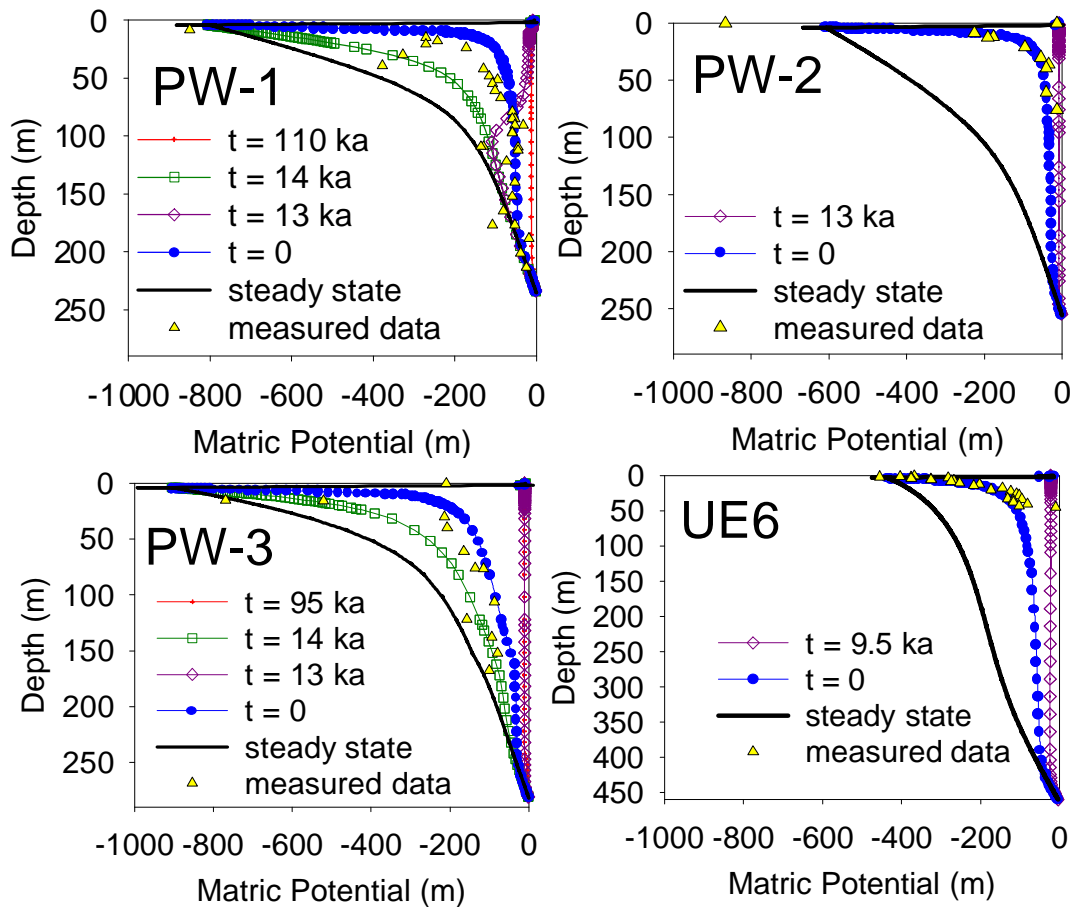


Figure 5-31. Model-simulated matric potential profiles developed over time in response to climate/vegetation transitions. The oldest age profile for each core is the beginning of the simulation for that core. The $t = 0$ profile represents the present and compares well with measured data from Frenchman Flat (PW-1, PW-2, and PW-3) and Yucca Flat (UE6) cores.

5.9.2. Chloride

The model-generated chloride profiles are shown for times corresponding to those given for the matric potential profiles in Figure 5-32. The single-bulge chloride profiles of PW-2 and UE6 are simulated by prescribing downward fluxes of 4.4 mm yr⁻¹ and 2.3 mm yr⁻¹ (based on deep-core chloride data) before 13 ka and 9.5 ka, respectively, and xeric conditions thereafter. Downward advection dominates the movement of chloride during the past period of downward flux. The shift to xeric conditions induces *upward* advection toward the base of the root zone (described in greater detail to follow), and chloride deposited at the surface begins to accumulate in the root zone. The upward advective flux below the root zone is extremely small owing to very low water content and thus, low unsaturated permeability. Consequently, the upward advective component contributes a negligible amount of chloride to the accumulating shallow bulge. Under the imposed xeric conditions, solute diffusion is the main mechanism of chloride transport. Chloride diffuses downward below the root zone, counter to the small upward advective flux.

The simulated chloride profiles for PW-1 and PW-3 display two chloride bulges resulting from two periods of aridity separated by a pluvial period. During the arid periods, chloride accumulates at the base of the root zone and diffuses downward. Initiation of the prescribed pluvial period induces downward advection and dispersion of the initial chloride bulge. Onset of the most recent transition to xeric conditions results in the formation of another chloride bulge above the initial bulge. Numerous attempts to match the measured chloride and matric potential profiles for PW-1 and PW-3 indicate that the pluvial period must have been quite

brief (less than 1 kyr), which is consistent with independent records [Benson, 1991]. Simulations specifying longer pluvial periods produce a single, merged chloride bulge due to solute dispersion. In addition to duration, the magnitude of the downward flux prescribed at the surface during the pluvial period is adjusted in attempts to best match the observed chloride data. The deeper location of the secondary bulge in PW-3 compared to PW-1 signifies either a higher infiltration rate or a longer duration of the pluvial period at PW-3 than at PW-1. Due to the close proximity of the boreholes, the former scenario is the more likely of the two and is accordingly employed in the modeling. Prescribed pluvial-period infiltration rates of 2 mm yr^{-1} and 5 mm yr^{-1} for PW-1 and PW-3, respectively, best match measured data.

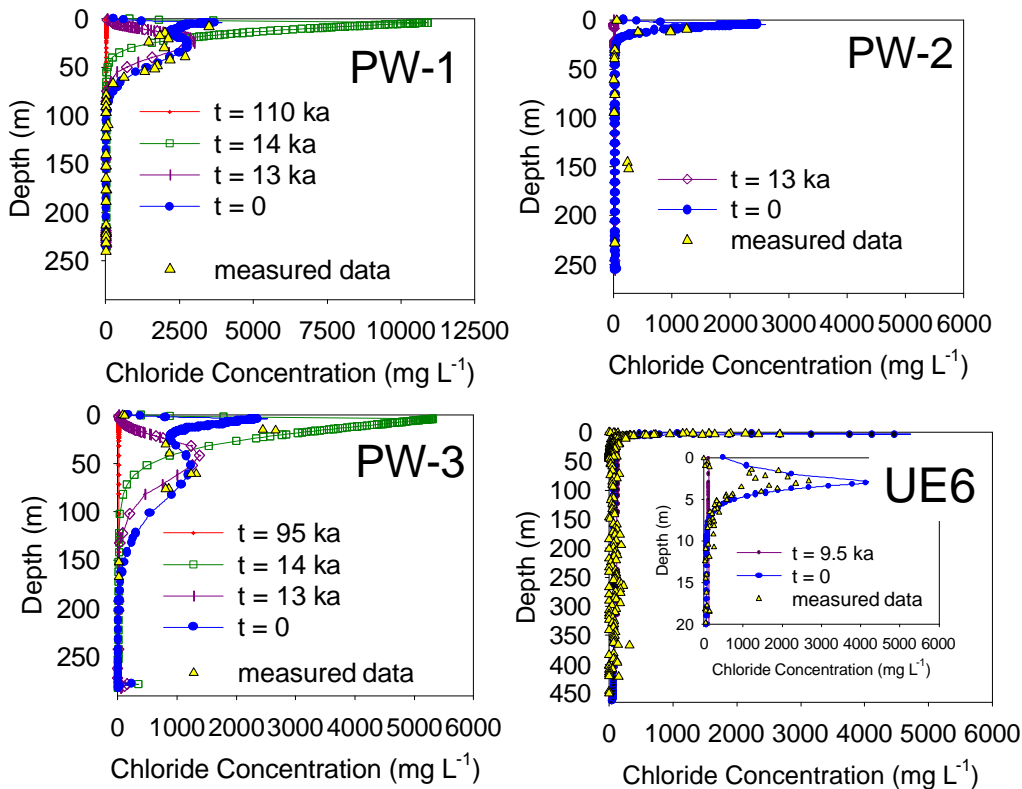


Figure 5-32. Model-simulated chloride profiles developed over time in response to climate/vegetation transitions. The $t = 0$ profile represents the present and compares well with measured data from Frenchman Flat (PW-1, PW-2, and PW-3) and Yucca Flat (UE6) cores. Chloride values are porewater concentrations.

5.9.3. Paleoflux Histories

The timelines in Figure 5-33 illustrate the prescribed surface boundary condition sequences associated with each core model that best reproduce the observed data. Moisture flux profiles at multiple snapshots in time show similar histories preserved in PW-1 and PW-3 in response to surface boundary transitions (Figure 5-34). At some time in the past (~110 ka), a wetter, colder climate in the region resulted in significant downward soil-water fluxes of 5 – 8 mm yr⁻¹. The arid period that followed spurred a drying trend in the vadose zone in Frenchman Flat causing moisture fluxes to become very small and directed upward below the root zone. The drying trend persisted until 14 ka at which point a major wet episode lasting 1 kyr induced below-root-zone infiltration of 2-5 mm yr⁻¹. From 14 to 13 ka, the infiltration pulse propagated steadily downward reaching depths of 90 –150 m in PW-1 and PW-3. At 13 ka, the shift back to xeric conditions initiated a second vadose-zone drying trend that has persisted through the present day. Flux profiles at snapshots in time subsequent to 13 ka illustrate the dissipation of the infiltration pulse and indicate only a slight rise in downward fluxes across the water table throughout the simulated period (Figure 5-34). In summary, the PW-1 and PW-3 profiles did not experience complete flushing to the water table induced by the pluvial interval, which effectively preserved the secondary chloride bulges.

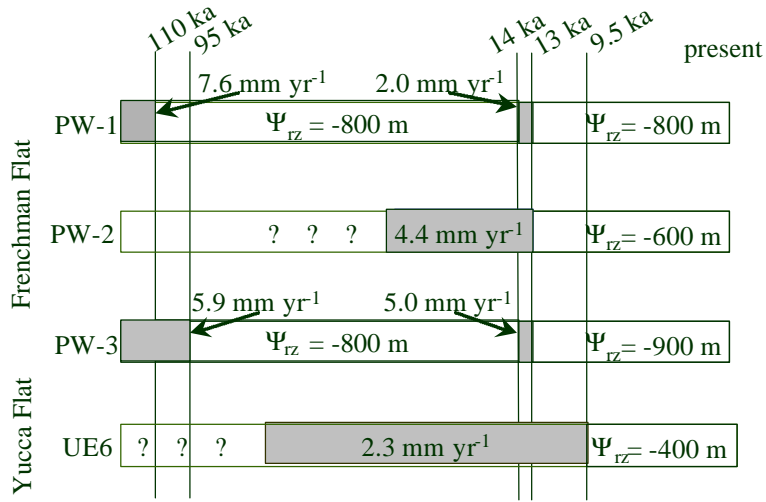


Figure 5-33. Surface boundary condition sequences used in model simulations to best match observed vadose-zone profile data from Frenchman Flat and Yucca Flat. Shaded intervals represent wet periods and non-shaded intervals represent arid periods during which vegetation sustained very low matric potentials.

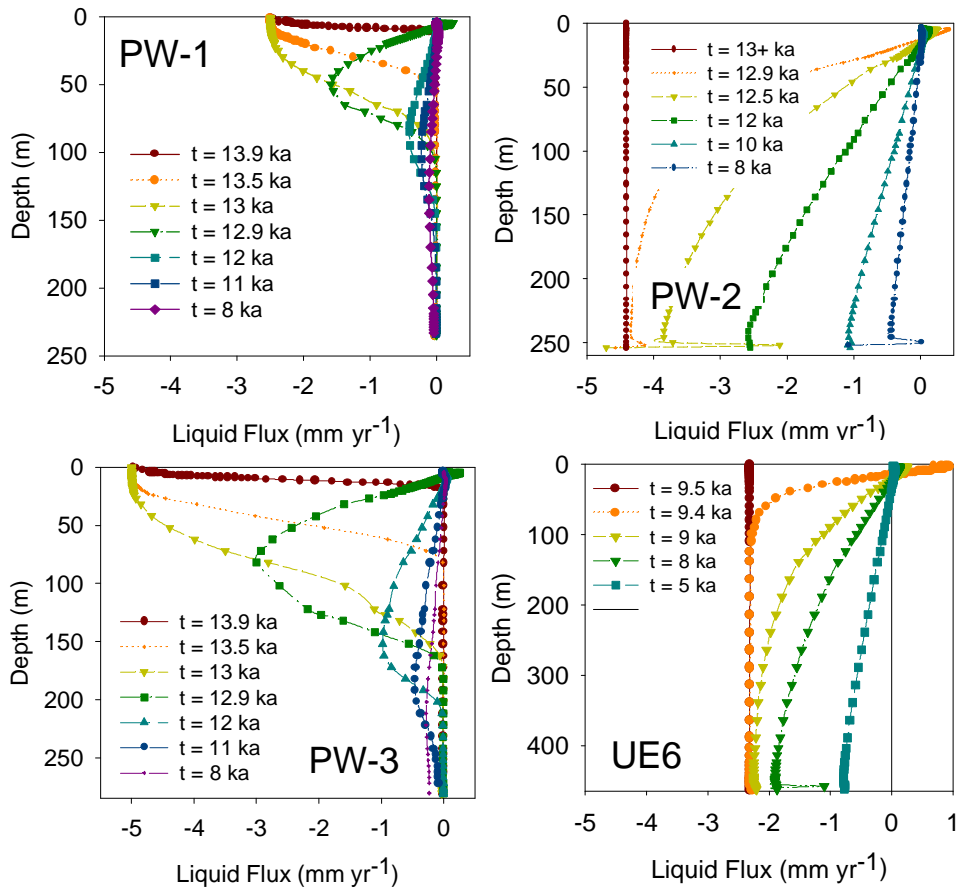


Figure 5-34. Model-predicted liquid flux profiles at several snapshots in time. Negative values indicate downward fluxes; positive values indicate upward fluxes.

Moisture flux profiles at several snapshots in time from PW-2 and UE6 exhibit similar character (Figure 5-34). Unlike PW-1 and PW-3, these two profiles archive only the most recent major surface boundary transition (Figure 5-33). No information prior to 30 ka can be inferred from these profiles. From 30 ka to the onset of the Holocene, downward soil-water fluxes of 2-5 mm yr⁻¹ presumably prevailed. PW-2 records a shift to xeric conditions at 13 ka at which point fluxes reversed to upward below the root zone. The timing and nature of this shift corresponds with paleoflux reconstructions from PW-1 and PW-3 that include a transition to xeric conditions at 13 ka. UE6, located in Yucca Flat, also records a transition to xeric conditions. However, the timing of the shift at UE6 is several thousand years later, at 9.5 ka. The moisture flux profiles for PW-2 and UE6 illustrate the vadose zone drying trends at these two sites. Downward fluxes deep in the profiles decrease and the drying front propagates downward through time.

5.9.4. Current Moisture Flux Regimes

The current moisture-flux profiles for the four vadose zone cores all display divergent liquid and net moisture flux patterns (Figure 5-35). Small upward liquid fluxes below the base of root zone, driven by capillary forces (i.e. large matric potential gradients), prevail to depths of 50 and 60 m for PW-1 and PW-3, respectively. Below these depths, gravitationally driven downward liquid fluxes predominate. Net moisture fluxes across the water table interface (recharge) range from -0.4 mm yr⁻¹ to -0.05 mm yr⁻¹. The plane of divergent liquid flux is located at a depth of 35 m in both PW-2 and UE6. The shallower location of the divergent flux

plane at PW-2 and UE6, compared to PW-1 and PW-3, results from shorter total drying times and moister antecedent conditions for PW-2 and UE6 at the time of the most recent transition to xeric conditions.

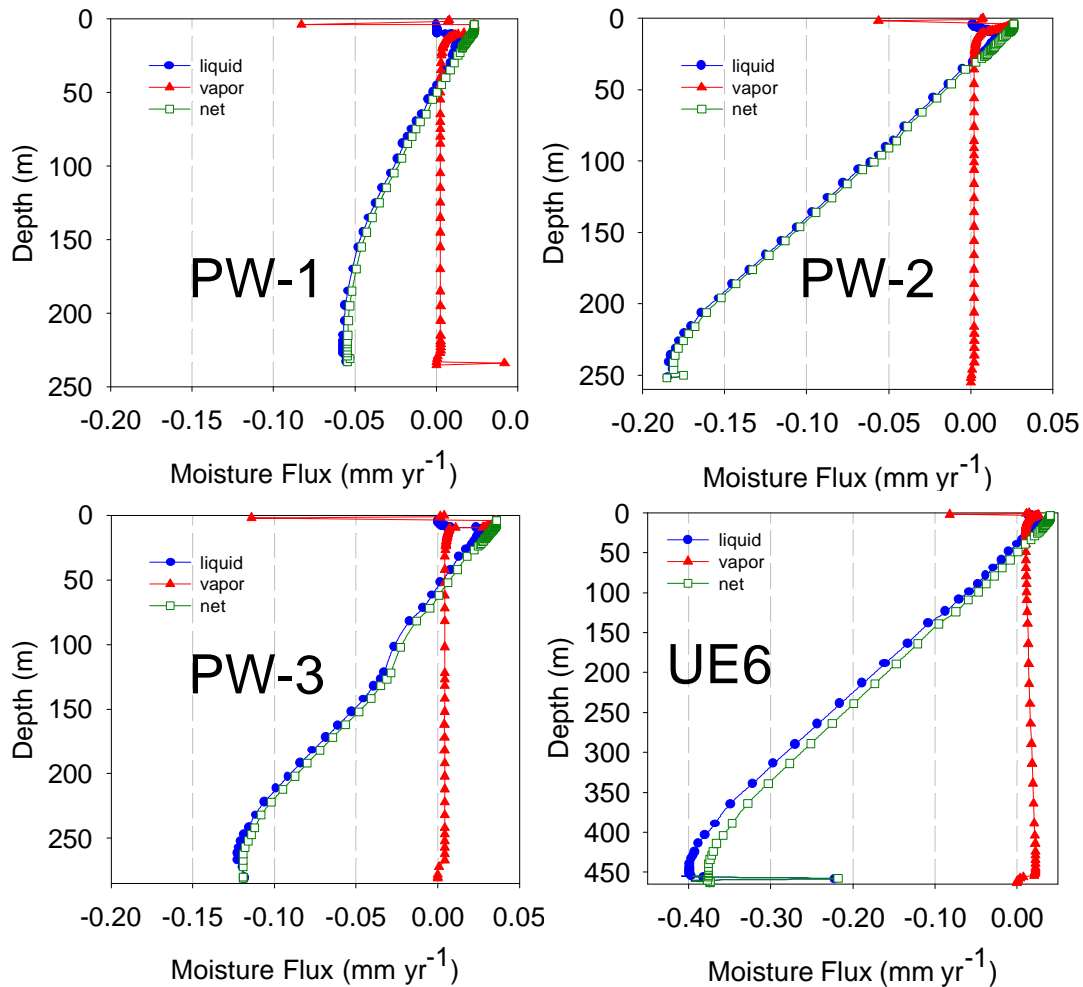


Figure 5-35. Model-predicted moisture flux profiles at $t = 0$ (the present). Negative values indicate downward fluxes; positive values indicate upward fluxes. Net moisture fluxes across the water table interface (recharge) range from -0.4 mm yr^{-1} to -0.05 mm yr^{-1} .

The direction of the vapor flux is upward throughout the profiles (Figure 5-35). The geothermal gradient drives an upward vapor flux in the deep portion of the profiles, which is about three times greater in UE6 than in the PW-series cores.

Vapor flux above the plane of divergent flux for each core is mainly driven by capillary forces (i.e., isothermal vapor flux). Due to the very dry conditions in the region above the plane of divergent flux and below the root zone, upward fluxes driven by the matric potential gradient are largely in the vapor phase; the liquid phase component is relatively small.

5.9.5. Discussion of DASH Model Application

Notable contrast between the boundary condition sequences used in the DASH model approach to simulate the Frenchman Flat and Yucca Flat vadose-zone profiles includes the timing and duration of the most recent wet episodes. The requisite timing of the most recent transition to xeric conditions at Frenchman Flat precedes the equivalent hydrologic transition at Yucca Flat by 3.5 kyr. Presumably, any major climate transition would affect the adjacent areas within the Nevada Test Site at approximately the same time. Therefore, the hydrologic transition from downward soil-water flux to net upward moisture (liquid and vapor) flux beneath the root zone must not have simply resulted from a regional climate change, but from a corollary vegetation transition. Paleoecological reconstructions from the northern Mojave Desert support this hypothesis. Desert scrub replaced woodland ~13 ka at the elevation of Frenchman Flat and ~9.5 ka at the elevation of Yucca Flat (Figure 5-5) [Spaulding, 1990]. The correlation between documented vegetation transitions and the modeled hydrologic transitions further supports the assumption that vegetation exerts a crucial control on deep vadose-zone hydrodynamics [Phillips, 1994].

Another notable contrast in the DASH model simulations consists of invoking several major hydrologic transitions for PW-1 and PW-3 compared to only one

required to simulate the profiles from PW-2 and UE6. The vadose-zone profiles of PW-1 and PW-3 preserve a record of an earlier arid period prior to the onset of desert scrub. Such a record provides a unique window into the local paleohydrologic fluctuations at Frenchman Flat across the Pleistocene – Holocene boundary, including a major pluvial event. Pluvials often erase evidence of the previous climate in vadose-zone profiles due to the short response time associated with vadose-zone wetting. However, in this case, the relatively short duration of the pluvial at 14 – 13 ka, coupled with the considerable vadose-zone thickness at Frenchman Flat, allow preservation of a long paleoflux history. The timing of the short infiltration pulse required to simulate the observed chloride profiles matches very well with the timing of the brief pluvial maximum event (14.5 – 13 ka) documented by paleolacustrine studies [Morrison, 1991; Benson et al., 1990]. Furthermore, Benson [1991] estimates that the Lake Lahonton highstand at ~14 ka may have been as short-lived as 200 yrs, based on accumulation time of calcium carbonate coatings on shoreline deposits. Evidence of a short-lived high stand concurs with the modeling results.

The model-calculated response times are 3 times longer for Frenchman Flat profiles than for Yucca Flat profiles, despite a 200 m thicker vadose zone at Yucca Flat. Differences in soil texture cannot explain the difference; coarser soils at Frenchman Flat should equilibrate more rapidly after a transition to xeric surface conditions. However, the significant contrast in geothermal gradient (12-14 °C km⁻¹ compared to 40 °C km⁻¹) between the two locations overrides the influence of soil texture. The greater thermal vapor flux at Yucca Flat quickens the drying response. The 65 % difference in the geothermal gradient between the two sites is

commensurate with the difference in calculated equilibrium response times between Frenchman Flat and Yucca Flat cores.

5.10. Implications for CMB Application to Desert Vadose-Zone Profiles

Paleoflux reconstructions generated using a conventional CMB approach and those calculated using the DASH model approach exhibit both similarities and differences. The CMB approach assumes that below-root-zone soil-water fluxes are always downward and attributes chloride bulge formation to fluctuations in infiltration over long timescales. In contrast, results from the approach based on the DASH model indicate that below-root-zone moisture fluxes are generally upward and include a significant vapor phase component. Such discordance in the conceptual models associated with each approach result in a large difference in the estimated timing of the pluvial period recorded in two profiles from Frenchman Flat: 50 ka using the CMB approach versus 14 ka using the DASH model approach. The latter interpretation agrees more closely with independent paleoclimate studies from the southern Great Basin. Application of the CMB method does not allow estimation of the duration or magnitude of the infiltration separating the two chloride bulges in PW-1 and PW-3. The DASH model approach constrains the timing, duration and intensity of the pluvial period, thereby demonstrating important advantages over the CMB approach concerning the application to paleoflux reconstruction. Also, use of the CMB equations to estimate current soil-water fluxes yields values that differ not only in magnitude, but also in direction from DASH model estimates (Table 5-5). CMB-calculated fluxes are downward and significantly greater in magnitude than

model-calculated divergent soil-water fluxes that are upward to depths of 35-60 m and downward in the deeper portions of the profiles (Figure 5-35).

Two main applications of the CMB approach yield concordant results with the DASH model approach. First, the amount of accumulated chloride with depth yields valuable information on the timing of hydrologic transitions when vadose-zone profiles record only a single major transition. Breaks in slope in chloride age versus depth profiles for PW-2 and UE6 (Figure 5-28) correspond well to hydrologic transitions in the DASH modeling approach. Second, consistent results between the CMB approach and the DASH model approach include retrodicted paleofluxes under the past wetter climate during which essentially steady downward soil-water fluxes prevailed throughout the entire vadose-zone thickness.

		CMB- calculated flux (mm yr ⁻¹)	DASH liquid flux (mm yr ⁻¹)	DASH vapor flux (mm yr ⁻¹)	DASH net moisture flux (mm yr ⁻¹)
PW-1	Root zone base	?	2 x 10 ⁻⁵	0.01	0.01
	W.t. interface	-7.6	-0.02	10 ⁻³	-0.02
PW-2	Root zone base	-0.7	1 x 10 ⁻³	0.03	0.03
	W.t. interface	-4.4	-0.18	2 x 10 ⁻³	-0.18
PW-3	Root zone base	?	3 x 10 ⁻⁴	0.02	0.02
	W.t. interface	-5.2	-0.12	4 x 10 ⁻³	-0.12
UE6	Root zone base	-0.6	0.02	0.02	0.04
	W.t. interface	-2.3	-0.40	0.02	-0.38

Table 5-5. Comparison of current net moisture fluxes estimated using a CMB approach and the DASH modeling approach taken in this study. Negative values indicate downward fluxes; positive values indicate upward fluxes. W.t.= water table.

5.11. Summary

Successful site-specific modeling of deep vadose zone profiles provides further support for the Deep Arid System Hydrodynamic (DASH) model. Vadose zones in the northern Mojave Desert located within the Nevada Test Site render detailed current hydrologic information and serve as archives of paleohydrologic information. Multiple lines of data, including matric potential and chloride porewater concentration are required to *approach* a unique solution regarding current flux regime and paleoflux history. This case study clearly demonstrates that data interpretation (i.e. implementation of a complete and correct conceptual model) is crucial in accessing such information. Upward liquid fluxes below the root zone limit the application of the CMB approach. The commonly applied downward-only soil-water movement assumption is not appropriate for describing moisture movement in these thick desert vadose zones, and consequently produces overestimates of current recharge. Along similar lines, the CMB approach to interpreting chloride profiles generates indeterminate and sometimes inaccurate paleohydrologic reconstructions, particularly when multiple climatic transitions are preserved. Due to the complexities and long-term transients in the moisture flux regimes associated with deep vadose-zones, a coupled field-measured and numerical model matching approach as demonstrated in this research yields a more detailed and accurate picture of the current flux and paleoflux regimes. The DASH model simulations resolve the major inconsistency associated with the conventional paleohydrologic reconstructions of the NTS cores. Under the DASH model, one general paleohydrologic reconstruction, in accordance with independent paleoclimatic and paleoecological records, explains

most of the observed data. The temporal coincidence between hydrologic transitions as indicated by measured vadose-zone profiles and vegetation transitions as indicated by independent paleoecological data, further implicates vegetation type as a major control on deep vadose zone hydrodynamics.

Data from a single core that has been subject to lateral redistribution of solutes will produce an incorrect hydrologic interpretation if vertical flow is assumed. The observed spatial variability in solute profiles from the Yucca Flat shallow series suggests that data from multiple cores in close proximity reduce the potential for biased recharge estimates and erroneous inferred moisture flux histories.

CHAPTER 6.

CASE STUDY 2: TRANS-PECOS REGION

6.1. Introduction

The Deep Arid System Hydrodynamic (DASH) conceptual model, developed and supported in the work presented in the previous three chapters, identifies desert vegetation as a key factor in controlling the upper vadose-zone flow boundary condition. Desert vegetation, capable of sustaining very negative matric potentials near the base of the root zone over long timescales, essentially buffers the deep vadose zone from temporal variations in moisture content near the surface, according to the DASH model. Case Study 2 attempts to build on the vegetative control component of the DASH model by addressing the link between vegetation type and deep vadose zone fluxes. This work describes a first step at developing a proxy relationship between vegetation type and interdrainage recharge in semiarid and arid basins.

The type and pattern of vegetation established in a region depend on the amount of precipitation, precipitation seasonality, soil moisture availability, soil texture, and many other factors [*Rodriguez-Iturbe*, 2000]. Vegetation serves as a filter between the elements comprising the near-surface water balance and the deeper vadose zone moisture regime. Available moisture (moisture which is free to enter the

roots) and temperature comprise the primary factors influencing vegetation patterns under semiarid climates [*Dick-Peddie*, 1993]. Vegetation in New Mexico changes on an available moisture gradient from desert scrub to grassland to woodland to forest as available moisture decreases [*Dick-Peddie*, 1993]. Although this viewpoint represents a major simplification of dynamic interactions between plants, climate and soil water, it possesses both merit and utility for examining large-scale trends. Similarly, we would like to develop an analogous, and perhaps more quantitative, relationship between vegetation type and deep vadose zone moisture fluxes in regions where water is a limiting ecological factor. If vegetation type, a readily observable surface property, serves as a reasonable indicator of deep moisture fluxes, then the spatial distribution of recharge through desert floors might be characterized using vegetation maps. Such a method would be time-efficient and relatively inexpensive. Application to the basin scale would require point measurements for ground-truthing, but field investigations could be minimized using vegetation distribution patterns to identify strategic sample core locations.

The site-specific research initiative conducted in the Trans-Pecos region of West Texas addresses the first basic question necessary for testing the applicability of vegetation type as a suitable proxy for interdrainage recharge. What types of matric potential and solute profiles are found beneath different vegetation types? We would expect to find significant differences between profiles taken under desert shrubs uptake water (transpire) most of the year and perennial grasses are active for three to four months of the year [*Powell*, 1994; *Powell*, 1998]. We would also expect vadose zones under wooded regions to contain distinct hydraulic and solute profiles from the

drought-resistant desert shrubs due to differences in their water uptake behavior, rooting distribution, and ability (or lack thereof) to survive in soils with very low water potentials [Sperry *et al.*, 1998; Jobaggy and Jackson, 2001]. The Trans Pecos region is appropriate for this study endeavor because several locations in different vegetation communities in the region satisfy the conditions necessary for the DASH conceptual model. However, it should be noted that wooded regions that overlie thick, unconsolidated vadose zones are sparse in the Trans-Pecos region. Generally, the woodland-type vegetation in the Trans-Pecos coincides with areas characterized by shallow bedrock or in riparian corridors [Turner, 1997], neither of which are appropriate locales for this study. Application of the DASH model requires a relatively flat (away from channels), vegetated site with an unconsolidated, deep (>30 m) vadose zone in a semiarid to arid climate. The primary aim of Case Study 2 is to collect, measure, and compare the hydraulic parameters and solute tracers in soil cores beneath various types of vegetation. Then, following the DASH model approach developed in the earlier part of this study, the goal is to elucidate the moisture flux regime and paleoflux history associated with each vegetation type and vegetation history.

One of the main limitations of this method anticipated prior to sample collection was that historic changes in vegetative communities fall far short of the time required for the current dominant species to affect the moisture flux regime at significant depths. In other words, the surface condition transient imposed by a historic vegetation change may not have propagated deeply. If true, information stored in deep vadose zones reflects the moisture flux regime associated with the

previous vegetation community, rather than by the current vegetation. Regard for this limitation prompted a comparison study between sites located in a long-established desert scrub and in a developing desert scrub. The Chihuahuan Desert in the Trans-Pecos continues to extend to the north [*Dick-Peddie*, 1993; *Powell*, 1998]. Documented evidence of historic desert scrub encroachment into a plains grassland in the study area [e.g. *Nelson and Beres*, 1987] enables investigation of vadose zone moisture flux regimes developing in response to a vegetation transition. A comparative analysis of vadose zone cores taken along a historical scrub-grassland ecotone attempts to address the following question: What effect does the recent vegetation transition from grassland to desert scrub have on deep vadose zone moisture fluxes?

Since moisture equilibration times in desert vadose zones are quite long, according to the modeling results presented in Chapters 3, 4 and 5, it is critical to identify the long-term vegetation history of each study site. Interpretation of measured vadose-zone hydrological data without the paleovegetational context severely limits the merit of the inferences constructed. Presumably, any variations revealed in the vegetation history correspond to transients in the near-surface boundary conditions. Vegetation history can be derived from paleoecological records including fossilized pollen and plant remains and from isotopic signatures imprinted in pedogenic carbonate. One advantage of incorporating vegetation history inferred from paleoecological records rather than using surface boundary transients inferred from paleoclimatic reconstructions is that it is unnecessary to make the assumption that vegetation species immediately equilibrated with environmental changes.

Possibilities of migrational lag and community inertia (resistance to change) are inherently incorporated into paleoecological records, but are not factored into inferred responses to paleoclimate variations.

6.2. Description of Study Location

Case Study Site 2 lies within the Trans-Pecos region of western Texas (Figure 6-1), which encompasses the Chihuahuan Desert transition zone and accommodates a diverse population of plant communities [Powell, 1994]. Four sites were targeted to address the link between vegetation type and vadose-zone moisture-flux regime. The sites included a long-established desert scrub, a developing desert scrub (grassland prior to ~100 years ago), a grassland, and a juniper stand. Comparison between the long-established (thousands of years) and recently-established (<100 yrs) Chihuahuan desert scrub sites was intended to address the effects of scrub establishment on vadose-zone moisture fluxes below the root-zone.

The long-established desert scrub site (designated as the McKeel site on Figure 6-1), located about 3 km north of Presidio, Texas, lies on private property owned by John McKeel. Two cores from this site, designated as SA (562284m easting, 3276037m northing) and SB (562285m easting, 3276009m northing), were drilled on October 13, 2000. The SB borehole lies 28 m directly south of the SA borehole. The intent was to test the reproducibility of the data collected at two adjacent locations that were seemingly identical from a surface morphology perspective. The elevation at the McKeel site is about 875 m.

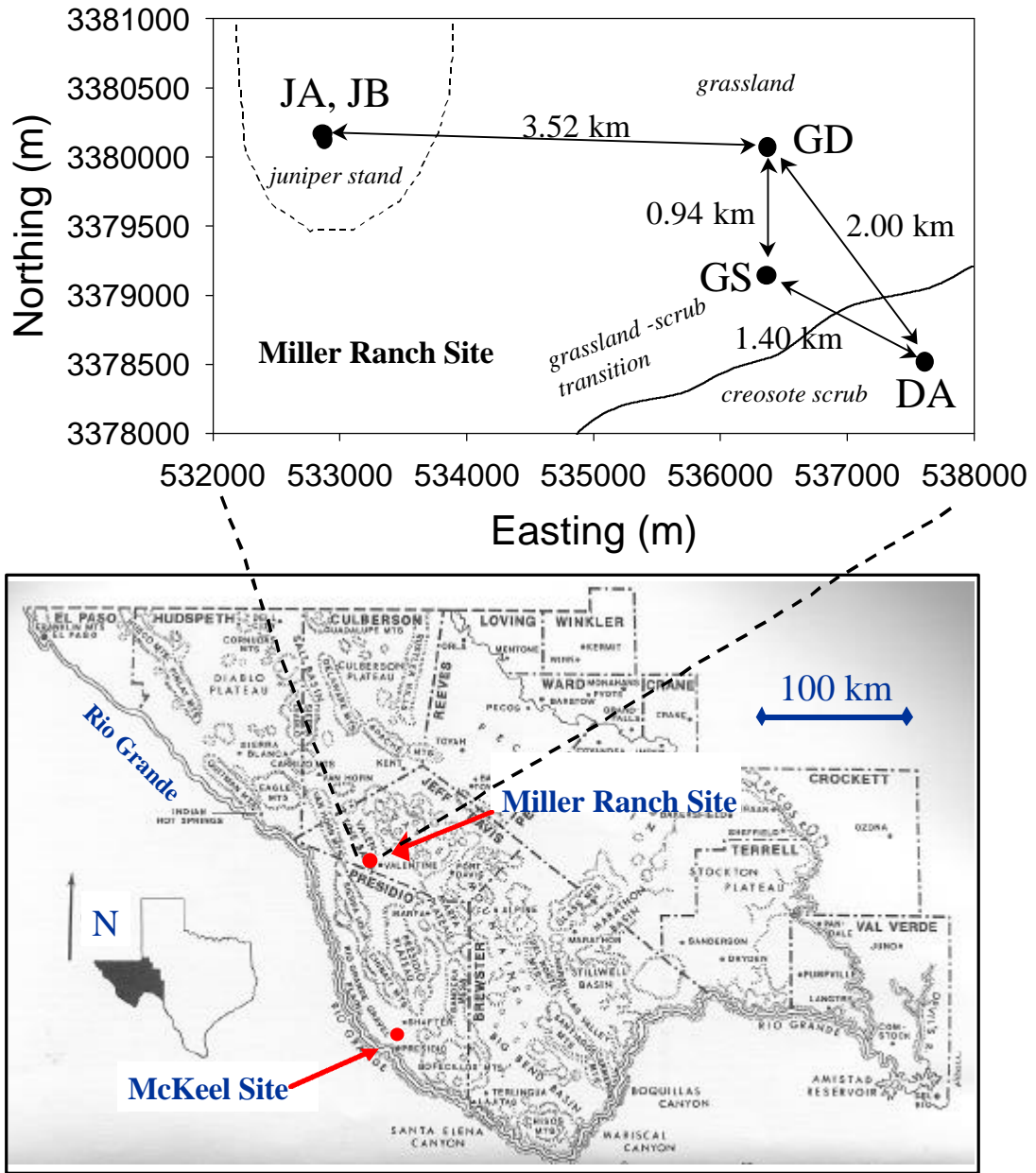


Figure 6-1. Location of Case 2 study sites, the Miller Ranch site and the McKel site, in the Trans-Pecos region, West Texas (Trans-Pecos map (bottom) modified from [Powell, 1998]). The upper map shows the locations of the five cores drilled on the Miller Ranch. Coordinates are in the UTM system.

All other cores collected as part of the Trans-Pecos research initiative were collected about 100 km north of the McKel site and within the Miller Ranch, privately owned property by Clay Miller (Figure 6-1). Valentine, Texas, a very small

community (population < 250 people) located 15 – 20 km east of the Miller Ranch, is situated in Jeff Davis county between Van Horn (63 km to the north) and Marfa (56 km to the south). The general elevation at the Miller Ranch site is 1300 m. The recently-encroached desert scrub site is located on a small rise at the southeastern end of the Miller Ranch. One core, designated as DA, was collected from this site (537613m easting, 3378510m northing) on October 11, 2000. The grassland site is located 1.4 – 2 km northwest of the DA borehole at surface elevation of 1320 m. The grassland site cores, designated as GD (536379m easting, 3380074m northing) and GS (536366m easting, 3379135m northing), were drilled on October 10 – 11, 2000. Borehole GS is situated very close to the ecotone that separates the grassland, represented by GD, and the encroaching desert scrub, represented by DA. The juniper site occupies the western boundary of the Miller Ranch that abuts the foothills of the north-south trending Sierra Viejas. The two cores from this site, designated as JA (532865m easting, 3380166m northing) and JB (532881m easting, 3380115m northing), were drilled on October 12, 2000 with a separation distance of 53 m.

6.2.1. Regional Geology

The Chihuahuan desert is the largest desert in North America extending from New Mexico southward into central Mexico and from southeastern Arizona to western Texas (Figure 6-2). This continental desert is bounded to the west by the Sierra Madre Occidental, to the east by the Sierra Madre Oriental, to the north by the Rocky Mountains and to the south by the highlands of the Mexican plateau. Basin and Range topography characterizes the Trans-Pecos region. Mountain ranges and

coalescing basins, resulting from Late Tertiary block faulting, generally trend north to northwest [Dickerson, and Hoffer, 1980]. The region supports considerable topographical relief with mountain peaks rising 600-1200 m above the Quaternary alluvium-filled bolsons. Tertiary igneous rocks typify mountain massifs in the western portion of the Trans-Pecos region, whereas Cretaceous limestones dominate to the east [Dickerson, and Hoffer, 1980].

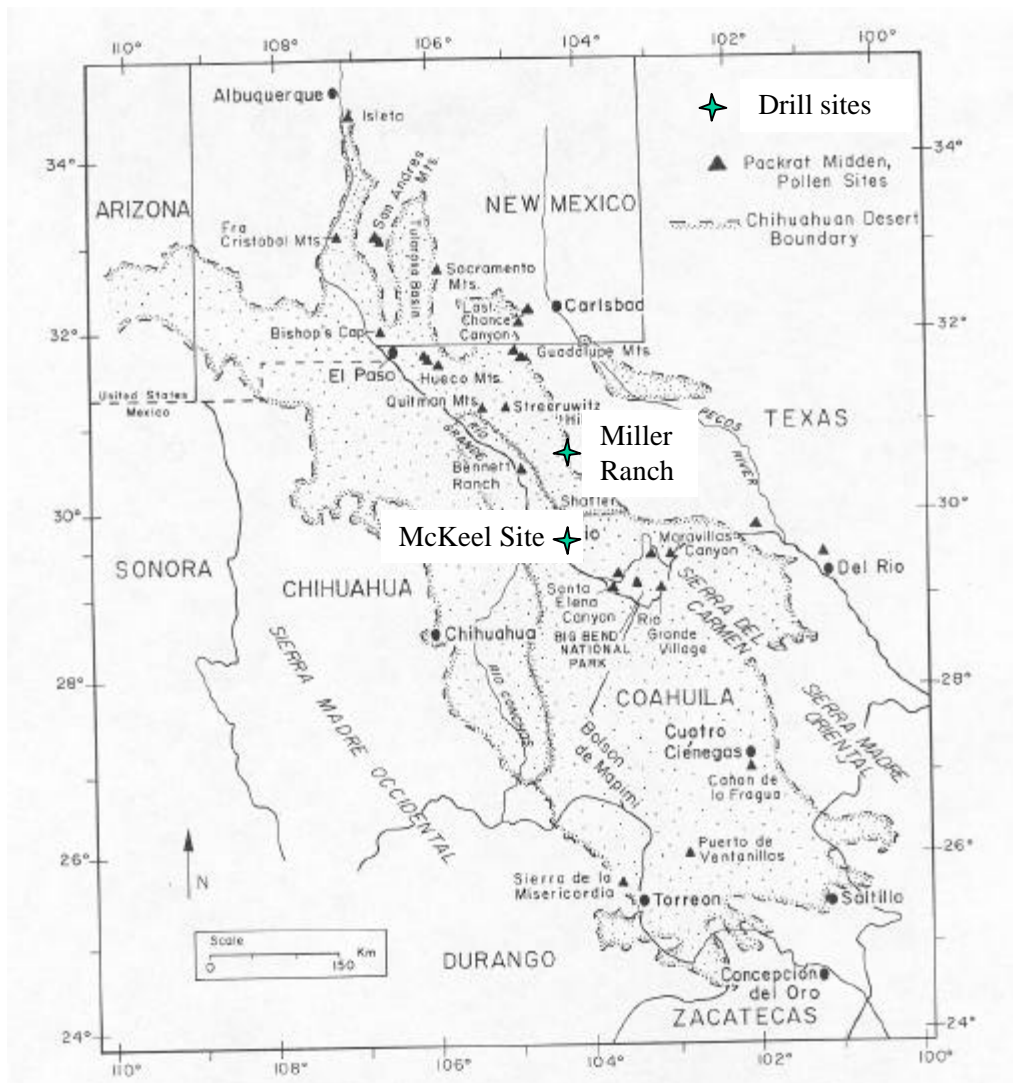


Figure 6-2. Areal extent of the Chihuahuan Desert (stippled). Triangles mark packrat midden or pollen sites used for paleovegetation studies discussed later in text. (modified from [Van Devender, 1990]).

A notable geologic feature in the Trans-Pecos region, which may have some bearing on the porewater chemistry results presented later in this study, consists of widespread fluorspar deposits in the Eagle Mountains. The Eagle Mountains are located to the west of the Van Horn Mountain and approximately 80 km northwest of the Miller Ranch site. Geologists have identified more than 30 fluorspar deposits in the Eagle Mountains in fissure veins along faults [*Dickerson, and Hoffer, 1980*].

6.2.2. Local Geology

The McKeel site (SA and SB cores) located in the northern part of Presidio County, consists of rolling hills and grasslands, which give way to rugged mountainous terrain to the west. The principal mountains include the Sierra Vieja and Chinati Mountains, both primarily composed of igneous rocks. The mountain ranges parallel the Rio Grande, which flows through a narrow valley eventually broadening until entering the canyons of Big Bend National Park (Figure 6-3). The McKeel property sits on an ancient Rio Grande terrace deposit. The terrace is relatively flat, but quite rocky. The terrace deposits range widely in grain size from fine silt to boulders and vary in composition.

The Miller Ranch in Jeff Davis county occupies the Valentine Basin trending north-south, flanked by nearby mountain ranges to the west, the Van Horn Mountains and the Sierra Viejas, and the Davis Mountains to the east (Figure 6-3). The Van Horn Mountains are composed mainly of Cretaceous limestone and sandstone, but also contain significant outcrops of Permian sedimentary and Tertiary volcanic rocks [*Dickerson and Hoffer, 1980*]. The Sierra Viejas, the result of Late Tertiary normal

faulting, are composed primarily of volcanic rocks. The Davis Mountains consist of vast Tertiary volcanic fields. Valley-fill sediments in the Valentine Basin consist of Quaternary alluvial deposits, derived from erosion of the surrounding mountains. Due to proximity within the western portion of the Valentine Basin, the overall topography of the Miller Ranch gently slopes to the east.

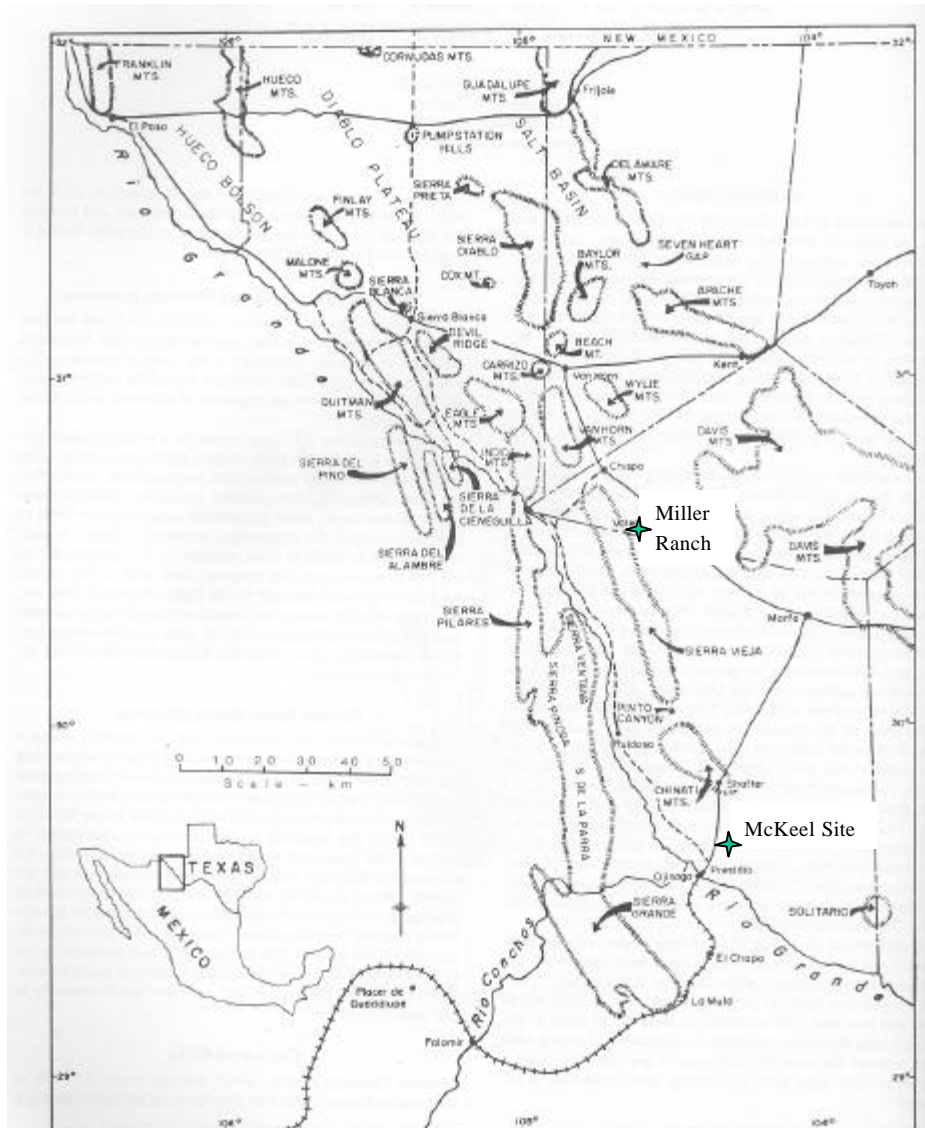


Figure 6-3. Physiographic features of the western Trans-Pecos region (from [Dickerson and Hoffer, 1980]).

Heat flow data from the general vicinity of the study areas indicates geothermal gradients of 20-30 °C km⁻¹ [Taylor and Roy, 1980]. These estimates were obtained for depth intervals below the water table. Geothermal gradient through the vadose zone would presumably be higher owing to the lower thermal conductivity of air than water.

6.2.3. Local Hydrology

Basin and Range topography dictates drainage patterns and groundwater flow in the study area. Alluvium-filled basins are generally considered to be hydrologically closed.

Depth to water table at the McKeel site is estimated to be between 90 and 110 m. The potential for surface flow resulting from intense precipitation events is high at the McKeel site, due to the large percentage of bare ground. However, the terrace surface itself, where cores SA and SB were drilled, is quite flat, and the rocky surface encourages infiltration under relatively short-lived or low intensity precipitation events.

Groundwater beneath the Miller Ranch flows in a southward direction. The depth to the water table in the valley ranges from 25 to 100 m. The estimated depth to the water table at the grassland and encroached desert scrub sites is about 75 m, based on data from several wells located on the Miller Ranch.

The depth to the water table at the Miller Ranch juniper site is constrained between 22 m and 30 m, also based on local well measurements. However, bedrock may be encountered at this site above the water table, which may cause perching.

Run-off from the Sierra Viejas that contain large areas of sloping, exposed bedrock probably contributes significantly to infiltration at the juniper foothill location.

6.2.4. Current Climate

The present climate in the Chihuahuan Desert ranges from arid to semiarid and is characterized by summer monsoons that deliver 70% of the region's precipitation, on average [Schmidt, 1979]. The climate associated with the McKeel site is arid. Presidio, Texas, the closest town to the McKeel site, reports an average high temperature of 40 °C during mid-June to late August and an average low temperature of 12 °C during the winter months. Days characterized by below-freezing temperatures are uncommon and generally only experienced in the latter part of December. Presidio records a mean annual temperature of 21 °C, an annual precipitation range of 250-280 mm yr⁻¹, and a potential evapotranspiration estimate of about 2000 mm yr⁻¹. The majority of the precipitation in the area falls during intense thunderstorms during the summer months, July through September. (Climatic data obtained from the National Climatic Data Center, National Atmospheric and Oceanic Organization web site at <http://www.noaa.gov>).

The climate of the Miller Ranch location borders classification as arid to semiarid. The area receives more yearly precipitation and experiences lower temperatures than the arid McKeel site due to its higher elevation. Climatic data from Valentine, Van Horn, and Marfa record average summer highs of 30 °C, average winter lows of -3 °C and a mean annual temperature of 16 °C. Annual precipitation ranges from 325 to 400 mm yr⁻¹. The area receives the majority of its annual

precipitation in the form of thundershowers during the summer months, July through September. (Climatic data obtained from the National Climatic Data Center, National Atmospheric and Oceanic Organization web site at <http://www.noaa.gov>).

6.2.5. Current Regional Vegetation

Flora in the Trans-Pecos region is quite diverse and can be broadly categorized into the following types: desert scrub, grassland, oak-piñon-juniper woodland, conifer forest, and riparian areas. This study focuses on two ecotones: 1) desert grassland as the ecological transition between desert scrub and grassland, and 2) mixed juniper savanna as the ecological transition between grassland and woodland). This study does not address areas that fall into the forest or riparian categories, due to the fact that the water table and/or bedrock is generally shallow in these zones [Turner, 1997].

Biodiversity in the Trans-Pecos results from the complex physiography and extreme range in elevation (300 m - 2700 m). Precipitation and temperature patterns exert major control on current vegetation patterns. The amount of precipitation generally increases with elevation and decreases from east to west in the Trans-Pecos region. Average annual temperatures decrease with elevation at a lapse rate of 5-7 °C km⁻¹ [Schmidt, 1979]. The elevational boundary of the present Chihuahuan Desert flora in the Trans-Pecos is approximately 1400 m [Powell, 1998]. However, due to competing influences such as slope aspect, soil type, and micrometeorological phenomena, there is no absolute elevational or geographic line separating characteristic Chihuahuan Desert vegetation from more mesic vegetation.

Additionally, the northern extent of the Chihuahuan Desert continues to grow due to the influence of grazing, subsequent soil erosion and periodic droughts that favor invasion of opportunistic desert scrub species [Powell, 1998].

Climax vegetation of the desert scrub vegetative community consists of drought-tolerant shrubs, cacti, and perennial grasses. Dominant plants include Creosotebush (*Larrea tridentata*), acacias (*Acacia* spp.), Ocotillo (*Fouquieria splendens*), yucca (*Yucca*, spp.), Lechuguilla (*Agave lechuguilla*), Catclaw Mimosa (*Mimosa aculeaticarpa*, var. *biunicifera*), Chino Grama (*Bouteloua ramosa*), Black Grama (*Bouteloua eriopoda*), Bush Muhly (*Muhlenbergia porteri*), threeawns (*Aristida* spp.), and Burrograss (*Scleropogon brevifolius*). Vegetation cover is generally low in desert scrub. The plants are generally widely spaced among barren soil or desert pavement [Turner, 1997].

Vegetation of grassland regions varies with elevation. Lower elevation grasses (1000-1200 m) are mainly short and mid-grasses such as Chino Grama, Black Grama, Six-week Grama (*Bouteloua aristidoides*), Bush Muhly, Tobosa Grass (*Hilaria mutica*), threeawns, Fluffgrass (*Dasyochloa pulchella*), Hairy Grama (*Bouteloua hirsuta*), and tridens (*Tridens* spp.). Shrubs associated with low elevation grasslands include Honey Mesquite (*Prosopis glandulosa*), Mormon tea (*Ephedra* spp.), acacias, Ocotillo, prickly pear (*Opuntia*, spp.), Catclaw Mimosa, Cane Cholla (*Opuntia imbricata*), sotol (*Dasyilirion* spp.), Lechuguilla, and Spanish Dagger (*Yucca torreyi*). Mid-elevation grasslands (1200-1400 m), referred to here as plains grasslands, support Blue Grama (*Bouteloua gracilis*), Sideoats Grama, Hairy Grama, Black Grama, Bluestem (*Andropogon cirratus*), Plains Lovegrass (*Eragrostic*

intermedia), Wolftail (*Lycurus phleoides*), Tobosa Grass, muhly (*Muhlenbergia* spp.), threeawns, Burrograss, Buffalograss (*Buchloe dactyloides*), and tridens [Powell, 1994]. Higher elevation (1400 - 1700 m) grassland climax vegetation is mainly Sideoats Grama, Cane Bluestem, Blue Grama, and Black Grama [Turner, 1997]. The mid-to-high elevation grasslands have experienced an increase in juniper, large shrubs, and leaf succulents in some regions, thereby modifying the original "pristine" grassland communities [Powell, 1994].

Trees associated with low elevation (< 1700 m) woodlands include Gray Oak (*Quercus grisea*), Emory Oak (*Q. emoryi*), Rose-fruited Juniper (*Juniperus coahuilensis*) and Red Berry Juniper (*J. pinchotii*), and Papershell Piñon (*Pinus remota*). At higher elevations (1700 - 2400 m), Alligator Juniper (*Juniperus deppeana*) and Mexican Piñon Pine (*Pinus cembrodies*) replaces other species of junipers and piñons. Grasses present in the woodlands consist of needlegrass, (*Stipa* spp.), Piñon Rice Grass (*Piptochaetium fimbriatum*), Bulb Panicum (*Panicum bulbosum*), and muhlys (*Muhlenbergia* spp.) [Powell, 1998].

6.2.6. Site Vegetation

Chihuahuan desert species identified at the McKeel desert scrub site (Figure 6-4) include: Creosotebush, Tarbush, Honey Mesquite, Ocotillo, Cane Cholla, Lechuguilla, Whitethorn acacia, Catclaw Mimosa, sotol, and yucca. Vegetation appears to grow in distinct clusters. The distance between shrub clusters varies from 1 to 3 meters. Bare ground predominates in the interspaces of these vegetation clusters. Even grasses, if present, reside within the clusters, and consist of gramas

and tobosa. Vegetation density appears to be correlated with biodiversity at the local scale. Areas of denser vegetation contain a greater diversity of scrub species. In areas of sparse vegetation, species diversity is extremely low and Creosotebush dominates.

The predominant vegetation species at the Miller Ranch DA site is Creosotebush (Figure 6-5). Very few other species coexist with this dominant species. Spacing between individual shrubs ranges from 1-2 meters. Average bush height is estimated to be about 0.75 m.

The grassland area of the Miller Ranch comprises part of the best remaining grassland in the Trans-Pecos [Powell, 1980]. Grass species at the Miller Ranch grassland site (Figure 6-6) consist predominantly of Blue Grama and Tobosa Grass. Ground cover ranges from 85-95% at the locations of the GD and GS boreholes. The GD location contains a higher ratio of Tobosa Grass to all other grasses present as compared to the GS location. The abundance of Tobosa Grass, sometimes referred to as Tobosa flats if extensive in area, correlates with occasional occurrences of ponded water [Powell, 1980].

Vegetation within the juniper stand displays high species diversity (Figure 6-7). Juniper is the predominant species. Other species consist of cholla, prickly pear, Catclaw Mimosa, Mormon Tea and some grama grasses.



Figure 6-4. Photos of the McKeel desert scrub site, near the SA and SB core locations.



Figure 6-5. Photos of the Miller Ranch recently-encroached desert scrub site, near the DA core location.



Figure 6-6. Photos of the Miller Ranch grassland site, near the GD and GS core locations. Upper photo taken in June, 2000, after two weeks of late spring rains. Lower photo taken in October, 2000 during the drilling project, after several dry summer months.



Figure 6-7. Photos of the Miller Ranch juniper site, near the JA and JB core locations.

6.2.7. Paleoclimate

Similar to most of the southwestern U.S., the Trans-Pecos region underwent a major climate change associated with the retreat of the North American continental glaciers prior to the onset of the Holocene. The Trans-Pecos region not only experienced a general warming trend, but the melting of the ice sheets modified the general circulation of the atmosphere in the Chihuahuan Desert, and thus the spatial and temporal distribution of precipitation [Allen and Anderson, 1993]. The position of the moisture-deficient Chihuahuan Desert, surrounded by high mountain ranges and highland plateaus, makes it particularly sensitive to changes in the polar jet stream and a prime location for paleoclimatic studies. Paleoclimate studies from the Trans-Pecos region unlock the histories stored in paleolake shorelines, paleolake sediments, Quaternary alluvial stratigraphy, speleothems, and packrat middens.

Closed-basin paleolake chronologies provide important paleoclimate inferences, based on the assumption that closed-basin lakes respond synchronously to changes in climate [Benson *et al.*, 1990]. The Trans-Pecos region contains a hydrologically-closed basin covering 20,000 km² centered on the Salt Basin [Wilkins and Currey, 1997]. Geomorphic features from two paleolakes identified in the area, Lake King and Lake Sacramento, point to four major highstands during the Last Glacial Maximum [Wilkins and Currey, 1997]. Radiocarbon-dated lacustrine deposits from Lake King indicate transgressions at 22,570, 19,090, 17,180, and 15,940 ¹⁴C yr B.P. The timing of these events correlates well with paleolake reconstructions in the Estancia and San Augustin basins in New Mexico [Allen and Anderson, 1993; Phillips *et al.*, 1992].

Speleothem geomorphologic chronologies supply information about moisture conditions and precipitation histories, based on the assumption that speleothems grow faster under wetter climates than under drier climates. Stalagmites from three caves in central Texas exhibit a dramatic reduction in growth rate between 15 ka and 12 ka (dated by U-series isotopes), and very slow growth up to the present [*Musgrove et al.*, 1999]. Such evidence supports the hypothesis of a drier climate transition at about 15 ka.

In summary, independent paleoclimatic indicators from the Trans-Pecos region agree that a wetter, colder climate persisted during the Late Wisconsin and that a transition to a drier, warmer latest Pleistocene climate occurred at around 16–15 ka.

6.2.8. Regional Paleoecology

Regional and local paleoecological records provide substantial evidence for a major vegetation transition in the early Holocene in the Trans-Pecos [*Wells*, 1966; *Spaulding*, 1983; *Van Devender*, 1990]. Based on macrofossils from packrat (*Neotoma*) middens, vegetation of the mid - late Wisconsin consisted of a piñon-juniper- oak woodland and remained relatively constant from 27.8 to 11.2 ka. Tree species included Papershell Piñon, shrub oak, Red Berry Juniper and rock cedar. The combined presence of shrubs such as honeysuckle and redbud and scarcity of desert succulents such as Lechuguilla, strongly indicate a relatively mesic woodland during the mid-late Wisconsin. A packrat midden collected from the Livingston Hills, about 5 miles north of the McKeel site, records the local full-glacial flora associated with a piñon-juniper woodland [*Van Devender et al.*, 1978] and is consistent with

paleobotanical records from the region [*Van Devender, 1990*]. Papershell Piñons disappeared rapidly throughout western Texas ~ 11 ka. The disappearance of Papershell Piñon and increase of shrub oak between 11.2 and 10.3 ka in the Chihuahuan Desert mark the transition from mesic to xeric vegetation, as evidenced in radiocarbon-dated packrat middens [*Van Devender, 1990*]. Around this time period, a climate approaching the modern climate regime developed. Dramatically increased summer temperatures produced maximum summer monsoonal rainfall. Consequently, desert scrub plants began to increase. By 8.2 ka, desert plants, such as Honey Mesquite, Lechuguilla, acacia, and prickly pear, were abundant and the earliest Creosotebush arrived. Packrat middens from Rio Grande Village, Dagger Mountain and Burro Mesa in Big Bend National Park also indicate a major vegetational transition from mesic woodlands to xeric desert scrub beginning between 9.4 and 8.2 ka, (depending on locality) [*Van Devender, 1990*]. However, severe winter freezes may have prevented desert scrub establishment in favor of grasses in the topographically higher regions of the Chihuahuan Desert. At elevations, similar to that of the McKeel study site near Presidio, TX, the transition to desert scrub vegetation commenced later at Big Bend valley sites. By the Late Holocene, 4 ka, the modern climatic regime was established and the frequency of winter freezes was reduced, thereby encouraging the expansion of succulent desert scrub into grassland [*Van Devender, 1990*]. Desert scrub establishment at the McKeel site is constrained between 8 ka and 4 ka and the arrival of creosote is estimated at 4.5 ka. [*Van Devender, 1986*].

Fossil vertebrate, pollen, and plant macrofossil data from the Edwards Plateau, located east of the Trans-Pecos region, indicates that Pleistocene and Holocene vegetation changes were coupled with changes in temperature and moisture regimes. Full-glacial temperatures were significantly cooler than those of today, at least 6 °C during the summer months. By 13 ka, summer temperatures were within 2-3 °C of present values [Toomey *et al.*, 1993]. During the late-glacial, ca.14,000-10,500, effective moisture first decreased then increased, while the early to middle Holocene was dominated by a protracted decrease in effective moisture. This long-term trend culminated in conditions that were drier than modern during the early part of the late Holocene from 5 ka to 2.5 ka. Conditions were more mesic than present from 2.5 ka to 1 ka while the modern drought-prone climate has characterized the last 1000 years [Toomey *et al.*, 1993].

6.2.9. Regional Historic Vegetation Changes

Some grassland areas in the Chihuahuan Desert transition zone have undergone a historic invasion of desert scrub [Powell, 1980; Dick-Peddie, 1993]. Intensive ranching in the Trans-Pecos region began in the 1880s, which presumably contributed to soil erosion and favored the establishment of opportunistic desert shrubs [Powell, 1980; Nelson and Beres, 1987]. Other factors promoting desert scrub encroachment include drought and human control on the natural fire regime [Humphrey, 1987]. In some areas, a complete transition from grassland to desert scrub has taken place, whereas in other areas, only partial encroachment has resulted. In the latter case, the grass coverage may remain similar, but the overstory has

become dominated by scrub species. Creosote and mesquite are common and particularly effective invasive scrub species in the Chihuahuan Desert at elevations below ~ 1400 m. At higher elevations, junipers and Catclaw Mimosa encroach onto open grassland [Powell, 1998].

Attempts to investigate recent changes in vegetation motivated studies to document pre-settlement vs. current vegetation in the Trans-Pecos region by repeat photography. Photos taken in 1899 by the U. S. Geological Survey were compared with photos of the same 4 areas within Brewster and Jeff Davis counties taken in 1984 [Nelson and Beres, 1987]. The southernmost areas, located 140 - 150 km south of Alpine, Texas, appeared in 1899 as well-established desert scrub communities that have subsequently undergone little change. In contrast, an area located just about 100 km south of Alpine, has undergone a transition from open grassland with scattered shrubs to desert grassland with Creosotebush, Whitethorn acacia (*Acacia constricta*) and mesquite. Grass cover has remained about the same since 1899, but Creosotebush has taken over as an overstory dominant [Nelson and Beres, 1987]. Comparison of past and modern photos of an area located in Jeff Davis county, 16 km north of Alpine, Texas, document the increase in density and cover of Catclaw Mimosa and the encroachment of juniper and mesquite onto a former open grassland. Similar to the scrub-encroached area south of Alpine, grass cover has remained stable. The Miller Ranch site lies within the historically scrub-encroached region south of Alpine, TX.

6.3. Field and Laboratory Methods

6.3.1. Sample Collection

Soil sample collection at the Trans-Pecos sites in October, 2000, involved hollow-stem augering, without the introduction of drilling fluids, to 7-15 m depths (Table 6-1, Figure 6-8). A geotechnical and environmental drilling company based out of El Paso, Texas, Raba-Kistner, Inc., completed the drilling and assisted in sample collection. Target depths ranging from 10-20 m were chosen in hopes of capturing the majority of the transient hydraulic and solute signatures preserved in these thick vadose zones. Coring to the water table would have provided the most ideal data sets. However, the time and expense of drilling deep cores had to be factored in, resulting in the following design strategy: 2 cores, one shallow (10 m) and one deep (20 m) for each location. Limited time and drilling difficulties precluded the fulfillment of the sampling strategy. The variety of geologic materials encountered at the drilling sites provided significant technical challenges and prevented penetration to the desired completion depths (see Table 6-1) in many cases. Auger refusal at the McKeel desert scrub site and Miller Ranch juniper site resulted from striking boulders larger in diameter than the boreholes. Compacted clay made drilling quite difficult at the Miller Ranch grassland sites and also induced drying in a few of the deep GD samples from the augers spinning in place for a total duration of one hour.

Core	SA	SB	DA	GS	GD	JA	JB
Location	McKeel	McKeel	Miller	Miller	Miller	Miller	Miller
Dominant vegetation	desert scrub	desert scrub	creosote	grass	grass	juniper	juniper
Surface elevation (m)	875	875	1322	1320	1319	1327	1327
Water table depth (m)	90-110	90-110	75	75	75	25-30	25-30
Sampling date	13-Oct-00	13-Oct-00	13-Oct-00	11-Oct-00	10/11-Oct-00	12-Oct-00	12-Oct-00
Target drill depth (m)	10	20	20	10	20	10	20
Actual core depth (m)	10	15	10	10	15	9	7

Table 6-1. Summary of site location and coring information.



Figure 6-8. Drilling using the hollow-stem augering method. Photo taken at the Miller Ranch grassland site, drilling borehole designated as GD.

Samples were collected using a 2' long, 1.5" diameter split- spoon sampler, lined with four 6" long brass sleeves, and driven ahead of the auger by hammer percussion. Samples in the brass sleeves were immediately capped with tight-fitting plastic caps, and sealed with electrical tape and parafilm to minimize moisture loss prior to moisture-dependent analyses (Figure 6-9).



Figure 6-9. Core sample collection in brass-sleeves lining the split spoon.

6.3.2. Laboratory Methods

Soil sample analyses for all the cores drilled in the Trans-Pecos region include gravimetric water content [ASTM, 1992], water potential [Gee *et al.*, 1992], soil-water extract chemistry [Hartsough, 2000] and bulk density [Black, 1965]. Identical laboratory methods were used on the Trans-Pecos samples as for the NTS samples. Water potential measurements were obtained using a WP4 water potential meter, a

newer Decagon model than the CX-2 water potential meter used for NTS sample measurements. Soil-water extracts of 1:1 mass proportions (soil to 18 Ω de-ionized H₂O) were analyzed for chloride, bromide, fluoride and nitrate concentrations using ion chromatography at the New Mexico Bureau of Mines and Mineral Resources in Socorro, NM. Selected samples from one core, SA, were analyzed for ³⁷Cl/³⁵Cl ratios by mass spectrometry at the University of Arizona’s Isotope Laboratory.

6.4. Results from the Trans-Pecos Cores

6.4.1. Soil Characteristics

Stratigraphic columns for the SA, SB, JA, and JB cores show minimal textural variability in marked contrast to the significant textural variability in the DA, GS and GD cores (Figure 6-10).

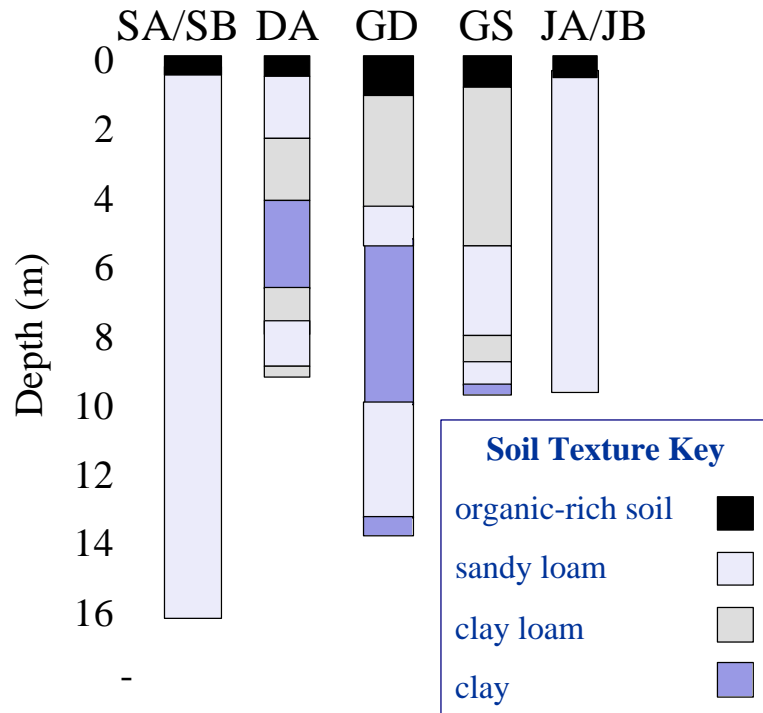


Figure 6-10. Stratigraphic columns for the Trans-Pecos cores.

Relatively uniform lithologic material from the SA and SB cores from the McKeel site consists of loose, poorly-sorted fluvial deposits having a sandy loam texture. Grain size, estimated by observation and sieve analysis, in collected samples ranges from fine silt to large gravel. Boulder-sized material was observed in the field on the surface and encountered during drilling, which manifested in auger refusal and suggests potentially significant heterogeneity.

Many samples taken beneath the grassland (GD and GS) and the encroached desert scrub (DA) on the Miller Ranch contain high clay content and display a high degree of compaction. The loamy and clayey alluvial sediment is derived mainly from igneous rock from the adjacent mountains, but may also contain material from nearby sedimentary mountains (predominately limestone). Sediment color ranges from light brown to dark reddish brown. Many samples contain a large amount of carbonate. Soil textures in the GD, GS, and DA cores ranges from sandy loam to clay.

Unlike the layered soil heterogeneity at the desert grassland sites on the Miller Ranch, the soil texture profiles at the nearby juniper site are relatively uniform. The material from JA and JB consists of loose, poorly-sorted alluvial deposits having a sandy loam texture. Grain size ranges from fine silt to large gravel. Boulder-sized material observed in the field and encountered during drilling instigated auger refusal at the bottom of the boreholes.

Bulk density values from the Trans-Pecos cores ranges widely between core sites and only slightly between samples within individual cores (data in Appendix C).

The relatively high bulk densities measured in the Miller Ranch grassland and encroached desert scrub reflect significant compaction of the clay matrix.

6.4.2. Water Content

Gravimetric water content taken from all cores ranges from 0.02 to 0.17 (Figure 6-11). Moisture content, not surprisingly, appears to be strongly correlated with clay content. Soils under grassland and recent desert scrub at the Miller Ranch contain the highest clay contents and the highest moisture contents. Moisture content varies considerably throughout the soil profiles that are characterized by heterogeneous soil texture distributions, i.e. the Miller Ranch grassland and recently-encroached desert scrub. In contrast, the McKeel desert scrub site and the Miller Ranch juniper site show relatively uniform soil type and moisture content profiles. In

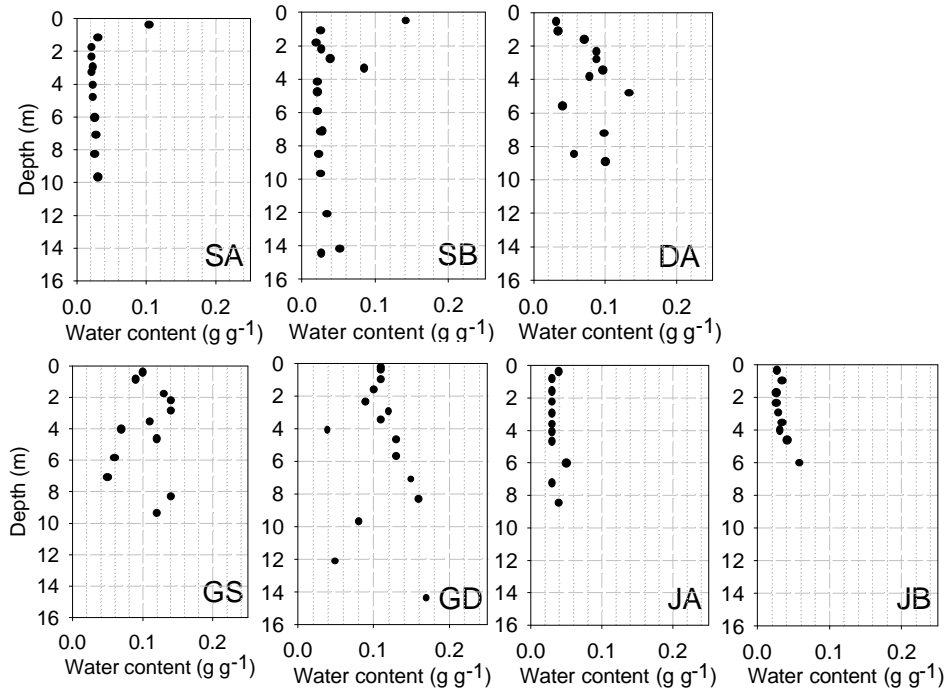


Figure 6-11. Gravimetric water content measurements from the Trans-Pecos cores.

summary, the more heterogeneous, clay-rich soil cores (DA, GS, and GD) contain higher mean water contents and higher variability from their means than do the homogeneous sandy loam cores (SA, SB, JA, and JB) (Figure 6-12).

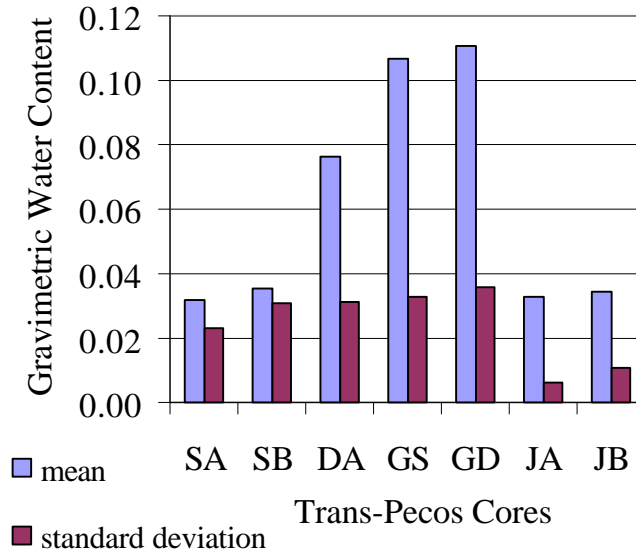


Figure 6-12. Graph of gravimetric water content means and standard deviations for the Trans-Pecos cores.

6.4.3. Water Potential

The water potential profiles measured for the Trans-Pecos cores exhibit somewhat similar character (Figure 6-13). In all cores, the minimum (most negative) measured water potentials are located within the upper 3 m and are extremely low. The most negative water potential measured is much lower than the negative gravitational potential at the surface for each of the cores. The water potential profiles show values generally increasing with depth and hydraulic gradients indicating upward flow.

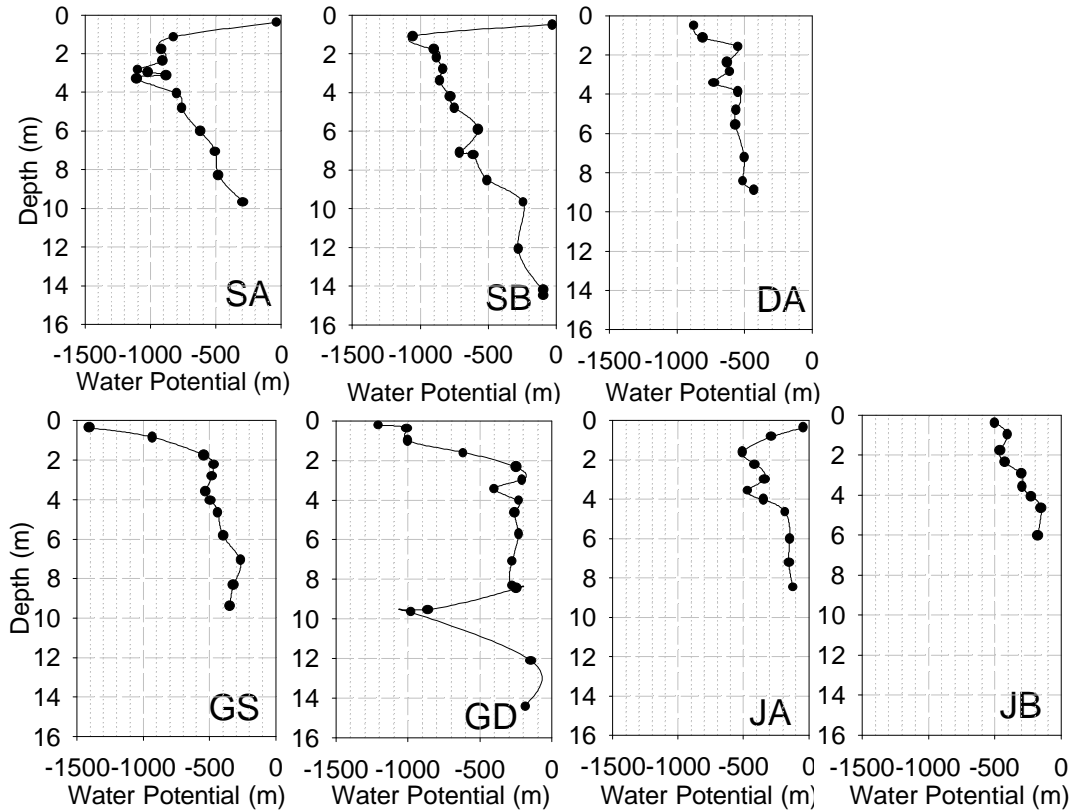


Figure 6-13. Water potential measurements from the Trans-Pecos cores.

The profiles from JA, SA and SB reveal high water potentials just below the surface, resulting from recent shallow infiltration. One to three days prior to sample collection, the area received precipitation [<http://nadp.sws.uiuc.edu>]. Interestingly, the profile from JB cored near, just hours after the JA core and ~50 m away, does not show similar high water potentials at the surface.

Profiles taken beneath the grassland sites exhibited the most negative near-surface water potentials at the time of sample collection. The minimum water potential measured is -13.5 MPa taken from the GS core just below the surface. Water potentials increase sharply with depth under grassland.

The most negative deep water potentials are observed in cores SA and SB taken under the long-established desert scrub (< -5.0 MPa above 8 m). The water potential profile beneath the creosotebush site on the Miller Ranch, DA, also shows very negative values several meters below the surface. Water potential profiles exhibit a trend of increasing dryness from wooded juniper to grassland to encroached desert scrub to long-established desert scrub.

6.4.4. Chloride, Bromide and Fluoride

The chloride profiles measured in the Trans-Pecos cores exhibit both similarities and differences (Figure 6-14). The profiles from SA and GS show the classic chloride bulge found in arid region vadose zones in the southwestern US, with high peak concentrations and significant chloride inventories. SB, JA and JB also display chloride peaks within the upper few meters of the surface. However, the peak concentrations and total chloride accumulations are significantly lower in SB, JA and JB than measured in the other cores. The chloride profiles measured from DA and GD record significant chloride inventories, but display broad distributions.

Chloride profiles show low near-surface concentrations resulting from leaching, with the exception of the JB profile. In fact, the highest chloride concentration measured in the JB core comes from the shallowest sample. The results suggest that the JB has not experienced recent infiltration, even to very shallow depths, which is consistent with the water potential profile measured under JB as compared with JA (Figure 6-13).

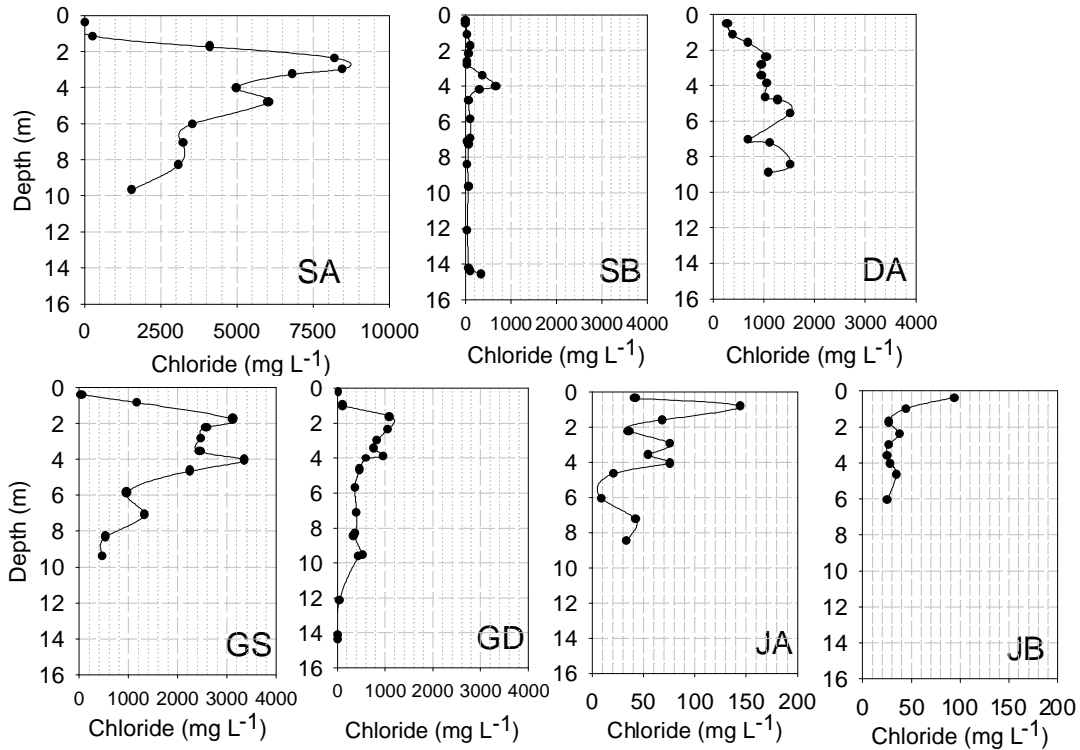


Figure 6-14. Measured chloride concentration profiles from the Trans-Pecos cores. Values reported as porewater concentrations. Notice the changes in horizontal scale for SA, JA, and JB cores.

Bromide, like chloride, is considered to behave as a conservative solute. Atmospheric deposition of bromide is generally lower than chloride by about 2 orders of magnitude. Bromide profiles that parallel chloride profiles (i.e. uniform Cl : Br ratios) provide strong evidence that the measured chloride has an atmospheric origin, thereby qualifying chloride as an appropriate environmental tracer. In contrast, significant deviation of chloride and bromide profiles suggest an in-situ source or sink of chloride that is not accounted for using a conventional chloride mass balance approach. Bromide and chloride concentrations are closely correlated in the SA, GS and GD cores (Figure 6-15). Correlation coefficients range from 0.94 – 0.99 for these

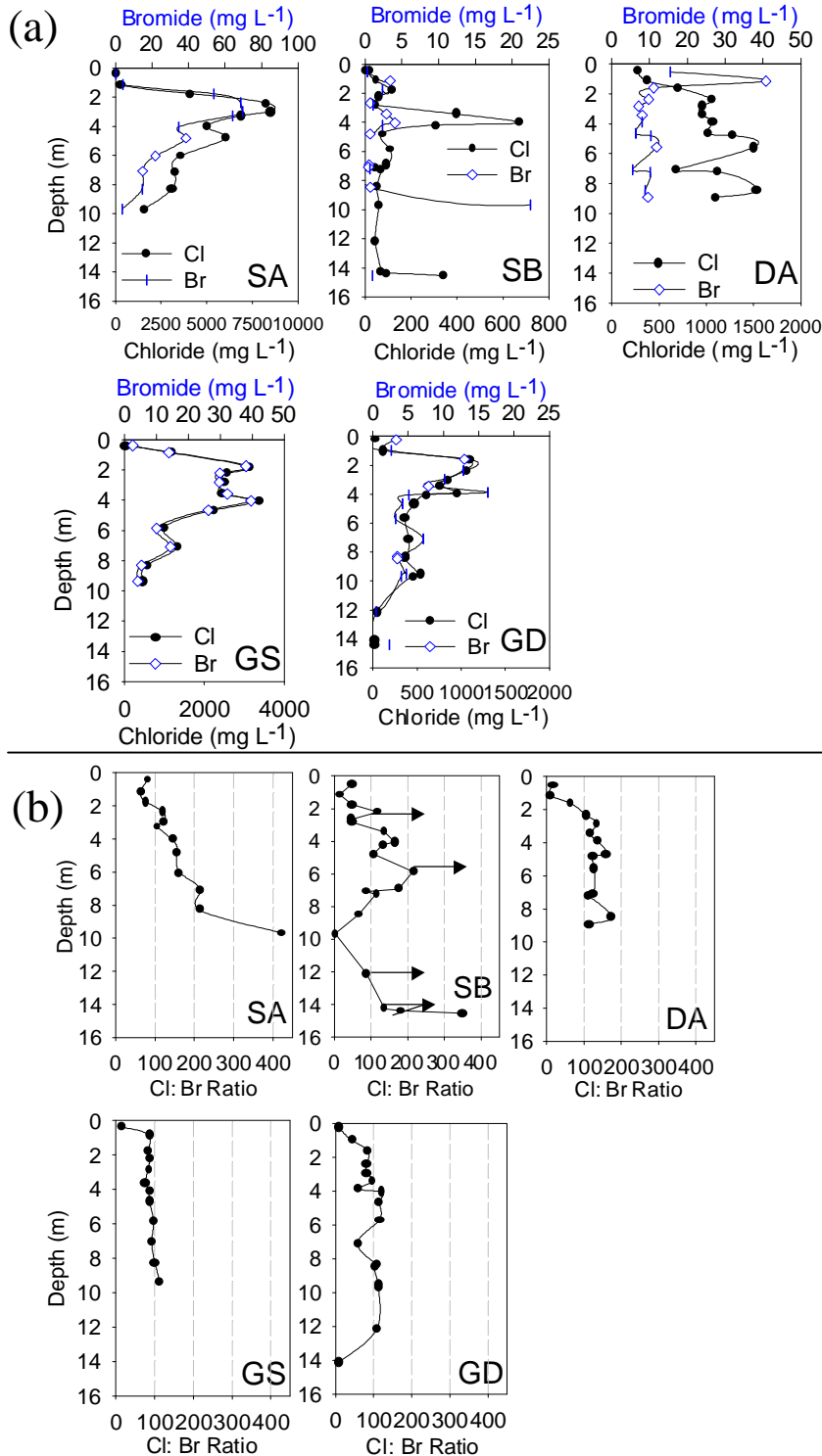


Figure 6-15. (a) Measured bromide concentration profiles with chloride profiles for comparison and (b) Cl:Br ratio profiles. Values (in a) reported as porewater concentrations. Data points with arrows (in b) indicate minimum ratios due to Br concentrations that fall below the analytical detection limit.

three cores (Table 6-2). Poor correlation observed in the SB and DA cores may be attributed to the lower bromide concentrations measured, which are close to the analytical detection limit. Alternatively, the poor Cl: Br correlation may suggest a non-atmospheric chloride source such as in-situ weathering. However, this proposition seems unlikely considering the excellent Cl: Br correlation from the nearby cores. A trend of Cl:Br ratios increasing with depth is detected in the SA, SB, and DA cores. The coincidence of this trend found only in soil profiles taken under desert scrub may suggest preferential anion uptake and/or vertical anion redistribution by their roots. However, the mechanisms responsible for this behavior are unknown and undocumented. Consequently, this assertion remains speculative. Bromide profiles from the juniper site are not shown due to fact that most porewater concentrations for JA and JB fall below the analytical detection limit.

Fluoride is rarely considered in environmental tracer studies due to its low concentrations in natural waters and precipitation, negligible amount of atmospheric deposition, and non-conservative behavior in systems containing high calcium ion concentrations. Several profiles from the Trans-Pecos cores exhibit anomalously high fluoride concentrations and roughly mimic the corresponding chloride profiles (Figure 6-16). Fluoride profiles from the juniper site are not pictured because most porewater concentrations for JA and JB fall below the analytical detection limit. The source of the fluoride is undetermined, but may be related to the widespread fluor spar deposits in the Eagle Mountains [*Dickerson, and Hoffer, 1980*]. The rough correlation between fluoride and chloride profiles points towards an atmospheric

source rather than an in-situ soil-derived source. However, the latter cannot be categorically ruled out.

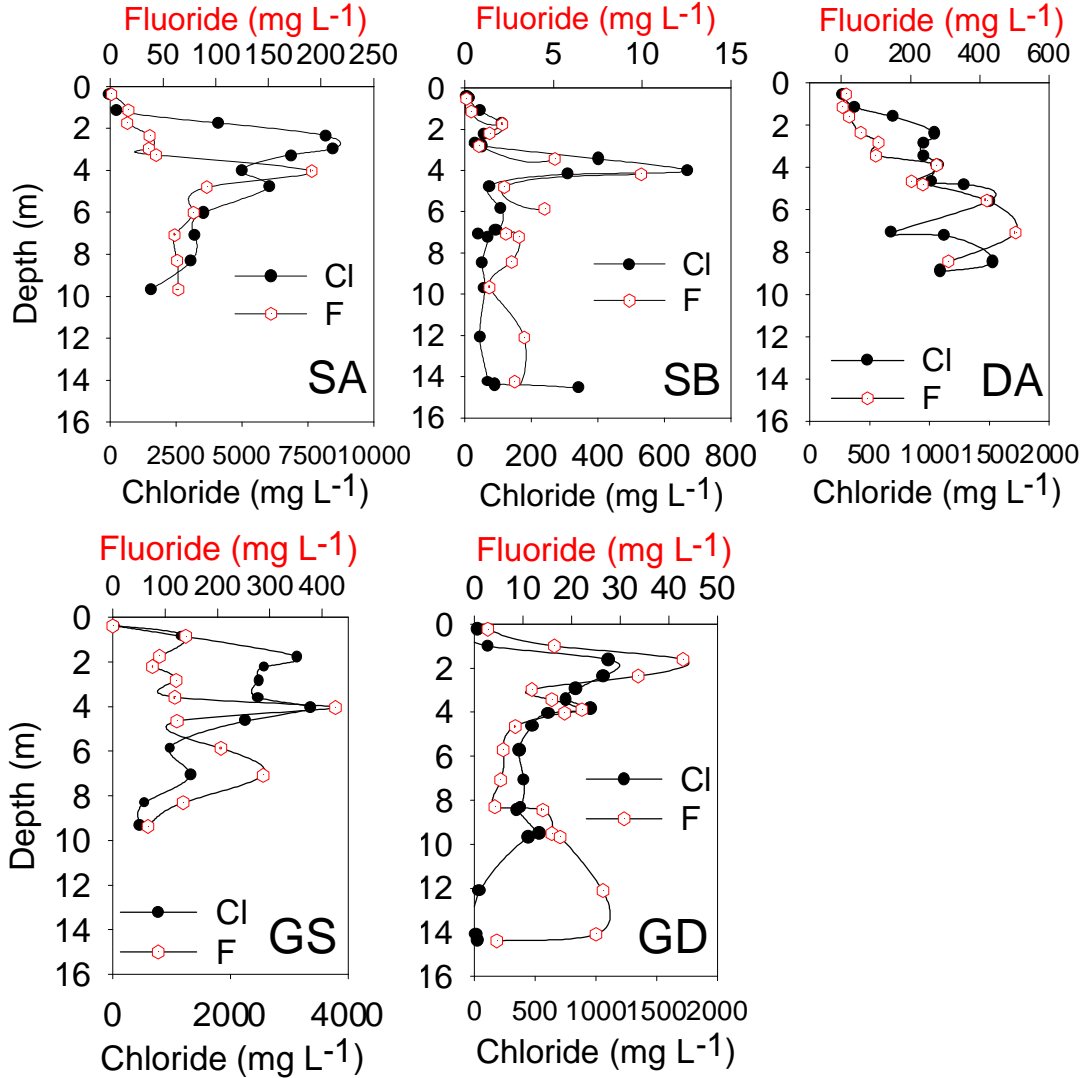


Figure 6-16. Measured fluoride concentration profiles, with chloride profiles for comparison, from the Trans-Pecos cores.

TRANS-PECOS CORES		SA	SB	DA	GS	GD	JA	JB
Gravimetric Water Content (g g ⁻¹)	Mean	0.03	0.04	0.08	0.11	0.11	0.03	0.03
	Std Dev	0.02	0.03	0.03	0.03	0.04	0.01	0.01
	Minimum	0.02	0.02	0.03	0.05	0.04	0.03	0.03
	Maximum	0.10	0.14	0.13	0.14	0.17	0.05	0.06
Bulk Density (g cm ⁻³)	Mean	1.35	1.35	1.76	1.59	1.60	1.40	1.39
	Minimum	1.28	1.30	1.52	1.22	1.40	1.26	1.28
	Maximum	1.53	1.51	1.92	1.79	1.71	1.50	1.51
Water Potential (MPa)	Mean	-7.94	-6.94	-5.81	-5.24	-5.10	-2.55	-3.07
	Minimum	-10.70	-10.10	-8.42	-13.50	-11.60	-4.81	-4.76
	Maximum	-4.55	-2.23	-4.07	-2.47	-1.89	-0.33	-1.39
Chloride Concentration (mg L ⁻¹)	Maximum	8,479	399	1,530	3,372	1,098	144	93
	Depth of max conc (m)	3.0	3.4	8.5	4.0	1.6	3.0	0.4
	Total Cl (g m ⁻³) (upper 10 m)	1,237	37	1,195	2,559	972	18	10
Bromide Concentration (mg L ⁻¹)	Maximum	70	22	41	40	13	12	10
	Depth of max conc (m)	3.0	9.7	1.1	4.0	1.6	7.2	2.4
Fluoride Concentration (mg L ⁻¹)	Maximum	191	18	275	425	43		
	Depth of max conc (m)	4.0	14.5	3.9	4.0	1.6		
NO₃⁻N Concentration (mg L ⁻¹)	Maximum	258	147	31	228	40	1	6
	Depth of max conc (m)	3.3	4.2	3.9	7.1	3.0	7.2	2.4
	Total NO ₃ ⁻ N (g m ⁻³) (upper 10 m)	37	24	12	91	43		
Mass ratio	Cl : NO ₃ ⁻ N	34	2	99	28	23		
Correlation coefficients	Cl, Br	0.94	-0.03	-0.58	0.99	0.94		
	Cl, NO ₃ ⁻ N	0.91	0.31	-0.08	0.53	0.43		

Table 6-2. Summary table for hydraulic, physical, and geochemical measurements completed on Trans-Pecos core samples.

6.4.5. Nitrate

The Trans-Pecos profiles show moderately high concentrations of NO_3^- -N, in all cores with the exception of the two drilled at the juniper site, JA and JB (Figure 6-17). Maximum porewater concentrations generally fall in the 2-5 meter depth interval and exceed 200 mg L^{-1} in the SA and GS cores. Maximum porewater concentrations of NO_3^- -N are highest in the SA core, although the cores taken beneath the grassland, GD and GS contain the greatest NO_3^- -N inventories (Table 6-2).

Nitrate profiles show variable degrees of correlation with the chloride profiles (Figure 6-17). The SA core exhibits the closest relationship between chloride and nitrate yielding a correlation coefficient of 0.91. Profiles from SB, GS and GD also demonstrate significant relationships between nitrate and chloride, with correlation coefficients of 0.31, 0.53 and 0.43, respectively. In contrast, the profile from DA shows major deviation between chloride and nitrate. The nitrate profile from DA also differs from the other nitrate profiles with regard to the lack of measurable NO_3^- -N below about 8 m.

Shallow porewater concentrations of NO_3^- -N are generally quite low, indicating nitrogen uptake by plants, loss to the atmosphere or loss to the deeper soil regime by leaching. One exception to this trend is seen in the SB core, which has a very high near-surface concentration of $147 \text{ mg NO}_3^- \text{ N L}^{-1}$.

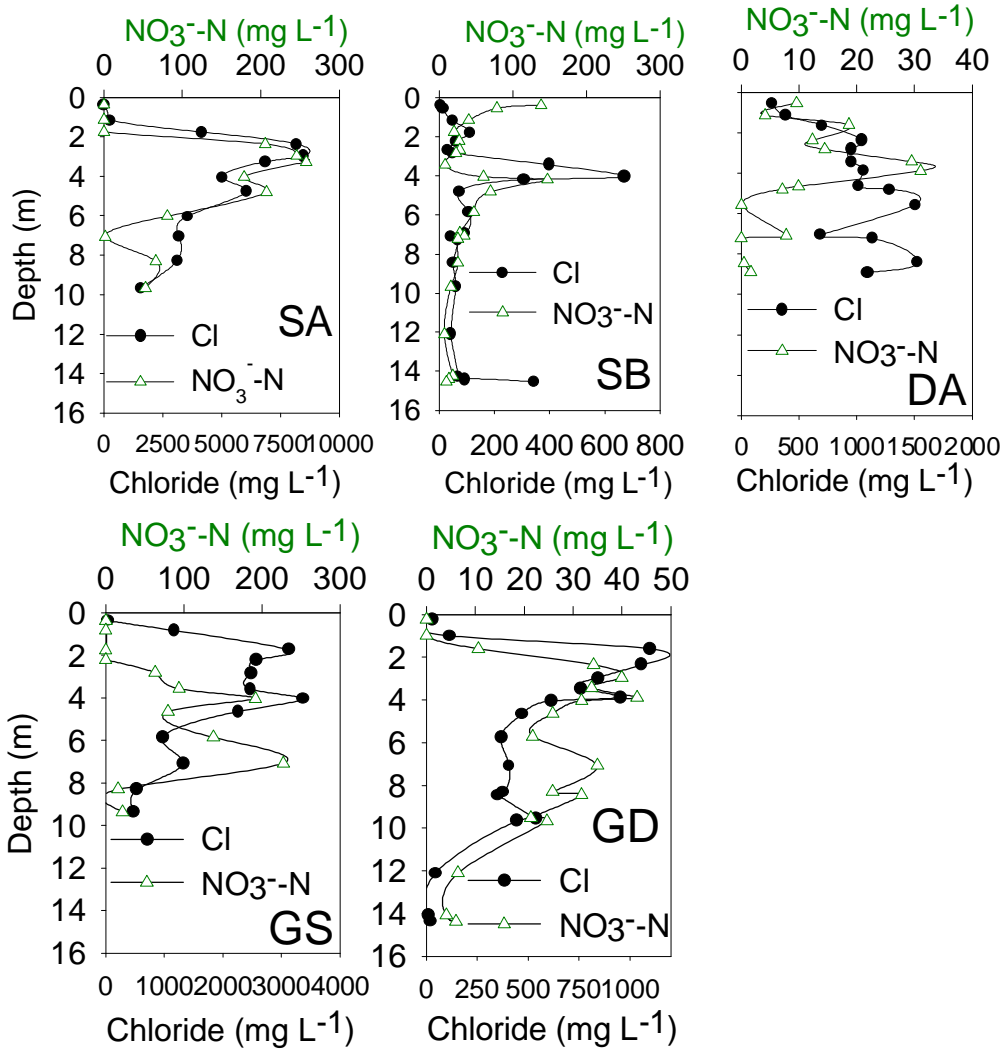


Figure 6-17. Measured nitrate profiles,with chloride profiles for comparison, from the Trans-Pecos cores. Values reported as NO₃⁻-N and Cl porewater concentrations. Notice the changes in horizontal scales.

In terms of nitrate inventories, the amount of NO₃⁻-N measured in the upper 10 m of the Trans-Pecos cores ranges (not including the cores taken under juniper) from 12 – 91 g NO₃⁻-N m⁻² (Table 6-2). The grassland sites contain the highest amount of NO₃⁻-N, followed by the McKeel desert scrub site (Figure 6-18). The

encroached desert scrub site contains the lowest amount of NO_3^- -N among the cores sampled in this study.

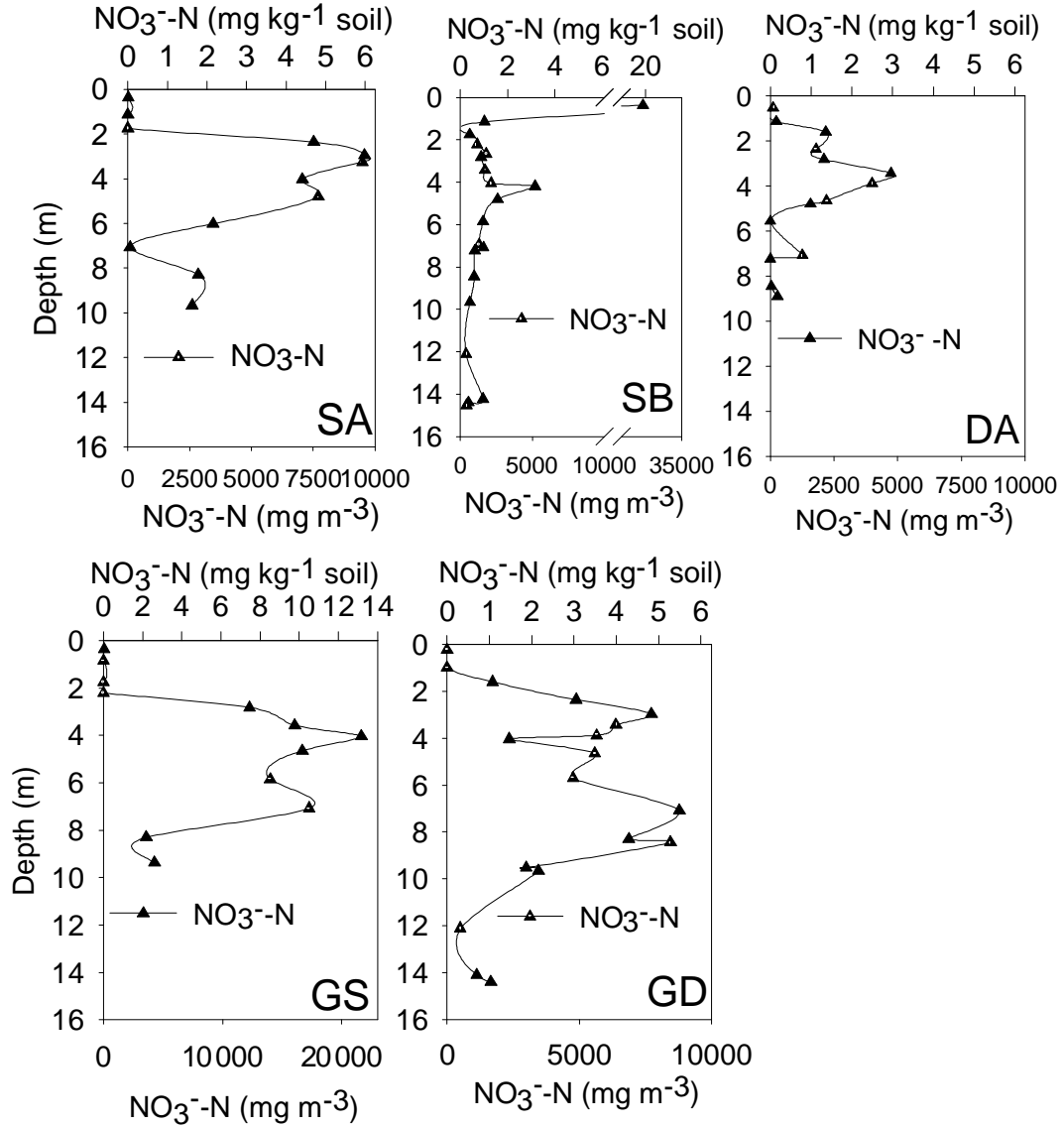


Figure 6-18. Measured nitrate concentration profiles from the Trans-Pecos cores. Values reported as NO_3^- -N concentrations in soil mass (top axis) and soil volume (bottom axis). Note the changes in horizontal scales.

6.4.6. Chlorine-37

The seven samples from the SA core that were analyzed for stable chlorine isotopes all showed some deviation from the standard mean ocean chloride (SMOC)

value of 0 ‰ (Figure 6-19). Samples collected between the depth interval of 1.5 - 5 m and the lowermost sample at 9.5 m deviated in the negative direction, or were depleted with respect to SMOC by up to -1 ‰. Two samples taken from depths of 6 and 9 meters deviated positively from SMOC by +0.4 to +0.5 ‰. These deviations are quite large compared to most $\delta^{37}\text{Cl}$ measurements on natural samples [Eggenkamp, 1997]. The observed deviations from 0 ‰ provide good evidence of transport processes dominated by diffusion (described in Sections 2.7 and 3.8 of this dissertation).

From the $\delta^{37}\text{Cl}$ trend, it appears that upward solute diffusion above a depth of 5 meters depletes the stable chlorine isotopic signature above 5 meters and leaves an enriched isotopic signature below 5 meters. However, the total chloride concentration profile does not support this interpretation (Figure 6-19). The main chloride peak at 2.5 to 3 meters suggests that solute diffusion should be in the downward direction below 3 meters, which would induce $\delta^{37}\text{Cl}$ depletion below 3 meters and enrichment above 3 meters rather than at 5 meter transition depth observed in the SA data.

An alternative interpretation may be invoked to explain the $\delta^{37}\text{Cl}$ and chloride trends, one which relies on transient processes and a speculative history. Perhaps the secondary chloride concentration peak observed in the current profile at 5 meters was the main chloride peak in the past, and chloride was also accumulating at a depth of about 1 meter. Convergent solute diffusion between 1 and 5 meters would result in a zone of isotopic depletion in that interval and a zone of enrichment below 5 meters. At some time in the not-too-distant past the uppermost chloride peak accumulating at

1 m may have been advected downward to its present depth of about 2.5 meters, presumably during a major wet period. In addition, the advective pulse would likely have reduced the isotopic fractionation effect preserved in the solute profile.

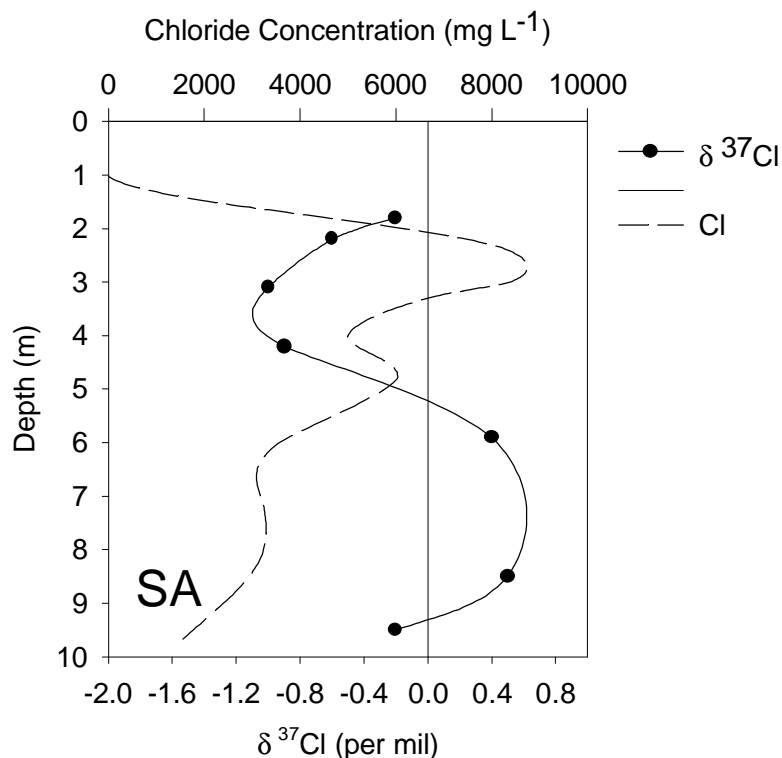


Figure 6-19. Measured $\delta^{37}\text{Cl}$ profile, with the chloride porewater concentration profile for comparison, from the SA Trans-Pecos core.

6.5. Chloride Mass Balance Application

Chloride mass balance calculations for the Trans-Pecos cores assume a constant chloride flux at the surface of $80 \text{ mg Cl m}^{-2} \text{ yr}^{-1}$, which includes the contribution from both wet and dry deposition [Scanlon, 1991]. The total amount of accumulated chloride is reasonably consistent among 3 of the 7 profiles and corresponds to the timing of the most recent major climate transition in the southwestern U.S. at 10-15 ka [Phillips, 1994]. The profiles from SA, DA and GD

yield total chloride ages of 15.4 kyr, 14.9 kyr, and 12.2 kyr, respectively (Figure 6-20). In contrast, the large chloride inventory measured in the GS core signifies a chloride mass balance age of 32 kyr. Either the chloride inventory in the GS core actually reflects 32 kyr of solute retention, well beyond the Last Glacial Maximum, or is an artifact of some CMB assumption violation. Considering the close proximity of the GS core to the GD and DA cores that yield much younger ages that agree well with regional paleoclimate and paleovegetation records, the 32 kyr apparent CMB age seems unlikely. Alternative explanations for the anomalously high chloride inventory in the GS core include: 1) a net surface water (and chloride input) that exceeds the areal average by about two times, 2) an input of chloride from the dissolution of evaporite minerals within the matrix, 3) a large fraction of immobile high chloride concentration porewater, and 4) a systematic analytical error. Replicate samples were analyzed later, and the results compared well with the original chloride values, thereby reducing the probability of an analytical error explanation. The DA and GD cores contain similar lithology to GS but do not contain the anomalously high chloride inventory measured in the GS core. Given the close proximity and lithology of all three cores, arguments invoking evaporite dissolution and immobile chloride possess weak foundations. Furthermore, the very uniform Cl:Br ratio measured throughout the GS core that is similar to the regional value of precipitation, convincingly rules out chloride derivation from another source besides atmospheric deposition. A chloride deposition rate that is twice that of the local average appears to be the most plausible explanation for the high chloride inventory in the GS core. This explanation implies that run-on has exceeded run-off by an average of two times

for thousands of years. The geomorphic location of the GS site provides some support for this contention. The GS site is positioned at the toe of a gradual slope. The DA site lies at the top of the raised area and the GD site lies further away from the slope. Of the three locations, the GS location is the most likely to be influenced by run-on. If run-on is the explanation, then the average chloride deposition is $160 \text{ mg m}^2 \text{ yr}^{-1}$, which is double the estimated atmospheric deposition.

On the other end of the spectrum, low chloride inventories measured in the SB, JA and JB cores, correspond to chloride ages of 470, 225 and 125 yr, respectively, and suggest relatively recent flushing.

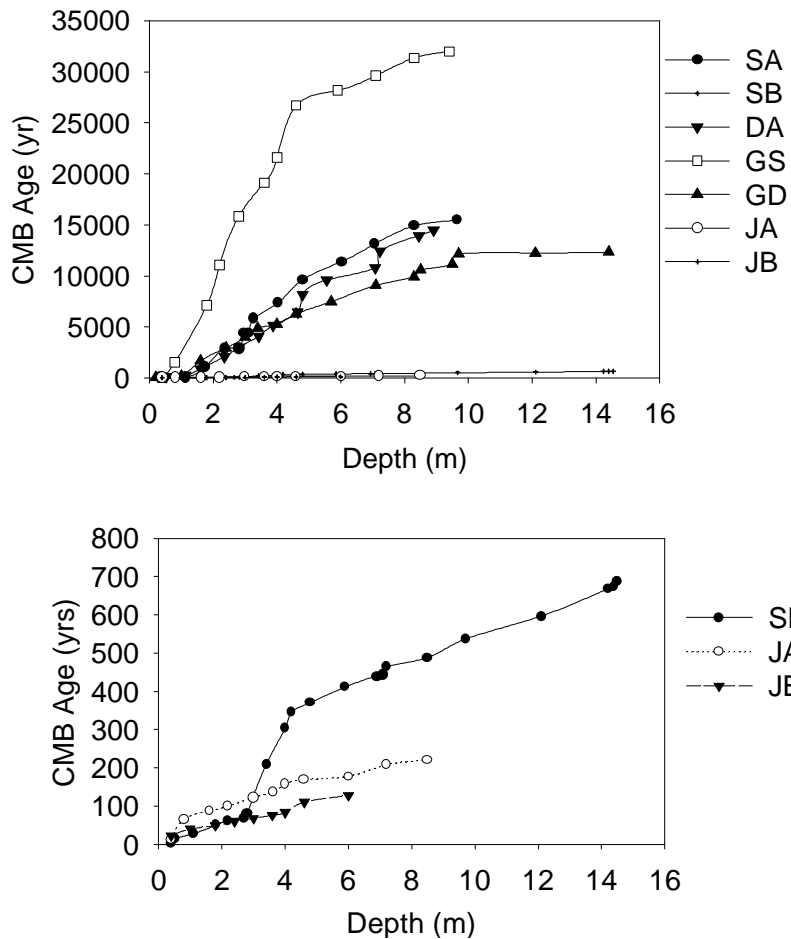


Figure 6-20. Graph of apparent chloride mass balance age with profile depth from the Trans-Pecos cores.

6.6. Nitrogen Fluxes

Nitrogen fluxes passing the root zone for the Trans-Pecos cores are calculated based on the amount of NO_3^- -N amassed in the core within the upper 10 m and the chloride mass balance age of the core at 10 m (Table 6-3). Vertical integration of the NO_3^- -N concentration profiles yields the accumulated nitrogen mass per area. Calculated NO_3^- -N accumulation rates range widely, from 0.8 to 36.9 $\text{mg m}^{-2} \text{yr}^{-1}$. The shallowest sample from SB contains a high NO_3^- -N concentration which is omitted for the purposes of calculating NO_3^- -N loss from the root zone. Still, the calculated NO_3^- -N flux for the SB core is much higher compared to the fluxes calculated for the other cores that fall below 4 mg NO_3^- -N $\text{m}^{-2} \text{yr}^{-1}$. NADP data from Panther Junction in Big Bend National Park, located southeast of the Miller Ranch and McKeel study site, indicates that ammonium and nitrate each comprise about 50 % of the total inorganic nitrogen deposition. Annual inorganic nitrogen wet deposition varies from 50 to 150 $\text{mg m}^{-2} \text{yr}^{-1}$, with a mean of about 110 $\text{mg m}^{-2} \text{yr}^{-1}$ over the past 20 years on record [NADP/NTN, 2001; <http://nadp.sws.uiuc.edu/>] (Figure 6-21).

The presence of notable quantities of accumulated NO_3^- -N implies that desert vegetation, both shrubs and grasses, at the Trans-Pecos sites does not use all of the NO_3^- -N in the root zone and consequently, periodically leaches through the root zone where it is slowly transported by diffusion. The NO_3^- -N flux measured beneath the creosote on the Miller Ranch is three to four times lower than the NO_3^- -N fluxes measured beneath the grassland sites, perhaps due to differences in seasonal patterns of nutrient uptake between grasses and shrubs [Jobaggy and Jackson, 2001]. The

NO_3^- -N flux measured beneath the creosote on the Miller Ranch is also three times lower than the NO_3^- -N fluxes measured beneath desert scrub at the McKeel site. The higher amount of available water in the root zone at the Miller Ranch compared to the McKeel site may result in a relatively lower water limitation and a more favorable environment for nutrient uptake.

TRANS-PECOS CORE	SA	SB	DA	GS	GD
CMB age at 10 m depth (yr)	15,500	470	15,000	32,000	12,200
	NO_3^--N (g m^{-2})				
Depth Interval					
(0.0 – 2.0 m)	0.01	13.96	1.73	0.03	1.18
(2.0 - 4.0 m)	19.4	2.9	7.2	29.7	11.3
(4.0 - 6.0 m)	11.6	4.1	1.7	30.7	10.3
(6.0 – 10.0 m)	5.6	3.4	1.5	30.1	20.0
(0 - 10.0 m)	36.6	24.3	12.1	90.6	42.8
Calculated NO_3^--N flux ($\text{mg m}^{-2} \text{yr}^{-1}$)	2.4	36.9*	0.8	2.8	3.5

* excluding surface sample

Table 6-3. Calculated chloride mass balance ages, measured accumulated nitrogen and calculated nitrogen fluxes for the Trans-Pecos cores.

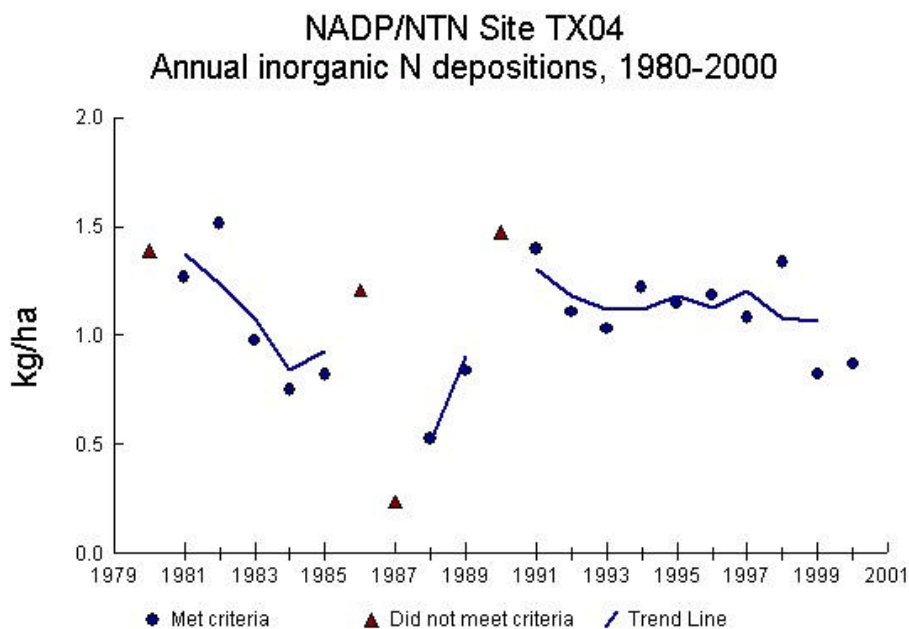


Figure 6-21. Graph of annual inorganic N deposition based on 20 years of data from Panther Junction, Big Bend National Park, Texas [NADP/NTN, 2001; <http://nadp.sws.uiuc.edu/>]. $1 \text{ kg ha}^{-1} = 100 \text{ mg m}^{-2}$.

6.7. Comparison of Nitrogen Fluxes at Case Study Sites 1 and 2

Calculated nitrogen losses from the root zone at the Nevada Test Site located in the northern Mojave Desert site exceed those calculated for the Trans-Pecos sites by several orders of magnitude. Yet, the input of inorganic N through atmospheric deposition is slightly higher over the Trans-Pecos region than over southern Nevada. Several factors favor nitrogen losses past the root zone at the NTS over the Trans-Pecos region including seasonal precipitation patterns and vegetation density. The Nevada Test Site receives ~50 % of its precipitation during the winter months when potential evapotranspiration is lowest. In contrast, the Trans-Pecos region receives ~70 % of its precipitation during the summer monsoons when potential evapotranspiration is highest [Schmidt, 1979]. The higher percentage of winter

precipitation favors the likelihood of solute leaching through the root zone at the NTS. Also, the NTS sustains a much lower vegetation density, at present, than the Trans-Pecos sites resulting in a lower potential for nitrogen uptake by plants. Yet another potentially important factor favoring elevated nitrogen levels at the NTS over the Trans-Pecos sites includes the presence of nitrogen-fixing microbiotic crusts, a source of additional N input, at the NTS. Microbiotic crusts are absent at the sample locations in the Trans-Pecos region. Previous studies suggest that crusts can be the dominant source of fixed N in semiarid ecosystems [Evans and Ehleringer, 1993]. The NTS location harbors relatively ideal conditions for microbiotic crustal growth including a sandy loam surface soil texture, abundant bare interspace patches, minimal compressional disturbance, an average annual temperature near the optimal temperature range for growth (51-61 °C) [Johnston, 1997]. In contrast, the Trans-Pecos sites contain one or more of the following elements that prevent significant crustal development: rocky surface soil texture (e.g. SA, SB, DA, JA, and JB), considerable compressional disturbances by human and livestock activity (GD, GS, DA), and minimal barespaces (GD, GS). It is difficult to assess to what extent the presence of nitrogen-fixing microbiotic crusts accounts for the distinctly different amounts of nitrogen losses past the root zone between the two study sites, particularly since nitrogen fluxes resulting from microbiotic crusts range from $< 10 \text{ mg m}^{-2} \text{ yr}^{-1}$ to $4000 \text{ mg m}^{-2} \text{ yr}^{-1}$ [West and Skujins, 1978; Evans and Ehleringer, 1993; Johnston, 1997]. Hartsough et al. [2001] report the input of nitrogen from fixation by algae and lichen communities at the soil surface to be bounded between $10 \text{ mg m}^{-2} \text{ yr}^{-1}$ and 110

mg m⁻² yr⁻¹ at the Yucca Flat site based on previous studies conducted in the northern Mohave Desert near playas [*West and Skuijins, 1978*].

6.8. DASH Model Application

Data interpretation regarding the Trans-Pecos cores employs the Deep Arid System Hydrodynamic (DASH) conceptual model described in Chapter 3. Numerical simulations using FEHM complement a qualitative comparison and chloride mass balance analytical approach. Model simulations are limited by the vertical extent (10-15 m total depths) of the collected data, but are nonetheless useful in constraining moisture fluxes and hydrologic histories.

Average measured soil parameters including ψ - θ measurements are used to develop soil moisture characteristic curves as model input. The soil textures for cores SA, SB, JA, and JB are homogeneous sandy loams (Figure 6-22). Three units including a sandy loam, a silty clay, and clay characterize the layered soil profile associated with the DA, GD, and GS cores (Figure 6-23). Model input values associated with each core are listed in Table 6-4. The matric potential at the bottom boundary (water table) is fixed at 0.1 MPa for all simulations. An average geothermal gradient of 35 °C km⁻¹ is established by specifying temperatures at the top and bottom boundaries. Specified surface temperatures of 21 °C for the McKeel site and 16 °C for the Miller Ranch sites are the mean annual air temperatures recorded for Presidio, Texas and Valentine, Texas, respectively. Table 6-5 lists the initial and time-varying boundary conditions for the Trans-Pecos simulations. The initial chloride profile consists of a uniform porewater concentration of 8 mg L⁻¹. This

value is relatively arbitrary due to the lack of deep chloride profile data, but has little effect on the model results. A prescribed solute flux of $80 \text{ mg m}^{-2} \text{ yr}^{-1}$ at the surface boundary simulates continuous atmospheric chloride deposition. Simulations pertaining to the McKeel site address the distribution of chlorine-37 in the porewater. Initial concentrations and input concentrations of $\delta^{37}\text{Cl}$ ‰ are prescribed to be 0‰. At the McKeel site, the annual precipitation prescribed is 275 mm, with an effective chloride concentration of 0.29 mg L^{-1} . For the Miller Ranch sites, the annual precipitation specified is slightly higher at 350 mm, with an effective chloride concentration of 0.23 mg L^{-1} . Initially, the modeled systems maintain a steady-state, uniform downward liquid flux (Table 6-5), representative of a past wetter climate. Transitions to a drier climate and the establishment of xeric vegetation are simulated by either reducing effective infiltration or by specifying a negative matric potential (ψ) at the base of the root zone (2-4 m depth) to represent the effect of water-efficient desert vegetation.

In order to match the measured matric-potential and chloride profiles, the timing of xeric transitions are varied within ranges considered reasonably consistent with independent paleoclimate and paleovegetation records. The surface boundary conditions given in Table 6-5 and effective chloride diffusion coefficients provided in Table 6-4 produce solutions that best match the observed data. The diffusion coefficient ratio of ^{35}Cl to ^{37}Cl used in the SA core simulations is 1.0023, taken from *Eggenkamp* [1997]. Effective chloride diffusion coefficients for the Trans-Pecos cores range from 6×10^{-12} to $3 \times 10^{-10} \text{ m}^2 \text{ s}^{-1}$. These value fall within the distribution

of experimentally determined chloride diffusion coefficients [Conca and Wright, 1992; Schaefer et al., 1995] for the range of corresponding moisture contents.

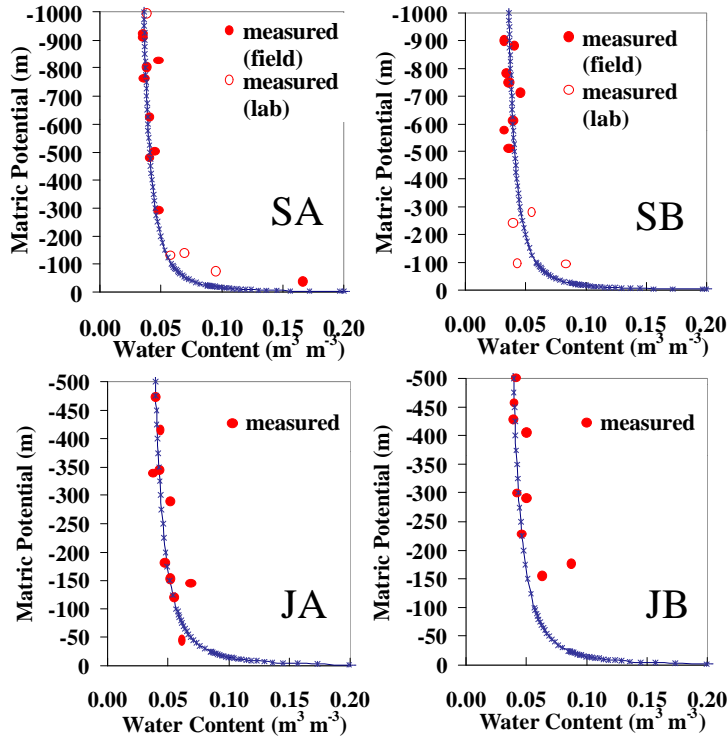


Figure 6-22. Soil moisture characteristic curves developed from field and lab measurements in the SA, SB, JA and JB cores. van Genuchten curve-fitted parameters are reported in Table 6-4.

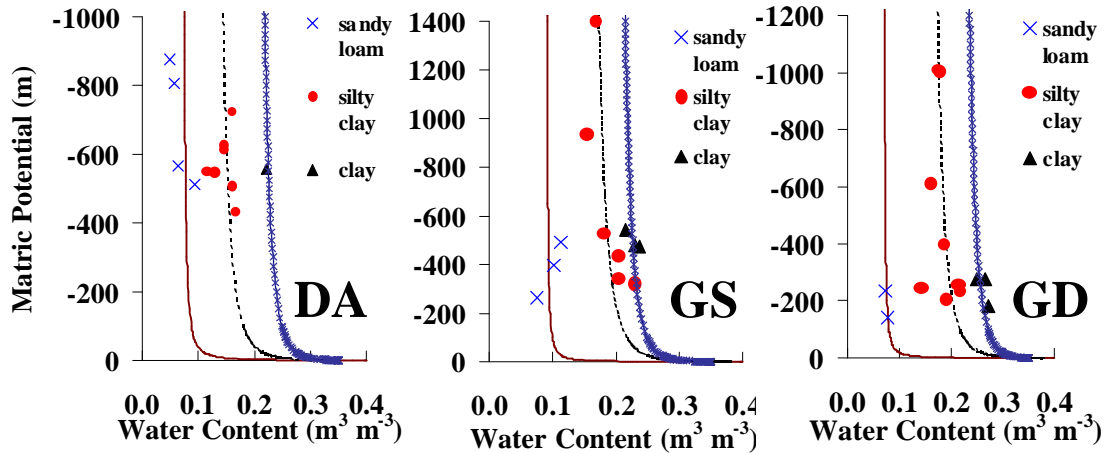


Figure 6-23. Soil moisture characteristic curves developed from field condition measurements in the layered DA, GS and GD cores. van Genuchten curve-fitted parameters are reported in Table 6-4.

	SA/SB Sandy loam	DA/GS/GD Sandy loam	DA/GS/GD Silty clay	DA/GS/GD Clay	JA/JB Sandy loam
Porosity [unitless]	0.47	0.42	0.35-0.39	0.36	0.47
Saturated permeability [m ²]	1 x 10 ⁻¹¹	1 x 10 ⁻¹²	1 x 10 ⁻¹⁴	1 x 10 ⁻¹⁵	1 x 10 ⁻¹¹
van Genuchten α^1 [m ⁻¹]	2.5	2.0	1.0	0.4-0.8	2.5
van Genuchten n ¹ [unitless]	1.40	1.55-1.65	1.20-1.22	1.10-1.16	1.42
Residual saturation	5.5 %,	16 %	28-31%,	30-42 %,	5 %,
Maximum saturation	97 %	95 %	95 %	90 %	98 %
Geothermal grad. [°C km ⁻¹]	35	35	35	35	35
Water table depth [m]	100	75	75	75	30
Root zone depth	3	3 /1.5 [§]	3 /1.5 [§]	3 /1.5 [§]	2
Effective diffusion coefficient [m ² s ⁻¹]*	7 x 10 ⁻¹¹	3 x 10 ⁻¹⁰	3 x 10 ⁻¹⁰	3 x 10 ⁻¹⁰	NA
Saturated diffusion coefficient [m ² s ⁻¹]	7 x 10 ⁻¹¹	3 x 10 ⁻¹⁰	3 x 10 ⁻¹⁰	3 x 10 ⁻¹⁰	NA

¹ unsaturated soil fitting parameters described in *van Genuchten* [1980]

[§] first value pertains to DA shrub rooting depth ; second value pertains to GD and GS grass rooting depth

*determined through iterative solute transport modeling to match chloride profiles

Simulations were also run using the *Conca and Wright* [1992] diffusion coefficient function (Figure 3-3) as a replacement for a constant effective diffusion coefficient.

Table 6-4. Input parameters for Trans-Pecos site-specific simulations.

SA	Time	~16* ka	16- 6 ka	6 – 0 ka
Climate/		Mesic/	Semiarid/	Arid/
Vegetation		Woodland	Xeric Woodland	Desert Scrub
Upper Boundary Condition		$q = 10 \text{ mm yr}^{-1}$	$q = \sim 0 \text{ mm yr}^{-1}$	$\psi_{rz} = -900 \text{ m}$

GD, GS	Time	~16* ka	16- 1 ka	1 – 0 ka
Climate/		Mesic/	Semiarid/	Semiarid/
Vegetation		Woodland	Xeric Woodland – Grassland	Grassland
Upper Boundary Condition		$q = 10 \text{ mm yr}^{-1}$	$q = \sim 0 \text{ mm yr}^{-1}$	$\psi_{rz} = -500 \text{ to } -200 \text{ m}$

DA	Time	~16* ka	16- 1 ka	1 – 0.1 ka	0.1 – 0 ka
Climate/		Mesic/	Semiarid/	Semiarid/	Semiarid/
Vegetation		Woodland	Xeric Woodland – Grassland	Grassland	Desert scrub
Upper Boundary Condition		$q = 10 \text{ mm yr}^{-1}$	$q = \sim 0 \text{ mm yr}^{-1}$	$\psi_{rz} = -500 \text{ m}$	$\psi_{rz} = -700 \text{ m}$

ψ_{rz} – fixed matric potential at the base of the root zone

q – downward soil-water flux

Table 6-5. Simulation histories and associated surface boundary conditions that best match profile data from the Trans-Pecos cores.

6.9. Interpretation of Trans-Pecos Vadose Zone Profiles

6.9.1. McKeel Desert Scrub Site

6.9.1.1. Matric Potential

Measured profiles from the SA core collected at the McKeel desert scrub site adhere well to the DASH conceptual framework. Accordingly, FEHM model simulations using the DASH concept produce results that match the data. The model-generated matric potential profiles are shown for the transition to a drier climate at 16 ka, the transition to Chihuahuan desert scrub at 6 ka and the present day (Figure 6-24). The matric potential profile development age of 6 kyr matches the observed profile data and concurs well with the timing of desertscrub establishment as constrained by local packrat midden data. Recall that the transition to desert scrub

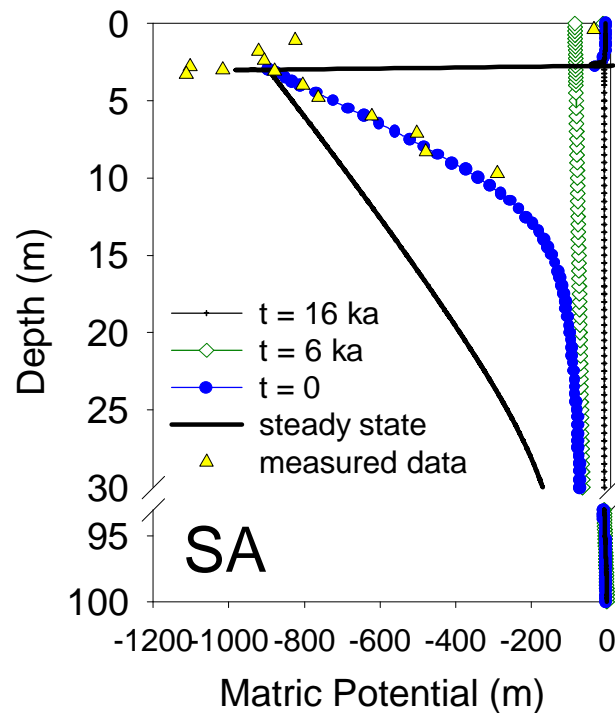


Figure 6-24. Model-simulated matric potential profiles developed over time in response to climate/vegetation transitions at McKeel site. The $t = 0$ profile represents the present conditions.

occurred between 8 ka and 4 ka at the elevation and location of the McKeel site [*Van Devender, 1986*]. Also shown in Figure 6-24 for comparison is the model-predicted profile at steady state under the present surface boundary condition. The steady-state matric potential profile differs significantly from the measured profile indicating the transient state of the current conditions. It is this transient characteristic that enables us to resolve the 6 kyr duration for profile development.

6.9.1.2. Chloride

The model-generated chloride profiles are shown for times corresponding to those shown for the matric potential profiles (Figure 6-25). The present day simulated chloride profile reasonably reproduces the observed chloride profile. The chloride bulge results from 16 kyr of shallow accumulation. The chloride-mass-balance age depth distribution for the SA measured profile compares favorably with the model-simulated profile (Figure 6-26). Under the imposed xeric conditions from 16 ka to the present, solute diffusion is the main mechanism of chloride transport. Chloride diffuses downward from the surface aided, to a very small degree, by a small downward advective flux from 16 ka to 6 ka. Then, from 6 ka to the present, chloride diffuses below the root zone counter to a small upward advective flux.

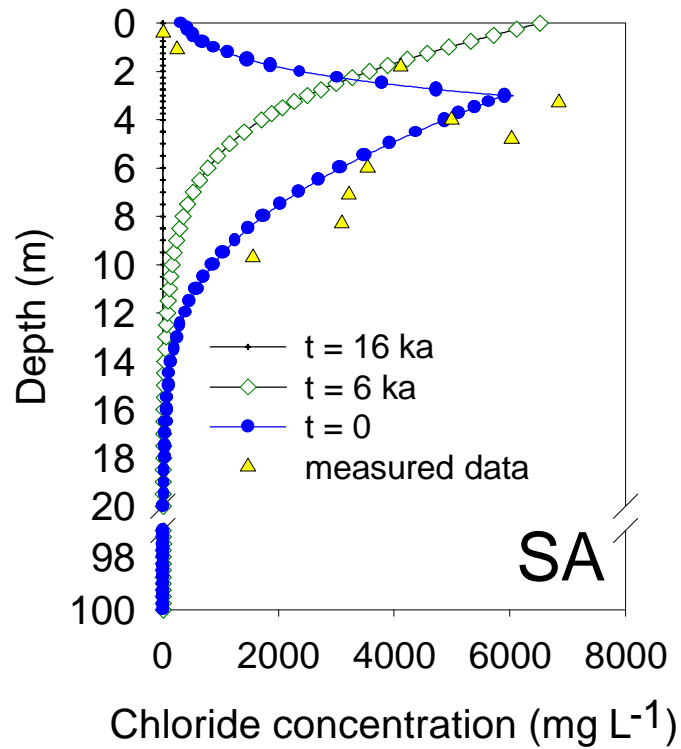


Figure 6-25. Model-simulated chloride profiles developed over time in response to climate/vegetation transitions at the McKeel site. The $t = 0$ profile represents the present. Chloride values are porewater concentrations.

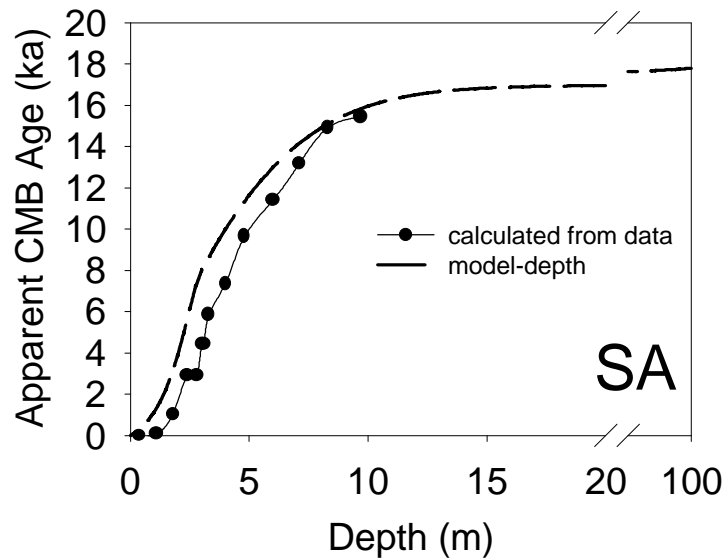


Figure 6-26. Apparent chloride-mass-balance age (CMB) distribution for the SA measured profile compared with the model-simulated profile.

6.9.1.3. Current Moisture Fluxes

The model-simulated moisture flux profiles for the SA core illustrate the transient hydraulic regime (Figure 6-27). First, it is important to emphasize the very small magnitude of all fluxes, both liquid and vapor, in the SA core from the base of the root zone to the water table. Upward liquid and vapor fluxes, driven by the high matric potential gradient, dominate from the depth just below the root zone to about 30 meters. The relative contribution of vapor and liquid flux in this region is predominately dependent upon the hydraulic properties of the soil. Below about 40 meters, the upward geothermally-driven vapor flux controls the hydraulic regime. Within this same interval, but excluding a narrow capillary zone above the water table, the direction of the liquid flux is downward and extremely small.

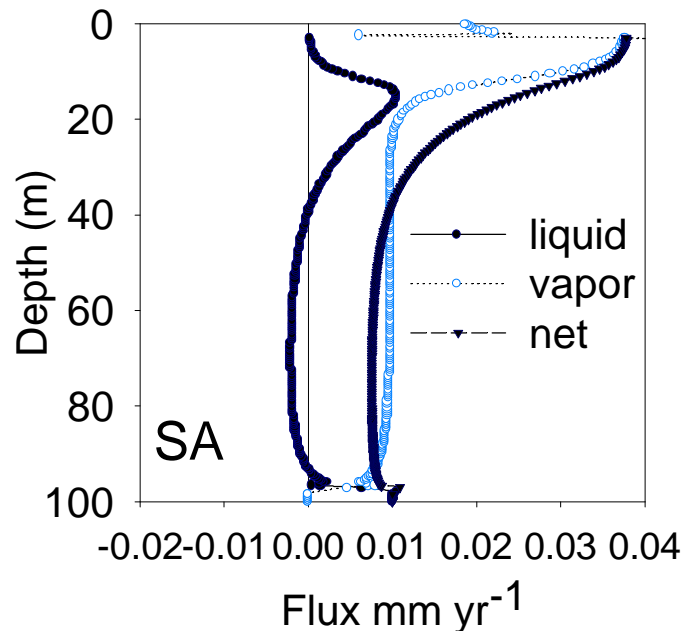


Figure 6-27. Model-predicted moisture flux profiles at $t = 0$ (the present) at the McKeel desert scrub site. Negative values indicate downward fluxes; positive values indicate upward fluxes.

The net moisture flux, as simulated by the model, is upward throughout the region extending from the base of the root zone to the water table. As such, the current recharge at the SA site is actually negative, or can be considered as discharge. The model-predicted upward moisture flux across the water table is about 0.01 mm yr⁻¹, which is essentially equivalent to the thermal vapor flux for the SA site at the depth of the water table. At the saturated zone – vadose zone interface, groundwater is evaporating above the water table to source the geothermal vapor flux.

6.9.1.4. Chlorine-37

The model-predicted $\delta^{37}\text{Cl}$ profile for the SA core indicates a significant fractionation effect that propagates to a depth of about 50 meters (Figure 6-28). Preferential diffusion of the lighter isotope from the near surface results in an isotopic enrichment near the surface of up to +2 ‰ and isotopic depletion below about 5.5 meters. The maximum isotopic depletion peaks at a depth of about 23 meters at a value of $\delta^{37}\text{Cl}$ -5.5 ‰. The observed data extends only to 10 meters, the total depth of the SA core. Within the upper 10 meters, the model predicts a $\delta^{37}\text{Cl}$ range of -2.3 ‰ to +1.4 ‰. The measured $\delta^{37}\text{Cl}$ values show a narrower margin, ranging from -1.0 ‰ to 0.5 ‰. In addition to the poor agreement between the amount of fractionation predicted by the model and observed in the SA core, the depth intervals of enrichment and depletion do not match. In fact, the model-predicted and observed profiles almost resemble mirror images of each other: the model predicts isotopic enrichment above 5.5 m where depleted values are observed, and the model predicts isotopic depletion below 5.5 m where some slightly enriched values are observed.

Considerations regarding surface transients, mentioned in section 6.4.6, are probably responsible for the lack of agreement between the model predicted $\delta^{37}\text{Cl}$ profile and the observed data.

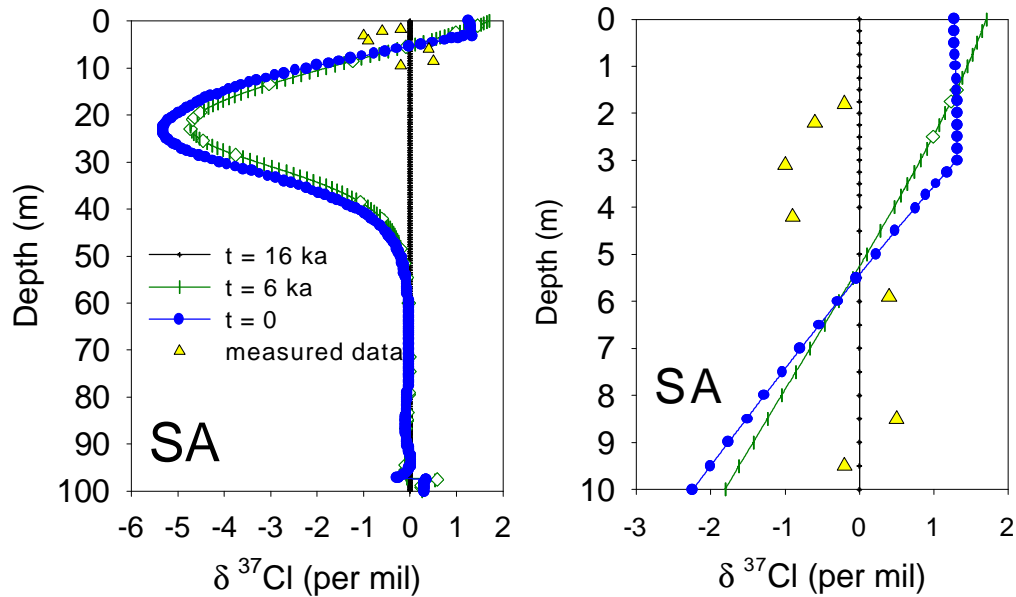


Figure 6-28. Model-simulated $\delta^{37}\text{Cl}$ profiles developed over time in response to climate/vegetation transitions at the McKeel site. The $t = 0$ profile represents the present. The left graphs shows the entire 100 m thick vadose zone at SA and the right graph focuses in on the upper 10 meters of the profile.

6.9.1.5. Evidence of Isolated Flushing

The DASH conceptual model does not explain the corresponding matric potential and chloride profiles collected from the SB core located 32 meters away from the SA core. The matric potential profile measured at SB strongly mimics the SA profile. Accordingly, the SB profile records 6 kyr of drying (upward fluxes in the upper vadose zone below the root zone) as indicated by SA modeling results. In contrast, the SB chloride inventory records a total of 660 years of accumulation within its length of 15 meters, thereby suggesting relatively recent flushing of the

profile. The flushing episode would have wiped out the very negative matric potentials throughout the profile. Attempts to reconcile the data from the SB core would require adding two spatial dimensions to the flow model. The SB core may represent an isolated flow conduit that was last activated about around 700 years ago. The flushing episode effectively leached the chloride to at least 15 m, the depth of the collected profile. The wetting episode would have also dramatically affected the matric potentials, significantly increasing their values. However, lateral radial drying during the past 700 years may have resulted in re-establishing the matric potential profile at SB to resemble profiles from the surrounding area that reflect 6 kyr of development influenced by the DASH xeric condition.

6.9.2. Miller Ranch Grassland - Creosote Ecotone Sites

6.9.2.1. Matric Potential

Measured matric potential profiles from the GD, GS, and DA cores collected at the Miller Ranch grassland-creosote ecotone sites are difficult to reconcile using the DASH conceptual framework. FEHM model simulations using the DASH concept produce results with mixed agreement to observed data. Model results for the Miller Ranch grassland-creosote ecotone sites are considered less robust than for the McKeel site, but nonetheless, useful for shaping the data interpretation.

The model-generated matric potential profiles are shown for the transition to a drier climate at 16 ka, the transition at 1 ka and the present day for two fixed root-zone matric potential conditions (Figure 6-29). Also shown in Figure 6-29 are the matric potential profiles at steady state with the prescribed root-zone conditions. The left graph illustrates the profiles resulting from a fixed root-zone matric potential

value of -500 m. The right graph illustrates the profiles resulting from a fixed root-zone matric potential value of -250 m. The model supplies a poor fit to the observed profile data regardless of the magnitude of root-zone matric potential condition or the development time. In addition to the poor agreement, the steady-state matric potential profile differs only slightly from the model-predicted profile that develops after 1 kyr. This precludes constraining the required duration for profile development. Similar difficulties are encountered using data from the GS and DA cores, which show greater deviation between observed and modeled matric potential profiles. Perhaps the most appropriate use of the matric potential data is a qualitative comparison of the profiles taken along the grassland-creosote ecotone.

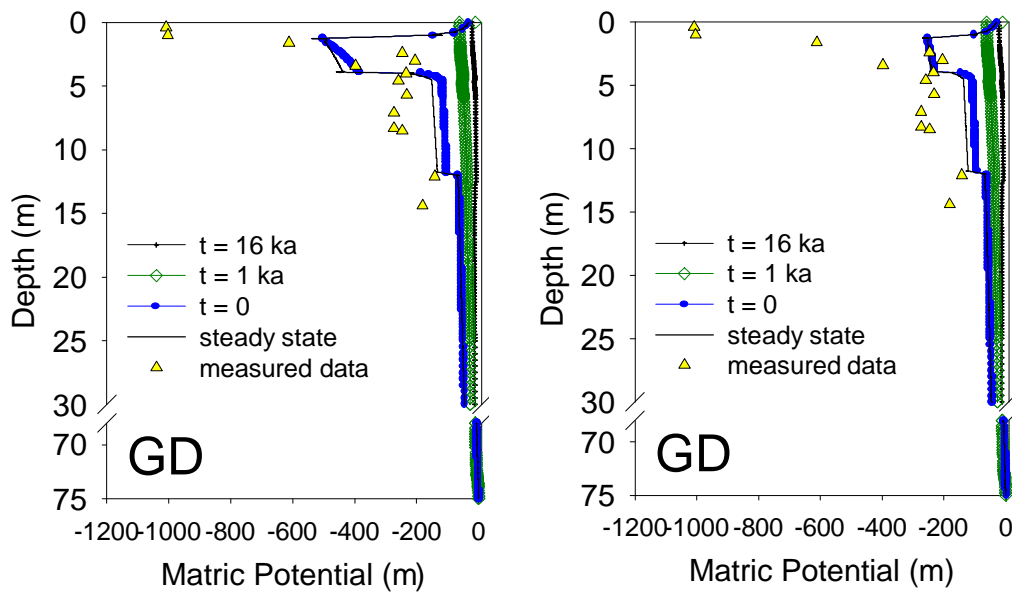


Figure 6-29. Model-simulated matric potential profiles developed over time in response to climate/vegetation transitions at the GD Miller Ranch site for fixed root-zone matric potential values of -500 m (left) and -250 m (right).

The measured matric potentials along the grassland - creosote ecotone at the Miller Ranch site show a distinctive trend in increasingly negative values along the grassland - creosote continuum, with the exception of the upper 2 meters (Figure 6-

30). Lithology alone cannot explain this trend. The soil textures in the three profiles below about 3 meters is relatively consistent and shows no apparent correlation with the observed trend in matric potentials. The lithology of the DA profile differs notably from the GD and GS cores only in the upper 3 meters where a sandy loam texture describes the soil at DA. Therefore, the trend of increasingly negative matric potentials along the grassland-creosote ecotone is probably strongly correlated with vegetation type. Contrasts in rooting depth, phenology and photosynthetic pathways among the vegetation species present along the grassland-creosote ecotone may contribute to the observed matric potential trend [Pockman and Sperry, 2001]. Factors associated with creosote that favor deeper drying under creosote than grasses include a deeper rooting depth and the possibility of all-season growth. Grasses may support drier conditions in the upper meter of soil, but maintenance of these very negative potentials is limited to their growing season during the late summer. To a first approximation, the vegetation factors cited above seem to explain the matric potential trend. Yet, this argument raises the paradoxical issue concerning the feedback of vegetation and soil moisture. Vegetation type strongly influences the soil moisture regime and the soil moisture regime plays a major role in dictating vegetation type. Why has creosote successfully invaded the area at the DA site, but not at the nearby GS and GD sites? At the Miller Ranch grassland-creosote ecotone, it is relatively apparent that near-surface soil texture plays a major role in the spatial distribution of successful encroachment by creosote. The coarse surface soil texture at the DA site enables deeper drainage through the root zone, favoring shrub invasion. In contrast, the fine soil texture at the GS and GD sites prevents deep drainage,

encourages ponding and shallow retention favoring the continued success of grasses. However, this site-specific explanation does not fully address or reconcile the paradoxical interplay between vegetation type and soil moisture regimes. This issue requires a much more detailed research initiative focused on answering this question.

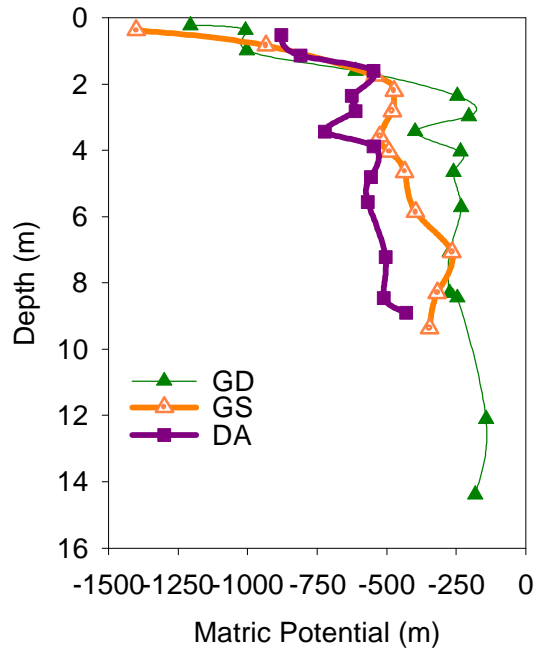


Figure 6-30. Measured matric potential profiles at the Miller Ranch grassland – creosote ecotone site. GD = pure grassland site; GS = site near grassland – shrub transition; DA = encroached creosote site.

6.9.2.2. Chloride

Similar to the matric potential profiles, interpretation of the chloride profiles measured at the Miller Ranch grassland - creosote ecotone requires a combination of approaches. FEHM model simulations using the DASH concept produce results with relatively good agreement to observed data.

The model-generated chloride profiles for the GD core are shown for the transition to a drier climate at 16 ka, the transition at 1 ka and the present day (Figure

6-31). The present day chloride profile reasonably reproduces the observed chloride profile. The chloride distribution results from 16 kyr of shallow accumulation. The chloride mass balance age depth distribution for the GD measured profile compares favorably with the model-simulated profile (Figure 6-32). Under the imposed xeric conditions from 16 ka to the present, solute diffusion is the main mechanism of chloride transport. The model-predicted profile corresponding to the present time shows propagation of the shallow chloride diffusion to a depth of about 12 meters.

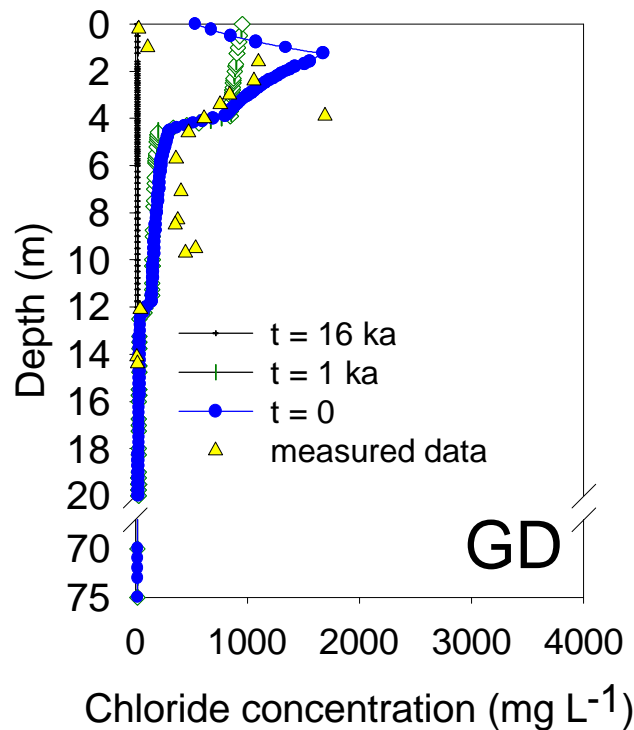


Figure 6-31. Model-simulated chloride profiles developed over time in response to climate/vegetation transitions at the GD Miller Ranch site. Chloride profiles were simulated using a moisture-dependent diffusion coefficient [Conca and Wright, 1992]. Chloride values are porewater concentrations.

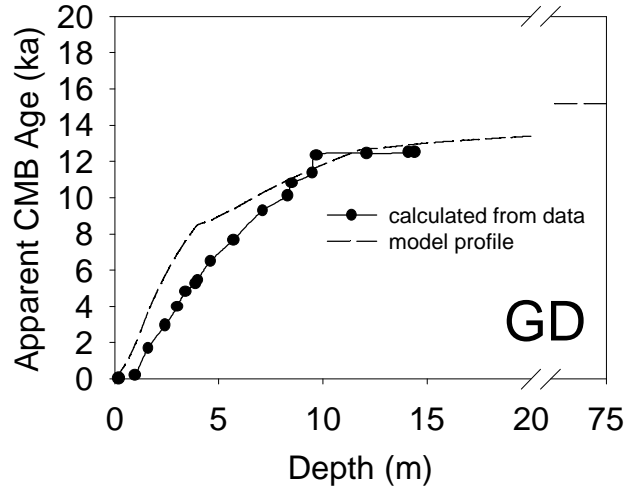


Figure 6-32. Apparent chloride-mass-balance (CMB) age distribution for the measured GD profile compared with the model-simulated profile.

The model-generated chloride profiles for the GS core are shown for the transition to a drier climate at 16 ka, the transition at 1 ka and the present day (Figure 6-33). The left graph illustrates simulations completed using the *Conca and Wright* [1992] moisture-dependent diffusion coefficient function (Figure 3-3). In comparison, the right graph illustrates simulations produced using a constant effective diffusion coefficient of $3 \times 10^{-10} \text{ m}^2 \text{ s}^{-1}$. Clearly, the present day chloride profile simulated using the variable diffusion coefficient (left) produces a better fit to observed data than does the chloride profile simulated using a constant diffusion coefficient (right). The comparison clearly demonstrates the importance of using a moisture-dependent diffusion coefficient relationship when modeling soil profiles that consist of a variety of soil textures.

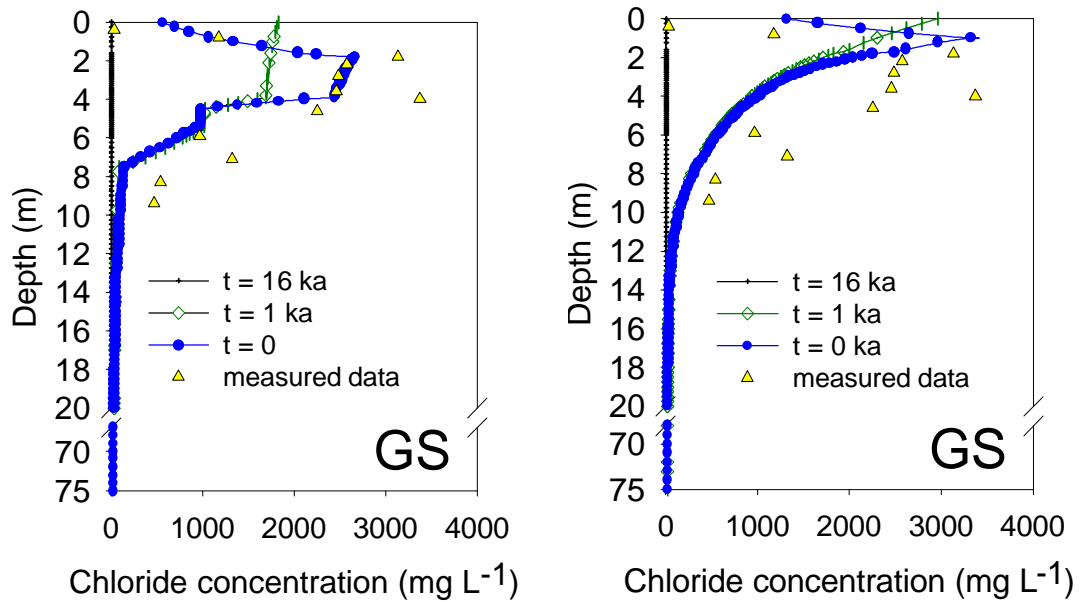


Figure 6-33 . Model-simulated chloride profiles developed over time in response to climate/vegetation transitions at the GS Miller Ranch site. Chloride profile simulations shown on the left were produced using a moisture-dependent diffusion coefficient [Conca and Wright, 1992]. Chloride profile simulations shown on the right were produced using a constant effective diffusion coefficient. Chloride values are porewater concentrations.

Model simulations to reproduce the measured chloride profile at GS require a chloride deposition equivalent that is double the estimated atmospheric deposition value of $80 \text{ mg m}^{-2} \text{ yr}^{-1}$. Justification for a value higher than the estimate is given in section 6.5. The chloride-mass-balance age depth distributions for the GS measured profile compare favorably with the model-simulated profiles (Figure 6-34). The top graph shows the “uncorrected” interpretation assuming a chloride deposition of $80 \text{ mg m}^{-2} \text{ yr}^{-1}$, and the bottom graph illustrates the “corrected” interpretation assuming a chloride deposition of $160 \text{ mg m}^{-2} \text{ yr}^{-1}$.

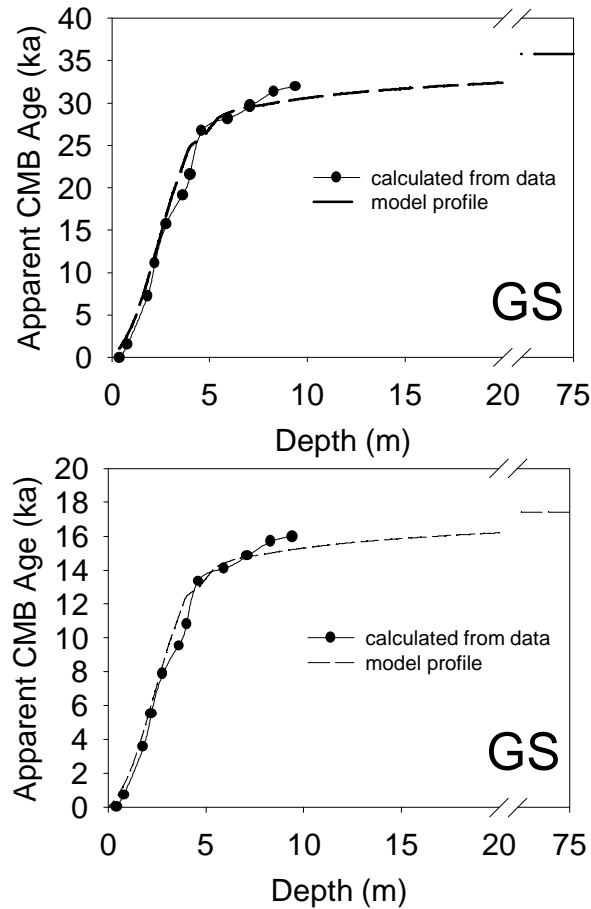


Figure 6-34. Apparent chloride-mass-balance (CMB) age distribution for the GS measured profile compared with the model-simulated profile. Calculations used for the upper graph assume a chloride deposition of $80 \text{ mg m}^{-2} \text{ yr}^{-1}$, whereas calculations used for the lower graph assume a chloride deposition of $160 \text{ mg m}^{-2} \text{ yr}^{-1}$.

The broad characteristic of the measured chloride bulge at the DA site is challenging to reproduce numerically using the DASH conceptual model. Also, the measured profile extends only to 10 meters and does not capture the entire chloride bulge, which significantly limits the interpretation. The model-generated chloride profiles for the DA core are shown for the transition to a drier climate at 16 ka, the transition at 1 ka and the present day (Figure 6-35). The present-day model chloride profile produces a reasonable fit to the data to a depth of 5 meters and a relatively poor fit to the data below 5 meters. The model does not capture the high chloride

concentrations observed within the depth interval of 5 to 9 meters. Likewise, the chloride-mass-balance age depth distribution for the DA measured profile compares favorably with the model-simulated profile to a depth of about 7.5 meters, below which the CMB from the model profile under-predicts the chloride age estimated from the DA chloride data (Figure 6-36). Poor agreement between the chloride model profile and the DA measured chloride profile derives from the limitation of FEHM in prescribing one value for the residual water content below which diffusion is negligible. This residual water content limiting diffusion applies to all lithologic units. Yet, within the spectrum of soil textures observed at the Miller Ranch grassland – desert scrub ecotone site, the residual water contents vary considerably (Table 6-4). I hypothesize that prescribing a unique diffusion-limiting residual water content for each soil texture would greatly improve the model fits to the observed data.

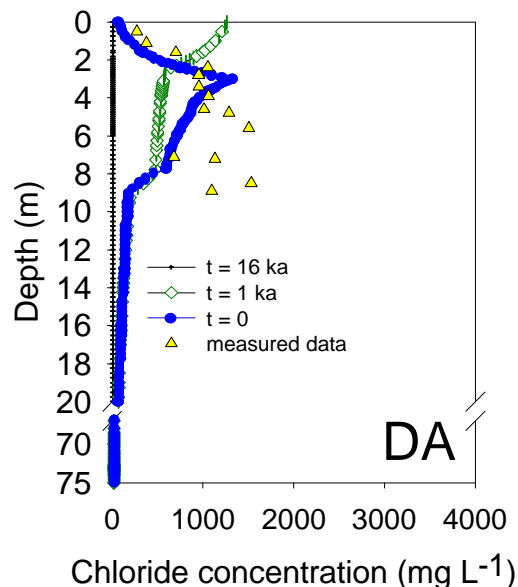


Figure 6-35 . Model-simulated chloride profiles developed over time in response to climate/vegetation transitions at the DA Miller Ranch site. Chloride values are porewater concentrations.

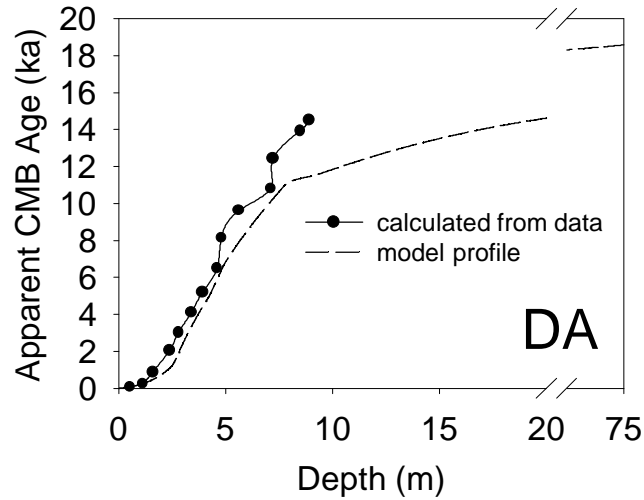


Figure 6-36. Apparent chloride mass balance (CMB) age distribution for the DA measured profile compared with the model-simulated profile.

6.9.3. Juniper Stand Site

The chloride profiles measured beneath the juniper stand show relatively low chloride accumulation and therefore deviate from the DASH conceptual model that invokes the persistence of thousands of years of drying related to climate and vegetation transitions. The 10^2 year chloride inventory indicates that the juniper community studied here is at or beyond the limits of the climatic/ ecological applicability of the DASH model. The chloride profiles show little retention of salts, presumably due to flushing, thereby indicating significant downward soil-water fluxes through time. Yet, an interesting result arises from applying the root-zone matric potential boundary condition (specified at -500 m) in FEHM simulations to model the JA and JB profiles. The matric potential profiles appear to be close to the model-predicted steady state (Figure 6-37) supporting a net upward moisture flux of 0.03 mm yr^{-1} (Figure 6-38).

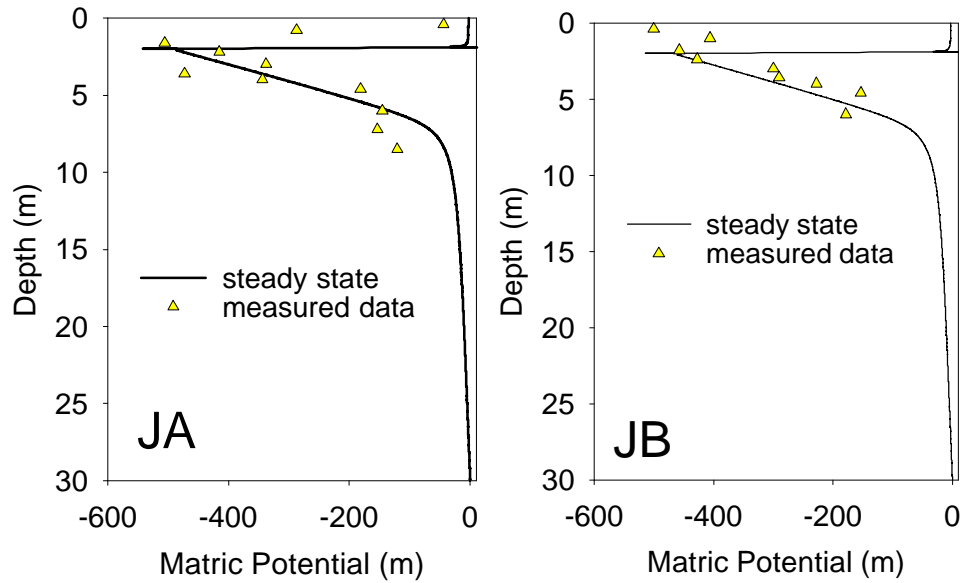


Figure 6-37. Model-simulated steady-state matric potential profiles for a specified root-zone matric potential condition of -500 m compared to data from JA and JB.

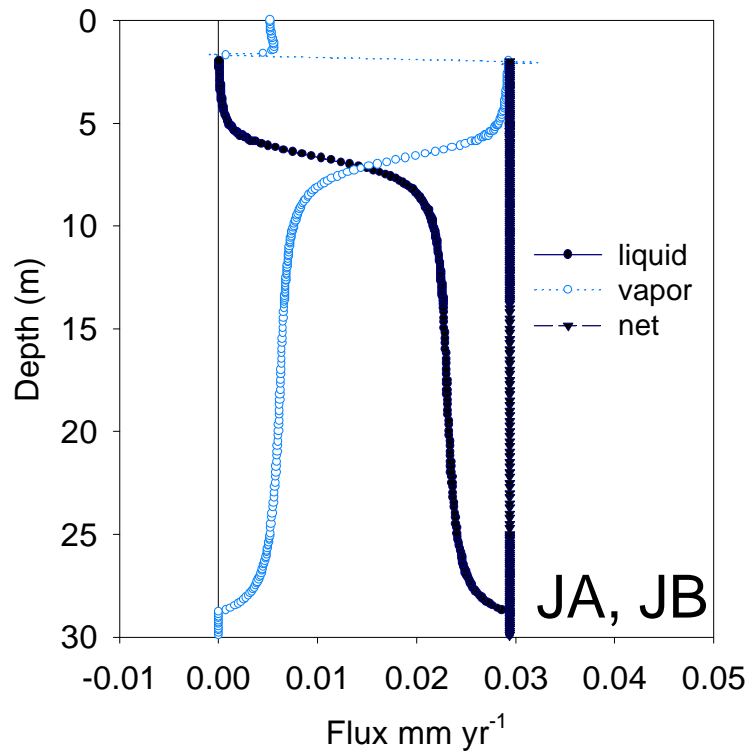


Figure 6-38. Model-predicted moisture flux profiles at steady state at the Juniper Miller Ranch site. Negative values indicate downward fluxes; positive values indicate upward fluxes.

In accordance with the JA / JB chloride profile interpretation, the hydraulic response time to the root-zone condition at the juniper site must be on the order of 10^2 years. Presumably the shallow water table contributes to a quick response time. Indeed, the model-calculated equilibrium response time of 6 kyr for JA / JB is significantly less than those estimated for thicker vadose zones (results from sensitivity analysis in Table 4-1). However, it is still much greater than the apparent chloride ages estimates of 125 - 250 years for the JA and JB cores. The matric potential profile that results after 250 years of the imposed root-zone matric potential condition displays a very steep, shallow character and does not match observed data (Figure 6-39).

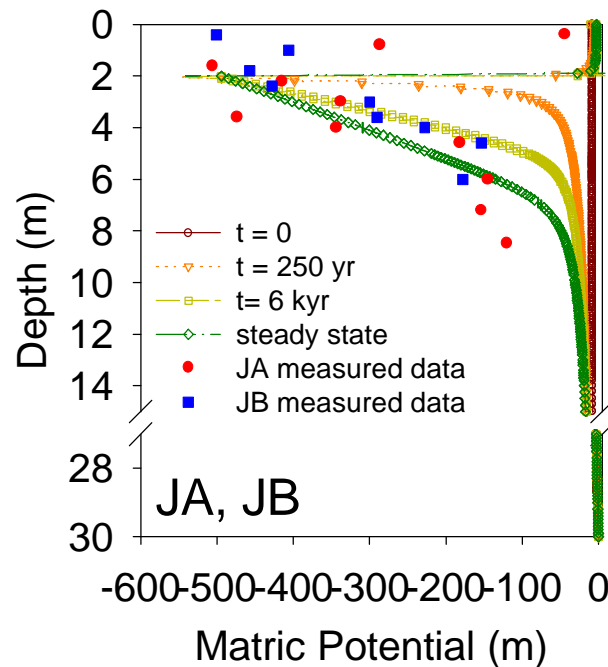


Figure 6-39. Model-simulated matric potential profiles for a specified root-zone matric potential condition of -500 m compared to data from JA and JB. The times correspond to development times from an initial steady-state downward flux condition. The steady-state profile (in green) is equivalent to the profile displayed in Figure 6-37.

Several alternative explanations can be advanced to resolve the apparent discrepancy between the 10^2 year chloride profile inventories and much longer development estimate of the matric potential profiles at the juniper site. First, isolated flushing in a region generally experiencing long-term upward fluxes, similar to the scenario invoked for the SB McKeel data set, *could* help explain the measured profiles. Perhaps, the matric potential profiles measured at JA and JB reflect the 6 kyr of drying, pervasive in the area. But macropores, such as hollowed decaying tree root tubules or animal burrows, have served to laterally channel flow within in the upper few meters and vertically focus flow (and chloride transport) through discrete conduits to the water table. The JA and JB cores could both be taken from these conduits flushed of chloride. Radial drying of the conduits subsequent to the most recent flushing event may reflect the 6 kyr of drying pervasive in the surrounding region. The likelihood of drilling cores at two locations and hitting the areas influenced by this “isolated” phenomenon lessens the credibility of this explanation. Alternatively, significant shallow subsurface lateral flow at the juniper site could result in major spatial redistribution of chloride to the point that very little chloride reached the JA and JB cores, but was rather is directed away laterally. Little evidence for macropore or focused flow observed on-site argues against the former explanations. A more likely explanation for the discrepant chloride and matric potential interpretations at the juniper site concerns the DASH modeling approach. Considering the deep root habits common in woody species [*Canadell et al.*, 1996],

the DASH model approach of specifying a fixed matric potential at a specified depth of 2 meters under a site vegetated with juniper is probably not appropriate. Although most of the root biomass may reside in the upper 50 cm of the soil, certainly some roots will extend to much greater depths. A mean maximum rooting depth for trees reported across biomes is 7.0 ± 1.2 m [*Canadell et al.*, 1996]. As such, it may be the deep juniper roots that are responsible for extracting a significant amount of soil moisture and pulling down the matric potentials at soil depths extending throughout the collected JA and JB cores. A more accurate representation of the root zone hydraulic regime would require a three-dimensional root-water uptake model that characterizes the root distribution within the upper 10 meter soil zone. This approach exceeds the scope of this study.

6.9.4. Discussion of Profile Interpretations

Site-specific modeling of the SA core from the McKeel site, using the DASH concept as a basis, demonstrates the utility of using both matric potential and chloride profiles to understand the moisture flux histories preserved in deep vadose zones. At the SA site, the matric potential profile reveals the timing of desert scrub establishment and the chloride profile records the major climate shift at 16 ka. Chlorine-37 measurements from the SA core that indicate fractionation in the upper 2-10 meters support the DASH concept that diffusion dominates chloride transport. However, model simulations do not capture the location of the isotopic enrichment and depletion. Also, the model over-predicts fractionation by several per mille. The discrepancy between the data and the model-predicted profile suggests the importance

of transient near-surface processes and perhaps the vertical movement of concentration peaks in the development of $\delta^{37}\text{Cl}$ profiles.

The chloride inventories between the two adjacent cores at the McKeel site, SA and SB, differed considerably resulting in chloride accumulation ages of . The combination of the large contrast in chloride inventories between the adjacent SA and SB cores, the nearly identical water potential profiles and the anomalously high proportion of NO_3^- -N to Cl in the SB core suggests an error in the low chloride results from the SB core. However, a second round of samples, leached and analyzed independently, confirmed the original results. Therefore, the low chloride profile from the SB core indicates an isolated area in which a significant downward soil-water flux has transported chloride to at least 15 meters and possibly flushed to the water table within the past 700 years.

In addition to the enigmatic core (SB), several cores from the Miller Ranch sites exhibit profiles that indicate deviation from DASH model assumptions. Consequently, a combination of approaches is required to best interpret the profiles from the Miller Ranch sites and the SB McKeel site. For example, the inventories of both chloride and nitrate in the GS core are twice those of the GD core, but both were taken under grassland. The high GS chloride inventory points towards lateral flow (surface run-on and/or shallow subsurface flow) contributing to a greater input (2x) at the GS site, which is located near the base of a raised area.

The moisture-dependent diffusion coefficient relationship plays a key role in successfully modeling the chloride profiles taken from the Miller Ranch cores that exhibit variable soil textures. In contrast, the SA McKeel core that consisted of

relatively homogeneous material shows no appreciable difference between chloride profiles generated using a moisture-dependent diffusion coefficient and chloride profiles generated using a constant diffusion coefficient. Future FEHM model development may allow specification of unique diffusion-limiting residual water content values for different soil textures.

In terms of recharge, the results indicate a very low *negative* net moisture recharge (or discharge) for the McKeel desert scrub site, with isolated preferential flow conduits as inferred from the SB chloride data. The model-determined recharge values pertaining to the Miller Ranch grassland – creosote ecotone sites are questionable considering the poor agreement between the simulated and observed matric potential profiles, but range from 0.03 to 0.08 mm yr⁻¹. Clearly, the highest recharge rates among the sites considered in this study are associated with the juniper site. Chloride concentrations and inventories measured in the JA and JB cores reflect average infiltration rates of 10¹ mm yr⁻¹. However, the corresponding matric potential profiles indicate that current conditions support upward fluxes on the order of 10⁻² mm yr⁻¹. The combination of solute and hydraulic data sets suggests that infiltration at the juniper site is significant but episodic.

6.10. Summary

Integrative field data and modeling results indicate that distinctly different soil-water flux regimes are associated with xeric and mesic vegetation. All cores, except those taken under the juniper and the SB core, contain chloride inventories corresponding to thousands of years of accumulation and very negative matric

potential profiles suggesting upward moisture fluxes towards the base of the root zone over long time-scales. The presence of juniper, and presumably other mesic vegetation, appears to be associated with episodes of downward soil-water fluxes below the root zone as shown by low chloride porewater concentrations. In contrast, desert vegetation, both shrubs and grasses, effectively prevent infiltration from penetrating below the root zone, indicated by thousands of years of chloride inventory in the upper 10 m. Very negative matric potential profiles under desert vegetation also supports the idea that xeric plants sustain *upward* moisture fluxes beneath the root zone over very long time-scales. A final line of support for the water-limited state of vegetation at the study sites, excluding the juniper sites, derives from the high nitrate concentrations measured below the root zone. Such high concentrations and the strong correlation with chloride trends suggests the conservative behavior of nitrate below the root zone and that vegetation is more water-limited than nutrient-limited.

CHAPTER 7.

CONCLUSIONS

A consensus regarding the important controls on flow and transport in most hydrologic environments including humid-region vadose zones was arrived at 20 to 50 years ago. This is not the case for deep desert vadose zones. Even such basic issues as the relationship between observed hydraulic head gradients and average directions of flow (up or down) remain controversial. The work encompassed in this study challenges conventional vadose zone data interpretation and common conceptual models of flow and transport in desert soils. An integrative approach using observed data and numerical modeling to understand important hydrologic processes in deep vadose zones over long timescales has led to a major revision of current understanding of the subsurface hydromechanics of arid and semiarid regions. The Deep Arid System Hydrodynamic (DASH) model developed in this study reconciles the apparent contradictions between current observations and theory regarding moisture flux directions in desert soils. Implications associated with the DASH model hold both fundamental and practical importance. Fundamental scientific findings involve hydraulic response times and hydrodynamic equilibrium states of deep arid vadose zones. Practical implications include water balance and contaminant transport issues in desert vadose and paleohydrologic reconstruction.

7.1. Influence of Climate and Vegetation Transitions on Vadose Zone Moisture Flux Regimes

Deep vadose zones below interdrainage desert floors record the most recent climate shift to arid conditions and the corresponding xeric vegetation transition. The DASH model supplements the previously posited reduced recharge hypothesis that invokes a dramatic change in the soil water balance coincident with the onset of the Holocene and arid climate transition in the southwestern U. S. Recharge, although significantly reduced in magnitude, has continued through time, according to the reduced recharge model. An extreme end member of the reduced recharge model is the zero recharge model which submits that current infiltration past the root zone is zero and further implies that fluxes through the entire vadose zone, including the flux across the water table, are also zero. Although the DASH model agrees with the zero recharge model with respect to the hypothesis that essentially no infiltration currently penetrates below the root zone under desert floors in interdrainage regions, conditions below the root zone are not hydrostatic according to the DASH model. The DASH conceptual model deviates from both the reduced and zero recharge models by proposing that the establishment of xeric vegetation following the arid climate change induced a reversal in moisture fluxes below the root zone from downward to upward. Subsequent to this transition, planes of divergent liquid and net moisture fluxes have propagated downward from the base of the root zone as the vadose zone slowly dries. This transient drying process continues through time to the present in many deep arid vadose zones due to the slow drying response. Above the plane of divergent moisture flux, transpiration by desert plants is the main mechanism of drying, and below the

plane of divergent liquid flux, drainage accommodates drying. The distinctions between the reduced/zero model and the DASH model are important, from both a heuristic and a practical standpoint. Discriminating between reduced downward, zero or upward net moisture fluxes strongly influences issues concerning water balance and contaminant transport. Deep vadose zone water drainage below desert floors is probably insufficient to contribute significantly to groundwater recharge according to the DASH model. However, even small downward fluxes carrying hazardous contaminants to the water table may have serious ramifications.

The DASH model explains both the matric potential and chloride profiles typically observed in southwestern U. S. desert vadose zones, whereas the reduced recharge model and the zero recharge model do not reproduce both sets of data. Integrating field observations with model simulations emphasizes the importance of considering both matric potential and chloride profiles in determining the direction of moisture fluxes below the root zone. Upward fluxes can easily be distinguished from small downward fluxes based on the combination of matric potential and chloride profiles that have evolved since the early to late Holocene. The ability to reliably determine the directions of moisture fluxes within thick vadose zones is a critical part of quantifying the contribution to recharge through desert floors or assessing the contaminant transport risks. Matric potential and chloride profiles, properly interpreted, can thus provide a valuable means of assessing the suitability of desert areas for waste emplacement in the vadose zone.

7.2. Deep Vadose Zone Hydraulic Response

Thick desert vadose zones, unlike most other hydrological environments, are typically far from equilibrium with their surface boundary conditions. Failure to account for this kind of persistent transient can result in significant misinterpretation of data from desert vadose zones. Response times for desert vadose zones experiencing a transition to dry conditions generally exceed the time scales of major climate change, the latter of which can be expected to vary on the order of $\sim 10^4$ years. Consequently, most deep desert vadose zones are currently in a state of slow transient response with respect to both moisture and solute fluxes. These transients may be so slow that deep vadose zones appear to be maintaining a steady state that is actually far from the true steady state. A hydrodynamic equilibrium state describes the true steady state in which vapor transport dominates the flow regime. The persistence of an upward geothermally-driven vapor flux that decreases with height above the water table produces a steady-state flow regime in which vapor and liquid fluxes are not uniform. The no-flow condition, characterized by the linear hydrostatic equilibrium line matrix potential profile, does not apply to thick desert vadose zones.

7.3. Subsurface Controls on Moisture Fluxes in Deep Vadose Zones

Transient responses of moisture fluxes in interdrainage vadose zones to long-term climate shifts depend on many factors including water table depth (to a critical depth), soil texture, permeability, and geothermal gradient. These factors should be considered when assessing the equilibrium state of deep desert vadose zones. Better characterization of these controlling parameters at study locations will increase the accuracy of site-specific modeling results.

Yet, despite the many factors influencing response times and equilibrium states in deep desert vadose zone, the DASH conceptual model and its implications are applicable over a broad range of desert-floor environments. The record of matric potential and chloride profiles from numerous sites in the desert southwest reflects long-term net upward moisture fluxes. Because of the prevalence of such profiles in deep unsaturated zone studies, it may be concluded that desert-floor environments are generally regions of negligible groundwater recharge. Quantifying diffuse recharge by estimating soil-water fluxes below the root zone and assuming that they are equivalent to groundwater recharge, i.e. fluxes across the water table interface, may not be applicable in semiarid and arid regions. The work described in this study illustrates that not only are moisture fluxes just below the root zone unequal to recharge, they are typically opposing in direction. Furthermore, moisture fluxes through deep vadose zones estimated using the DASH model are several orders of magnitude smaller than estimates obtained by assuming downward-only flow. This implies a negligible contribution to groundwater recharge through desert floors in interdrainage areas and supports the idea that, in the absence of preferential flowpaths, a thick desert vadose zone serves as an effective barrier to groundwater. However, since desert vegetation, a major shallow subsurface controlling factor, is critical in maintaining upward fluxes below the root zone, vegetation removal and re-establishment is of primary importance for waste repository site assessment and emplacement procedure strategy.

7.4. Paleohydrologic Records in Deep Vadose Zones

In the past two decades, hydrologists have begun to look to vadose zones of arid regions as possible sources of paleoclimate proxies. Desert vadose zone attributes favoring preservation of long hydrologic histories include low porewater velocities, minimal solute mixing, and deep water tables. Although there is significant promise in accessing the paleohydrologic archives contained in deep vadose zones, several issues require consideration to ensure appropriate interpretation. Standard models used to interpret flow and transport in the vadose zones of arid regions lead to erroneous conclusions regarding paleohydrologic reconstruction. Concentration-driven chloride diffusion strongly controls the distribution of chloride past the root zone. Realization that chloride bulges are not the result of simple downward advection and dispersion warrants reinterpretation of deep vadose zone profiles using the DASH model for paleohydrologic reconstruction. The chloride mass balance method used to estimate paleorecharge must be applied with proper consideration of the main mechanisms of chloride transport and of the assumption of spatially and temporally uniform chloride deposition. Chloride profiles do have significance for vadose-zone recharge histories, but it is the inventory of chloride that is most significant. The chloride inventories in vadose zone bulges mainly reflect the transition from a mesic to an arid climate closely coinciding with the establishment of desert vegetation. Hopefully, this work will stimulate research to develop increasingly robust approaches for paleohydrologic reconstruction.

7.5. Vegetation Type and Moisture Flux Relationships

Perhaps the most surprising inference of this study is that, over large interdrainage areas of the desert, xeric vegetation appears to be capable of extracting all of the water that infiltrates the surface. Precipitation events in the desert are often very intense and several such events occurring in a short span of time, even if very infrequent, would seem to produce at least a small amount of recharge periodically, whether with a recurrence rate of 10, 100 or 1000 years. For the vast majority of profiles that have been measured, both in this study and by others, water potential and chloride profiles dispute the propagation of such events past depths of a few meters. Yet, as observed in both the Nevada Test Site and Trans-Pecos case studies, we find evidence of preferential flushing in small discrete zones reflected in low chloride concentration profiles with very negative matrix potential profiles. Whether or not these preferential flow conduits serve to episodically transport water through the entire thick vadose zone and actively supply recharge remains uncertain. These cases demonstrate that there continues to be much to learn about the temporal and spatial distribution of soil moisture in the root zone and how vegetation and climate act to control recharge.

REFERENCES

- Allen B. D., and R. Y. Anderson, Evidence from western North America for rapid shifts in climate during the last Glacial Maximum, *Science*, 260, 1920 – 1923, 1993.
- Allison, G. B., A review of some of the physical, chemical, and isotopic techniques available for estimating groundwater recharge, in *Estimation of Natural Groundwater Recharge*, edited by I. Simmers, pp. 49-72, D. Reidel, Norwell, Mass., 1988.
- Allison, G. B., and M. W. Hughes, The use of natural tracers as indicators of soil water movement in a temperate semi-arid region, *J. Hydrol.*, 60, 157-173, 1983.
- Allison, G. B., C. J. Barnes, and M. W. Hughes, The distribution of deuterium and ^{18}O in dry soils, 2. Experimental, *J. Hydrol.*, 64, 377-397, 1983.
- Allison, G. B., G. W. Gee, and S. W. Tyler, Vadose-zone techniques for estimating ground-water recharge in arid and semiarid regions, *Soil Sci. Soc. Am. J.*, 58, 6-14, 1994.
- Andraski, B. J., Soil-water movement under natural-site and waste-site conditions: A multiple-year field study in the Mojave Desert, Nevada, *Water Resour. Res.*, 33, 1901-1916, 1997.
- Barnes, C. J., and G. B. Allison, The distribution of deuterium and ^{18}O in dry soils, 1. Theory, *J. Hydrol.*, 60, 141-156, 1983.
- Barnes, C. J., and G. B. Allison, The distribution of deuterium and ^{18}O in dry soils, 3. Theory for non-isothermal water movement, *J. Hydrol.*, 74, 119-135, 1984.
- Barnes, C. J., and G. B. Allison, Tracing of water movement in the unsaturated zone using stable isotopes of hydrogen and oxygen, *J. Hydrol.*, 100, 143-176, 1988.
- Bechtel Nevada, Hydrogeologic characterization of the unsaturated zone at the Area 3 Radioactive Waste Management Site, Vol. 1, *Contract. Rep. DOE/NV/11718-204*, U.S. Dept. of Energy, Nev. Oper. Office, Las Vegas, NV, 64 pp., 1998.
- Benson, L. V., Timing of the last highstand of Lake Lahonton, *J. Paleolimnol.*, 5, 115-126, 1991.

- Benson, L. V., D. R. Currey, R. I. Dorn, K. R. Lajoie, C. G. Oviatt, S. W. Robinson, G. I. Smith, and S. Stine, Chronology of expansion and contraction of four Great Basin lake systems during the past 35,000 years, *Palaeog.*, *Palaeoclim.*, *Palaeoecol.*, 78, 241-286, 1990.
- Betancourt, J. L., T. R. Van Devender, and P. S. Martin, *Packrat Middens: The Last 40,000 Years of Biotic Change*, The University of Arizona Press, Tucson, AZ, 467 pp., 1990.
- Black, C. A., (ed.), *Methods of Soil Analysis, Part 1*, Amer. Soc. Agron., Inc, Madison, WI, pp. 374-383, 1965.
- Brooks, R. J., and A. T. Corey, Hydraulic properties of porous media, *Hydrol. Pap. 3*, Colo. State Univ., Fort Collins, 1964.
- Canadell, J., R. B. Jackson, and J. R. Ehleringer, Maximum rooting depth of vegetation types at the global scale, *Oecologia*, 108, 583-595, 1996.
- Classen, H. C., and D. R. Halm, Estimates of evapotranspiration or effective moisture in Rocky Mountain watersheds from chloride ion concentrations, *Water Resour. Res.*, 32, 363-372, 1996.
- Conca, J. L., and J. Wright, Diffusion and flow in gravel, soil, and whole rock, *Appl. Hydrogeol.*, 1, 5-24, 1992.
- Cook, P.G., W. M. Edmunds, and C. B. Gaye, Estimating paleorecharge and paleoclimate from unsaturated zone profiles, *Water Resour. Res.*, 28, 2721-2731, 1992.
- Cussler, E. L., *Diffusion: Mass transfer in fluid systems*, Cambridge University Press, Cambridge, 525 pp., 1984.
- Davisson, M. L., J. M. Kenneally, D. K. Smith, G. B. Hudson, G. J. Nimz, and J. H. Rego, Preliminary report on the isotope hydrology investigations at the Nevada Test Site: Hydrology resources management program FY1992-1993, Lawrence Livermore National Laboratory, 1994.
- Desaulniers, D. E., R. S. Kaufmann, J. A. Cherry, and H. W. Bentley, ^{37}Cl - ^{35}Cl variations in a diffusion-controlled groundwater system, *Geochim. Cosmochim. Acta*, 50, 1757-1764, 1986.
- Dettinger, M. D., Reconnaissance estimates of natural recharge to desert basins in Nevada, USA, by using chloride-mass balance calculations, *J. Hydrol.*, 106, 55-87, 1989.

- de Vries, J. J., E. T. Selaolo, and H. E. Beekman, Groundwater recharge in the Kalahari, with reference to paleo-hydrologic conditions, *J. Hydrol.*, 238, 110-123, 2000.
- Dickerson, P. W., and J. M. Hoffer (ed), *New Mexico Geological Society Guidebook, 31st Field Conference, Trans-Pecos Region*, New Mexico Geol. Soc. Inc., NM, 314 pp., 1980.
- Dick-Peddie, W. A., *New Mexico Vegetation: Past, Present and Future*, Univ. of New Mexico Press, Albuquerque, NM, 244 pp. 1993.
- Dindler, T., and G. H. Davis, Application of environmental isotope tracer to modeling in hydrology, *J. Hydrol.*, 68, 95-113, 1984.
- Eggenkamp, H. G. M., The geochemistry of chlorine isotopes, Ph.D. dissertation, Utrecht University, Utrecht, The Netherlands, 1997.
- Enfield, C. G., J. J. C. Hsieh, and A. W. Warrick, Evaluation of water flux above a deep water table using thermocouple psychrometers, *Soil Sci. Soc. Amer. Proc.*, 37, 968-970, 1973.
- Estrella, R., S. Tyler, J. Chapman, and M. Miller, Area 5 site characterization project-report of hydraulic property analysis through August 1993, Water Resour. Center DRI, Publication No. 45121, DOE/NV, 51 pp., 1993.
- Evans, J. R., and J. L. Ehleringer, Broken nitrogen cycles in arid lands, evidence from ¹⁵N of soils, *Oecologia*, 94, 314-317, 1993.
- Fabryka-Martin, J. T., A. L. Flint, D. S. Sweetkind, A. V. Wolfsberg, S. S. Levy, G. J. C. Roemer, J. L. Roach, L. E. Wolfsberg, and M. C. Duff, Evaluation of flow and transport models of Yucca Mountain, based on chlorine-36 studies for FY97, *YMP Milestone Report SP2224M3*, Los Alamos National Laboratory, 1997.
- Faust, C. R., and J. W. Mercer, Geothermal reservoir simulation; I, Mathematical models for liquid and vapor-dominated hydrothermal systems, *Water Resour. Res.* 15, 23-30, 1979.
- Fischer, J. M., Sediment properties and water movement through shallow unsaturated alluvium at an arid site for disposal of low-level radioactive waste near Beatty, Nye County, Nevada, *U. S. Geol. Surv., Water Resour. Invest. Rep.*, 92-4032, 48 pp., 1992.
- Fontes, J. Ch., M. Yousfi, and G. B. Allison, Estimation of long-term, diffuse groundwater discharge in the northern Sahara using stable isotope profiles in soil water, *J. Hydrol.*, 86, 315-327, 1986.

- Frizzell, V. A. Jr., and J. Shulters, Geologic map of the Nevada Test Site, Southern, Nevada, *U. S. Geol. Surv., Map, I-2046*, 1990.
- Gardner, W. R., Water uptake and salt distribution patterns in saline soils, in *Isotope and Radiation Techniques in Soil Physics and Irrigation Studies, Proceedings of an International Symposium on Isotope and Radiation Techniques in Soil Physics and Irrigation Studies, Aix-en-Provence, France*, pp. 335-340, Int. Atom. Energy Agency, Vienna, 1967.
- Gee, G. W., and R. R. Kirkham, Arid site water balance: Evapotranspiration modeling and measurements, *Rep. PNL-5177*, 38 pp., Pac. North. Lab., Richland, Wash., 1984.
- Gee, G. W., M. D. Campbell, G. S. Campbell, and J. H. Campbell, Rapid measurement of low soil water potentials using the water activity meter, *Soil Sci. Am. J.*, 56, 1068-1070, 1992.
- Gee, G. W., P. J. Wierenga, B. J. Andraski, M. H. Young, M. J. Fayer, and M. L. Rockhold, Variations in water balance and recharge potential at three western desert sites, *Soil Sci. Soc. Am. J.*, 58, 63-72, 1994.
- Ginn, T. R., and E. M. Murphy, A transient flux model for convective infiltration: Forward and inverse solutions for chloride mass balance studies, *Water Resour. Res.*, 33, 2065-2079, 1997.
- Green T. R., and D. L. Freyberg, State-dependent anisotropy: Comparisons of quasi-analytical solutions with stochastic results for steady gravity drainage, *Water Resour. Res.*, 31, 2201-2211, 1995.
- Guymon, G. L., *Unsaturated Zone Hydrology*, Prentice Hall, Englewood Cliffs, New Jersey, p. 12, 1994.
- Gvirtsman, H., and S. M. Gorelick, Dispersion and advection in unsaturated porous media enhanced by anion exclusion, *Nature*, 352, 793-795, 1991.
- Harr, L., J. Gallagher, and G. S. Kell, *NBS/NRC Steam Tables, Thermodynamics, and Transport Properties and Computer Programs for Vapor and Liquid States of Water*, Hemisphere Press, 1984.
- Hartsough, P., S. W. Tyler, J. Sterling, and M. Walvoord, A 14.6 kyr record of nitrogen flux from desert soil profiles as inferred from vadose zone pore waters, *Geophys. Res. Let.*, 28, 2955 - 2958, 2001.

- Hartsough, P., The use of environmental tracers as indicators of paleoclimate and the paleohydrologic response, M.S. thesis, University of Nevada, Reno, NV, 142 pp., 2000.
- Hendrickx, J. M. H., and G. R. Walker, Recharge from Precipitation, in *Recharge of Phreatic Aquifers in (Semi-) Arid Areas*, edited by I. Simmers, pp. 19-111, Balkema, Rotterdam-Brookfield, Netherlands, 1997.
- Hillel, D., *Fundamentals of Soil Physics*, Academic Press, Inc., San Diego, CA, 413 pp., 1980.
- Hinton, E., and D. R. J. Owen, *A Simple Guide to Finite Elements*, Pineridge Press, Swansea, Wales, 136 pp., 1980.
- Hostetler, S., and L. V. Benson, Paleoclimatic implications of the high stand of Lake Lahontan derived from models of evaporation and lake level, *Climate Dynam.*, 4, 207-217, 1990.
- Humphrey, R. R., *90 Years and 535 Miles*, University of New Mexico Press, Albuquerque, NM, 448 pp., 1987.
- Ingraham, N. L., and C. Shadel, A comparison of the toluene distillation and vacuum/heat method for extraction of soil water for stable isotopic analysis, *J. Hydrol.*, 140, 371-387, 1992.
- Jannik, N. O., F. M. Phillips, G. I. Smith, and D. Elmore, A ^{36}Cl chronology of lacustrine sedimentation in the Pleistocene Owens River system, *Geol. Soc. Am. Bull.*, 103, 1146-1159, 1991.
- Jobaggy, E. G., and R. B. Jackson, The distribution of soil nutrients with depth: Global patterns and the imprint of plants, *Biogeochemistry*, 53, 51-77, 2001.
- Johnston, C., Preferred water flow and localised recharge in a variable regolith, *J. Hydrol.*, 94, 129-142, 1987.
- Johnston, R., Introduction to Microbiotic Crusts (on line), *Natural Resour. Conserv. Serv.*, 16 pp., 1997.
- Junge, C. E., and R. T. Werby, The concentration of chloride, sodium, potassium chloride and sulfate in rain water over the United States, *J. Meteorol.*, 15, 417-425, 1957.
- Jury, W. A., W. R. Gardner, and W. H. Gardner, *Soil Physics*, John Wiley & Sons, New York, NY, 328 pp., 1991.

- Kaufman, R., H. W. Bentley, S. N. Davis, and A. Long, Application of chloride stable isotope analysis to hydrogeology in *Hydrology and Water Resources in Arizona and the Southwest, Proceedings of the 1983 meetings of the American Water Resources Association, Arizona Section and the Arizona-Nevada Academy of Science, Hydrology Section*, Tucson, AZ, 13, 85-90, 1983.
- Khaleel, R., J. F. Relya, and J. R. Conca, Evaluation of van Genuchten-Mualem relationships to estimate unsaturated hydraulic conductivity at low water contents, *Water Resour. Res.*, 31, 2659-2668, 1995.
- Koorevaar, P., G. Menelik, and D. Dirksen, *Elements of Soil Physics* (third edition), Elsevier, Amsterdam, The Netherlands, 230 pp., 1983.
- Laczniak, R. J., J. Cole, D. A. Sawyer, and D. A. Trudeau, Summary of Hydrogeologic controls on ground-water flow at the Nevada Test Site, Nye County, Nevada, *U. S. Geol. Surv., WRI Report 96-4109*, Carson City, NV, 59 pp., 1996.
- Liu, B., F. Phillips, S. Hoines, A. Campbell, and P. Sharma, Water movement in desert soil traced by hydrogen and oxygen isotopes, chloride, and chlorine-36, southern Arizona, *J. Hydrol.*, 168, 91-110, 1995.
- Looney, B. and R. Falta (ed.), *Vadose Zone Science and Technology Solutions, Vol. I*, Battelle Press, Columbus, OH, 590 pp., 2000.
- Looney, B. and R. Falta (ed.), *Vadose Zone Science and Technology Solutions, Vol. II*, Battelle Press, Columbus, OH, 949 pp., 2000.
- Mathieu, R., and T. Bariac, A numerical model for the simulation of stable isotope profiles in drying soils, *J. Geophys. Res.*, 101, 12685-12696, 1996.
- McCord, J. T., D. B. Stephens, and J. L. Wilson, Hysteresis and state-dependent anisotropy in modeling unsaturated hillslope hydrologic processes, *Water Resour. Res.*, 27, 1501-1518, 1991.
- McCord, J. T., C. A. Gotway, and S. H. Conrad, Impact of geologic heterogeneity on recharge estimation using environmental tracers: Numerical modeling investigation, *Water Resour. Res.*, 33, 1229-1240, 1997.
- McCraw, D. J., A phytogeographic history of larrea in southwestern New Mexico illustrating the historical expansion of the Chihuahuan Desert, M. S. thesis, University of New Mexico, Albuquerque, NM, 137 pp., 1985.
- Merlivat L., and M. Coantic, Study of mass transfer at the air-water interface by an isotopic method, *J. Geophys. Res.*, 80, 3455-3464, 1975.

- Meyers, J. S., Evaporation from the 17 western states, *U. S. Geol. Surv. Prof. Paper 272-D*, pp. 71-100, 1962.
- Milly, P.C., Effects of thermal vapor diffusion on seasonal dynamics of water in the unsaturated zone, *Water Resour. Res.*, *32*, 509-518, 1996.
- Morel-Seytoux, H. J., and J. R. Nimmo, Soil water retention and maximum capillary drive from saturations to oven dryness, *Water Resour. Res.*, *37*, 2031-2041, 1999.
- Morrison, R. B., Quaternary stratigraphic, hydrologic, and climatic history of the Great Basin, with emphasis on Lakes Lahonton, Bonneville and Tecopa, in *Quaternary nonglacial geology: Conterminous U. S. Vol. K-2 The geology of North America*, edited by R. B. Morrison, pp. 283-320, Geol., Soc. Am., Boulder, CO, 1991.
- Mualem, Y., A new model for predicting the hydraulic conductivity of unsaturated porous media, *Water Resour. Res.*, *12*, 513-522, 1976.
- Murphy, E. M., T. R. Ginn, and J. L. Phillips, Geochemical estimates of paleorecharge in the Pasco Basin: Evaluation of the chloride mass balance technique, *Water Resour. Res.*, *32*, 2853-2868, 1996.
- Musgrove, M., J. L. Banner, and L. E. Mack, Temporal variations in cave dripwater geochemistry: implications for speleothems as recorders of long-term variations in groundwater chemistry, *Abstracts with Programs, Geol. Soc. of Amer.*, *31* (7), 90, 1999.
- National Atmospheric Deposition Program (NRSP-3)/National Trends Network, NADP Program Office, Illinois State Water Survey, 2204 Griffith Dr., Champaign, IL 61820, 2001.
- National Research Council, *Ward Valley: An Examination of Seven Issues in Earth Sciences and Ecology*, National Academy Press, Washington DC, 1995.
- Nimmo J., D. A. Stonestrom, and K. A. Akstin, The feasibility of recharge rate determination using the steady-state centrifuge method, *Soil Sci. Am. J.*, *58*, 49-56, 1994.
- Oviatt, C. G., Lake Bonneville fluctuations and global climate change, *Geology*, *25*, 155-158, 1997.
- Penman, H. L., Gas and vapor movements in the soil: I. The diffusion of vapors through porous solids, *J. Agr. Sci.*, *30*, 437-462, 1940a.

- Penman, H. L., Gas and vapor movements in the soil: II. The diffusion of carbon dioxide through porous solids, *J. Agr. Sci.*, 30, 570-581, 1940b.
- Philip, J. R., and D. A. de Vries, Moisture movement in porous materials under temperature gradients, *Trans. Am. Geophys. Union*, 38, 222-228, 1957.
- Phillips, F. M., A. R. Campbell, C. Kruger, P. Johnson, R. Roberts, and E. Keyes, A reconstruction of the water balance in western United States lake basins to climate change, *New Mexico Water Resour. Res. Institute Rep. 269*, Las Cruces, NM, 1992.
- Phillips, F. M., Environmental tracers for water movement in desert soils of the American southwest, *Soil Sci. Soc. Am. J.*, 58, 15-24, 1994.
- Phillips, F. M., J. L. Mattick, and T. A. Duval, Chlorine 36 and tritium from nuclear weapons fallout as tracers for long-term liquid movement in desert soils, *Water Resour. Res.*, 24, 1877-1891, 1988.
- Pockman, W. T., J. S. Sperry, and J. W. O'Leary, Sustained and significant water pressure in xylem, *Nature*, 378, 715-716, 1995.
- Pockman, W. T., and J. S. Sperry, Vulnerability to xylem cavitation and the distribution of in the Sonoran Desert vegetation, *Amer. J. Botany*, 87, 1287-1299, 2000.
- Post, W. M., J. Pastor, P. J. Zinke, and A. G. Stagenberger, Global patterns of soil nitrogen storage, *Nature*, 317, 613-616, 1985.
- Powell, A. M., Vegetation of Trans-Pecos Texas, in *New Mexico Geological Society Guidebook, 31st Field Conference, Trans-Pecos Region*, edited by Dickerson, P. W. and J. M Hoffer, pp. 299-302, New Mexico Geological Society, Inc., 1980.
- Powell, A. M., *Grasses of the Trans-Pecos and Adjacent Areas*, University of Texas Press, Austin, TX, 377 pp., 1994.
- Powell, A. M., *Trees and Shrubs of the Trans-Pecos and Adjacent Areas*, University of Texas Press, Austin, TX, 498 pp., 1998.
- Pruess, K., TOUGH2 - A General-Purpose Numerical Simulator for Multiphase Fluid and Heat Flow, *Lawrence Berkeley Lab. Rep. LBL-29400*, 1991.
- Prudic, D. E., Estimates of percolation rates and ages of water in unsaturated sediments at two Mojave Desert sites, California – Nevada, *U. S. Geol. Surv. Water Res. Invest. Rep. 94-4160*, 19 pp., 1994.

- Prych, E. A., Using chloride and chlorine-36 as soil-water tracers to estimate deep percolation at selected locations on U.S. Department of Energy Hanford site, Washington. *US Geol. Surv. Open File Rep. 94-514*, 125 pp., 1995.
- Reith, C. C., and B. M. Thompson (ed.), *Deserts as Dumps? The Disposal of Hazardous Materials in Arid Ecosystems*, Univ. of New Mexico Press, Albuquerque, NM, 330 pp., 1992.
- Reynolds Electrical and Engineering Company (REECo), Site characterization and monitoring data from area 5 pilot wells, Nevada Test Site, Nye County, Nevada, *Contract. Rep. DOE/NV/11432-74*, Nev. Oper. Off., U. S. Dept. of Energy, Las Vegas, NV, 1994.
- Rodriguez-Iturbe, I., Ecohydrology: A hydrologic perspective of climate-soil-vegetation dynamics, *Water Res. Res.*, 36, 3-9, 2000.
- Ross, B., A conceptual model of deep unsaturated zone with negligible recharge, *Water Resour. Res.*, 20, 1627-1629, 1984.
- Scanlon, B., Evaluation of moisture flux from chloride data in desert soils, *J. of Hydrol.*, 128, 137-156, 1991.
- Scanlon, B., Evaluation of liquid and vapor water flow in desert soils based on chlorine 36 and tritium tracers and nonisothermal flow simulations, *Water Resour. Res.*, 28, 285-297, 1992.
- Scanlon, B. R., Uncertainties in estimating water fluxes and residence times using environmental tracers in an arid unsaturated zone, *Water Resour. Res.*, 36, 395-409, 2000.
- Scanlon, B. R., S. W. Tyler, and P. J. Wierenga, Hydrologic issues in semi-arid, unsaturated systems and implications for contaminant transport, *Rev. Geophys.*, 35, 461-490, 1997a.
- Scanlon, B. R., R. S. Goldsmith, and W. F. Mullican III, Spatial variability in subsurface flow through the unsaturated zone in the southern high plains, Texas, *Rep. Inv. 243*, Univ. of Tex. at Austin, Bur. Econ. Geol., Austin, TX, 46 pp., 1997b.
- Scanlon, B. R., R. P. Langford, and R. S. Goldsmith, Relationship between geomorphic settings and unsaturated flow in an arid setting, *Water Resour. Res.*, 35, 983-999, 1999.
- Schlesinger, W. H., J. F. Reynolds, G. L. Cinngham, L F Huenneke, W. M. Jarrell, R. A. Virginia, and W. G. Whitford, Biological feedbacks in global desertification, *Science*, 247, 1043-1048, 1990.

- Schmidt, R. H., A climatic delineation of the “real” Chihuahuan Desert, *J. Arid Environments*, 2, 243-250, 1979.
- Shurbaji, A. M., and F. M. Phillips, A numerical model for the movement of H₂O, H₂¹⁸O, and ²H₂O in the unsaturated zone, *J. of Hydrol.*, 171, 121-142, 1995.
- Shurbaji, A. M., and F. M. Phillips, A. R. Campbell, and R. G. Knowlton, Application of a numerical model for simulating water flow, isotope transport, and heat transfer in the unsaturated zone, *J. of Hydrol.*, 171, 143-163, 1995.
- Silverman, T., A pore-scale experiment to evaluate enhanced vapor diffusion in porous media, M.S. thesis, New Mexico Institute of Mining and Technology, Socorro, NM, 117 pp., 1999.
- Smith, G. I., J. L. Bischoff, and J. P. Bradbury, Synthesis of the paleoclimatic record from Owens Lake core OL-92, in *An 800,000-year paleoclimatic record from core OL-92, Owens Lake, Southeast California*, edited by G. I. Smith and J. L. Bischoff, Special Paper, Geol. Soc. Amer., Boulder, CO, 317 pp., 143-160, 1997.
- Spaulding, W. G., Vegetational and climatic development of the Mojave Desert: The last glacial maximum to the present, in *Packrat Middens: The Last 40,000 Years of Biotic Change*, edited by Betancourt J. L., T. R. Van Devender, and P. S. Martin, pp. 166-199, The Univ. of Arizona Press, Tuscon, AZ, 1990.
- Spaulding, W. G., and L. J. Graumlich, The last pluvial climatic episodes in the deserts of southwestern North America, *Nature*, 320, 441-444, 1986.
- Sperry, J. S., F. R. Adler, G. S. Campbell, and J. P. Comstock, Limitation of plant water use by rhizosphere and xylem conductance: results from a model, *Plant, Cell and Environment*, 21, 347-359, 1998.
- Stephens, D. B., A perspective on diffuse natural recharge mechanisms in areas of low precipitation, *Soil Sci. Am. J.*, 58, 40-48, 1994.
- Stephens, D. B., *Vadose Zone Hydrology*, Lewis Publishers, Boca Raton, FL, 347 pp., 1996.
- Stephens, D. B., and R. K. Knowlton, Jr., Soil water movement and recharge through sand at a semiarid site in New Mexico, *Water Resour. Res.*, 22, 881-889, 1986.
- Stedle, E., Water uptake by plant roots: an integration of views, *Plant and Soil*, 226, 45-56, 2000.

- Stone, W. J., Recharge in the Salt Lake Coal Field based on chloride in the unsaturated zone, *New Mexico Bur. of Mines and Min. Res. Open-File Rep. 217*, Socorro, NM, 64 pp., 1984.
- Stone, W. J., Paleohydrologic implications of some deep soilwater chloride profiles, Murray Basin, South Australia, *J. Hydrol.*, 132, 201-223, 1992.
- Stone, W. J., and B. E. McGurk, Ground-water recharge on the southern high plains, east-central New Mexico, *New Mexico Geol. Soc. Guidebook, 36th Field Conference*, pp. 331-335, Santa Rosa, NM, 1985.
- Swadley, W.C., and D.L. Hoover, Geologic Map of the Surficial Deposits of the Yucca Flat area, Nye County, Nevada, *U. S. Geol. Surv., Map I-2047*, 1990.
- Taylor, B. and R. F. Roy, A preliminary heat flow map of West Texas, in *New Mexico Geological Society Guidebook, 31st Field Conference, Trans-Pecos Region*, edited by Dickerson, P. W. and J. M. Hoffer, pp. 137-139, New Mexico Geol. Soc., Inc., 1980.
- Toomey, R. S. III, M. D. Blum, and S. Valastro, Jr., Late Quaternary climates and environments of the Edwards Plateau, Texas, *Global Planet. Change*, 7, 299-320, 1993.
- Turner, A. J., Soil Survey of Jeff Davis County, Texas, *U. S. Dept. of Agriculture, Soil Conservation Service*, 93 pp., 1997.
- Tyler, S. W., J. B. Chapman, S. H. Conrad, D. P. Hammermeister, D. O. Blout, J. J. Miller, M. J. Sully, and J. M. Ginanni, Soil-water flux in the southern Great Basin, United States: Temporal and spatial variations over the last 120,000 years, *Water Resour. Res.*, 32, 1481-1499, 1996.
- Van Devender, T. R., C. E. Freeman, and R. D. Worthington, Full-glacial and recent vegetation of Livingston Hills, Presidio County, Texas, *The Southwestern Naturalist*, 23, 289-302, 1978.
- Van Devender, T. R., Pleistocene climates and endemism in the Chihuahuan Desert flora, in *Transactions of the Second Symposium on the Resources of the Chihuahuan Desert*, edited by J. C. Barlow, A. M. Powell, and B. N. Timmermann, pp.1-19, Chihuahuan Desert Res. Institute, Alpine, Texas, 1986.
- Van Devender, T. R., Late Quaternary Vegetation and Climate of the Chihuahuan Desert, United States and Mexico, in *Packrat Middens: The Last 40,000 Years of Biotic Change*, edited by J. L. Betancourt, T. R. Van Devender, and P. S. Martin, pp. 104-133, The University of Arizona Press, Tuscon, AZ, 1990.

- van Genuchten, M. Th., A closed-form equation for predicting the hydraulic conductivity of unsaturated soils, *Soil Sci. Soc. Am. J.*, 44, 892-898, 1980.
- Wells, P. V., and C. D. Jorgensen, Pleistocene woodrat middens and climatic change in the Mojave Desert: A record of juniper woodlands, *Science*, 143, 1171-1174, 1964.
- Wells, P. V., and R. Berger, Late Pleistocene history of coniferous woodland in the Mojave Desert, *Science*, 155, 1640-1647, 1967.
- West, N. E., and J. J. Skujins, *Nitrogen in Desert Ecosystems*, Dowden, Hutchinson and Ross, Stroudsburg, PA, 253 pp., 1978.
- Wilkins, D. E., and D. R. Currey, Timing and extent of late Quaternary paleolakes in the Trans-Pecos closed basin, West Texas and South-central New Mexico, *Quat. Res.*, 47, 306-315, 1997.
- Winograd, I. J., Radioactive waste storage in thick unsaturated zone, *Science*, 212, 1457-1464, 1981.
- Winograd, I., and W. Thordarson, Hydrogeologic and hydrochemical framework, south-central Great Basin, Nevada-California, with special reference to the Nevada Test Site, *U. S. Geol. Surv. Prof. Paper: C1-C23*, 126 pp., 1975.
- Wood, W. W., Use and misuse of the chloride-mass balance method in estimating ground water recharge, *Ground Water*, 37, 2-3, 1999.
- Yeh, J., L. W. Gelhar, and A. L. Gutjahr, Stochastic analysis of unsaturated flow in heterogeneous soils, 3, Observations and applications, *Water Resour. Res.*, 21, 465-471, 1985.
- Young, L. C., A Finite Element Method for Reservoir Simulation, *Soc. Pet. Eng. J.*, 21, 115-128, 1981.
- Zienkiewicz, O. C., *The Finite Element Method, third edition*, McGraw-Hill, London, 787 pp., 1977.
- Zyvoloski, G. A., B. A. Robinson, Z. V. Dash, and L. L. Trease, Summary of the models and methods for the FEHM application – A finite-element heat-and mass-transfer code, *Los Alamos National Lab. Rep. LA-13307-MS*, Los Alamos, NM, 1997a.
- Zyvoloski, G. A., B. A. Robinson, Z. V. Dash, and L. L. Trease, User's manual for the FEHM application – A finite-element heat-and mass-transfer code, *Los Alamos National Lab. Rep. LA-13306-M*, Los Alamos, NM, 1997b.

APPENDIX A

DESCRIPTION AND APPLICATION OF FEHM

Introduction

FEHM Description

List of Symbols

Flow and Energy Equations

Solute Transport Equations

Boundary Conditions

Constitutive Relationships

Discretization and Numerical Solution Methods

FEHM Application

Matrix Properties

Solute Parameters

Initial and Boundary Conditions

Finite-element Mesh

Numerical Routine Parameters

INTRODUCTION

FEHM is the acronym for the Finite Element Heat and Mass Transfer code developed at Los Alamos National Laboratory, originally designed to characterize the flow field and complex multi-component transport at the proposed Yucca Mountain nuclear waste repository [Zyvoloski *et al.*, 1997]. The purpose of this appendix is to provide a more thorough description of FEHM's mathematical models and numerical methods as applied in this study, beyond the description supplied in the main text. The following explanation should not be regarded as a comprehensive description of FEHM capabilities. For brevity, only the equations, model routines and parameters employed for this study are discussed in this appendix. For a more complete report of FEHM capabilities, the reader is referred to the Summary of the Models and Methods [Zyvoloski *et al.*, 1997a] and the FEHM User's Manual [Zyvoloski *et al.*, 1997b] from which most of the following first section, "FEHM Description", is taken.

FEHM DESCRIPTION (modified from *Zyvoloski et al. [1997a]*)**List of Symbols (used in *Zyvoloski et al. [1997a]*)***Subscripts*

<i>a</i>	Subscript denoting air properties
<i>c</i>	Subscript denoting concentration
<i>cap</i>	Subscript denoting capillary values
<i>dry</i>	Subscript denoting value at 0 saturation
<i>e</i>	Subscript denoting energy
<i>flow</i>	Subscript denoting properties of flowing fluid
<i>l</i>	Subscript denoting liquid properties
<i>lr</i>	Subscript denoting residual liquid
<i>max</i>	Subscript denoting maximum value
<i>min</i>	Subscript denoting minimum value
<i>P</i>	Subscript denoting derivative with respect to pressure
<i>r</i>	Subscript denoting rock properties
<i>ref</i>	Subscript denoting value at reference conditions
<i>S</i>	Subscript denoting derivative with respect to saturation
<i>sat</i>	Subscript denoting saturation dependence
<i>T</i>	Subscript denoting derivative with respect to temperature or temperature dependence
<i>v</i>	Subscript denoting vapor properties
<i>vr</i>	Subscript denoting residual vapor
<i>w</i>	Subscript denoting water properties
<i>x, y, z</i>	Subscripts denoting coordinate direction
η	Subscript denoting noncondensable gas
<i>1, 2, . . . , n</i>	Subscripts denoting the species or component (i.e., nth component)
<i>m, m+1, . . . , n</i>	

Superscripts

<i>n, n+1</i>	Superscripts denoting timestep (i.e., nth timestep)
0	Superscript denoting initial value

List of Symbols (continued)*Parameters*

Units given in dimensions of mass [M], length [L], time [θ], temperature [T]

A_c	Concentration (solute) accumulation term [moles L ⁻³]
A_e	Energy accumulation term [M L ⁻¹ θ^{-2}]
A_m	Mass accumulation term [M L ⁻³]
A_η	Noncondensable gas accumulation term [M L ⁻³]
C	Concentration (solute) [moles M ⁻¹]
c_p	Heat capacity/specific heat [L ² θ^{-2} T ⁻¹]
D_{AB}	Solute diffusion coefficient [L ² θ^{-1}]
D_{cl}	Combination of molecular diffusion and dispersivity [L ² θ^{-1}]
D_{va}	Air/water diffusivity [L ² θ^{-1}]
D_c	Dispersion coefficient for tracer [L ² θ^{-1}]
D_e	Energy transmissibility term [L ² θ^{-1}]
D_m	Mass transmissibility term [θ]
\overline{f}_c	Flux vector for concentration equations [moles L ⁻² θ^{-1}]
\overline{f}_e	Flux vector for energy equation [M θ^{-3}]
\overline{f}_m	Flux vector for mass equation [M L ⁻² θ^{-1}]
\overline{f}_h	Flux vector for noncondensable gas equation [M L ⁻² θ^{-1}]
$f(t)$	Function at time t
$f'(t)$	Derivative of with respect to time
g	Acceleration of gravity [L θ^{-2}]
h	Enthalpy [L ² θ^{-2}]
I_m	Mass flow impedance [θ L ⁻²]
I_e	Heat flow impedance [M L ⁻³ θ^{-1} T ⁻¹]
K	Thermal conductivity [M L θ^{-3} T ⁻¹]
K_H	Henry's law constant [L θ^2 M ⁻¹]
k	Intrinsic rock permeability [L ²]

Parameters (continued)

M_v	Molecular mass of vapor [moles M^{-1}]
M_w	Molecular mass of water [moles M^{-1}]
n	Parameter in van Genuchten R_p and capillary pressure models
P	Pressure [$M L^{-1} \theta^{-2}$]
q_c	Concentration source term [moles $L^{-3} \theta^{-1}$]
q_e	Energy source term [$M L^{-1} \theta^{-3}$]
q_m	Mass source term [$M L^{-3} \theta^{-1}$]
q_η	Noncondensable gas source term [$M L^{-3} \theta^{-1}$]
R	Universal gas constant (8.314 kJ mol $^{-1}$ K $^{-1}$)
R_p	Relative permeability
S	Saturation
T	Temperature [T]
t	Time [θ]
u	Internal energy [$L^2 \theta^{-2}$]
v	Darcy velocity [$L \theta^{-1}$]
w	Weighting factor for time discretization
z	Coordinate oriented in the direction of gravity
α_D	Dispersivity of solute in transport calculations [L]
α_G	Parameter used in van Genuchten capillary pressure model [L^{-1}]
ε	Tolerance for solution scheme
η	Mass fraction of air
θ	Exponent used in the air/water diffusion model
λ	Parameter in van Genuchten R_p and capillary pressure models
μ	Viscosity [$M L^{-1} \theta^{-1}$]
ν	Fractional vapor flow parameter
ρ	Density [$M L^{-3}$]
τ	Tortuosity factor in the air/water diffusion model
ϕ	Porosity [$L^{-3} L^{-3}$]

Flow and Energy Transport Equations

The standard governing equations used in FEHM describe heat and mass transfer, noncondensable gas flow and solute transport within porous and permeable media (e.g. *Faust and Mercer [1979]*).

Conservation of mass for water is expressed as:

$$\frac{\partial A_m}{\partial t} = \bar{\nabla} \cdot \bar{f}_m + q_m = 0 \quad (\text{A-1})$$

where the mass per unit volume, A_m , is given by

$$A_m = f(S_v \mathbf{r}_v (1 - \mathbf{h}_v) + S_l \mathbf{r}_l (1 - \mathbf{h}_l)) \quad (\text{A-2})$$

and the mass flux, f_m , is given by

$$\mathbf{f}_m = (1 - \mathbf{h}_v) \mathbf{r}_v \bar{v}_v + (1 - \mathbf{h}_l) \mathbf{r}_l \bar{v}_l \quad (\text{A-3})$$

Here, ϕ is the porosity, S is saturation, ρ is density, η is the concentration of the noncondensable gas expressed as a fraction of the total mass, v is velocity, source and sink terms are represented by the term q_m and the subscripts v and l indicate quantities for the vapor phase and the liquid phase, respectively.

Conservation of energy is expressed as:

$$\frac{\partial A_e}{\partial t} = \bar{\nabla} \cdot \bar{f}_e + q_e = 0 \quad (\text{A-4})$$

where the energy per unit volume, A_e , is given by

$$A_e = (1 - f) \mathbf{r}_r u_r + f(S_v \mathbf{r}_v u_v + S_l \mathbf{r}_l u_l) \quad (\text{A-5})$$

with $u_r = c_{pr}T$, and the energy flux, f_e , expressed as

$$\mathbf{f}_e = \mathbf{r}_v h_v \bar{v}_v + \mathbf{r}_l h_l \bar{v}_l - K \bar{\nabla} T \quad (\text{A-6})$$

Here, u is specific internal energy, c_{pr} is specific heat, h is specific enthalpy; K is effective thermal conductivity, T is temperature, q_e is the energy contributed from

sources and sinks, and the subscripts v, l , and r refer to vapor, liquid and solid (*rock*) phases, respectively.

To complete the governing equations, it is assumed that Darcy's Law applies to the movement of the vapor and liquid phases:

$$\bar{v}_v = \frac{k R_v}{\mathbf{m}_v} (\bar{\nabla} P_v - \mathbf{r}_v \bar{g}) \quad (\text{A-7})$$

and

$$\bar{v}_l = \frac{k R_l}{\mathbf{m}_l} (\bar{\nabla} P_l - \mathbf{r}_l \bar{g}). \quad (\text{A-8})$$

Here k is the permeability, R is the relative permeability, μ is viscosity, g represents the acceleration due to gravity, and P_v and P_l are phase pressures. The phase pressures are related by: $P_v = P_l + P_{cap}$, where P_{cap} refers to the capillary pressure.

By applying Darcy's Law, the basic conservation Equations (A-1) through (A-4) are combined to yield the fluid flow and energy equations for an isotropic medium:

$$\begin{aligned} & -\bar{\nabla} \cdot ((1-h_v) D_{mv} \bar{\nabla} P_v) - \bar{\nabla} \cdot ((1-h_l) D_{ml} \bar{\nabla} P_l) + q_m + \\ & \frac{\partial}{\partial z} g ((1-h_v) D_{mv} \mathbf{r}_v + (1-h_l) D_{ml} \mathbf{r}_l) + \frac{\partial A_m}{\partial t} = 0 \end{aligned} \quad (\text{A-9})$$

and

$$\begin{aligned} & -\bar{\nabla} \cdot (D_{ev} \bar{\nabla} P_v) - \bar{\nabla} \cdot (D_{el} \bar{\nabla} P_l) + \bar{\nabla} \cdot (K \bar{\nabla} T) + q_e + \\ & \frac{\partial}{\partial z} g (D_{ev} \mathbf{r}_v + D_{el} \mathbf{r}_l) + \frac{\partial A_e}{\partial t} = 0 \end{aligned} \quad (\text{A-10})$$

where z is oriented in the direction of gravity. Here, the transmissibilities are given by

$$D_{mv} = \frac{k R_v \mathbf{r}_v}{\mathbf{m}_v}, \quad D_{ml} = \frac{k R_l \mathbf{r}_l}{\mathbf{m}_l} \quad (\text{A-11a,b})$$

and

$$D_{ev} = h_{mv} D_{mv}, \quad D_{el} = h_{ll} D_{ml} \quad (\text{A-12a,b})$$

If the total mass withdrawal, q_m , is specified in the input file, then the energy withdrawal, q_e , is determined as: $q_e = q_v h_v + q_l h_l$ (A-13)

where $q_v = n q_m$, $q_l = (1-n) q_m$, (A-14)

and $n = \frac{1}{1 + \frac{\mathbf{r}_l R_l \mathbf{m}_v}{\mathbf{r}_v R_v \mathbf{m}_l}}$. (A-15)

The form of Equation (A-15) shows how important the relative permeability ratio R_l/R_v is in controlling the discharge composition.

The mass flux, \underline{f}_η , source (or sink) strength, q_η , and accumulation term, A_η , are defined as follows for the noncondensable gas conservation equation:

$$\overline{f}_h = \mathbf{h}_v \mathbf{r}_v \overline{v}_v + \mathbf{h}_l \mathbf{r}_l \overline{v}_l, \quad (\text{A-16})$$

$$q_h = \mathbf{h}_v q_v + \mathbf{h}_l q_l, \quad (\text{A-17})$$

and $A_h = \mathbf{f}(\mathbf{h}_v S_v \mathbf{r}_v + \mathbf{h}_l S_l \mathbf{r}_l)$. (A-18)

The noncondensable gas conservation equation is:

$$-\overline{\nabla} \cdot ((\mathbf{h}_v) D_{mv} \overline{\nabla} P_v) - \overline{\nabla} \cdot ((\mathbf{h}_l) D_{ml} \overline{\nabla} P_l) - \overline{\nabla} \cdot (D_{va} \overline{\nabla} \mathbf{h}_v) + q_h + \frac{\partial}{\partial z} g((\mathbf{h}_v) D_{mv} \mathbf{r}_v + (\mathbf{h}_l) D_{ml} \mathbf{r}_l) + \frac{\partial A_h}{\partial t} = 0 \quad (\text{A-19})$$

Here, η is the concentration of the noncondensable gas expressed as a fraction of the total mass. The molecular diffusivity of water vapor in air (from *Pruess* [1991]) is given by:

$$D_{va} = t f S_v D_{va}^0 \mathbf{r}_v \frac{0.101325 \left[\frac{T + 273.15}{273.15} \right]^q}{P}, \quad (\text{A-20})$$

where τ is the tortuosity factor and D_{va}^0 is the value of D_{va} at standard conditions. Within FEHM, the value of D_{va} is set to $2.4 \times 10^{-5} \text{ m}^2 \text{ s}^{-1}$, θ is set to 2.334, and the tortuosity factor is an input parameter.

The Equations (A-9), (A-10), and (A-20) represent the model equations for fluid and energy transport in the computer code FEHM.

Solute Transport Equations

FEHM simulates the movement of tracer solutes traveling in either the liquid or gas phases and allows for a variety of reactive transport capabilities, but only passive transport equations and model applications are described in this Appendix. It is important to note that solutes are assumed to be present in trace quantities, such that their presence does not impact the fluid properties or the computed flow fields. For example, osmotic potential is not considered. The solute transport equations are not directly coupled to the heat and mass transfer system, but use the flow rates and temperatures obtained by the heat and mass transfer solution. The mass flux, f_c , source (or sink) strength, q_c , and accumulation term, A_c , are defined as follows for a

$$\text{solute:} \quad \bar{f}_c = C_v \mathbf{r}_v \bar{v}_v + C_l \mathbf{r}_l \bar{v}_l \quad (\text{A-21})$$

$$q_c = C_v q_v + C_l q_l \quad (\text{A-22})$$

$$A_c = f(C_v S_v \mathbf{r}_v + C_l S_l \mathbf{r}_l) \quad (\text{A-23})$$

The transport equation for a solute is expressed as:

$$\begin{aligned} & -\bar{\nabla} \cdot (C_v D_{mv} \bar{\nabla} P_v) - \bar{\nabla} \cdot (C_l D_{ml} \bar{\nabla} P_l) - \bar{\nabla} \cdot (D_{cv} \bar{\nabla} C_v) - \bar{\nabla} \cdot (D_{cl} \bar{\nabla} C_l) + \\ & \frac{\partial}{\partial z} g(C_v D_{mv} \mathbf{r}_v + C_l D_{ml} \mathbf{r}_l) + \frac{\partial A_c}{\partial t} = 0 \end{aligned} \quad (\text{A-24})$$

Here, C is the concentration of the solute. The term, $\bar{\nabla} \cdot (D_c \bar{\nabla} C)$, is the dispersion term. Equation (A-24) is the equation for a non-reactive solute present in either the liquid or gas phases, or one that partitions between the liquid and gas. Several solutes can be simulated simultaneously. The transport terms can be set as a function of position, and there is no requirement that they be the same for all solutes present in a phase. For example, a solute may possess different diffusion coefficients associated with specified regions within the mesh, and multiple solutes may possess different diffusion coefficients. For a Henry's Law species, one that partitions between the liquid and vapor phases, all transport terms of Equation A-26 are retained. The vapor concentration is related to the liquid concentration assuming the equilibrium Henry's

Law equation:

$$C_v = \frac{M_w C_l}{M_v K_H P_v} \quad (\text{A-25})$$

where M_w is the molecular mass of water, M_v is the molecular mass of the vapor, P_v is the gas pressure, and K_H is the Henry's Law coefficient. FEHM uses a standard formulation for the dispersion coefficient: $D_c = D_{AB} + \alpha_d \nu$ (A-26)

The Darcy velocity is computed from the solution of the fluid flow equation. The dispersivity, α_d , and the molecular diffusion coefficient, D_{AB} , are properties of the medium, the fluid and the solute.

Boundary Conditions

FEHM allows for two types of fluid (mass) sources and sinks: a specified-flow-rate source/sink and a specified-pressure condition at a source/sink. No-flow or impermeable boundary conditions are assumed for the perimeter of the finite-element mesh unless specified otherwise. The energy (temperature) and solute concentration

specified at a source/sink or flowing pressure node refers only to the incoming fluid value. If there is fluid flow out of the node, stability dictates that the energy and solute concentration of the in-place fluid be used in calculations. However, the user may opt to override the last stipulation with regard to solute calculations and specify that a tracer species be prevented from leaving a fluid sink node. Specified saturations, relative humidities, air mass fractions as well as specified air flows may also be held constant at specified nodes using source/sinks to achieve the fixed variable values, analogous to the method for implementing pressure boundary conditions.

The constant pressure boundary condition uses a pressure dependent flow term: $q_{m,i} = I_{m,i}(P_{flow,i} - P_i)$, (A-27)

where, P_i is the pressure at the source node i , $P_{flow,i}$ is the specified flowing pressure, $I_{m,i}$ is the impedance, and $q_{m,i}$ is the mass flow rate. By specifying a large I , the pressure is forced to equal P_{flow} . Likewise, a specified heat flow can be input or a specified temperature obtained as follows: $q_{e,i} = I_{e,i}(T_{flow,i} - T_i)$. (A-28)

Here, T_i is the temperature at the source node i , $T_{flow,i}$ is the specified flowing temperature, $I_{e,i}$ is the impedance to heat flow (thermal resistance), and $q_{e,i}$ is the heat flow.

In FEHM, there is also a provision for creating large volume reservoirs that effectively hold variables at constant values. The nodes are labeled on input and the volumes replaced after the calculation of the geometric coefficients with a reservoir volume of 10^{13} m^3 . For example, the solute concentration at a node can be fixed using this approach. In that case, the fixed-concentration node can act as either a

source or a sink for solute, depending on the concentration gradient at adjacent locations.

Constitutive Relationships

FEHM uses the National Bureau of Standards Steam Tables given in *Harr et al.* [1984] to compute the densities, viscosities, and enthalpies of water, water vapor, and air, given nodal pressures and temperatures. Because FEHM is an implicit code that uses a Newton-Raphson iteration scheme, derivatives of the thermodynamic functions with respect to pressure and temperature are also required to calculate pressure- and temperature-dependent fluid properties. FEHM uses saturation line equations in determining the phase state of the liquid-vapor system. In a mixture of water and air or other noncondensable gas, the saturation line is simply the partial pressure of water or the vapor pressure of water.

FEHM allows for the inclusion of a vapor pressure lowering term, which may be important in situations where high capillary forces are present. The modified vapor pressure (modified from *Jury et al.* [1991]) is given by:

$$P_v^*(T, P_{cap}) = P_v(T) \exp\left(\frac{P_{cap} M_w}{R(T + 273.15)}\right), \quad (\text{A-29})$$

where P_v^* is the new vapor pressure of water, P_{cap} is the capillary pressure, and R is the gas constant and M_w molecular mass of water. The vapor pressure lowering routine allows for isothermal vapor transfer, i.e. vapor density dependence on pressure.

Appropriate thermodynamic information for air and air/vapor mixtures are contained within FEHM. The density of air, ρ_a is assumed to obey the ideal gas law. Using atmospheric conditions as the reference state,

$$\mathbf{r}_a = 1.292864 \left(\frac{273.15}{T + 273.15} \right) \left(\frac{P_a}{0.101325} \right), \quad (\text{A-30})$$

where ρ_a has the units kg m^{-3} , T is in $^{\circ}\text{C}$, and P is in MPa. The mixture density is given by: $\mathbf{r}_v = \mathbf{r}_{v,w} + \mathbf{r}_a$, (A-31)

where $\rho_{v,w}$ is the density of water vapor. The enthalpy of air, h_a , is specified as a function of temperature only as: $h_a = (c_{pa}(T))(T \cdot 10^{-6})$, (A-32)

where c_{pa} is the temperature-dependent heat capacity of air ($\text{MJ kg}^{-1} \text{ }^{\circ}\text{C}^{-1}$). The mixture enthalpy for the vapor phase is given by: $h_v = h_{v,w}(1 - \mathbf{h}_v) + h_a \mathbf{h}_v$, (A-33)

where $h_{v,w}$ is the enthalpy of steam and η_v is the fraction by mass of air in the vapor phase. The mixture enthalpy of the liquid phase is given by:

$$h_l = h_{l,w}(1 - \mathbf{h}_l) + h_a \mathbf{h}_l, \quad (\text{A-34})$$

where $h_{l,w}$ is the enthalpy of liquid water and η_l is the mass fraction of air in the liquid phase. Assuming ideal gas behavior, the mass fraction of air in the vapor phase

may be expressed as: $\mathbf{h}_v = \frac{\mathbf{r}_a}{\mathbf{r}_v}$. (A-35)

The mass fraction of air in the liquid phase is assumed to obey Henry's law:

$$\mathbf{h}_l = K_{H,a} P_a, \quad (\text{A-36})$$

where K_H is the Henry's law constant for air ($= 1.611 \times 10^{-4} \text{ Pa}^{-1}$) and P_a is the partial pressure of air. The viscosity of the vapor phase is assumed to be a linear combination of the air viscosity and the water viscosity:

$$\mathbf{m}_v = \mathbf{m}_{v,w} (1 - \mathbf{h}_v) + \mathbf{m}_a \mathbf{h}_v, \quad (\text{A-37})$$

where $\mu_{v,w}$ is the steam viscosity and is obtained from steam data. The viscosity of air, $\mu_{v,w}$, is assumed constant at $1.82 \times 10^{-8} \text{ N s m}^{-2}$. The liquid phase viscosity is assumed to be independent of the amount of dissolved air and is computed from look-up tables.

Relative permeabilities and capillary pressures depend on saturation. The well-known van Genuchten relative permeability functions [*van Genuchten*, 1980] are among those available within FEHM and are described as follows:

$$R_l = \begin{cases} \frac{\left[1.0 - \left(1.0 \hat{S}_l^{\frac{1}{I}} \right)^n \right]^2 \sqrt{\hat{S}_l}}{1.0}, & \hat{S}_l < \hat{S}_{l\max} \\ 1.0, & \hat{S}_l \geq \hat{S}_{l\max} \end{cases} \quad (\text{A-38})$$

$$R_v = 1.0 - R_l \quad (\text{A-39})$$

Here, $\hat{S}_l = \frac{S_l - S_{lr}}{S_{l\max} - S_{lr}}$ and $I = 1 - \frac{1}{n}$, where n is an experimentally determined

parameter. R_l and R_v are values between 0 and 1. The van Genuchten functions [*van Genuchten*, 1980] for capillary pressure are described by the following equations:

$$P_{cap} = \begin{cases} P_{capmax}, & P_{cap1} \geq P_{capmax} \\ P_{cap1}, & P_{cap1} < P_{capmax} \\ 0.0, & S_l \geq S_{lmax} \end{cases} \quad (\text{A-40})$$

where $P_{cap1} = P_0 \left[\hat{S}^{\frac{1}{I}} - 1.0 \right]^{1.0-I}$, and $P_0 = \frac{1.0}{\alpha_G}$ (α_G is another experimentally

determined parameter). The van Genuchten capillary pressure curves approach an infinite value as S_l approaches 0 and 1. This requires the use of extrapolation techniques. At low saturations, linear or cubic fits are available. At high saturations, a linear fit is used.

Discretization and Numerical Solution Methods

FEHM uses the standard first order method [*Hinton and Owen, 1980*] to discretize the time derivatives as follows:

$$f(t^{n+1}) = f(t^n) + \mathbf{Dt} [w f'(t^{n+1}) + (1-w) f'(t^n)] \quad (\text{A-41})$$

Spatial discretization is accomplished using the finite-element method that is based on the Galerkin formulation [*Zienkiewicz, 1977*]. The application of the discretization methods to the governing partial differential equations yields a system of nonlinear algebraic equations. To solve these equations, FEHM allows for either Gauss or Lobatto integration and a Newton-Raphson iterative procedure. The Newton-Raphson iteration method makes use of the derivative information to reduce mass balance residuals. The procedure begins by making an initial guess at the solution, which is usually taken as the solution from the previous timestep. At each step, the residuals are compared with a prescribed error tolerance to determine if the convergence criterion has been met. Semiautomatic timestep control is based on the

number of iterations required for convergence. If the code is unable to find a solution such that the residuals become less than the tolerance within the specified number of iterations, the timestep is reduced and the procedure repeated. On the other hand, if convergence is rapid, the timestep is multiplied by a user-supplied factor (>1), thus allowing for large timesteps when appropriate. Minimum and maximum timestep sizes, specified as input, bound the timestep extremes. The linear equations are solved at each Newton-Raphson iteration by employing orthogonalizations to Jacobian matrices.

FEHM APPLICATION

The remaining sections in Appendix A describe the direction application of FEHM to the flow and transport problems addressed in this dissertation. Parameters related to matrix and solute properties, boundary condition implementation, spatial and temporal discretization, and numerical routines are provided here.

Matrix Properties

Matrix properties including tortuosity factor, rock thermal conductivity, saturated permeability, van Genuchten relative permeability parameters, and porosity were specified in the **adif**, **cond**, **perm**, **rpl**, and **rock** control statements, respectively (refer to Table A-1 at the end of Appendix A for a complete list of control statements used). Values unique to individual simulations are provided in the main text of this dissertation. The following parameter constants were common to all simulations: tortuosity factor= 0.66 (following *Penman* [1940a,b]), rock thermal conductivity =

$2.5 \text{ W m}^{-1} \text{ K}^{-1}$, rock (solid particle) density = 2650 kg m^{-3} , and rock specific heat = $1000 \text{ J kg}^{-1} \text{ K}^{-1}$.

Solute Parameters

Each simulation that included solution transport required the following information in the **trac** control statement: initial solute condition, injection or fixed concentrations at the boundary nodes, duration of injection, solute molecular diffusion coefficient and dispersivity. These parameters varied among the simulations presented in this study and are described within the main text. The simulations were rather insensitive to dispersivity values due to the low flow rates within the modeled systems. In contrast, most simulations displayed rather high sensitivity to diffusion coefficients. Two approaches were used in FEHM to describe solute molecular diffusion coefficient. The first approach employed a user-specified constant effective molecular diffusion coefficient. The second more rigorous approach used the empirical relationship developed in *Wright and Conca* [1992] to calculate a moisture-dependent diffusion coefficient. Input required for bounding the *Wright and Conca* [1992] function included a diffusion coefficient value at saturation and a residual water content, below which diffusion is negligible.

Initial and Boundary Conditions

For simulations that addressed transient flow and transport, the initial conditions were read in from a restart file. Information contained in the restart file included saturation, temperature, pressure, and concentration (if used) values assigned

to each node. The restart file was generated by running an initial simulation to steady state. Or, in the case of series-simulations, the restart file consisted of an output file generated by the previous simulation (not necessarily run to steady state). Initial conditions required for the simulation to generate the first restart file included arbitrary assignment of nodal temperatures, saturations (or pressures) and concentrations (if used).

A fixed pressure equivalent to atmospheric pressure specified for the bottom boundary nodes represented the water-table condition. A constant mass flux of water at the upper boundary nodes served as a continuous fluid source and represented either precipitation or effective precipitation, depending on the specific case modeled. Here, effective precipitation refers to the residual soil-water flux, i.e. precipitation – evaporation – transpiration. Specified concentrations, in terms of moles per kg of water, at the source nodes (upper boundary) produced a constant solute flux. A unique approach was taken in this study to represent the hydraulic conditions at the base of root zone. A fixed saturation was applied to the two nodes that defined the base of the root zone. Specified saturations near the residual values corresponded to very negative matric pressures, as related by the van Genuchten function, and served as sinks for water. The fixed-saturation/liquid pressure condition, below the upper boundary of the model domain, took up all water from the above source, and drew water from below, as well. However, the fixed-saturation/pressure condition did not serve as a solute sink. An input flag designated in the **trac** control statement prevented the solute species to exit through root-zone sink nodes. This specification

was critical for simulating chloride behavior: chloride is nonvolatile and is not taken out of the system by plants.

Fixed temperatures at the bottom boundary nodes and the top boundary nodes were implemented as the energy boundary conditions in the **hflx** and **flow** control statements. The resulting temperature gradient established a heat flux through the vertical column. The heat flux was essentially linear for the examples provided in this study, since the low fluid flow rates did not significantly perturb the temperature profile, nor did the bulk thermal conductivity vary significantly along the temperature gradient.

Finite-element Mesh

A ladder-type finite-element mesh representing a 1-D vertical column was employed for all simulations conducted in this study. The simulations presented here employed a grid containing 500 nodes and 249 elements. Grids containing both more and less nodes were used in experimental simulations to test sensitivity and assess the distances at which the solution became affected or did not converge, but are not shown here. Variable nodal spacing was used in all grids to achieve finer resolution near the boundaries and coarser resolution away from the boundaries. Minimum nodal distances ranged from 5 cm to 25 cm and maximum nodal distances ranged from 1 m to 5 m.

Numerical Routine Parameters

Specifications associated with the numerical routine and calculations were given in the **ctrl**, **iter**, **sol**, and **time** control statements of the input deck. A standard

pure implicit formulation (backward-in-time Euler) was used for discretization of the time derivatives ($w = 1$ in Equation A-41, Appendix A). A value of 1.0 was specified for upstream weighting in the spatial discretization using finite-element Galerkin formulation. The integration scheme employed was Lobatto integration [Young, 1981]. The nonlinear equation tolerance (Newton cycle) was set at the default value of $1e-5$. The linear equation solver used eight orthogonalizations. Second order partial Gauss elimination was specified.

For most simulations, an initial timestep size of 1 day was specified. However, if the convergence criteria for solution specified were not met, the timestep would be reduced until either 1) the convergence was achieved and the simulation proceeded, or 2) the timestep reduction reached the minimum timestep size and/or the number of iteration exceeded the maximum number iterations allowed, resulting in simulation termination. The minimum time-step size of $1 e-9$ day and maximum number of 40 iterations were set in the **ctrl** control statement. The timestep multiplier allowed the timestep to increase from the previous timestep by a factor of 1.2 to 1.8 if ten or less iterations were required for solution convergence at the previous timestep. If more than ten iterations were necessary, the timestep size remained the same for the next time. A maximum timestep size of 10 years was specified for flow-only solutions. The maximum timestep size was limited to 1 year for simulations that considered solute transport.

NAME	FUNCTION
adif	Enables air-water diffusion, input for tortuosity factor
cond	Input for thermal conductivity parameters
coor	Input for node-coordinate data
ctrl	Input for program-control parameters
elem	Input for element-node data
flow	Input for flow boundary conditions
iter	Input for iteration parameters
ngas	Input for noncondensable gas data
node	Input for node numbers for output and time histories
perm	Input for permeability parameters
pres	Input for initial P,T, and S conditions (unless using restart file)
rlp	Input for relative permeability data
rock	Input for rock parameters (density, specific heat and porosity)
sol	Input for solver specifications
stop	Signal for the end of input
text	Input for text to be written to the output file
time	Input for timestep and flow simulation time
trac	Input for solute simulation
vapl	Enables isothermal vapor flow
zone	Defines geometry of grid for input-parameter assignment

Table A-1. List of control statements employed for simulations presented in this study.

APPENDIX B**DATA FROM THE NEVADA TEST SITE UNSATURATED ZONE CORES**

Frenchman Flat Cores Water Potential

Frenchman Flat Cores Chloride

Frenchman Flat Cores Stable Isotopes, δD and $\delta^{18}O$

UE6s Grain Size Analysis

Shallow series A1 Grain Size Analysis

Shallow series A3 Grain Size Analysis

UE6e Grain Size Analysis

UE6s Bulk Density

UE6s Gravimetric Water Content

Yucca Flat Shallow Series Cores Gravimetric Water Content

UE6s Water Potential

Yucca Flat Shallow Series Cores, Water Potential

Yucca Flat Shallow Series Cores, Chloride and Nitrate

UE6s Chloride

UE6e Chloride

UE6s Stable Isotopes, δD and $\delta^{18}O$

Frenchman Flat PW-1 Core Water Potential Measurements

Core	Depth (m)	Water Potential (MPa)	Water Potential (m)
PW-1	8.26	-8.15	-850
	14.96	-2.53	-271
	17.93	-2.25	-242
	20.75	-2.53	-271
	23.87	-1.57	-172
	29.81	-3.08	-328
	39.03	-3.56	-377
	42.15	-1.15	-129
	48.24	-1.02	-115
	51.44	-0.814	-94
	54.64	-0.95	-108
	60.88	-0.882	-101
	66.75	-0.746	-87
	78.93	-0.474	-59
	85.02	-0.406	-52
	85.19	-0.474	-59
	90.67	-0.203	-31
	90.81	-0.406	-52
	96.82	-0.474	-59
	97.13	-0.474	-59
	109.08	-1.15	-129
	109.16	-1.22	-136
	109.62	-0.339	-45
	112.36	-0.339	-45
	121.88	-0.61	-73
	140.15	-0.406	-52
	152.26	-0.474	-59
	164.52	-0.678	-80
	176.74	-0.95	-108
	176.90	-0.406	-52
188.45	-0.0677	-17	
201.15	-0.271	-38	
213.64	-0.135	-24	
221.25	-0.339	-45	

Frenchman Flat PW-2 and PW-3 Cores Water Potential Measurements

Core	Depth (m)	Water Potential (MPa)	Water Potential (m)
PW-2	0.25	-0.14	-24
	0.42	-8.66	-902
	8.95	-2.25	-242
	12.09	-1.77	-193
	12.45	-1.91	-207
	20.92	-0.95	-108
	30.27	-0.54	-66
	36.21	-0.34	-45
	39.19	-0.41	-52
	60.82	-0.41	-52
	76.05	-0.14	-24
	PW-3	0.34	-1.94
1.03		-37.5	-3873
15.18		-7.37	-769
15.72		-4.96	-521
30.57		-1.98	-214
39.94		-1.91	-207
61.03		-1.5	-165
75.88		-1.22	-136
76.72		-1.02	-115
106.42		-0.746	-87
121.74		-1.43	-158
137.72		-0.814	-94
152.03		-0.678	-80
167.57		-0.882	-101

Frenchman Flat Cores Chloride Measurements (in porewater concentrations)

Depth (m)	Chloride (mg L ⁻¹)	Depth (m)	Chloride (mg L ⁻¹)	Depth (m)	Chloride (mg L ⁻¹)
PW-1		PW-2		PW-3	
8.34	3500.0	0.34	52.3	0.19	80.2
14.58	2000.0	0.80	8974.4	0.88	116.6
17.78	1836.1	9.10	1254.9	15.35	2444.4
20.60	2125.0	11.77	974.4	15.95	2664.8
23.72	1454.6	12.15	421.1	30.42	810.2
29.97	1978.3	30.58	21.8	39.49	867.8
39.10	2690.2	36.44	14.7	60.73	1320.4
42.38	2184.8	39.49	14.3	60.88	1237.6
48.70	1744.7	61.11	4.6	76.04	864.0
51.59	1654.6	76.34	23.1	76.42	803.2
54.41	1323.9	94.77	10.3	152.19	17.2
60.65	617.0	145.64	238.1	167.34	20.3
66.82	244.9	152.19	260.0		
78.70	22.7	228.03	21.7		
84.87	9.8				
85.25	7.9				
90.73	17.7				
90.89	11.5				
96.90	16.1				
97.05	14.3				
109.09	82.0				
112.44	12.9				
122.11	10.2				
140.23	8.1				
152.19	3.7				
164.75	11.2				
176.66	33.3				
176.81	8.3				
188.59	8.0				
213.26	4.8				
219.43	5.4				
220.87	8.2				
221.33	17.5				
221.56	6.5				
225.29	9.1				
231.54	8.8				
240.29	12.6				

Frenchman Flat PW-1 Core Stable Isotope, δD and $\delta^{18}\text{O}$, Measurements

Sample	Depth	δD	$\delta^{18}\text{O}$
PW-1	(m)	(‰)	(‰)
	8.47	-89	-6.6
	14.73	-94	-8.6
	20.65	-97	-9.2
	29.72	-98	-9.7
	38.92	-99	-10.4
	48.36	-107	-12.3
	54.45	-108	-12.4
	60.53	-109	-13.1
	66.62	-111	-13.8
	78.74	-111	-13.9
	90.92	-114	-14.4
	109.25	-109	-14.0
	121.90	-113	-14.5
	140.00	-112	-13.9
	151.74	-109	-13.7
	164.52	-111	-13.8
	176.90	-109	-13.9
	188.27	-109	-13.7
	200.75	-108	-12.8
	213.46	-112	-13.9
	225.11	-100	-12.5
	240.03	-108	-13.6
	243.61	-106	-13.6

Frenchman Flat PW-2 and PW-3 Cores
Stable Isotope, δD and $\delta^{18}\text{O}$, Measurements

Sample	Depth	δD	$\delta^{18}\text{O}$
PW-2	(m)	(‰)	(‰)
	0.65	-66	-1.5
	9.02	-87	-6.6
	12.29	-95	-8.2
	12.60	-95	-8.4
	19.45	-112	-12.7
	30.33	-119	-14.2
	36.27	-120	-13.9
	39.24	-124	-15.6
	60.85	-127	-15.7
	76.06	-118	-14.1
	94.57	-119	-14.6
	121.69	-115	-14.4
	145.78	-101	-11.8
	151.96	-112	-13.8
	218.81	-78	-9.6
	248.99	-95	-11.2
PW-3	(m)	(‰)	(‰)
	0.15	-53	4.8
	1.23	-57	2.3
	19.78	-94	-8.4
	20.57	-100	-10.2
	39.51	-115	-13.1
	51.62	-119	-13.9
	78.57	-119	-14.0
	78.97	-119	-14.2
	98.60	-119	-14.1
	98.90	-122	-14.6
	137.98	-118	-14.3
	157.77	-115	-13.3
	178.51	-110	-12.7
	197.05	-112	-13.5
	216.96	-110	-12.9
	251.90	-97	-10.8
	283.37	-103	-13.3

UE6s Grain Size Analysis Measurements

Sample	Depth	Gravel	Sand	Silt	Clay
	(m)	(weight %)	(weight %)	(weight %)	(weight %)
2-4	1.00	10.3	75.7	8.2	5.7
3-3	1.45	21.9	38.6	24.0	15.4
4-3	2.20	6.7	59.0	23.3	11.0
5-3	2.82	9.9	64.9	13.0	12.1
7-2	3.58	24.0	55.4	10.0	10.6
9-3	4.39	30.5	44.3	9.4	15.8
12-2	5.14	12.5	62.1	15.1	10.3
15-3	6.55	21.1	53.3	15.7	9.9
48-4	35.28	15.6	57.2	13.7	13.5
57-1	45.14	7.1	68.9	15.7	8.2

Shallow series A1 Grain Size Analysis Measurements

Sample	Depth	Gravel	Sand	Silt	Clay
	(m)	(weight %)	(weight %)	(weight %)	(weight %)
A1-1	0.08	10.4	51.7	22.4	15.5
A1-2	0.53	2.8	49.7	35.3	12.2
A1-4	1.45	20.1	69.9	3.4	6.5
A1-6	2.36	6.7	66.4	10.7	16.3
A1-8	3.28	1.9	57.3	17.6	23.1
A1-10	4.19	10.1	61.4	18.8	9.7
A1-11	4.65	1.9	74.7	14.8	8.6
A1-12	4.95	8.1	63.2	16.6	12.1

Shallow series A3 Grain Size Analysis Measurements

Sample	Depth	Gravel	Sand	Silt	Clay
	(m)	(weight %)	(weight %)	(weight %)	(weight %)
A3-1	0.08	3.5	56.1	27.2	13.1
A3-2	0.53	17.7	31.4	27.4	23.5
A3-4	1.45	3.3	47.1	29.1	20.4
A3-6	2.36	4.6	60.4	21.8	13.1
A3-8	3.28	15.5	57.6	14.0	12.9
A3-10	4.19	28.1	48.3	10.7	13.0
A3-12	4.95	13.6	63.9	11.9	10.6

UE6e Grain Size Analysis Measurements

Depth	Gravel	Sand	Silt	Clay
(m)	(weight %)	(weight %)	(weight %)	(weight %)
42.0	18.3	57.1	12.2	12.4
46.9	7.3	71.6	12.5	8.7
52.4	21.2	48.9	19.8	10.1
57.9	20.1	51.1	18.8	10.1
65.8	12.7	47.4	24.8	15.2
72.5	10.1	61.6	17.6	10.9
78.6	20.3	53.1	16.2	10.3
83.8	13.3	61.5	17.0	8.2
94.1	21.1	47.3	21.1	10.6
100.5	21.2	56.7	13.6	8.5
106.6	14.8	65.8	12.3	7.1
111.8	30.2	52.1	11.3	6.4
116.4	20.7	48.2	21.8	9.4
124.0	3.7	56.3	26.6	13.5
134.0	8.4	56.1	26.1	9.4
138.6	17.9	52.2	22.6	7.3
141.0	21.5	40.2	28.2	10.1
145.3	8.2	67.7	15.8	8.3
147.7	5.2	55.1	29.0	10.8
152.3	11.6	55.0	20.9	12.5
156.3	11.8	57.7	15.6	14.8
158.7	12.8	54.8	16.9	15.6
163.9	35.7	32.2	23.6	8.5
173.0	29.8	53.9	10.7	5.5
176.1	9.8	37.1	41.5	11.6
182.8	29.7	32.8	24.7	12.8
185.8	13.8	54.4	24.7	7.2
190.4	10.1	55.0	20.0	14.8
198.0	26.1	47.4	16.4	10.2
204.7	6.5	48.1	32.8	12.5
207.4	5.1	41.3	37.3	16.3
211.4	1.3	44.2	32.9	21.6
213.2	25.5	43.5	20.8	10.2
216.3	1.2	41.4	45.4	12.1
219.3	13.1	54.4	19.1	13.4
223.9	2.6	33.0	48.1	16.3
226.9	5.4	52.9	24.8	17.0
230.0	1.4	55.2	26.1	17.2
233.0	7.4	49.1	26.7	16.7
236.1	8.5	44.0	33.7	13.9
239.1	4.4	50.9	27.8	16.8
243.7	13.5	48.6	20.0	17.9
251.3	8.1	47.2	30.5	14.3

UE6e Grain Size Analysis Measurements - continued

Depth	Gravel	Sand	Silt	Clay
(m)	(weight %)	(weight %)	(weight %)	(weight %)
257.4	19.1	45.6	22.1	13.2
260.4	15.2	35.0	39.8	10.0
263.5	5.8	45.7	35.3	13.2
266.2	16.5	41.8	19.1	22.6
269.3	12.1	43.9	33.1	11.0
274.7	24.2	37.1	25.2	13.4
278.7	23.0	44.1	21.9	10.9
281.8	13.9	44.0	32.2	9.9
284.5	12.5	44.2	33.8	9.4
287.5	26.5	39.5	24.7	9.4
290.9	14.6	46.6	29.2	9.6
294.2	12.2	69.5	14.7	3.6
297.3	6.9	67.1	21.1	4.9
300.0	26.3	42.1	22.8	8.8
303.1	31.0	27.2	33.8	8.0
306.1	17.0	39.4	34.8	8.8
310.7	13.7	34.3	41.8	10.1
315.3	22.1	61.6	11.1	5.3
318.3	35.7	48.1	8.3	7.8
321.4	31.4	35.8	21.9	11.0
324.4	61.1	26.1	10.8	2.0
327.4	20.2	50.8	20.2	8.8
330.5	16.2	69.2	10.7	3.8
335.1	24.6	50.1	15.3	10.0
341.2	31.5	51.3	13.3	3.9
348.8	48.9	37.6	11.2	2.3
352.7	18.2	61.2	16.4	4.2
361.0	30.9	54.2	12.5	2.5
366.1	44.3	44.0	9.4	2.2
373.1	28.8	53.4	13.7	4.0
378.6	18.7	65.8	12.1	3.4
385.3	33.1	51.5	12.2	3.1
389.9	21.6	60.7	15.5	2.2
396.0	24.2	56.9	15.6	3.3
401.2	69.1	26.0	3.8	1.0
408.2	44.2	42.6	11.0	2.2
409.7	23.2	34.9	36.6	5.3
412.7	74.1	21.1	3.5	1.2
414.3	4.8	43.1	27.5	24.6
420.3	16.9	48.9	29.8	4.3
447.2	74.4	16.0	6.4	3.2
449.3	89.5	3.4	4.4	2.7

UE6s Bulk Density Measurements

Depth	Bulk Density		Depth	Bulk Density
(m)	(g cm ⁻³)		(m)	(g cm ⁻³)
0.84	1.50		26.42	1.38
1.60	1.38		28.05	1.39
1.90	1.63		28.33	1.40
2.36	1.58		29.72	1.43
3.43	1.35		30.23	1.53
3.71	1.48		31.45	1.49
4.11	1.95		33.25	1.45
4.52	1.61		33.68	1.40
4.70	1.62		34.80	1.55
5.06	1.52		35.11	1.42
5.22	1.72		36.26	1.55
5.61	1.43		36.35	1.44
5.72	1.58		36.65	1.54
6.12	1.56		37.86	1.40
6.24	1.56		38.30	1.54
6.65	1.57		39.37	1.39
6.78	1.68		41.20	1.52
7.28	1.66		41.65	1.42
7.70	1.44		42.80	1.62
7.82	1.65		43.02	1.53
8.20	1.64		44.55	1.34
8.26	1.87		45.00	1.54
9.24	1.49		45.36	1.50
10.43	1.69		45.64	1.52
10.74	1.59			
11.92	1.57			
12.18	1.66			
14.09	1.48			
16.24	1.53			
18.50	1.60			
18.43	1.49			
19.85	1.42			
20.08	1.53			
20.15	1.50			
20.48	1.26			
20.89	1.53			
22.62	1.60			
22.92	1.60			
23.07	1.51			
24.44	1.44			
24.90	1.40			
25.97	1.27			

UE6s Gravimetric Water Content Measurements

Sample	Depth	Water Content	Sample	Depth	Water Content
UE6s	(m)	(g g ⁻¹)		(m)	(g g ⁻¹)
1-1 top	0.0	0.16	30-2	18.2	0.07
1-1 bottom	0.1	0.16	31-1	18.4	0.12
2-1 top	0.5	0.19	31-2	18.5	0.14
2-1 bottom	0.6	0.19	32-1	18.4	0.12
2-3	0.8	0.20	33-1	19.8	0.11
2-4	1.0	0.16	34-1	20.1	0.14
3-1	1.1	0.16	34-2	20.2	0.15
3-3	1.4	0.10	34-4	20.4	0.13
3-4	1.6	0.12	35-1	20.5	0.13
4-1	1.9	0.14	35-4	20.9	0.07
4-3	2.2	0.09	36-1	22.6	0.09
4-4	2.4	0.09	37-1	22.8	0.09
5-1	2.5	0.12	37-2	22.9	0.11
5-3	2.8	0.08	37-3	23.1	0.10
6-1	3.1	0.10	39-1	24.4	0.14
7-1	3.4	0.14	39-4	24.9	0.10
7-2	3.6	0.08	40-1	26.0	0.16
8-1	3.7	0.07	40-3	26.3	0.14
9-1	4.1	0.04	40-4	26.4	0.15
9-3	4.4	0.08	41-1	28.1	0.15
9-4	4.5	0.08	42-1	28.2	0.13
10-1	4.6	0.08	42-3	28.6	0.11
10-2	4.7	0.08	43-1	29.7	0.08
12-1	5.1	0.09	44-1	30.2	0.17
12-2	5.1	0.08	45-1	31.4	0.12
13-1	5.2	0.09	45-4	31.9	0.08
13-4	5.6	0.07	47-1	33.3	0.14
14-1	5.7	0.07	47-4	33.7	0.12
14-4	6.1	0.13	47-5	33.8	0.11
15-1	6.2	0.10	48-1	34.8	0.10
15-3	6.5	0.10	48-3	35.1	0.12
15-4	6.2	0.12	48-4	35.3	0.15
16-1	6.7	0.12	49-1	36.3	0.11
17-1	7.3	0.07	49-2	36.3	0.14
17-3	7.6	0.09	49-4	36.7	0.12
17-4	7.7	0.10	50-1	37.8	0.13
18-1	7.8	0.11	50-2	37.9	0.11
18-4	8.2	0.08	50-5	38.3	0.15
19-1	8.3	0.08	51-1	39.4	0.10
19-3	8.5	0.08	52-1	41.0	0.08
20-3	9.2	0.09	52-2	41.2	0.09
21-1	10.4	0.08	53-1	41.5	0.12
21-3	10.7	0.07	53-2	41.7	0.17
22-1	11.0	0.07	54-1	42.8	0.09
23-1	11.9	0.11	54-2	43.0	0.11
23-3	12.2	0.12	55-1	43.4	0.10
23-5	12.5	0.09	56-1	44.5	0.18
25-1	14.1	0.13	56-4	45.0	0.10
25-4	14.5	0.14	57-1	45.1	0.13
27-1	16.2	0.06	57-3	45.2	0.13
29-1	17.7	0.04	57-5	45.6	0.11

**Yucca Flat Shallow Series Cores
Gravimetric Water Content Measurements**

Sample	Depth	Water Content		Sample	Depth	Water Content
	(m)	(g g ⁻¹)			(m)	(g g ⁻¹)
A1-1	0.08	0.06		B1-1	0.08	0.05
A1-2	0.53	0.12		B1-2	0.53	0.11
A1-4	1.45	0.06		B1-4	1.45	0.09
A1-6	2.36	0.07		B1-6	2.36	0.06
A1-8	3.28	0.13		B1-7	2.82	0.10
A1-10	4.19	0.07		B1-9	3.73	0.06
A1-11	4.65	0.09		B1-11	4.65	0.07
A1-12	4.95	0.07				
				B2-1	0.08	0.04
A2-1	0.08	0.06		B2-2	0.53	0.10
A2-2	0.53	0.15		B2-4	1.45	0.10
A2-4	1.45	0.09		B2-6	2.36	0.06
A2-6	2.36	0.10		B2-8	3.28	0.08
A2-8	3.28	0.07		B2-10	4.19	0.07
A3-1	0.08	0.03				
A3-2	0.53	0.11				
A3-4	1.45	0.10				
A3-6	2.36	0.08				
A3-8	3.28	0.06				
A3-10	4.19	0.06				
A3-12	4.95	0.06				
A4-1	0.08	0.03				
A4-2	0.53	0.07				
A4-4	1.45	0.05				
A4-6	2.36	0.08				
A4-8	3.28	0.08				
A5-1	0.08	0.03				
A5-2	0.53	0.10				
A5-4	1.45	0.10				
A5-6	2.36	0.07				
A5-8	3.28	0.07				
A5-10	4.19	0.11				
A5-12	4.95	0.08				

UE6e Gravimetric Water Content Measurements

Depth (m)	Water Content (g g ⁻¹)	Depth (m)	Water Content (g g ⁻¹)
42.0	0.20	257.4	0.17
46.9	0.12	260.4	0.12
52.4	0.11	263.5	0.17
57.9	0.10	266.2	0.20
65.8	0.14	269.3	0.19
72.5	0.10	274.7	0.16
78.6	0.12	278.7	0.18
83.8	0.11	281.8	0.16
94.1	0.12	284.5	0.18
100.5	0.12	287.5	0.16
106.6	0.11	290.9	0.17
111.8	0.11	294.2	0.11
116.4	0.15	297.3	0.08
124.0	0.11	300.0	0.18
134.0	0.12	303.1	0.17
138.6	0.13	306.1	0.19
141.0	0.13	310.7	0.18
145.3	0.11	315.3	0.09
147.7	0.14	318.3	0.18
152.3	0.18	321.4	0.16
156.3	0.15	324.4	0.12
158.7	0.14	327.4	0.16
163.9	0.17	330.5	0.09
173.0	0.13	335.1	0.09
176.1	0.16	341.2	0.09
182.8	0.16	348.8	0.10
185.8	0.16	352.7	0.09
190.4	0.17	361.0	0.08
198.0	0.17	366.1	0.10
204.7	0.15	373.1	0.11
207.4	0.17	378.6	0.10
211.4	0.17	385.3	0.12
213.2	0.15	389.9	0.08
216.3	0.18	396.0	0.10
219.3	0.18	401.2	0.10
223.9	0.14	408.2	0.11
226.9	0.19	409.7	0.13
230.0	0.17	412.7	0.14
233.0	0.18	414.3	0.19
236.1	0.16	420.3	0.10
239.1	0.19	447.2	0.16
243.7	0.18	449.3	0.16
251.3	0.15		

UE6s Water Potential Measurements

Sample	Depth	Water Potential	Water Potential
UE6s	(m)	(MPa)	(m)
2-4	1.00	0.00	
3-3	1.45	-3.47	-368
4-3	2.20	-3.82	-404
5-3	2.82	-4.32	-456
7-2	3.58	-3.55	-376
9-3	4.39	-2.64	-282
12-2	5.14	-3.55	-376
15-3	6.55	-3.06	-325
17-3	7.56	-3.06	-325
19-3	8.48	-2.50	-268
22-3	10.97	-2.57	-275
23-5	12.47	-2.36	-253
25-4	14.57	-1.87	-203
30-2	18.23	-2.01	-217
34-4	20.39	-1.31	-145
37-1	22.86	-1.59	-174
40-3	26.30	-1.11	-124
42-3	28.60	-0.97	-110
45-4	32.93	-0.90	-103
47-5	33.80	-1.17	-131
48-4	35.28	-0.83	-96
50-1	37.80	-1.04	-117
52-1	41.00	-1.03	-117
55-1	43.40	-0.69	-81
57-1	45.14	-0.90	-103

Yucca Flat Shallow Series “A” Cores, Water Potential Measurements

Sample	Depth	Water Potential	Water Potential
	(m)	(MPa)	(m)
A1-1	0.08	-18.9	-1957
A1-2	0.53	-2.1	-224
A1-4	1.45	-4.1	-434
A1-6	2.36	-5.3	-558
A1-8	3.28	-4.7	-499
A1-10	4.19	-13.9	-1437
A1-11	4.65	-3.1	-333
A1-12	4.95	-2.9	-311
A2-1	0.08	-5.5	-575
A2-2	0.53	-3.5	-371
A2-4	1.45	-4.5	-470
A2-6	2.36	-5.1	-535
A2-8	3.28	-6.4	-668
A3-1	0.08	-23.4	-2418
A3-2	0.53	-3.3	-354
A3-4	1.45	-4.5	-469
A3-6	2.36	-4.7	-499
A3-8	3.28	-5.8	-609
A3-10	4.19	-5.2	-543
A3-12	4.95	-4.2	-448
A4-1	0.08	-32.0	-3305
A4-2	0.53	-2.6	-281
A4-4	1.45	-3.0	-317
A4-6	2.36	-4.5	-476
A4-8	3.28	-4.7	-491
A5-1	0.08	-23.4	-2422
A5-2	0.53	-1.4	-159
A5-4	1.45	-1.2	-138
A5-6	2.36	-3.1	-331
A5-8	3.28	-6.3	-660
A5-10	4.19	-4.1	-433
A5-12	4.95	-5.2	-550

Yucca Flat shallow series "B" cores, Water Potential Measurements

Sample	Depth	Water Potential	Water Potential
	(m)	(MPa)	(m)
B1-1	0.08	-8.2	-854
B1-2	0.53	-1.1	-124
B1-4	1.45	-2.6	-274
B1-6	2.36	-4.8	-506
B1-7	2.82	-4.8	-506
B1-9	3.73	-5.0	-528
B1-11	4.65	-4.2	-441
B2-1	0.08	-13.1	-1360
B2-2	0.53	-1.6	-174
B2-4	1.45	-6.3	-661
B2-6	2.36	-6.4	-668
B2-8	3.28	-5.9	-617
B2-10	4.19	-5.7	-602

**Yucca Flat Shallow Series cores, Chloride and Nitrate Measurements
(in porewater concentrations)**

Sample	Depth (m)	Chloride (mg L ⁻¹)	NO ₃ ⁻ N (mg L ⁻¹)
A1-1	0.08	73.6	148.5
A1-2	0.53	51.2	55.3
A1-3	0.99	57.9	2129.4
A1-4	1.29	2276.0	3404.2
A1-5	1.75	1885.9	2921.1
A1-6	2.21	2412.2	3678.6
A1-7	2.67	1739.9	2598.6
A1-8	3.12	1557.0	2265.4
A1-9	3.58	590.9	966.5
A1-10	4.04	935.3	1531.2
A1-11	4.49	749.3	1064.5
A1-12	4.95	418.1	650.7
A2-1	0.08	42.9	50.0
A2-2	0.53	127.1	101.1
A2-3	0.99	1076.8	775.0
A2-4	1.45	3480.4	495.5
A2-5	1.90	995.6	1015.8
A2-6	2.36	1423.9	1698.2
A2-7	2.82	1347.5	1677.8
A2-8	3.27	789.2	1011.3
A3-1	0.08	54.2	27.9
A3-2	0.53	26.9	64.5
A3-3	0.84	5.7	8.5
A3-4	1.45	4.7	19.2
A3-5	1.90	431.4	285.0
A3-6	2.36	561.4	363.8
A3-7	2.82	270.0	195.5
A3-8	3.27	178.1	5.3
A3-9	3.73	30.1	31.4
A3-10	4.19	40.3	26.7
A3-11	4.49	69.1	75.2
A3-12	4.95	13.5	2.0
A4-1	0.08	1006.2	83.1
A4-2	0.53	77.4	4.4
A4-3	0.99	42.7	38.9
A4-4	1.45	49.3	27.3
A4-5	1.90	156.6	106.2
A4-6	2.36	133.5	403.0

**Yucca Flat shallow series cores, Chloride and Nitrate Measurements
(in porewater concentrations) continued**

Sample	Depth (m)	Chloride (mg L ⁻¹)	NO ₃ ⁻ N (mg L ⁻¹)
A4-7	2.82	1156.1	918.3
A4-8	3.27	676.3	575.9
A5-1	0.08	79.8	104.9
A5-2	0.53	155.7	96.3
A5-3	0.99	88.5	28.9
A5-4	1.45	115.0	21.5
A5-5	1.90	2055.7	1475.5
A5-6	2.36	636.8	4601.8
A5-7	2.82	2592.5	2492.7
A5-8	3.27	2463.8	2451.4
A5-9	3.73	814.2	964.6
A5-10	4.19	549.6	606.8
A5-11	4.65	650.9	791.4
A5-12	4.95	573.4	650.5
B1-1	0.08	33.9	29.7
B1-2	0.53	103.9	25.9
B1-3	0.99	781.9	1127.0
B1-4	1.45	869.6	789.5
B1-5	1.90	2218.2	2668.3
B1-6	2.36	2631.6	3304.2
B1-7	2.82	1458.4	2032.3
B1-8	3.27	1209.6	1761.4
B1-9	3.73	764.4	1309.8
B1-10	4.19	1012.1	1358.3
B1-11	4.65	558.8	793.3
B1-12	4.95	856.1	1106.2
B2-1	0.08	44.8	51.6
B2-2	0.53	108.1	166.1
B2-3	0.99	638.9	2336.3
B2-4	1.45	460.0	4873.4
B2-5	1.90	3705.9	4653.1
B2-6	2.36	1454.7	3776.9
B2-7	2.82	3161.2	4402.8
B2-8	3.27	1881.4	2466.5
B2-9	3.73	1077.1	1516.1
B2-10	4.19	1088.4	1601.0
B2-11	4.65	803.8	1213.8
B2-12	4.95	619.8	969.2

UE6s Chloride Measurements (in porewater concentrations)

Sample	Depth	Chloride	Sample	Depth	Chloride
UE6s	(m)	(mg L ⁻¹)	UE6s	(m)	(mg L ⁻¹)
1-1	0.08	0	31-1	18.35	53
2-1	0.53	89	31-2	18.50	137
2-3	0.84	75	32-1	18.43	139
2-4	0.99	26	33-1	19.85	51
3-1	1.14	139	34-1	20.08	123
3-3	1.45	1251	34-2	20.15	160
3-4	1.60	1900	34-4	20.38	8
4-1	1.90	1156	35-1	20.48	35
4-3	2.21	1615	35-4	20.89	157
4-4	2.36	2135	36-1	22.62	19
5-1	2.51	1312	37-1	22.82	16
5-3	2.82	2455	37-2	22.92	31
6-1	3.12	2179	37-3	23.07	99
7-1	3.43	1657	39-1	24.44	22
7-2	3.58	981	39-4	24.90	113
8-1	3.71	1875	40-1	25.97	13
9-1	4.11	1459	40-3	26.27	10
9-3	4.39	750	40-4	26.42	90
9-4	4.52	565	41-1	28.05	18
10-1	4.59	704	42-1	28.33	92
10-2	4.70	547	42-3	28.58	16
12-1	5.06	582	43-1	29.72	13
12-2	5.14	332	44-1	30.23	15
13-1	5.22	330	45-1	31.45	14
13-4	5.61	391	45-4	31.91	9
14-1	5.72	279	47-1	33.25	ND
14-4	6.12	341	47-4	33.68	61
15-1	6.24	272	47-5	33.78	9
15-3	6.52	156	48-1	34.80	ND
15-4	6.65	387	48-3	35.11	43
16-1	6.78	212	48-4	35.26	11
17-1	7.28	229	49-1	36.26	ND
17-3	7.56	139	49-2	36.35	17
17-4	7.70	259	49-4	36.65	48
18-1	7.82	141	50-1	37.78	7
18-4	8.20	255	50-2	37.86	ND
19-1	8.26	136	50-5	38.30	61
19-3	8.48	91	51-1	39.37	ND
20-3	9.24	244	52-1	40.97	6
21-1	10.43	102	52-2	41.20	ND
21-3	10.74	264	53-1	41.50	ND
22-1	10.97	45	53-2	41.65	10
23-1	11.92	135	54-1	42.80	ND
23-3	12.18	47	54-2	43.02	ND
23-5	12.45	33	55-1	43.41	4
25-1	14.09	59	56-1	44.55	ND
25-4	14.54	41	56-4	45.00	ND
27-1	16.24	59	57-1	45.09	5
29-1	17.74	72	57-3	45.36	ND
30-2	18.20	34	57-5	45.64	ND

UE6e Chloride Measurements (in porewater concentrations)

Depth (m)	Chloride (mg L ⁻¹)	Depth (m)	Chloride (mg L ⁻¹)	Depth (m)	Chloride (mg L ⁻¹)
41.6	123	213.9	82	348.2	67
42.5	75	217.8	ND	350.5	95
47.1	25	220.8	110	353.0	69
53.8	21	223.5	27.38	355.0	77
55.1	28.	231.0	49.28	360.3	83
58.7	53	233.3	ND	362.8	72
65.8	52	237.4	107	365.9	144
71.9	161	240.0	ND	367.4	323
73.5	21	243.2	111	381.1	76
77.5	78	246.0	111	384.0	ND
79.2	128	249.0	96	388.6	80
84.6	50	252.1	97	390.3	69
90.7	49	254.9	74	394.2	123
94.1	66	258.0	166	397.1	130
111.6	54	261.0	191	401.0	ND
113.8	71	264.3	229	402.8	ND
116.7	26	267.0	ND	407.8	59
123.7	47	270.5	177	409.3	ND
126.2	65	274.0	106	413.7	ND
132.3	51	276.4	181	416.8	ND
134.7	79	279.4	ND	419.9	ND
138.8	83	282.1	94	421.5	153
141.2	87	285.0	85		
146.2	ND	287.5	115		
148.5	16	290.4	ND		
157.3	70	294.4	177		
159.4	129	298.1	48		
164.7	96	301.1	1214		
167.3	123	304.8	117		
171.7	62	306.3	ND		
174.1	100	310.1	94		
176.1	94	312.7	ND		
176.6	171	316.8	ND		
183.9	ND	319.5	59		
186.6	115	322.9	ND		
192.1	76	325.0	90		
194.6	191	328.7	54		
198.5	70	330.9	89		
201.1	ND	334.9	71		
204.8	110	336.7	71		
207.2	97	340.9	ND		
211.7	137	343.7	100		

UE6s Stable Isotope, δD and $\delta^{18}\text{O}$, Measurements

Sample	Depth	δD	$\delta^{18}\text{O}$
UE6s	(m)	(‰)	(‰)
1-2	0.23	-85	-8.0
4-2	2.07	-91	-9.0
8-2	3.83	-100	-11.6
14-2	5.85	-101	-11.4
17-2	7.41	-99	-11.4
20-2	9.06	-108	-13.0
23-2	12.03	-106	-12.7
25-2	14.24	-106	-12.7
29-2	17.91	-106	-13.2
35-2	20.64	-108	-12.9
39-2	24.60	-109	-13.3
43-2	29.98	-111	-13.8
47-2	33.53	-110	-14.5
51-2	39.52	-115	-15.2
57-2	45.21	-118	-15.3

APPENDIX C

DATA FROM THE TRANS-PECOS UNSATURATED ZONE CORES

Trans-Pecos Cores Bulk Density Measurements

Trans-Pecos Cores Gravimetric Water Content and Water Potential Measurements

Trans-Pecos Cores, Chloride, Bromide, Fluoride, and Nitrate Measurements

Trans-Pecos Cores - Bulk Density Measurements

Sample	Depth	Bulk Density	Ave*. Bulk Density
	(m)	(g cm ⁻³)	(g cm ⁻³)
GD5-4A	2.97	1.54	1.63
GD5-4B	2.97	1.60	
GD5-4C	2.97	1.76	1.57
GD6-3A	3.43	1.46	
GD6-3B	3.43	1.68	1.68
GD11-3A	8.30	1.66	
GD11-3B	8.30	1.71	1.50
GD12-4A	9.67	1.40	
GD12-4B	9.67	1.60	
GS5-3A	2.82	1.56	1.54
GS5-3B	2.82	1.53	
GS7-3A	4.04	1.79	1.75
GS7-3B	4.84	1.71	
GS8-3A	4.65	1.72	1.68
GS8-3B	4.65	1.63	
GS9-3A	5.86	1.22	1.28
GS9-3B	5.86	1.34	
GS11-3A	8.30	1.71	1.70
GS11-3B	8.30	1.69	
GS12-2A	9.37	1.58	1.59
GS12-2B	9.37	1.60	
DA5-3A	2.97	1.70	1.61
DA5-3B	2.97	1.52	
DA6-3A	3.43	1.88	1.83
DA6-3B	3.43	1.79	
DA7-2A	3.88	1.78	1.72
DA7-2B	3.88	1.66	
DA11-4A	8.45	1.92	1.87
DA11-4B	8.45	1.83	

*average for duplicate samples A and B

**Trans-Pecos Desert scrub (SA and SB) Cores
Water Content and Water Potential Measurements**

Sample	Depth	Gravimetric Water Content	Water Potential	Water Potential
	(m)	(g g ⁻¹)	(MPa)	(m)
SA1-3	0.38	0.10	-0.24	-35
SA2-4	1.14	0.03	-7.90	-824
SA3-4	1.75	0.02	-8.84	-921
SA4-4	2.36	0.02	-8.70	-906
SA5-3	2.82		-10.60	1102
SA5-4	2.97	0.02	-9.76	-1016
SA6-1	3.12		-8.43	-879
SA6-2	3.27	0.02	-10.70	-1112
SA7-3	4.04	0.02	-7.71	-804
SA8-4	4.80	0.02	-7.31	-763
SA9-4	6.02	0.03	-5.94	-622
SA10-3	7.08	0.03	-4.78	-503
SA11-3	8.30	0.03	-4.55	-479
SA12-4	9.67	0.03	-2.72	-290
SB1-4	0.50	0.14	-0.14	-25
SB2-4	1.10	0.03	-10.10	-1051
SB3-4	1.80	0.02	-8.61	-897
SB4-3	2.20	0.03	-8.46	-882
SB5-3	2.80	0.04	-8.00	-834
SB6-3	3.40	0.09	-8.24	-859
SB7-4	4.20	0.02	-7.48	-781
SB8-4	4.80	0.02	-7.14	-746
SB9-3	5.90	0.02	-5.49	-576
SB10-3	7.10	0.03	-6.80	-711
SB10-4	7.20	0.03	-5.84	-612
SB11-4	8.50	0.02	-4.83	-508
SB12-4	9.70	0.03	-2.23	-240
SB13-4	12.10	0.04	-2.62	-280
SB14-2	14.20	0.05	-0.81	-94
SB14-4	14.50	0.03	-0.82	-95

**Trans-Pecos Grassland (GD and GS) Cores
Water Content and Water Potential Measurements**

Sample	Depth	Gravimetric Water Content	Water Potential	Water Potential
	(m)	(g g ⁻¹)	(MPa)	(m)
GD1-2	0.23	0.11	- -11.60	-1205
GD1-3	0.38	0.11	-9.69	-1009
GD2-3	0.99	0.11	-9.64	-1003
GD3-3	1.60	0.10	-5.84	-612
GD4-4	2.36	0.09	-2.29	-246
GD5-4	2.97	0.12	-1.89	-205
GD6-3	3.43	0.11	-3.76	-398
GD7-3	4.04	0.04	-2.17	-234
GD8-3	4.65	0.13	-2.41	-259
GD9-2	5.71	0.13	-2.15	-232
GD10-3	7.08	0.15	-2.56	-274
GD11-3	8.30	0.16	-2.56	-274
GD11-4	8.45		-2.29	-246
GD12-3	9.52		-8.22	-856
GD12-4	9.67	0.08	-9.37	-975
GD13-4	12.11	0.05	-1.28	-142
GD14-3	14.39	0.17	-1.66	-181
GS1-3	0.38	0.10	-13.50	-1401
GS2-2	0.84	0.09	-8.97	-934
GS3-4	1.75	0.13	-5.16	-542
GS4-3	2.21	0.14	-4.49	-473
GS5-3	2.82	0.14	-4.55	-479
GS6-4	3.58	0.11	-5.00	-525
GS7-3	4.04	0.07	-4.67	-491
GS8-3	4.65	0.12	-4.12	-435
GS9-3	5.86	0.06	-3.74	-396
GS10-3	7.08	0.05	-2.47	-265
GS11-3	8.30	0.14	-2.98	-317
GS12-2	9.37	0.12	-3.25	-345

**Trans-Pecos Recently Encroached Desert scrub (DA) Core
Water Content and Water Potential Measurements**

Sample	Depth	Gravimetric Water Content	Water Potential	Water Potential
	(m)	(g g ⁻¹)	(MPa)	(m)
DA1-4	0.53	0.03	-8.42	-878
DA2-4	1.14	0.04	-7.75	-809
DA3-3	1.60	0.07	-5.22	-548
DA4-4	2.36	0.09	-5.97	-625
DA5-3	2.82	0.09	-5.83	-611
DA6-3	3.43	0.10	-6.91	-722
DA7-2	3.88	0.08	-5.20	-546
DA8-4	4.80	0.13	-5.31	-557
DA9-1	5.56	0.04	-5.40	-567
DA10-4	7.23	0.10	-4.79	-504
DA11-4	8.45	0.06	-4.86	-511
DA12-3	8.91	0.10	-4.07	-430

**Trans-Pecos Juniper Stand (JA and JB) Cores
Water Content and Water Potential Measurements**

Sample	Depth	Gravimetric Water Content	Water Potential	Water Potential
	(m)	(g g ⁻¹)	(MPa)	(m)
JA1-3	0.38	0.04	-0.33	-44
JA2-2	0.84	0.03	-2.69	-287
JA3-3	1.60	0.03	-4.81	-506
JA4-3	2.21	0.03	-3.93	-415
JA5-4	2.97	0.03	-3.18	-338
JA6-4	3.58	0.03	-4.49	-473
JA7-3	4.04	0.03	-3.24	-344
JA8-3	4.65	0.03	-1.66	-181
JA9-4	6.02	0.05	-1.31	-145
JA10-4	7.23	0.03	-1.39	-153
JA11-3	8.45	0.04	-1.07	-121
JB1-3	0.38	0.03	-4.76	-501
JB2-4	0.99	0.03	-3.84	-406
JB3-4	1.75	0.03	-4.34	-457
JB4-4	2.36	0.03	-4.05	-427
JB5-4	2.97	0.03	-2.81	-300
JB6-4	3.58	0.03	-2.72	-290
JB7-3	4.04	0.03	-2.11	-228
JB8-3	4.65	0.04	-1.39	-153
JB9-4	6.02	0.06	-1.63	-178

Trans-Pecos Desert scrub (SA and SB) cores
Chloride, Bromide, Fluoride, and Nitrate Measurements
(as porewater concentrations)

Sample	Depth	Chloride	Bromide	Fluoride	NO ₃ ⁻ -N
	(m)	(mg L ⁻¹)			
SA1-3	0.38	14.4	0.2	< 1.0	0.5
SA2-4	1.14	253.2	3.9	17.1	< 0.5
SA3-4	1.75	4113.8	53.7	16.1	< 0.5
SA4-4	2.36	8203.8	68.4	37.4	911.5
SA5-4	2.97	8479.4	69.6	36.5	1087.1
SA6-2	3.27	6845.5	63.9	43.4	1140.9
SA7-3	4.04	4993.1	34.5	191.4	790.6
SA8-4	4.80	6029.3	38.6	91.6	916.5
SA9-4	6.02	3541.9	21.9	79.1	358.0
SA10-3	7.08	3218.8	14.9	61.0	8.1
SA11-3	8.30	3096.2	14.5	63.4	294.7
SA12-4	9.67	1559.9	3.7	64.4	234.0
SB1-3	0.38	4.0	<0.5		32.4
SB1-4	0.53	13.6	0.3	0.1	18.5
SB2-4	1.14	46.8	3.4	0.4	1.7
SB3-4	1.75	113.1	2.4	2.1	0.7
SB4-3	2.21	58.9	<0.5	1.4	1.2
SB5-2	2.67	30.7	0.7		1.8
SB5-3	2.82	49.0	1.0	0.8	1.5
SB6-3	3.43	399.1	2.9	5.1	1.7
SB7-3	4.04	670.8	4.1		2.1
SB7-4	4.19	307.1	2.3	9.9	5.2
SB8-4	4.80	73.0	0.7	2.2	2.6
SB9-3	5.86	106.9	<0.5	4.5	1.6
SB10-2	6.93	93.0	0.5		1.3
SB10-3	7.08	42.3	0.5	2.3	1.6
SB10-4	7.23	68.4	0.6	3.1	1.0
SB11-4	8.45	50.5	0.8	2.6	1.0
SB12-4	9.67	60.2	22.5	1.4	0.7
SB13-4	12.11	43.4	<0.5	3.4	0.4
SB14-2	14.24	68.3	<0.5	2.8	1.6
SB14-3	14.39	90.2			0.6
SB14-4	14.54	341.3	1.0	18.3	0.5

Trans-Pecos Grassland (GD and GS) cores
Chloride, Bromide, Fluoride, and Nitrate Measurements
(as porewater concentrations)

Sample	Depth	Chloride	Bromide	Fluoride	NO ₃ ⁻ -N
	(m)	(mg L ⁻¹)			
GD1-2	0.23	29.4	3.3	2.8	0.02
GD2-3	0.99	109.5	2.6	16.4	0.02
GD3-3	1.60	1098.2	13.0	42.9	10.6
GD4-4	2.36	1059.1	12.8	33.8	34.2
GD5-4	2.97	841.7	10.1	11.8	39.9
GD6-3	3.43	758.3	7.9	15.9	33.9
GD7-2	3.88	1690.8	16.2		76.4
GD7-3	4.04	615.5	5.1	33.0	31.8
GD8-3	4.65	473.6	4.1	8.4	25.9
GD9-2	5.71	363.9	3.2	5.9	21.7
GD10-3	7.08	406.8	7.1	5.4	35.0
GD11-3	8.30	379.3	3.5	4.2	25.8
GD11-4	8.45	354.8	3.5	14.1	31.8
GD12-3	9.52	536.1	4.7	16.0	21.4
GD12-4	9.67	446.9	4.0	17.6	24.7
GD13-4	12.11	44.7	0.4	26.4	6.4
GD14-2	14.09	11.6			4.1
GD14-3	14.39	19.5	2.3	4.6	6.1
GS1-3	0.38	33.7	2.6	0.1	0.4
GS2-2	0.84	1177.9	13.9	139.2	<0.02
GS3-4	1.75	3132.0	38.0	89.5	<0.02
GS4-3	2.21	2575.6	29.9	76.6	<0.02
GS5-3	2.82	2483.9	29.7	121.2	63.3
GS6-4	3.58	2458.0	32.2	118.7	93.9
GS7-3	4.04	3372.1	39.6	425.2	191.6
GS8-3	4.65	2254.1	26.2	123.0	80.0
GS9-3	5.86	969.1	10.0	>159	137.8
GS10-3	7.08	1324.0	14.3	>221	227.6
GS11-3	8.30	540.5	5.3	>71	16.0
GS12-2	9.37	470.5	4.2	67.9	21.8

**Trans-Pecos Recently Encroached Desert scrub (DA) cores
Chloride, Bromide, Fluoride, and Nitrate Measurements
(as porewater concentrations)**

Sample	Depth	Chloride	Bromide	Fluoride	NO ₃ ⁻ -N
	(m)	(mg L ⁻¹)			
DA1-4	0.53	271.8	15.4	14.4	9.6
DA2-4	1.14	378.5	40.8	3.8	4.1
DA3-3	1.60	699.0	11.1	22.8	18.7
DA4-4	2.36	1050.4	9.7	55.9	12.4
DA5-3	2.82	951.9	7.1	107.4	14.5
DA6-3	3.43	954.8	8.0	140.7	29.5
DA7-2	3.88	1063.7	7.9	275.3	31.1
DA8-3	4.65	1012.4	6.3	5.1	10.0
DA8-4	4.80	1285.4	10.3	235.0	7.1
DA9-1	5.56	1506.4	11.9	419.8	<0.06
DA10-3	7.08	681.8	5.5		7.8
DA10-4	7.23	1129.0	10.1	>100	<0.02
DA11-4	8.45	1529.9	8.8	309.4	0.5
DA12-3	8.91	1094.4	9.5	>100	1.7

**Trans-Pecos Juniper Stand (JA and JB) Cores
Chloride, Bromide, Fluoride, and Nitrate Measurements
(as porewater concentrations)**

Sample	Depth	Chloride	Bromide
	(m)	(mg L ⁻¹)	(mg L ⁻¹)
JA1-3	0.38	41.8	0.7
JA2-2	0.84	143.9	1.6
JA3-3	1.60	67.9	1.7
JA4-3	2.21	35.6	3.6
JA5-4	2.97	76.8	<0.4
JA6-4	3.58	55.1	<0.4
JA7-3	4.04	76.1	0.8
JA8-3	4.65	20.6	<0.2
JA9-4	6.02	8.7	<0.2
JA10-4	7.23	42.1	11.8
JA11-3	8.45	33.1	9.6
JB1-3	0.38	93.3	3.5
JB2-4	0.99	44.0	3.0
JB3-4	1.75	27.3	0.9
JB4-4	2.36	37.6	10.0
JB5-4	2.97	27.0	<0.3
JB6-4	3.58	25.0	0.5
JB7-3	4.04	28.6	0.7
JB8-3	4.65	34.5	0.6
JB9-4	6.02	25.7	0.3

**Trans-Pecos McKeel Desert scrub (SA) Core
Stable Chlorine Isotopic Ratios**

Sample	Depth	$\delta^{37}\text{Cl}$
	(m)	(‰ SMOC)
SA3-4	1.80	-0.2
SA4-3	2.20	-0.6
SA6-1	3.10	-1.0
SA7-4	4.20	-0.9
SA9-3	5.90	+0.4
SA11-4	8.50	+0.5
SA12-3	9.50	-0.2